

THERMAL-MECHANICAL DESIGN AND DETECTOR
CHARACTERIZATION OF THE LIMB IMAGING
FOURIER TRANSFORM SPECTROMETER
EXPERIMENT

A Thesis Submitted to the
College of Graduate and Postdoctoral Studies
in Partial Fulfillment of the Requirements
for the degree of Master of Science
in the Department of Physics & Engineering Physics
University of Saskatchewan
Saskatoon

By
Connor J. Schentag

©Connor J. Schentag, May/2020. All rights reserved.

PERMISSION TO USE

In presenting this thesis in partial fulfilment of the requirements for a Postgraduate degree from the University of Saskatchewan, I agree that the Libraries of this University may make it freely available for inspection. I further agree that permission for copying of this thesis in any manner, in whole or in part, for scholarly purposes may be granted by the professor or professors who supervised my thesis work or, in their absence, by the Head of the Department or the Dean of the College in which my thesis work was done. It is understood that any copying or publication or use of this thesis or parts thereof for financial gain shall not be allowed without my written permission. It is also understood that due recognition shall be given to me and to the University of Saskatchewan in any scholarly use which may be made of any material in my thesis.

Requests for permission to copy or to make other use of material in this thesis in whole or part should be addressed to:

Head of the Department of Physics & Engineering Physics
163 Physics Building, 116 Science Place
University of Saskatchewan
Saskatoon, Saskatchewan, S7N 5E2, Canada

OR

Dean
College of Graduate and Postdoctoral Studies
University of Saskatchewan
116 Thorvaldson Building, 110 Science Place
Saskatoon, Saskatchewan, S7N 5C9, Canada

ABSTRACT

The Limb Imaging Fourier Transform Experiment (LIFE) is a prototype of a satellite remote sensing instrument being developed at the University of Saskatchewan in collaboration with the Canadian Space Agency and ABB Inc. The prototype instrument is designed to take measurements of key atmospheric greenhouse gases on-board a high-altitude balloon gondola, to test the concept and provide insight towards future versions of the instrument. It will take measurements from the stratosphere, providing a vertical profile from the lower stratosphere to the upper troposphere, known as the UTLS region, an important region for understanding climate change. LIFE is conceptually similar to the Gimballed Limb Observer for Radiance Imaging in the Atmosphere (GLORIA), and aims to create a less expensive and smaller instrument to show that a cost-effective infrared Fourier Transform Spectrometer based atmospheric instrument is feasible.

This thesis describes two main aspects of the LIFE prototype: The thermal-mechanical design and the characterization of the infrared detector. As a thermal imaging instrument, LIFE has strict thermal requirements and constraints in the harsh high-altitude environment. A thermal-mechanical design is developed and simulated to ensure that all requirements are met and the instrument will operate nominally during its high-altitude balloon flight. The infrared detector must be carefully characterized and optimized for the LIFE application through the altering and optimization of detector settings, to ensure that the measurements taken are of the best possible quality.

The instrument successfully flew on its first test flight in Timmins, Ontario in August of 2019. All design requirements were met and the instrument operated nominally, taking numerous successful measurements of the UTLS. The goal of creating a design that would allow the survival and operation of the instrument in a high-altitude environment as well as the goal of optimizing the detector were both completed successfully. Overall, the goal of creating a low cost instrument that allows thermal emission measurements to be taken in the UTLS region was completed, and the knowledge gained from the project can be used to inform future improvements to the LIFE instrument.

ACKNOWLEDGEMENTS

I would first like to offer my deepest thanks to my supervisors, Doug Degenstein and Adam Bourassa. They brought me onto the LIFE team and gave me a project that I felt very proud to be part of. Their help and support through this thesis and through the development of LIFE has been greatly appreciated.

I would also like to thank the rest of the members of the LIFE team, Paul Loewen, Jeff Langille, Ethan Runge, and Daniel Letros. They made working on LIFE even better than it would have been alone. Spending long hours building with Paul, figuring out the detector with Jeff, and hanging out in both the lab and in Timmins with Ethan and Daniel was always fun, even if we were in the midst of a LIFE crisis. This thanks extends to all fellow members of ISAS and the Atmospheric Research Group, who provided a very welcoming environment that I loved being part of.

Finally, I thank my family and friends for supporting me through this project, for never complaining after hearing me talk about all the bolts in my mechanical design for hours.

CONTENTS

Permission to Use	i
Abstract	ii
Acknowledgements	iii
Contents	iv
List of Tables	vii
List of Figures	viii
List of Abbreviations	xii
1 Introduction	1
1.1 Overview	1
1.2 LIFE	5
1.3 Outline	6
2 Background	8
2.1 Limb Imaging & The Atmosphere	8
2.1.1 UTLS Overview	8
2.1.2 Techniques	13
2.1.3 Instruments	17
2.2 Thermal Design	19
2.2.1 Heat Transfer	20
2.2.2 Balloon Environment	29
2.2.3 Self-Emission	31
2.2.4 Thermal Control Methods	32
2.2.5 Instruments	37
2.3 IR Detectors	42
2.3.1 IR Detector Types	42
2.3.2 MCT Detectors	45
2.3.3 Non-linearity	46
2.3.4 Responsivity	47
2.4 Summary	50
3 Thermal-Mechanical Design	51
3.1 Overview	51
3.2 Requirements	51
3.2.1 Optical Requirements	52

3.2.2	Electronics Requirements	54
3.2.3	Mechanical Requirements	55
3.3	Thermal Environment	57
3.4	Thermal-Mechanical Design & Simulation Software	60
3.4.1	Computer Assisted Design Software	61
3.4.2	Finite Element Analysis	62
3.5	LIFE Thermal-Mechanical Design Process	67
3.5.1	LIFE Preliminary Design: Blackbody Assembly	69
3.5.2	LIFE Preliminary Design: Version 1	74
3.5.3	LIFE Preliminary Design: Version 2	79
3.5.4	LIFE Preliminary Design: Version 3	89
3.5.5	LIFE Preliminary Design: Version 4	95
3.5.6	LIFE Preliminary Design: Version 5	100
3.5.7	LIFE Preliminary Design: Version 6	111
3.5.8	Final LIFE Design: Version 5 Revisited	114
3.6	Pre-flight Construction & Analysis	125
3.6.1	Construction	126
3.6.2	TVAC Tests	128
3.6.3	Final Simulations	131
3.7	Summary	134
4	Post-Flight Analysis	136
4.1	Overview	136
4.2	Flight Campaign & Results	136
4.3	Mechanical Results	139
4.4	Flight Temperature Model	141
4.4.1	Ascent	144
4.4.2	Float	154
4.4.3	Sunrise	157
4.4.4	Full model	165
4.5	Summary	168
5	Detector Characterization	170
5.1	Overview	170
5.2	LIFE Detector	170
5.3	Detector Verification	171
5.4	Characterization	178
5.4.1	Responsivity	178
5.4.2	Non-linearity	182
5.5	Summary	183
6	Future Work	185
6.1	Overview	185
6.2	LIFE Thermal-Mechanical Design Changes	185
6.3	Further MCT Characterization	189

6.4	Updates to Atmospheric Instrument Flight Thermal Model	190
6.5	Conclusion	191
References		193
Appendix A Post-Flight Simulation Thermal Properties		198
A.1	Ascent Phase: Part 1	199
A.2	Ascent Phase: Part 2	215
A.3	Float Phase	229
A.4	Sunrise Phase	243

LIST OF TABLES

- 3.1 Optical system thermal-mechanical requirements. 54
- 3.2 Temperature limits of the major electrical system components. 55
- 3.3 Equivalentents between thermal and mechanical simulations. 65
- 3.4 Temperature sensor values 700 minutes into the updated SolidWorks simulation and TVAC test. 132

- 5.1 Bias voltage and offset currents as used in the factory calibration, used here as a baseline. 175

LIST OF FIGURES

2.1	Atmospheric layers with a typical pressure and temperature profile. The upper troposphere/lower stratosphere region is shaded grey (Hedin, 1990) (Dee et al., 2011).	10
2.2	Limb emission observation example. For solar or stellar occultation, the sun or a star would be at the end of the LOS, respectively.	14
2.3	Example of a near-perfect blackbody, known as a <i>hohlraum</i> . This is a cross-section of a cylindrical system similar to what is used on the LIFE instrument.	25
2.4	High altitude balloon temperatures in °C during 2018 flight in Timmins, Ontario.	30
2.5	Diagram of a basic Stirling cooler.	33
2.6	Step 1 of the Stirling cycle: isothermal expansion leading to cold absorption.	34
2.7	Step 2 of the Stirling cycle: Both pistons move, there is a constant volume and an increase in pressure.	34
2.8	Step 3 of the Stirling cycle: isothermal compression leading to heat being radiated to surroundings.	34
2.9	Step 4 of the Stirling cycle: Both pistons move, there is a constant volume and a drop in pressure.	35
2.10	An ideal pressure-volume diagram of the Stirling cycle. Non-ideally, this plot is elliptical.	35
3.1	CAD model of LIFE optical system.	52
3.2	The CNES Carmencita gondola which carried LIFE for the test flight.	56
3.3	A shape being converted to finite elements, or a mesh.	63
3.4	Block diagram of the LIFE instrument.	68
3.5	CAD model of LIFE blackbody system.	71
3.6	Oscillation of hot blackbody temperature over 5 hours.	73
3.7	LIFE Version 1.	75
3.8	Original design of the Optics Box.	76
3.9	Version 1.1 of the Optics Box, with dampening and cross-bracing components removed.	78
3.10	CAD model of Version 1 of the Electronics Box.	79
3.11	LIFE Version 2	80
3.12	Version 2 of the Optics Box, which incorporates external radiation plates.	82
3.13	Initial temperature simulation of Optics Box V2, with no heaters and a direct connection to the Electronics Box.	84
3.14	Simulation of Optics Box V2 without an outer wall between the Optics Box and Electronics Box.	85
3.15	Simulation of Optics Box V2 with three heaters at 30 W.	85
3.16	Simulation of Optics Box V2 without any heat flow from the electronics box, and four heaters.	86
3.17	Initial thermal simulation of Electronics Box V1, with a base temperature of -20°C.	88

3.18	Second thermal simulation of Electronics Box V1, with an expanded electronics mounting plate.	88
3.19	Third version of LIFE, with an updated optics box.	89
3.20	Third version of the Optics Box, based on the CATS design.	91
3.21	Simulation of Optics Box V3 with a heater and thermal connection to the Electronics Box.	92
3.22	Simulation of Optics Box V3 with no thermal connection to the Electronics Box.	93
3.23	Simulation of Optics Box V3 with titanium spacers added between the optics breadboard and the side wall.	94
3.24	Second version of the electronics box, following the design of the Optics Box.	96
3.25	Simulations for LIFE V4, Optics Box view, boxes connected.	98
3.26	Simulations for LIFE V4, Electronics Box view, boxes connected.	99
3.27	Simulations for LIFE V4, Optics Box view, with no direct thermal path between boxes.	101
3.28	Simulations for LIFE V4, Electronics Box view, with no direct thermal path between boxes.	102
3.29	Initial version of LIFE Version 5, with the new Blackbody Electronics Box.	103
3.30	Electronics Box Version 3, with more components added.	105
3.31	Initial model of the Blackbody Electronics Box, which contains components which control the blackbodies.	106
3.32	Front and rear view of LIFE V5 cold scenario simulation.	108
3.33	Front and rear view of LIFE V5 average scenario simulation.	109
3.34	Front and rear view of LIFE V5 warm scenario simulation.	110
3.35	LIFE Version 6, which shifted components between electronics boxes to better protect the optics electronics.	112
3.36	A new box, meant to replace the Blackbody Electronics Box, which houses only the optics electronics.	112
3.37	The fourth version of the Electronics Box, which here houses all electronics except the optical system components.	113
3.38	Front and rear view of the final LIFE model cold scenario simulation.	116
3.39	Front and rear view of the final LIFE model average scenario simulation.	117
3.40	Front and rear view of the final LIFE model warm scenario simulation.	118
3.41	The final model of LIFE.	120
3.42	Final version of the Optics Box.	121
3.43	Final version of the Electronics Box.	121
3.44	Final version of the Blackbody Electronics Box.	122
3.45	Mechanical simulation of instrument baseplate, to minimize thickness and weight while maintaining strength.	122
3.46	A top down view of LIFE V5, with bolt locations to the gondola highlighted.	124
3.47	An image provided for the spreadsheet which shows distances to all bolt locations from the centre of the plate.	124
3.48	A render of the LIFE final model, from SolidWorks.	125
3.49	A few images through the LIFE construction process. Images courtesy Paul Loewen.	127

3.50	LIFE after completion, performing initial tests in the lab.	128
3.51	LIFE in the TVAC tank for testing. The silver box beside LIFE is the external cold blackbody used for self-emission tests.	129
3.52	Temperature measurements throughout the second TVAC test.	130
3.53	Front and rear view of the final LIFE model after updates to the thermal model based on the TVAC test data.	133
4.1	LIFE integrated into the CNES gondola.	137
4.2	LIFE being prepared for launch.	138
4.3	Gondola after landing.	139
4.4	A gap between the Electronics Box and baseplate, due to bolt stretching caused by the shock of landing.	140
4.5	Temperatures over the course of the August/September 2019 Timmins flight.	143
4.6	Flight temperatures through the ascent, the first three hours of the flight.	145
4.7	An example of creating the ambient temperature curve for the radiation of a component, specifically for the top surfaces of the boxes for the first half of the ascent.	149
4.8	LIFE thermal model following first half of the ascent.	151
4.9	LIFE thermal model, as the instrument is reaching the float altitude.	152
4.10	Flight temperatures through the ascent, compared to the simulated temperature curves after model updates. The corresponding actual and simulated temperature data is the same colour, with the simulated data shown dashed.	153
4.11	Flight temperatures through the float phase, five and a half hours where most measurements were taken.	155
4.12	LIFE thermal model at the end of the nominal float stage of the flight.	158
4.13	Flight temperatures during the float phase, compared to the simulated temperature curves after model updates. The corresponding actual and simulated temperature data is the same colour, with the simulated data shown dashed.	159
4.14	Flight temperatures as the sun rose and shone on the instrument, up until the end of the flight.	161
4.15	LIFE thermal model at the end of the sunrise stage of the flight, shortly before descent.	163
4.16	Flight temperatures during the sunrise phase, compared to the simulated temperature curves after model updates. The corresponding actual and simulated temperature data is the same colour, with the simulated data shown dashed.	164
4.17	The actual and simulated temperature curves for the entire flight. The corresponding actual and simulated temperature data is the same colour, with the simulated data shown dashed.	166
4.18	A comparison between the current curves of what was measured during flight, and what was input into the simulation.	167
5.1	Image of the MCT Detector in the LIFE instrument.	171
5.2	The result of changing the blackbody temperature on the raw detector signal.	173
5.3	The result of the ambient room temperature changing throughout a longer term test, causing temperature changes in the blackbodies.	174

5.4	Detector raw data output dependence on bias voltage.	176
5.5	Detector raw data output dependence on offset current.	177
5.6	Detector responsivity change with different offset settings.	180
5.7	Detector responsivity change with different bias voltage settings.	181
6.1	Mirror system for viewing vertically upwards towards space, for ground testing.	187

LIST OF ABBREVIATIONS

ACE	Atmospheric Chemistry Experiment
CAD	Computer Assisted Design
CATS	Canadian Atmospheric Tomography System
CSA	Canadian Space Agency
CNES	National Centre for Space Studies
FEA	Finite Element Analysis
FOV	Field of View
FTS	Fourier Transform Spectrometer
GLORIA	Gimballed Limb Observer for Radiance Imaging of the Atmosphere
IFTS	Imaging Fourier Transform Spectrometer
IR	Infrared
LOF	List of Figures
LOS	Line of Sight
LOT	List of Tables
LIFE	Limb Imaging Fourier Transform Spectrometer Experiment
MCT/HgCdTe	Mercury Cadmium Telluride
MIPAS	Michelson Interferometer for Passive Atmospheric Sounding
SPARC	Stratosphere-troposphere Processes And their Role in Climate
STE	Stratosphere-Troposphere Exchange
TVAC	Thermal Vacuum Chamber
UTLS	Upper Troposphere - Lower Stratosphere

1 INTRODUCTION

1.1 Overview

The subject of this thesis is the design, construction and initial post-flight analysis of a new atmospheric remote sensing instrument prototype, the Limb Imaging Fourier Transform Experiment (LIFE). This work focuses on a balloon-borne prototype, which will inform the design of a future satellite-borne version. This instrument is designed to take measurements of greenhouse gases in the atmosphere critical to climate change, in the upper troposphere/lower stratosphere (UTLS) region. Constituents and species in this part of the atmosphere must be measured to fill a gap in data and observations regarding this region, which is important for research into climate change. Measurement of the necessary greenhouse gases requires a thermal imaging instrument, a growing technology in the area of atmospheric instrument research. The LIFE instrument is the first thermal imaging atmospheric research instrument developed by the University of Saskatchewan Institute of Space and Atmospheric Science Atmospheric Research Group, and as such will have constraints and design considerations that are different than previous instruments that have operated in the visible and near infrared spectral range. This includes a highly developed and simulated thermal-mechanical model, which is required due to the thermal imaging capabilities of the instrument, and the complexities of the electronics. The instrument also requires a custom infrared detector, which needs to be characterized and optimized for the LIFE instrument application. LIFE is designed following the success of similar thermal imaging instruments such as the Gimballed Limb Observer for Radiance Imaging in the Atmosphere (GLORIA). LIFE is developed as a cost-effective thermal imaging instrument to allow collaboration and the confirmation of measurements taken by GLORIA. Overall, LIFE is designed as a new instrument prototype to take measurements of greenhouse gases, allowing better knowledge of climate change and

the atmosphere.

There are many reasons why it is important to measure and understand the atmosphere of Earth. The atmosphere, most importantly, is critical to all life on Earth. Without the atmosphere, water would not exist on the surface, life would not be shielded from dangerous cosmic radiation, and the average temperature would be drastically lower. It is important, therefore, to measure how it is changing, and specifically the impact of human activity. Climate change, along with other important atmospheric phenomena such as weather patterns, are all researched through atmospheric models. These models allow prediction of weather, which is important to prepare and mitigate for serious weather effects such as natural disasters. For climate change, it is crucial to understand the effects of pollution in the atmosphere to know the damage caused and what needs to be done to mitigate this. To allow these models to be used in these applications, they need to be as accurate as possible. This requires up-to-date measurements of the atmosphere and its constituents, such as greenhouse gases and aerosols. They also need to be known at all atmospheric layers as the vertical distribution changes the climate sensitivity.

There are many forms of atmospheric instrumentation. Some are launched as satellites, some are implemented as ground-based systems, and many between such as aircraft or balloon-mounted instruments. The majority of these instruments are passive, or *remote sensing*, which gather data without emitting any radiation from the instrument. Data is imaged by looking at the radiation from the atmospheric constituents or the effect they have on radiation from other sources. For all non-ground based instruments, there are two main types: nadir-sounding instruments and limb-sounding instruments. Nadir-sounding instruments take measurements by looking directly down towards Earth, while limb-sounding is when the instrument examines the *limb* of the atmosphere, or tangentially through the atmosphere towards space (Hegglin and Tegtmeier, 2017). Most instruments that gather data on the atmospheric region of interest to this thesis use the limb-sounding method.

Limb-sounding instruments can be classified depending on the source of the measured radiation: solar occultation, stellar occultation, limb scattering, and limb emission. Limb emission works by measuring radiation emitted by the atmosphere, either thermally or photochemically, along the instrument line of sight (LOS). A problem with this method is that

these are generally low signal level measurements, but can be detected with sensitive instruments. This method does not rely on the sun as a source of radiation, so measurements can be made during day or night. Limb scattering instruments measure photons originating from the sun that have been scattered from the atmosphere. This does not require very sensitive instruments but measurements can only be taken in sunlight. Solar occultation measurements look through the atmosphere directly at the sun and measure the spectral attenuation of the solar irradiance. This requires measurements to be taken with the LOS towards the sun. Stellar occultation is similar to solar occultation, however the stars are used as a radiation source rather than the sun, which allows a longer measurement window (Hegglin and Tegtmeier, 2017).

As technology improves and more sensitive detectors are readily available, limb emission and limb scattering methods are becoming more popular. With a complete independence on source for limb emission and only sunlight necessary for limb scattering, measurements can be taken much more often and with less constraint than with other methods. Limb emission in particular has no viewing angle requirements, and can be chosen freely, as long as it is well known to prevent data propagation errors (Griessbach et al., 2016) (Hegglin and Tegtmeier, 2017). This allows a large vertical range, so more of the atmospheric region of interest can be measured. This method is used by LIFE, as well as similar instruments such as the Michelson Interferometer for Passive Atmospheric Sounding (MIPAS) and GLORIA. A common remote sensing device used in limb emission instruments is the Fourier Transform Spectrometer (FTS). FTS systems have a high sensitivity compared to other spectrometers, and can be used with an infrared detector to allow thermal emission measurements. They also have the ability to capture high spectral resolution over a wide spectral range. Almost all thermal limb emission imaging instruments utilize an FTS with an infrared detector to take measurements (Friedl-Vallon et al., 2014) (Fischer et al., 2008).

A key early instrument that utilized an FTS to measure limb emissions from space was the MIPAS instrument. It provided atmospheric data on temperature, trace species and cloud distributions. The overall goal of the instrument was to observe global changes in the composition of the atmosphere resulting from pollution and other man-made effects. On-board the EnviSat satellite developed by the European Space Agency, it provided profiles

of H₂O, O₃, CH₄, N₂O, HNO₃, and NO₂ (Fischer et al., 2008). However, a limitation of this instrument, and similar instruments at the time such as the Atmospheric Chemistry Experiment FTS (ACE-FTS), was that it only had a single detector pixel (Hegglin and Tegtemeier, 2017) (Bernath, 2002). To cover a larger field-of-view (FOV) and measure the atmospheric limb, limb scanning was used, where the instrument moves the LOS upwards and downwards. Eventually, a new type of FTS, known as an Imaging Fourier Transform Spectrometer (IFTS) allowed multiple pixels to image through the FTS at once, removing the need for limb scanning, and creating a better and more uniform image. The first instrument to utilize this technology was GLORIA.

GLORIA is an airborne limb imaging instrument operating in the thermal infrared region, and is conceptually similar to the LIFE instrument that is the focus of this thesis. GLORIA consists of an IFTS device mounted on a gimbal and provides high spatial and spectral resolution measurements of the upper troposphere/lower stratosphere (UTLS) region (Friedl-Vallon et al., 2014) (Sha, 2013). GLORIA utilizes a two-dimensional pixel array to obtain this resolution, as no spatial scanning of the imager is necessary. The detector is sensitive to numerous species, including H₂O, O₃, CCl₄, HNO₃, ClONO₂, HO₂NO₂, and CFCs. With the high spatial resolution, GLORIA will measure the steep gradients in trace gases and characteristics of clouds in the UTLS region, as well as provide insight into the stratosphere-troposphere exchange (STE) that has been affected by climate change and plays an important role in climate models (Sha, 2013) (Riese et al., 2014).

The instruments described above, and any that are operating at atmospheric altitudes, have many design constraints that must be considered as a result of this harsh environment. An important part of the LIFE design and key part of this thesis was considering these constraints and ensuring that it would survive and still be able to take optimal measurements. The thermal environment at these altitudes has a number of considerations that may not have to be considered for either ground based or space based systems. Temperatures during ascent can reach as low as -50°C, and instruments that are operated during daylight can heat drastically due to the sun. This is of particular importance to thermal imaging instruments, as drastic temperature changes in the instrument can effect the data through self-emission, the imaging of instrument optics. Thermal control measures must be used, and thermal

simulations are important to instrument survival. This thesis describes the design process for LIFE, which relies heavily on the thermal requirements and constraints placed on the instrument to develop an operational instrument.

1.2 LIFE

LIFE is designed to use new imaging Fourier Transform Spectrometer (IFTS) technology to image the atmosphere in the thermal regime. It is the second atmospheric instrument to be developed around an IFTS, following the successful development and operation of the GLORIA instrument from the Karlsruhe Institute of Technology (KIT). The improvement in technology of GLORIA and LIFE over previous atmospheric thermal imaging instruments, such as MIPAS, is the vertical imaging capabilities with the IFTS. Previous FTS based instruments took atmospheric images through the use of a single pixel scanning the atmosphere; The use of a pixel array allows single images to be taken and avoid the need for scanning (Riese et al., 2014). LIFE is designed in the footsteps of GLORIA, which aims to meet the capabilities of GLORIA while creating an instrument that is less expensive and has a smaller footprint.

The instrument is designed to measure trace greenhouse gases in the UTLS region. These greenhouse gases play a critical role in climate change, and it is important that information is gathered to inform climate models. There is a gap in knowledge of key greenhouse gases in this region of the atmosphere, and the LIFE and GLORIA instruments aim to close that gap and provide measurements on levels of various constituents in this region. Some of the important greenhouse gases that are measured by the LIFE instrument are as follows: H_2O , O_3 , N_2O , and CH_4 . Operating in a similar spectral range to GLORIA, it is designed to measure in the wavenumber region of 700 cm^{-1} to 1400 cm^{-1} . It will take these measurements from the lower stratosphere, at an altitude of 35 km. The instrument will image vertically from this altitude down to an altitude of 8km (Runge, 2018). This contrasts to the GLORIA instrument, which took measurements from an aircraft at lower altitudes.

The first version of the instrument, as developed in this thesis, is a prototype designed to fly on a high-altitude balloon at the aforementioned altitude of 35 km. As a prototype it

is designed to demonstrate that a IFTS based thermal imaging instrument can be developed and take good measurements for a reasonable cost and size. It will inform future designs of the instrument, eventually leading to a satellite based design. The initial development of the LIFE instrument, including the core optical design and the initial modelling of the optical system, was done by Ethan Runge for his MSc. thesis. This thesis discusses two core tasks of the development of this core prototype: The thermal-mechanical design, and the characterization of the infrared detector.

1.3 Outline

This thesis discusses the thermal-mechanical design of the first balloon-borne prototype of the LIFE instrument, as well as the characterization of the MCT infrared detector. Chapter 2 presents background for the rest of the thesis. A discussion is given for limb imaging in the UTLS, and previous instruments that are the inspiration for the LIFE instrument. Background on the thermal regime of the balloon flight and environment is also discussed, including thermal phenomena, thermal controls and the thermal designs of similar instruments. Finally, this chapter also contains background on different types of infrared detectors, why the MCT detector was chosen, and issues to be characterized.

One of the two main aspects of this thesis is the thermal-mechanical design, which is discussed in Chapter 3. This chapter discusses the requirements for the thermal design, both for the optical system and the electronics. It also discusses the mechanical requirements for the instrument and the flight on-board the National Centre for Space Studies (CNES) gondola. The thermal environment is described in more detail, and the operations of the software used for the simulations is discussed. The majority of this chapter is the process of the thermal and mechanical design of the LIFE instrument, through a variety of iterations, simulations and environments.

Following the flight of the LIFE instrument in the late summer, the thermal model was compared to temperatures seen in flight. This is discussed in Chapter 4. It also discusses the building of a full flight model for future atmospheric flight instruments for all stages of the flight. This section also covers the results of the flight more generally, including the campaign

and mechanical results.

The infrared (IR) detector in the LIFE instrument needed to be characterized with settings chosen for optimal measurements. The process of this characterization is described in Chapter 5. This involves numerous measurements and testing to ensure proper operation and knowledge of the detector. The detector itself is described in detail, as well as the results of this characterization.

Chapter 6 goes into detail on the future work necessary for LIFE and the thermal model of the instrument. Thermal-mechanical changes based on what was seen during flight are discussed, continuing characterization of the MCT detector, as well as recommended updates to the atmospheric instrument thermal model.

2 BACKGROUND

2.1 Limb Imaging & The Atmosphere

This section provides an overview of the atmosphere, specifically the upper troposphere/lower stratosphere (UTLS) region that the LIFE instrument is designed to measure. This region is discussed in detail, with topics including the species found in both the troposphere and stratosphere, the mixing of these regions that form the UTLS region, and the need for better measurements in the future. This section will also discuss atmospheric limb remote sensing, including different methods as well as instruments that have been important to this field.

2.1.1 UTLS Overview

The atmosphere of Earth is divided into several layers, according to its thermal structure. The two lowest layers, the troposphere and stratosphere, are described here as they are most relevant to the LIFE instrument. Also described here are the main constituents of interest to LIFE: Methane (CH_4), Water Vapour (H_2O), Ozone (O_3), and Nitrous Oxide (N_2O). Finally an overview is given of the border region of these two layers, known as the UTLS, the measurement region of the LIFE instrument.

Troposphere & Stratosphere Species

From ground level up to roughly 10 km, temperature decreases steadily. This region is known as the troposphere and its temperature is dependent on surface heating from Earth. As such, the altitude in this region increases as the temperature decreases. The upper boundary of this region is known as the tropopause, marked by a temperature minimum. This boundary is typically 10 km but is different depending on the geographic region, such as the tropics, where the boundary can be as high as 17 km (Gettelman et al., 2011). This is the region

where most weather occurs, and as a result it is continuously being cleaned of aerosols via cloud droplets, falling to the ground as rain. This region is also quite turbulent, leading to a generally well-mixed region of gases and aerosols. Throughout this region, the concentrations of long-lived atmospheric constituents are relatively uniform and independent of height, due to mixing caused by the turbulence (Salby, 2012).

Above the tropopause is the stratosphere, which covers the region from roughly 15 km to 50 km, and is characterized by an increase in temperature. This temperature increase continues until the stratopause, the region between the stratosphere and mesosphere, where there is a temperature maximum. The warming in this region is due to absorption of solar radiation by the ozone layer and also causes very little mixing, which is an important difference between the stratosphere and troposphere. Unlike the troposphere, where a decrease in temperature causes turbulence, the stratosphere is relatively calm and as a result there is a less homogeneous mix of constituents in this region, such as the ozone layer (Wallace and Hobbs, 2006). Figure 2.1 shows a temperature and pressure profile of the atmosphere, with the atmospheric layers and the UTLS region of interest.

This has a large affect on one of the constituents measured by LIFE, methane (CH_4). As a long-lived gas, methane can remain in the troposphere for a long period and become well-mixed. If it travels upwards to the stratosphere, it will become oxidized. As a result, methane decreases steadily as altitude increases in the stratosphere. The oxidation of methane leads to water vapour, an important greenhouse gas. Methane itself also plays a major role in the atmosphere as a greenhouse gas, which has increased exponentially in the last few hundred years as a result of human activities such as farming (Salby, 2012).

Similar to methane, nitrous oxide (N_2O) is a long-lived constituent and as such is well-mixed in the tropopause. It comes from a variety of sources, from bacterial processes to human processes of fossil fuel combustion. In the stratosphere, it decreases with altitude, disassociating into NO. NO is important to study as it can cause the destruction of ozone, and has played a role in the thinning of the ozone layer. N_2O is also a greenhouse gas and plays a role in climate change (Salby, 2012).

Ozone (O_3) is an atmospheric species mainly concentrated in the stratosphere, in the ozone layer. Below the stratosphere, it is quickly destroyed through oxidation or absorbed

Pressure and Temperature Reference

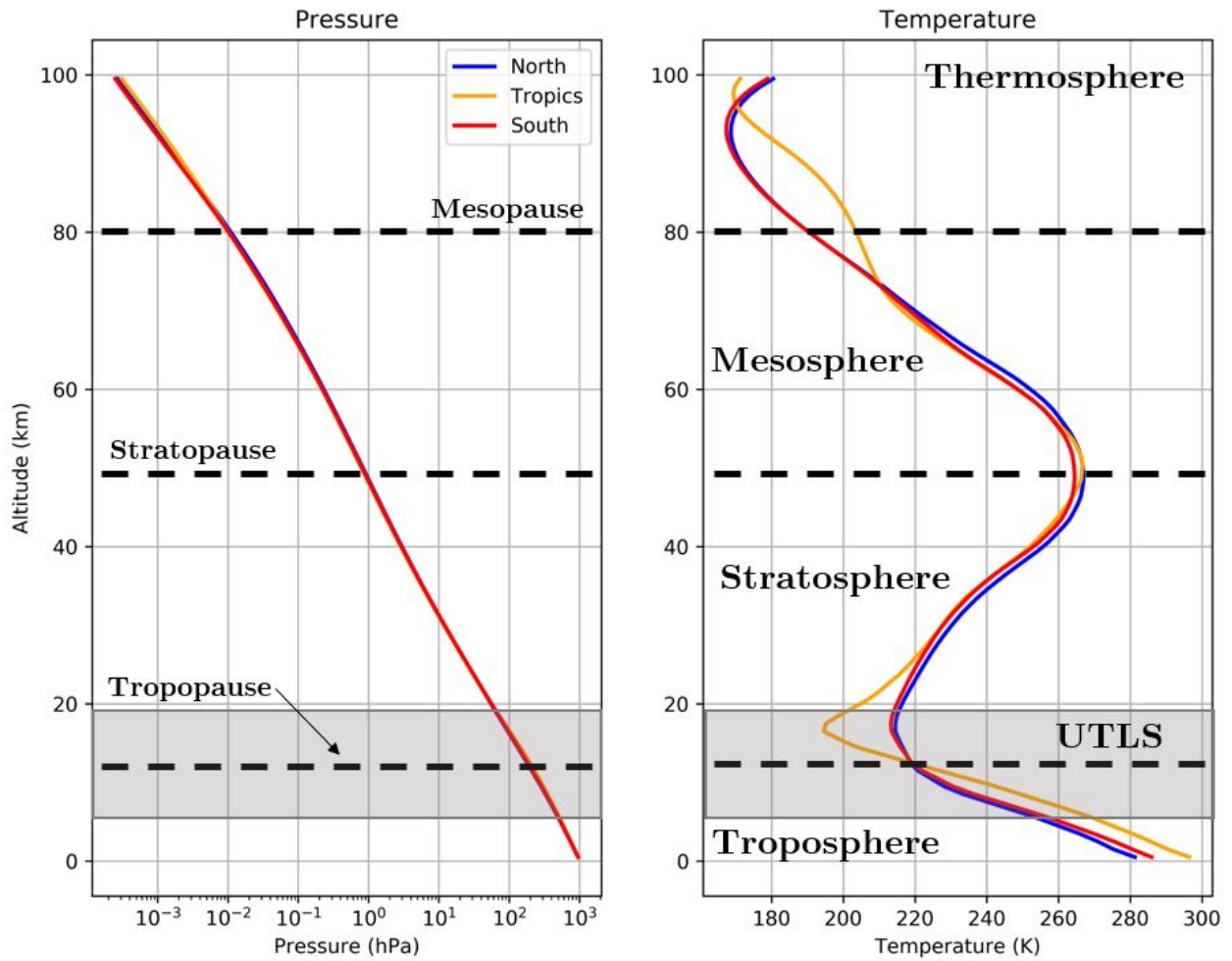


Figure 2.1: Atmospheric layers with a typical pressure and temperature profile. The upper troposphere/lower stratosphere region is shaded grey (Hedin, 1990) (Dee et al., 2011).

due to its water-solubility. It is important to study, as it is essential to life on Earth due to its absorption of UV radiation. As it also absorbs IR radiation, it also plays a role in climate change as a greenhouse gas (Salby, 2012). The majority of ozone being concentrated in the lower stratosphere as the ozone layer, it is within the area of interest for the LIFE instrument.

In the low troposphere, water vapour is abundant, and is perhaps one of the most important atmospheric species to study. Due to its strong absorption of IR radiation it is an extremely important greenhouse and plays a major role in climate change. Stratospheric concentrations are much lower due to condensation at higher altitudes as temperature decreases, where it falls as rain or snow. If it does reach the stratosphere, it often dissociates to the free radical OH, which can damage to the ozone layer (Salby, 2012). The results of these processes are measured by the LIFE instrument for study.

The UTLS

Now that the troposphere and stratosphere are described, the region that is of most interest to this thesis and the LIFE instrument is discussed: The upper troposphere/lower stratosphere region. This part of the atmosphere is roughly defined as the region ± 5 km around the boundary between the troposphere and stratosphere, and is important to study for a number of reasons. The tropospheric and stratospheric regions have very different processes, and as a result the boundary between these regions has a large affect on the chemistry of both. The exchange between the two is known as the *stratosphere-troposphere exchange (STE)* (Gettelman et al., 2011).

STE is part of the atmospheric circulation that moves air, pollutants, and other constituents from the troposphere to the stratosphere. The air movement is largely due to the surface of Earth heating the air, so it rises. As a result the convection and movement of air is strongest around the tropics, where the air is the warmest for most of the year (Mohanakumar, 2008). It cools in the UTLS region and moves toward the poles, where it falls again. This is an important process to study, as the movement of chemical constituents across this layer has direct effects on chemicals in the atmosphere, such as ozone. The destruction of ozone as well as the greenhouse gases that travel to the stratosphere via STE means that

this process and the UTLS region have a critical role in studying climate change.

Research has shown that the STE has direct implications on atmospheric ozone, specifically the destruction of ozone in the stratosphere (the ozone layer) and an increase in tropospheric ozone. As mentioned previously, nitrous oxide can travel upwards through the stratosphere and disassociate to NO, a free radical. This can combine with ozone to form NO_x, causing a thinning of the ozone layer in the stratosphere. Likewise, water vapour that rises to the stratosphere can disassociate to OH, a free radical similar to NO with the same ability to combine with ozone and cause damage to the ozone layer (World Meteorological Organization, 1986). Water vapour and ozone are particularly sensitive to the rise and fall of air in this region due to their steep gradients in both regions (the water vapour nearer to Earth and the concentrated ozone layer) (Riese et al., 2014). As air travels downwards via STE, it carries many of the pollutants that can affect the ozone layer, but can carry ozone into the troposphere as well. Ozone in the troposphere can have large effects on both air quality and climate change. Thus, STE plays a major role in climate change, as greenhouse gases are moved between these two layers where they have different effects (Mohanakumar, 2008) (Holton et al., 1995).

Due to the impact of chemical exchanges between the tropospheric and stratospheric layers, variability and changes to the UTLS are important in studying climate change. Changes to greenhouse gases such as ozone or water vapour in either of these regions have significant effects on chemical balance and IR absorption, leading to climate change (Solomon et al., 2007). In addition to this, the temperature minimum in the tropopause causes the region to be a key part of IR radiation escaping from the tropopause to space, further effecting surface climate and the climate feedback system (Gettelman et al., 2011). It is clear that this region must be adequately measured to further research climate change.

These processes have been measured and studied, but not in depth due to a lack of high temporal and spatial resolution measurements. Simulations and models have been created of this region, but there is a large amount of uncertainty. Some models have shown that with even small uncertainties in the exchange and processes of trace gases in the UTLS region, there is a significant effect on estimated concentrations of species such as ozone and water vapour. As a result, the radiative effects that are to be studied are highly uncer-

tain. Measurements must be improved of trace gases and constituents in the UTLS to fix this issue. A major instrument in this area, MIPAS (Michelson Interferometer for Passive Atmospheric Sounding), took measurements from a satellite platform but with low spatial resolution. There is a gap in trace gas measurements in the UTLS that would better inform simulations of the region. The GLORIA (Gimballed Limb Observer for Radiance Imaging of the Atmosphere) instrument was the first to provide insight into this region with multiple two and three dimensional measurements with high spatial resolution (Riese et al., 2014). LIFE is designed to follow in the GLORIA instrument footsteps in measuring this region using similar limb imaging methods via Fourier transform spectrometer. Both the GLORIA and MIPAS instruments and their objectives are described in Section 2.1.3 as forerunners to the LIFE project. GLORIA, MIPAS, and LIFE all use limb-emission imaging to take measurements; an overview of limb imaging is provided in the section below.

2.1.2 Techniques

There are many atmospheric measuring techniques, but can initially be split into two groups: passive and active sensing. Active sensing techniques involve emitting high-energy radiation and detecting its reflection to perform measurements, such as LIDAR (Light Detection And Ranging) instruments. However, most instruments that measure in the troposphere/stratosphere region that is of interest are passive, from balloon-borne or satellite-borne instruments. Passive instruments can be further split into two groups: nadir-sounding and limb-sounding. Nadir-sounding instruments have downwards pointing geometry, and are useful for tropospheric measurements that have a high horizontal resolution. Limb-sounders look tangentially through the atmosphere, or the *limb*. This method is useful for stratospheric measurements, where the constituents are less dense; with the long ray path of this method, the lower troposphere may saturate measurements due to cloud cover. This method can also provide good vertical resolution, depending on the instrument (Hegglin and Tegtemeier, 2017). An example of limb-sounding is shown in Figure 2.2. Depending on what the instrument is scanning through the atmosphere, limb measurements are classified into four major groups: solar occultation, stellar occultation, limb scattering, and limb emission.

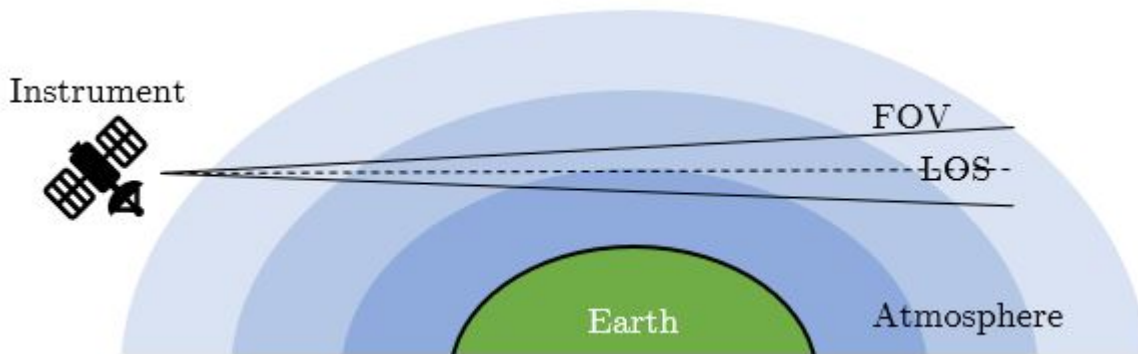


Figure 2.2: Limb emission observation example. For solar or stellar occultation, the sun or a star would be at the end of the LOS, respectively.

Solar & Stellar Occultation

Solar occultation measurements are made by looking through the atmospheric limb at the sun. The radiance emitted by the sun and attenuated by the atmosphere through absorption or scattering is measured. This method allows for altitude resolved measurements as the satellite orbits the Earth (Hegglin and Tegtmeier, 2017). SAGE II (Stratospheric Aerosol and Gas Experiment), a solar occultation measurement taken as an example, begins taking measurements at a tangent height of 150 km, and continues until the sun is obscured by clouds or is below the horizon. This particular approach for SAGE II worked well as at a height of 150 km there is very little attenuation, allowing a self calibration process at lower tangent heights against 150 km (Mauldin et al., 1985). An issue with this method is the lack of freedom in measurement geometry, as the position of the sun and the satellite orbit defines its measurements. This leads to reduced data density compared to emission-sounding instruments, as the instrument can only take images at orbital sunrise or sunset (Hegglin and Tegtmeier, 2017). In the case of SAGE II, it took measurements 30 times per day, 15 per sunrise and sunset. Through a number of orbits, this eventually leads to global coverage (Mauldin et al., 1985). However, although the data density is lower than other options, the solar signal is much stronger than emission or scattering imaging, and allows for high precision measurements. Measurements from solar occultation are usually in the UV to mid-IR wavelength range (Hegglin and Tegtmeier, 2017). Some instrument examples of this method include the ACE-FTS (Atmospheric Chemistry Experiment - Fourier Transform

Spectrometer) and SAGE I, II and III instruments, which primarily examined ozone but have also measured other species such as water vapour and nitrogen dioxide in the case of SAGE III (Hase et al., 2010) (McComrick et al., 1989) (Thomason and Taha, 2003).

Stellar occultation is similar to solar occultation, except the radiance from stars is measured instead. The advantage of this method over solar occultation is the greater data density that can be achieved as there is a larger time period for measuring stellar radiance over solar radiance. This method can be used during both daytime and nighttime for higher data density, but daytime measurements are typically of lower quality as the signal caused by the sun can interfere with the stellar measurements (Hegglin and Tegtmeier, 2017). The GOMOS (Global Ozone Monitoring by Occultation of Stars) instrument is an example of a stellar occultation instrument, which measures a number of species but mainly ozone. The good global coverage and measurement time of stellar occultation allows GOMOS to take 400-600 occultation measurements in 24 hours, with data being taken in both daytime and nighttime (Kyrölä et al., 2004). This instrument, and most similar stellar occultation instruments, measure in the spectral range shorter than $1\mu\text{m}$ due to thermal emission interference at longer wavelengths (Hegglin and Tegtmeier, 2017).

Limb Scattering

Another method of limb-sounding is to measure scattered photons from the sun. These photons are scattered into the FOV of the instrument, which provides information on the atmosphere either by the scattering itself or the absorption of photons through the atmosphere. The requirement for this method is that measurements must be taken in the daytime, since the sun is the source (Hegglin and Tegtmeier, 2017). An example of limb scattering is OSIRIS (Optical Spectrograph and InfraRed Imaging System), which was the first instrument to routinely gather ozone retrieval measurements (Degenstein et al., 2008). Other examples of limb scattering measurements are the SCIAMACHY (SCanning Imaging Absorption SpectroMeter for Atmospheric CHartographY) instrument, which observes photons scattered by nitrogen, oxygen, and other aerosols, and the SME instrument which measures ozone (Kaiser et al., 2004) (Thomas et al., 1983).

Limb Emission

Limb emission instruments measure radiation emitted by the atmosphere, either thermally or photochemically, along the instrument line of sight (LOS). These are generally low signal level emissions, but can be measured with sensitive instruments. Variation of the LOS or a wide FOV allows altitude-resolved measurements from clouds in the troposphere up through the thermosphere. Limb emission focuses on the $2.5\mu\text{m}$ wavelength region and above, as the Planck function is very low for wavelengths any shorter than this at the temperatures expected in the atmosphere. In this range atmospheric scattering will not have an effect on measurements. However, a large advantage to this method is the ability to take measurements both at day and night. As no direct illumination source is needed as in other methods, a very dense spatial coverage can be created if the instrument is on a satellite platform. The viewing angle can also be freely chosen as long as it does not directly look at the sun, but this angle must be known to a high degree of accuracy to prevent any propagation errors in the data (Griessbach et al., 2016) (Hegglin and Tegtmeier, 2017).

Many early instruments to use this method were low-Earth-orbit instruments that were used to measure vertically resolved profiles of temperature, trace gases, clouds, and aerosols. With many temperature measurements and three-dimensional chemical structure information, these instruments immensely improved understanding of the middle atmosphere region. Instruments such as CRISTA (Cryogenic Infrared Spectrometers and Telescopes for the Atmosphere) focused on high-spatial resolution, and MIPAS followed with a focus on high spectral resolution to acquire the most complete set of data in the stratosphere over its decade on-board the ESA satellite Envisat Riese et al. (2014).

This method is of most interest to this thesis, as it is the method used by the LIFE instrument, as well as instruments described below that paved the way for LIFE such as MIPAS and GLORIA. This is chosen for these instruments due to the vertical resolution given by a limb-viewing geometry, as well as the trace gases and constituents that are better detected with limb-viewing thermal emission.

2.1.3 Instruments

There have been a number of instruments that have taken measurements in the UTLS region using a number of different imaging methods, as described in Section 2.1.2. However, out of these instruments, two in particular are similar to the LIFE instrument: MIPAS, developed at the University of Karlsruhe in Germany and launched in 2002 aboard the Envisat from the European Space Agency (Fischer et al., 2008), and GLORIA, also developed at the University of Karlsruhe and was flown multiple times on aircraft in the last 10 years (Friedl-Vallon et al., 2014). These instruments, like LIFE, are thermal emission instruments that use a Fourier transform spectrometer to image the atmosphere. As these instruments lay the foundation for the development of the LIFE instrument, the background and description of each of these instruments are given in this section.

MIPAS

A key early instrument in the measurement of limb emissions from space is the Michelson Interferometer for Passive Atmospheric Sounding (MIPAS). It was the first instrument to use a high resolution FTS for limb emission measurements on-board a satellite. This FTS was used to measure profiles of numerous atmospheric species: H_2O , O_3 , CH_4 , N_2O , HNO_3 , and NO_2 , as well as aerosols such as ice clouds. To capture the radiances of these species, MIPAS had a number of spectral ranges: $685\text{-}970\text{ cm}^{-1}$, $1020\text{-}1170\text{ cm}^{-1}$, $1215\text{-}1500\text{ cm}^{-1}$, $1570\text{-}750\text{ cm}^{-1}$, and $1820\text{-}2410\text{ cm}^{-1}$. This spectral range is used as the atmospheric signals are higher in this range to maximize the Planck function around $10\mu\text{m}$ at atmospheric temperatures (Fischer et al., 2008) (Endemann, 1999).

The main purpose of this instrument is to study dynamics and chemistry from the upper troposphere region to the lower thermosphere. Studying this area of the atmosphere stems from a number of scientific objectives. The first objective is the study of stratospheric chemistry, and specifically the ozone layer. This includes studying the effect of cooling in this region, as a result of ozone depletion and increasing carbon dioxide. Another objective is studying the STE, an important part of the UTLS region as described in Section 2.1.1. Finally, similar to LIFE, an objective was studying various constituents in the upper tropo-

sphere, such as water vapour, for its great importance in climate change. This also includes NO_x gases and gases moving down from the stratosphere such as ozone. Overall, one of the main goals of this instrument is to observe global changes in the composition of the atmosphere resulting from pollution and other man-made effects throughout its multi-year lifetime (Fischer et al., 2008).

MIPAS, and similar instruments such as the Atmospheric Chemistry Experiment Fourier Transform Spectrometer (ACE-FTS), utilize Fourier transform spectrometers in their measurements (Hegglin and Tegtmeier, 2017) (Bernath, 2002). However, a limitation of these instruments is that they are not imaging instruments; they have only a single detector pixel. Limb scanning must be used to cover the atmospheric limb, where the instrument moves the line of sight upwards and downwards. However, new and larger data storage and transfer techniques have led to the usage of the imaging Fourier Transform Spectrometer (IFTS), which generates a high amount of data. With a larger throughput, more pixels can be used to create a much wider FOV that covers the atmospheric limb, thus not needing any movement of the instrument. The first instrument to demonstrate the imaging FTS concept for atmospheric measurements is a second generation MIPAS instrument, the GLORIA instrument (Friedl-Vallon et al., 2014).

GLORIA

The Gimballed Limb Observer for Radiance Imaging in the Atmosphere (GLORIA) instrument is an airborne limb imaging instrument operating in the thermal infrared region, similar in concept to MIPAS and LIFE. The instrument was designed to take advantage of two dimensional infrared detector array technology that had become available in the last few decades. This allowed the instrument to overcome one of the primary issues with MIPAS, which was the scanning of the atmosphere with one pixel. This two dimensional array also means that three dimensional measurements can be made when using an aircraft and tomographic techniques. This large array was designed to work with an IFTS to provide very high spectral coverage, sensitivity and spectral resolution that no instrument before has managed to achieve. This followed from a need to take measurements in the region of the UTLS where mission objectives similar to MIPAS and LIFE are to address the gap in data

from satellite and airborne instruments of phenomena in this region. This includes the STE, pollutant transport across the region and ozone in both the ozone layer and the upper troposphere. Further mission objectives include measurements of gravity wave propagation in the tropopause, requiring three-dimensional observations of trace gases and temperatures with a high vertical resolution and moderate horizontal resolution (Friedl-Vallon et al., 2014) (Riese et al., 2014).

The instrument consists of a cooled imaging Fourier transform spectrometer with a cryogenic Mercury-Cadmium-Telluride (MCT) two-dimensional detector array for detection of infrared radiation. This is mounted on a gimbal that is attached to a research aircraft, allowing for free viewing where needed. For calibration, two blackbodies are also mounted on-board, along with a deep-space view for further calibration (Friedl-Vallon et al., 2014). GLORIA operates in the region of 780 cm^{-1} to 1400 cm^{-1} , making the detector sensitive to numerous species, including H_2O , O_3 , CCl_4 , HNO_3 , ClONO_2 , HO_2NO_2 , and chloro-fluorocarbons (CFCs). The instrument will image from 4 km up to the height of the aircraft, and with its high vertical resolution be able to measure steep gradients in trace gases and characteristics of clouds in this region to help meet its mission objectives. (Sha, 2013) (Riese et al., 2014).

GLORIA can also operate in two different measurements modes: chemistry mode (CM) and dynamics mode (DM). In chemistry mode, spectral resolution is maximized to increase the number of retrieved gas species with a reasonable spatial sampling. Dynamics mode is used to be able to take three dimensional data of species and temperature, with the disadvantage being a lowered spectral resolution. The instrument used both of these measuring modes successfully on multiple airborne flights on the German High Altitude and Long Range research aircraft (HALO) (Friedl-Vallon et al., 2014).

2.2 Thermal Design

The thermal environment of a balloon-borne atmospheric instrument is complex, as it goes through a number of stages: It must stay cool in the lab environment, be able to survive ascent through various temperature gradients, thermally remain steady throughout the measurement window in the float portion of the flight, be able to survive the thermal radiation of

sunlight later in the flight, and survive the descent. The thermal design of the LIFE instrument, and similar thermal imaging instruments, are of particular importance as the thermal signature of the instrument can have a large affect on the noise of the measurements. As a result of complexity and importance of this problem, the thermal design (with the interconnected mechanical design) of the LIFE instrument is one of the main components of this thesis.

In this section, a background of thermal design is given that is relevant for thermal imaging balloon borne instruments. Central to thermal design is heat transfer, or the thermal phenomena of radiation, conduction and convection. These are described in detail. Following, the balloon environment is described in more detail, with an example from a previous instrument flight. Self-emission, very important for the design of a thermal emission imaging instrument, is discussed. Thermal control methods that are considered when designing an instrument for extreme temperatures are discussed after. The thermal designs of MIPAS and GLORIA, which have similar thermal requirements to LIFE as thermal imaging instruments, are described at the end of this section.

2.2.1 Heat Transfer

Heat transfer is a very broad topic, covering theoretical physics and engineering physics as well as engineering design. It is covered in many articles, journals, and textbooks. Only a high level of background is given here to help understand the thermal phenomena important to thermal analysis, particularly for a balloon-borne atmospheric instrument. At its most basic, heat transfer is dependent on the Second Law of Thermodynamics: *Heat flows from a hot body to a cold body, increasing the entropy of a closed system.* Heat is a form of measurable energy, discussed in terms of the temperature of bodies. Heat of a material may be related to a number of phenomena, such as atomic or molecular motion of a material, or to electromagnetic radiation (Greve and Bremer, 2010).

Heat transfer occurs in three different ways: Radiation, conduction, and convection. These control the flow of heat energy through an object, and each play a different role; radiation emits heat from an object into space, not requiring any outer medium. Conduction defines how heat travels through an object, or a connection between two objects, and con-

vection describes heat moving from an object to a surrounding fluid medium. Each of these phenomena are described in detail here.

Conduction

Thermal conduction is the process of heat transfer across solids. This can be done through molecules, atoms, electrons or photons carrying energy. As mentioned previously, the second law of thermodynamics states that heat will always flow from a hot body to a cold body (von Böckh and Wetzels, 2012). As a result, thermal conduction will occur in any material where a temperature gradient exists, and as such can play a very important role in thermal design where heat must be moved away from components generating high heat power.

When there is a temperature gradient in a material, there will be heat flux, q . Heat flux, also known as thermal flux, is the flow of energy per unit area. Most often in units of W/m^2 , heat flux is used to calculate how much heat is traveling through a medium. Through a body, heat flux is described by *Fourier's Conduction Law*, shown in Equation 2.1.

$$\mathbf{q}(T) = -k\nabla T \tag{2.1}$$

Here k is the thermal conductivity of the material and ∇T is the spacial temperature gradient (Lienhard IV and Lienhard V, 2019). This equation can be used to develop the equation for the heat through a surface area:

$$Q = \int_A q_n dA \tag{2.2}$$

Here, q_n is the same heat flux vector as above, but normal to the surface (von Böckh and Wetzels, 2012).

The thermal conductivity is an important aspect of this equation. For an anisotropic material, the conductivity is a tensor and the temperature gradient forms a vector, which makes the Equation 2.2 very difficult to solve. For most designs and technical applications, especially as most materials are isotropic at a macroscopic level, the thermal conductivity can be taken as a mean value. The thermal conductivity is dependent on the material and has units of W/mK (Lienhard IV and Lienhard V, 2019) (Ed Akin, 2009). The design control for the conduction of heat relies on k , thus the material chosen.

Another aspect of thermal conduction that must be considered for thermal simulations are boundaries. In many cases, contact between two parts can be simplified to 'bonded' or 'insulated', meaning either full contact as if they were one part, or completely disconnected, respectively. Often parts can be thermally connected using a thermal paste, increasing the contact by as much as 75% (Holman, 1981), making the bonded simplification reasonably accurate. However, in the cases of junctions with a large surface area where thermal paste is not applied, a more careful examination is needed. Instead of a smooth temperature gradient across the connection, there can be a discontinuity, due to the surfaces not being perfectly connected. This is known as *thermal contact resistance*.

Thermal contact resistance is largely a result of surface roughness. At a joint, there are two main contributions to heat flow: Solid-to-solid conduction at points of contact between the two bodies, and the conduction through entrapped gases in the spaces between contact. Conduction happens easily through direct solid-to-solid contact, but not in gases. These gases are the major cause of thermal contact resistance, as the thermal conductivity of gases is very small compared to solids and particularly metals. This plays an even larger role in the atmospheric balloon environment, where vacuum means that there are not even gases to transfer heat, so the thermal resistance is larger (Holman, 1981).

An equation for heat conduction across a joint can be developed, leading to an equation for solving for h_c , known as the contact coefficient. This contact coefficient determines how well heat flows across a joint. If the contact area of a junction is denoted by A_c and the void area by A_v , the equation for heat flow across a joint is given by Equation 2.3.

$$q = \frac{T_1 - T_2}{\frac{L_g}{2k_1 A_c} + \frac{L_g}{2k_2 A_c}} + k_f A_v \frac{T_1 - T_2}{L_g} = \frac{T_1 - T_2}{\frac{1}{h_c A}} \quad (2.3)$$

In this equation T_1 is the temperature of the first body, T_2 is the temperature of the second body, k_1 is the thermal conductivity of the first body, k_2 is the thermal conductivity of the second body, L_g is the thickness of the void space between bodies, k_f is the thermal conductivity of the fluid filling this void space, and A is the total area that should be in contact between the two bodies (at a macro scale). $1/h_c A$ is the thermal contact resistance. The left side of this equation is the heat flow due to the solid conduction plus the heat flow due to the fluid conduction, and the right side is the full heat flow (Holman, 1981). From

these equations the contact coefficient h_c can be solved for to obtain Equation 2.4.

$$h_c = \frac{1}{L_g} \left(\frac{A_c}{A} \frac{2k_1k_2}{k_1 + k_2} + \frac{A_v}{A} k_f \right) \quad (2.4)$$

This equation can be slightly simplified for a balloon environment (vacuum, hence $k_f = 0$) as well as the conductivity of the materials being equal, shown in Equation 2.5.

$$h_c = \frac{A_c}{A} \frac{k}{L_g} \quad (2.5)$$

From the above equation, it appears that the contact coefficient could be calculated rather simply. However, it is extremely difficult to find an accurate value for either the contact area or the size of the gap between parts. There is no theory or even empirical evidence that is reliable. This is to be expected due to the high amount of unknowns involved, mainly direct surface area contact of a material, which cannot be accurately quantified (Holman, 1981) (Gendron, 2019). The most accurate way of finding this is often through finding a rough estimate, building, and testing the joint in a thermal vacuum chamber. This was done with the LIFE instrument. Further analysis for the thermal resistance in the case of LIFE is described in Section 3.6.3.

In a vacuum environment, conduction is one of two forms of heat transfer, due to the lack of convection. Thus it is more important to take this into account for any electronics or instruments operating in a vacuum environment, such as an atmospheric instrument. Heat must be able to flow between parts in order to dump heat properly, or they will overheat. A good contact between all parts is essential to an operational instrument. The only other method of heat transfer in this environment is through radiation.

Radiation

Thermal radiation is heat transfer carried by electromagnetic waves, in the wavelength range of 0.1-1000 μm . As electromagnetic waves do not require any medium to travel, neither does thermal radiation. As such, radiation occurs in vacuum, and with the absence of convection in a vacuum due to the need of a medium, it plays an important role in these environments (von Böckh and Wetzel, 2012). Radiation can often be neglected, but in a vacuum environment and at higher temperatures it must be included in the thermal design process.

The intensity of the energy flux radiated from the body is dependent on the temperature of the surface, and increases with temperature. In addition to temperature, the radiation from a surface depends on its emissivity ϵ , which is a characteristic of the material or its coating. A blackbody is an object that has a very high emissivity, and an ideal blackbody has an emissivity of 1, meaning that it can emit electromagnetic waves at any temperature with maximum intensity. For a typical blackbody, the emissivity is equal to its absorptivity α , which is how much radiation is absorbed by the surface. This is why they are known as blackbodies; for comparison, whitebodies would absorb no radiation, with an absorptivity of zero. In reality, all surfaces and materials are somewhere in between these two extremes, and are known as greybodies (von Böckh and Wetzell, 2012) (Lienhard IV and Lienhard V, 2019). The material or coating, and thus the emissivity, must be taken into account in thermal design and is a method of controlling the thermal design to allow the object to emit more or less heat.

It is possible to make an almost perfect blackbody ($\epsilon > 0.99$), which is often used for calibrating instruments to precise temperatures. A common device is known as a *hohlraum*, German for "hollow space". It is a hollow cylinder or sphere with an opening, with an interior coated with an extremely high emissivity black coating. The interior of the hohlraum is designed to have some sort of rough surface (such as pyramidal structures). With this setup, radiation enters the opening and is almost entirely absorbed by the coating. The parts that do not get absorbed are reflected from the rough surface to another part of the cylinder, where it is absorbed further. In this way, almost all radiation is absorbed, allowing the temperature of the surface to be very clearly and accurately seen by an infrared detector (von Böckh and Wetzell, 2012) (Lienhard IV and Lienhard V, 2019). An example diagram of this device can be seen in Figure 2.3. This sort of device plays an important role in LIFE and similar thermal imaging instruments for calibrating the detector at various temperatures.

The spectral intensity of the radiation emitted from an ideal blackbody surface can be calculated, and is given by Planck's radiation law, in Equation 2.6.

$$L(\lambda) = \frac{2hc^2}{\lambda^5} \cdot \frac{1}{e^{\left(\frac{hc}{\lambda k_B T}\right)} - 1} \quad (2.6)$$

Here h is Planck's constant, c is the speed of light, λ is the wavelength of incoming

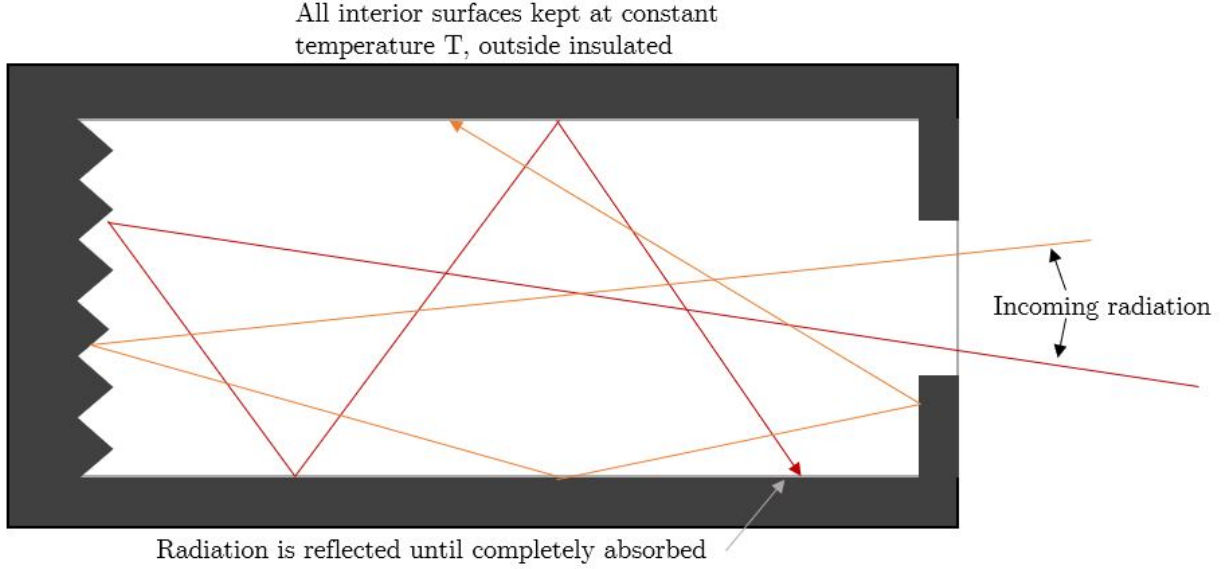


Figure 2.3: Example of a near-perfect blackbody, known as a *hohlraum*. This is a cross-section of a cylindrical system similar to what is used on the LIFE instrument.

radiation, k_B is the Boltzmann constant ($1.38 \cdot 10^{-23}$ J/K), and T is the blackbody temperature (von Böckh and Wetzel, 2012). This equation gives the Planck curve of the radiation emitted from an object, and is important to the calibration of thermal imaging instruments. This equation is used when calculating spectral radiances for the LIFE detector responsivity, discussed in Chapter 5. Its units are $\text{Wm}^{-2}\text{sr}^{-1}$.

The energy emitted from the blackbody surface reaches a theoretical maximum due to the emissivity of 1, and this maximum is given by the Stefan-Boltzmann Law. This law is calculated by the integration of wavelength of Equation 2.6 from zero to infinite wavelength (von Böckh and Wetzel, 2012). This equation, which gives the flux of energy radiation for a blackbody q_b in W/m^2 , is shown in Equation 2.7.

$$q_b(T) = \sigma T^4 \quad (2.7)$$

where the Stefan-Boltzmann constant, σ , is $5.67 \cdot 10^8 \text{ W/m}^2\text{K}^4$ (equal to all constants left from integration), ϵ is the emissivity of the surface, and T is the absolute temperature. For non-blackbodies, the heat flux emitted is the blackbody heat flux multiplied by the emissivity. The total energy radiated can also be shown by multiplying by the area, A . Thus the Stefan-Boltzmann Law equation for general surfaces is given below as Equation 2.8 (von

Böckh and Wetzel, 2012).

$$q(T) = \epsilon\sigma T^4 A \quad (2.8)$$

In most situations, radiation from one surface will intersect with objects in its surroundings. Equation 2.7 and 2.8 both assume the radiated energy is absorbed by the medium or far surroundings, thus having no affect on the emitting object. In reality, an object emitting energy will have energy emitted to it by a nearby body. The Stefan-Boltzmann Law must be altered for this scenario.

The simplest form of this problem is that all radiation from a blackbody object, say object 1, is absorbed by another blackbody object, say object 2. Likewise, all radiation from object 2 is radiated to object 1 and absorbed. The net heat transferred from object 1 to object 2, known as Q_{net} , is the difference of the radiation from object 1 to object 2 and the radiation from object 2 to 1 (Lienhard IV and Lienhard V, 2019). This is shown in Equation 2.9.

$$Q_{net} = A_1 q_b(T_1) - A_1 q_b(T_2) = A_1 \sigma (T_1^4 - T_2^4) \quad (2.9)$$

Here, T_1 is the temperature of the first object, T_2 is the temperature of the second object, A_1 is the area of the first object, q_b is the heat flux emitted from the first object, and σ is the Stefan-Boltzmann constant. In many situations, this is often good enough. However, the more realistic scenario is that the objects see other objects too, and not all radiation from one object is absorbed by a single other object. To account for this, a view factor F_{1-2} must be included in the equation. Essentially, this view factor is how well the surface 'sees' the other surface (Lienhard IV and Lienhard V, 2019) (Ed Akin, 2009). Assuming two small areas A_1 and A_2 , the view factor can be calculated using Equation 2.10.

$$F_{1-2} = \frac{1}{A_1} \int_{A_1} \int_{A_2} \frac{\cos\theta_1 \cos\theta_2}{\pi R_{1-2}^2} dA_1 dA_2 \quad (2.10)$$

Here, θ_1 and θ_2 are the angles between the unit normal of each area, and R_{1-2} is the line connecting the two areas. This equation is inserted into Equation 2.9 with the surface emissivity to create Lambert's Law, giving the heat flow rate between two gray diffuse surfaces, shown in Equation 2.11.

$$Q_{net} = \epsilon A_1 \sigma F_{1-2} (T_1^4 - T_2^4) \quad (2.11)$$

This equation assumes the surfaces have the same emissivity. If they have different values, this equation becomes more complex.

As discussed in Section 3.4.2, a thermal simulation often breaks a surface into many small surfaces to be able to run the simulation. As such, this equation, and particularly Equation 2.10, must be solved hundreds of thousands of times for each simulation. As such, it requires major computational power to run simulations that include surface-to-surface emissivity. For the purpose of saving time in simulations, this is often approximated by estimating the ambient temperature an object will see when radiating, along with an estimated view factor, and changing if necessary. This will make simulations less accurate but many more simulations are able to be run, so these settings can be iterated with trial and error until they are deemed accurate.

In relation to the thermal design, the two main variables that can be altered when running simulations and testing designs are the surface area and emissivity. Choosing the right material to either maintain or emit heat through radiation to stop freezing or overheating, as well as designing to allow heat to be dumped to less heat-sensitive parts of the instrument through conductivity, are critical parts of thermal design.

Convection

For most of the LIFE thermal simulations, convection does not play a part. This is because at the altitude LIFE floats at, roughly 30-35 km, there is essentially a vacuum. There is no medium for convection to act in, thus it is not considered in the simulations. However, the ascent from the ground through the tropopause to the float altitude was simulated, and convection still played a part in this aspect of the flight; especially through the cold tropopause. As such, and as it often plays an extremely important role in thermal design, it is discussed here. However, convection is more complex than the previous two methods of heat transfer, due to the involvement of fluid dynamics. It will only be discussed here at a high level.

Convection occurs when a cool fluid flows past a warm body, carrying away heat. The

air closest to the body forms a boundary layer, where the moving air is slow. In this region, conduction moves heat from the body to the fluid. The fluid then carries this heat away downstream, and in this way the heat from the body is constantly being stripped away (Lienhard IV and Lienhard V, 2019). Cooling through the convective process can be described by a simple formula, originally developed by Isaac Newton. If the energy of a body is constantly replenished, and the temperature of the oncoming fluid remains constant, the heat removed by the convective fluid is proportional to the difference of the object temperature and the fluid temperature. This equation can be written to solve for the heat flux from the object, shown in Equation 2.12.

$$q = \bar{h}(T_{body} - T_{\infty}) \quad (2.12)$$

This is known as Newton’s law of cooling in the steady state, and here T_{body} is the temperature of the body, T_{∞} is the temperature of the fluid, and \bar{h} is the average heat transfer coefficient. The units of q are W/m^2 as usual with heat flux, so the units of \bar{h} are W/m^2K (Lienhard IV and Lienhard V, 2019).

An issue with simulating convection is the heat transfer coefficient; it is very difficult to find an accurate value for \bar{h} , as it is dependent on a large number of variables. Firstly, it is sometimes dependent on $(T_{body} - T_{\infty})$, or ΔT . This dependence is based on if the fluid is forced past a body, known as *forced convection*, or if the fluid is still, known as *free* or *natural convection*. If ΔT is small, there is a negligible dependence, but can have a large effect (up to ΔT^2) if the temperature difference is large. Natural convection, which behaves differently than forced convection as it is more dependent on the heat from the object causing air to rise (and thus bringing colder air back down against the object, causing a cycle). This leads to a small dependence on ΔT , on the order of $\Delta T^{1/3}$. In addition to these dependencies, it is dependent on pressure through the Reynolds number (used through fluid turbulence calculations near the object surface), the material and its conductivity, and the material surface and shape (Lienhard IV and Lienhard V, 2019).

Due to this large variety of unknowns, it is quite complex to calculate the heat transfer coefficient, even for just one scenario, which can change quickly. Calculated values of \bar{h} for one scenario (for forced convection over an aluminum surface, for example) can vary over 6

orders of magnitude, causing massive changes to the simulation (Lienhard IV and Lienhard V, 2019). It is recognized that this is one of the largest unknowns with the thermal design and simulations as a result.

If a heat transfer coefficient is known, Equation 2.12 can estimate the heat flux reasonably well, enough for LIFE thermal simulation purposes. Much theory surrounding convection is solving for the heat transfer coefficient, and even then still have a large amount of error, and solving equations related to the boundary layer. For the purposes of the LIFE thermal simulations, and considering that convection plays a role in only a small portion of the flight, these equations will not be described. In the simulations, as described in Chapter 4, a heat transfer coefficient is chosen out of an estimated range from literature, and iterated through multiple simulations, as is often the most practical way of finding the coefficient.

2.2.2 Balloon Environment

Thermal design is a crucial part of atmospheric instruments, and particularly thermal imaging instruments. The thermal environment seen by these instruments varies widely, in a number of different scenarios: In the lab on the ground, during the ascent, during float, both with and without the sun. For example, when a balloon-borne instrument is travelling upwards through the tropopause, where the temperature reaches extreme temperatures as low as -80°C , the temperature of the instrument can drop very rapidly. When working with delicate thermal imaging instruments where the temperature can affect measurements, this can be catastrophic, and it is important that this is taken into account during design.

On the ground, most instruments are cooled with a combination of conduction and convection. Convection often plays a large role in the lab by using fans to cool the instrument. However, at high altitudes, the pressure is very low and can be considered vacuum. As described in Section 2.2.1, convection requires a medium to move heat away to cooler areas. Without any fluid, heat is only transferred through conduction and radiation. Convection will play a role during ascent, as the air is still dense enough in the lower troposphere to have an affect, but decreases rapidly. This lends complexity to the thermal design, as there is little information on how the convection coefficient changes at higher altitudes.

If the instrument is not flying overnight, the sun will have a large affect on heating

at these altitudes. The solar flux is the heat transferred to an object from the sun. The atmosphere lowers this flux by attenuation, so that it is not as intense at ground level. In the lower stratosphere where the instrument will sit for the majority of its flight, the sun can be extremely intense and can heat the instrument very quickly if no shielding is provided. It should be known if the sun will be seen during the balloon flight of an instrument so it can be shielded and able to dump heat accordingly.

Due to the extreme variation in temperatures that the instrument will see from the ascent through the tropopause to the sun, it is helpful to have data on what can be expected. Data is provided from a previous atmospheric balloon-borne instrument from the University of Saskatchewan, launched from the same location as LIFE in Timmins, Ontario. This data was measured throughout the flight in August of 2018 by the National Centre for Space Studies (CNES), who operated the balloon. It is shown in Figure 2.4, which shows temperatures for numerous sensors scattered around the balloon gondola (Haley, 2018).

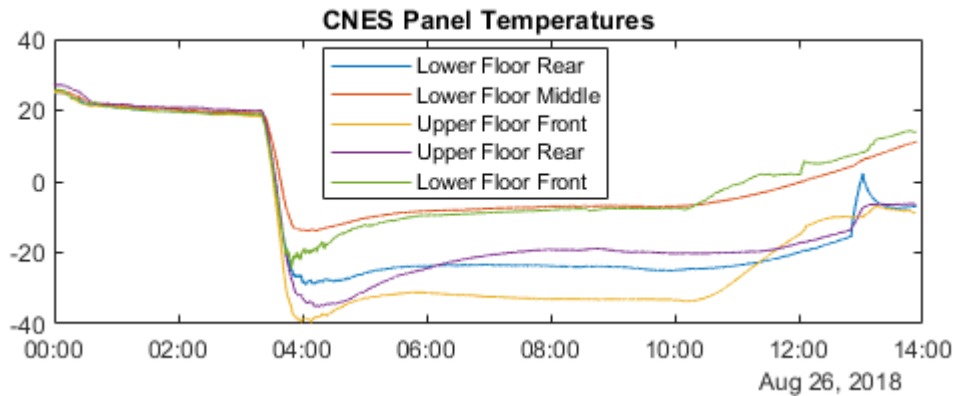


Figure 2.4: High altitude balloon temperatures in °C during 2018 flight in Timmins, Ontario.

It can be seen in Figure 2.4 that the lowest gondola temperature reached during the flight was -40°C , while travelling through the tropopause. Of note in this region is the sharp decrease in temperature throughout this region, in a matter of minutes. The thermal shock of this temperature drop must be considered for delicate electronic components and optics. Temperatures for thermal simulation scenarios were chosen based on what was seen here, which is described further in Chapter 3.

Atmospheric instruments often have delicate optics or electronics, so the thermal charac-

teristics of the instrument are a very important part of the design. Particularly for thermal imaging instruments, the optics must be carefully controlled in order to reduce the thermal radiation background, or self-emission, effect on measurements. Self-emission can lead to systematic errors in the data, as part of the data collected are thermal emission signatures from the optics rather than the atmosphere. This is gone over in further detail in Section 2.2.3. Various instruments use different methods to maintain appropriate operational conditions for the instrument. The MIPAS and GLORIA thermal designs are discussed in Section 2.2.5 for context.

2.2.3 Self-Emission

Self-emission is an important part of limb-emission imaging instruments and must be considered in the thermal design. As limb-emission instruments measure in the infrared range to detect thermal signatures of species from emissions, they detect all thermal signatures. This will include anything that is in the path of the detector, which includes any lenses or windows in the optical system. Self-emission is known as the aspect of the measurement signal that is not from the atmospheric measurements but from elements of the instrument, usually the lenses, that are also in the path of the detector. This addition to the signal causes issues in the signal-to-noise ratio, if the temperature of the lenses as seen by the detector begins to wash out any signal of the atmosphere, and also the radiometric calibration and phase determination of the data, as this self-emission also has signal phase effects on the measurements.

The addition of the self-emission signal to the total measured signal can be shown mathematically. The signal measured by the detector can be split into three major sources: radiation from the atmosphere S_b (the goal of the measurement), emission from optical components S_o , and emission from the beam-splitter of the FTS S_b (Kleinert and Trieschmann, 2007). Together, these make up the total interferogram signal.

These self emission components can be calibrated out through the Revercomb method (Revercomb et al., 1988) that is used to calibrate the GLORIA measurements (Kleinert et al., 2014). A core assumption in this calibration process is that the temperature causing the self-emission signal is constant with time in a sample window. This leads to the requirement for many of

the thermal emission imaging systems having steady temperature optics, with no gradients across lenses and very small temperature drift over the course of a sample window. MIPAS, GLORIA, and LIFE all have this requirement.

As self-emission is caused by the thermal signal of the instrument, a simple way to remove a large part of this signal is by cooling the optical system to low temperatures, greatly improving the signal to noise ratio. The MIPAS and GLORIA methods use this, as described in Section 2.2.5. The LIFE solution, which is a different approach, is described in Chapter 3 of this thesis.

2.2.4 Thermal Control Methods

When designing an instrument with thermal requirements, it is often not possible to design to the correct temperature ranges without adding specific methods to heat or cool components of the design. There are a wide variety of methods for all applications, but this section will be just describing methods used in the LIFE instrument and similar instruments described in Section 2.2.5, specifically for heating, cooling, and insulation.

Coolers

While there are a vast number of types of coolers that are used in a variety of applications, there are a few that are most often used in atmospheric instrument design. Of these few, there are two that are of interest to LIFE and other instruments described in this thesis: Thermo-electric coolers (TECs) and Stirling cycle cryocoolers. Stirling coolers are used in cryogenic applications and TECs are heat pumps usually used for transferring heat from one side of a device to another in a solid-state form, and do not cool to as low of temperatures as Stirling coolers.

Thermo-electrical coolers are based upon the Peltier Effect. A simple TEC is a junction formed by semiconductors, one doped to have more holes and one doped to have more electrons. When an electric current is passed through the junction, both charge carriers move away from the junction, and there is a decrease in temperature here. Heat is thus absorbed from the environment, and carried along by electrons to the cool side. As a result a junction can be placed against a hot surface and heat will be transferred to the other side of

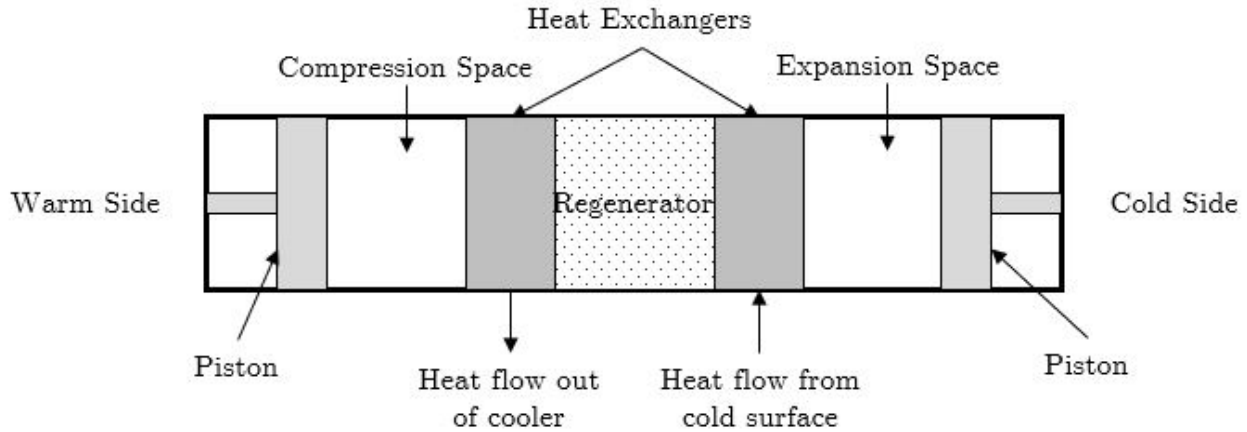


Figure 2.5: Diagram of a basic Stirling cooler.

the cooler where it can be radiated away. These devices have the advantage of being solid-state and having long lifetimes due to their simplicity, but are low-efficiency and thus are used only in specialized applications (DiSalvo, 1999). In the LIFE instrument, a TEC is used to cool the cold blackbody surface used for detector calibration.

Stirling coolers are most often used to cool a small surface area or component to cryogenic temperatures, and operate using the Stirling cooling cycle. At its basis, it can be described as a piston system, which moves heat away from the contact surface of the cold side of the cooler and radiates on the warm side to the environment through a process of isothermal expansion and compression similar to the Carnot cycle. It is made up of a piston on the warm side, a gas compression space, a heat exchanger, a regenerator in the middle, and another heat exchanger, expansion space, and a piston on the cold side. A diagram of this system is in Figure 2.5. Heat is transferred through the cooler via a fluid, and for most cryogenic applications this is either gaseous or liquid helium (de Waele, 2011).

The regenerator at the centre is a porous material that has good contact with the gas, a low flow resistance, and a high heat capacity. Its goal is to stop heat from transferring from the warm side to the cold side by absorbing heat from the fluid, so that the surface is not heated during the cooling step. The heat is transferred from the regenerator to the heat exchangers which radiate it away from the cooler (de Waele, 2011). In the ideal case, the Stirling cycle which this piston system uses to operate can be described in four steps. The first step of the cycle is shown in Figure 2.6.

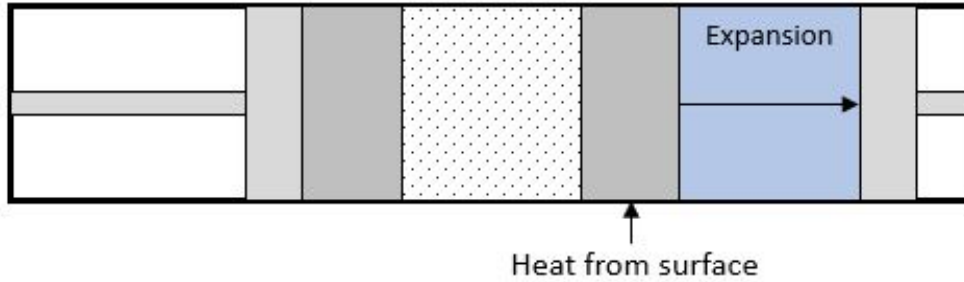


Figure 2.6: Step 1 of the Stirling cycle: isothermal expansion leading to cold absorption.

In this step, the cold piston moves to the right, causing expansion. As this expansion is ideally isothermal, heat is absorbed from the surface into the heat exchanger, which transfers it to the fluid. The next step is shown in Figure 2.7.

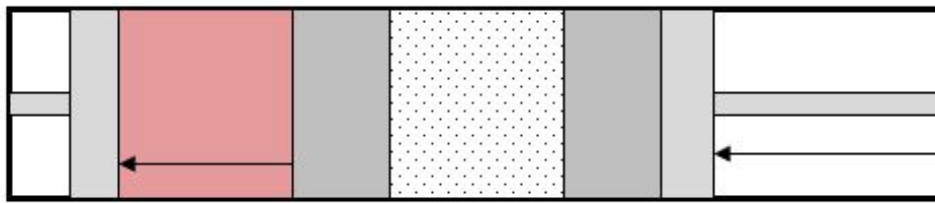


Figure 2.7: Step 2 of the Stirling cycle: Both pistons move, there is a constant volume and an increase in pressure.

Here both pistons move equally, so the volume remains constant. There is an increase in pressure so to keep temperatures constant, heat is extracted from the regenerator (it is stored here from step 4). Thus there is heat in the compression chamber from both the regenerator and the surface. It is removed from the system in step 3, shown in Figure 2.8.

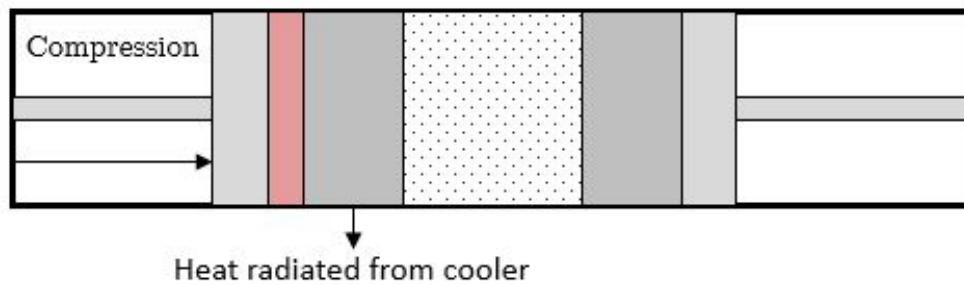


Figure 2.8: Step 3 of the Stirling cycle: isothermal compression leading to heat being radiated to surroundings.

In this step the warm side piston moves to the right, causing compression. Ideal isothermal compression leads to heat being radiated away to the environment via the warm heat exchanger. The final step leads back to step 1, shown in Figure 2.9.

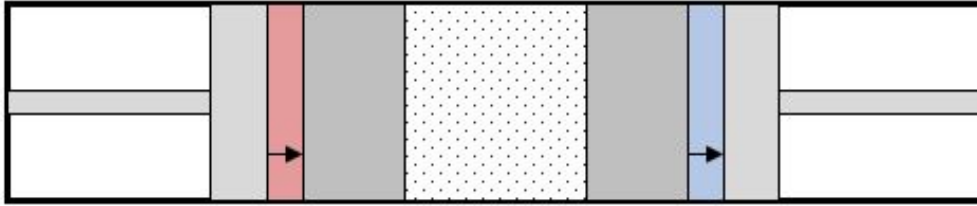


Figure 2.9: Step 4 of the Stirling cycle: Both pistons move, there is a constant volume and a drop in pressure.

In this final step, both pistons move equally once again to keep volume constant. Here there is a decrease in pressure, and to keep temperatures constant heat is trapped by the regenerator. As a result, there is little heat (what remained after radiation) in the fluid that is transferred to the expansion chamber. This means that the fluid is cool in the expansion chamber, causing more heat absorption from the surface and less warming of the surface by the fluid. The cycle then restarts (de Waele, 2011). An ideal Stirling cycle pressure-volume diagram is shown in Figure 2.10 to summarize the steps.

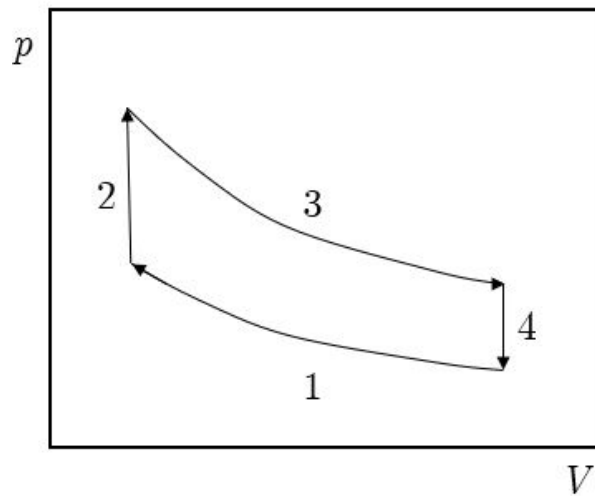


Figure 2.10: An ideal pressure-volume diagram of the Stirling cycle. Non-ideally, this plot is elliptical.

Realistically, this cycle is not split into four discrete steps. Many modern Stirling coolers

use a phase difference of around 90° between pistons, making a harmonic motion and can be driven by a common rotary axis. There are also more complex versions of the Stirling cooler that use a compressor and magnetic field to drive pistons (de Waele, 2011). Stirling coolers are useful for cooling specific small surfaces to very low temperatures, and is used in many instruments to cool small, cryogenic instruments. It is used in LIFE to cool the infrared detector to below 70K to obtain the required sensitivity.

Heaters

Heaters are often needed in instruments to ensure that electronics do not freeze during operation. The most common type of heater is a high-power dissipating resistor encased in some type of conducting material. The maximum heat power that is dissipated from the heater can be chosen based on the size, and the amount of current applied to the heater can control the heat power precisely. These are most often used with a PID controller, which will raise or lower the current applied to the heater until the object being heated has reached the desired temperature (Wertz et al., 2015). Components that are heated can sometimes be quite large, and if the instrument is continuously in a cold environment these heaters can draw a very large percentage of the total power of the instrument.

Insulation

A key part of thermal design is insulating heat-sensitive components from other components where the temperature can vary rapidly or become extreme. For example, to help avoid self-emission as described previously, temperatures should be kept as steady as possible across optics. To help maintain steady temperatures even if the environmental temperatures are changing rapidly, insulation must be used. Insulators are any material that have a very low conductivity, that is $k \ll 1$. There are two insulation scenarios, one for radiation and one for conduction. A method of thermal control for each is given that pertains to this thesis.

In the case of conduction, there is a solid point of contact between two components for heat transfer, thus a solid insulator must be used. Most non-metals, typically plastics, are useful here, as they have a low conductivity. But plastics will off-gas in a vacuum environment, so cannot be used for balloon or satellite-borne instruments. Most often this is solved by using

titanium. Unlike most metals, it has a very low thermal conductivity, meaning that is a good choice of material between two objects that should be isolated from each other. This is often done in the form of titanium spacers or joints, and is used on LIFE to help dissipate thermal fluctuations to the optics module.

A common insulation that is used to protect instruments from exterior heat flux, such as the sun, is multi-layer insulation (MLI). MLI blankets are the most common form of insulation for delicate instruments in extreme temperature environments. It is composed of multiple layers of low-emissivity material with a low conductivity. The material is often embossed, and made of one side aluminum and one side mylar. The embossing allows little conduction between layers due to less contact, and the mylar acts as a low conductivity spacer. Any number of layers can be used, but the effect decreases exponentially with the amount of layers (Wertz et al., 2015). MLI is most often used to lessen the effects of the solar flux falling on an instrument, and as such is most often used in spacecraft. It was not considered for the LIFE instrument due to the short flight time of the instrument and flying mostly during night, but was used for insulation on MIPAS.

2.2.5 Instruments

As briefly described in Section 2.2.2, the environment of balloon instruments, as well as the space environment, has many thermal implications that must be accounted for in the design. The instruments that are used for atmospheric sensing often have important thermal requirements for delicate systems, such as the Fourier Transform Spectrometers and MCT detectors. Self-emission as described in Section 2.2.3 also plays a very large role in the design and must be considered carefully to minimize its effect. Different instruments use different methods to meet these requirements to ensure that they survive the flight. The thermal designs of MIPAS and GLORIA, as forerunners to LIFE, are described here. Research done into the design of these instruments helped form the basis for the design of LIFE, although it was ultimately taken in a different direction.

MIPAS

MIPAS is different from GLORIA and LIFE in that it flew on-board the ESA Earth observation satellite Envisat (Doornink, 1996), so it is the only instrument of the three to be designed for a satellite environment. However, as the design with regards to the FTS, lens system and detector is similar to GLORIA and LIFE it is still helpful to discuss here.

The electronics have a relatively small required temperature range at 273-313K. However, operating at a room temperature range meant avoiding the need for any coolers. These temperatures were achieved using heaters during cooler periods and a radiator during warm periods. The radiator was designed to be able to be changed late in the design, and was highly based on results of testing (Doornink, 1996).

MIPAS had to be actively designed to remove as much noise caused by self-emission as possible. To achieve this, the following requirements were placed on the MIPAS optical module: Maintain temperature level of the main interior of the module around 200K, minimize gradients in the optics, and minimize temperature fluctuations in the module. Also, the radiative part of the coolers for the optical module that maintain temperature at 200K must also be isolated and remain between 263-293K to dump heat effectively. The detector and optics must be kept at cryogenic temperatures below 70K to avoid saturation of the MCT and further reduce self-emission. It was difficult to meet these requirements in the space allowed, and required trade-offs between thermal constraints and instrument performance (Doornink, 1996).

Externally, MIPAS is thermally insulated from the rest of EnviSat through the use of titanium spacers and brackets. As the exterior of the instrument will face different thermal problems as a satellite instrument than LIFE, it will not be described in detail here. The main aspect of the exterior thermal design was to avoid temperature fluctuations seen by the sun in daylight and eclipse, so heavy layers of Multi-Layer Insulation were used to minimize these temperature fluctuations (Doornink, 1996). This did not need to be considered for LIFE or GLORIA as they are designed for smaller time periods on an aircraft or balloon and likely not see the sun rise or fall more than once.

The majority of the internal temperature requirements were met using two Stirling coolers.

These were in a separate detector and optical chamber from the rest of the optical module interior, so that it could be maintained at 70K. This also helped to achieve the requirements of small thermal fluctuations and gradients across the optics. The rest of the interior was cooled via a radiator to 210K. One of the main aspects of this instrument, the Fourier transform spectrometer, is also in this radiator-cooled compartment to lower the effects of the FTS mirrors and lenses on self-emission. It would have been ideal to lower noise even further to cool the FTS to 70K, but this was not possible both thermally and mechanically for the FTS to maintain operation. These radiators were held in a separate compartment cooled with a smaller radiator to allow heat to be dumped from these larger radiators to outer radiators and into space (Fischer et al., 2008) (Doornink, 1996).

Between many parts of the interior, such as the cooled optics/detector chamber and the larger interior module, is a goldised metal sheet. This is used as a thermal shield between components, due to the very high heat reflectivity of gold. As a result, very little heat is absorbed by the outer metal walls of the cooled optics/detector chamber and lessens workload on the Stirling coolers, and keeps optical temperatures steady. This is used around this chamber, including the module walls and housing (Doornink, 1996).

There were a number of design considerations and implementations necessary to meet all requirements. Through the use of a variety of coolers, shielding and radiators, requirements were met but with effects on the optical design. The optical system design, itself being relatively simple, was complicated by the numerous thermal requirements that led to numerous interfaces needing to be considered more carefully (Fischer et al., 2008). This shows how thermal measures can easily complicate a simple design and must be considered at all stages of the design process.

GLORIA

GLORIA, as an airborne thermal imaging instrument, is similar to LIFE in the thermal issues it will face, with the only major difference being altitude. The difference in altitude means that air density, and therefore convection, needed to be considered at the altitude the experiments took place (around 10-15km). During its test flights, environmental conditions for GLORIA reached 225K in its instrument bay, with an exterior temperature of almost

190K at the coldest. Affects of heating due to adiabatic compression around the aircraft led to some heating at higher speeds (Piesch et al., 2015). Another aspect of the design that did not need to be considered for LIFE that provided challenges for GLORIA was aircraft vibrations. Due to the steady nature of the balloon this was not an issue for LIFE.

Temperature requirements for the optical components of GLORIA were set as 220K or below to lower noise due to self-emission. This temperature requirement was set as a trade-off between complexity and performance; a lower temperature would have led to the need for an evacuated compartment, and would not have led to a much higher signal-to-noise ratio. The requirement for the detector itself as an MCT array was 50K or below. The temperature of the optical compartment and specifically the components needed to be uniform, for two reasons: self-emission calibration, and to avoid thermo-mechanical misalignment of the spectrometer system, and specifically disturbances to air density around the spectrometer itself. In addition to the uniform temperature, the required temperature drift of the optics was set as less than 2 K/h. This is to provide long sampling windows between blackbody calibrations to achieve high radiometric accuracy. In addition, as GLORIA is a gimballed instrument, the cooling system needed to be near the optical system, to avoid any connections between the gimbal and other parts of the instrument or the aircraft which may compromise the gimbal system. The cooling system also needed to be small and lightweight to easily fit and operate within the gimballed instrument housing. Finally, the solution chosen needed to have reproducible temperatures and operations in both the flight and lab environment (Piesch et al., 2015). The thermal design to be able to meet these requirements is complex, and required the use of a variety of systems. They are split between three main parts: The insulation, optics chamber, and detector.

The insulation was an important aspect of this instrument due to the lower temperatures required internally and the air outside the aircraft that would lead to heating through convection, or unstable temperatures due to the turbulent air around the aircraft. Thermal insulation was accomplished through the use of vacuum insulated panels (VIP), manufactured from porous silicon dioxide, and sealed with aluminumized polyester foil. VIP are very good insulators as through the evacuation of air convection does not have an effect, and in the case of GLORIA using silicon dioxide the conduction of the panels themselves is very low

as well. Glass-fibre reinforced plastic (GFRP) spacers are used throughout to lower conduction, and polyethylene foam was used where VIP could not be used (i.e. many mechanical interfaces) however it is less effective than VIP (Piesch et al., 2015).

MCT detectors are typically required to operate at 70K or below to avoid saturation of the highly sensitive detector semiconductor pixels. GLORIA set a requirement to run their detector array at 50K, which was accomplished through the use of a Stirling cooler. As this runs at least 150K cooler than the optical unit, it is thermally isolated through the use of GFRP spacers from the rest of the unit, and is mounted to a separate plate from the optical system. This also helps isolate the Stirling cooler compressor vibrations from the optics (Piesch et al., 2015).

The largest and most complex component of the GLORIA thermal system is the optical cooling system. It was determined that Stirling coolers would be too large and heavy to be able to cool the entire optics array and FTS, so a coolant system of dry ice was used. The optics system and FTS is placed within a sealed optics compartment, which sits in a larger compartment. Solid CO₂ within this larger compartment cools the optics compartment to between 200-220K, which meets temperature requirements. However, it would be difficult to move solid CO₂ into this compartment, without disrupting insulation and convection through a large opening. In addition to this, dry ice is costly to transport and difficult to store and handle, especially in remote areas where the GLORIA research aircraft often needed to land (Piesch et al., 2015).

To solve this issue the GLORIA team created a method of using liquid CO₂ (LCO₂) to create a dry ice 'snow' that would fall over the sealed optical system. This would solve the issues of transportation as the liquid form of carbon dioxide can be transported via gas cylinders. The creation of this dry ice snow is done through the use of a polyethylene pipe that runs through the cooled compartment, which has small holes along the side. LCO₂ is pumped along this pipe at high pressure, and due to the sharp lowering of pressure at these holes, adiabatic cooling occurs and the LCO₂ turns to snow. This snow falls upon the sealed optical system and keeps it at the desired temperature. Sublimated CO₂ gas is pumped from the chamber via another tube. There is enough LCO₂ stored during an experiment to cool the system for 24 hours. This dry ice solution has proven successful during experiments, with

the only problem due to the sublimation of gas slowly leading to a temperature drift of 1 K/h during flight and 1.6 K/h on the ground (due to the higher environmental temperature in the lab) however this was still within the required range (Friedl-Vallon et al., 2014) (Piesch et al., 2015).

This system can be both operated in flight and in the lab, but there is also the option to use liquid nitrogen in the lab to cool to similar temperatures. This method was determined too difficult to use during flight. This entire system is able to operate at required temperatures for at least 24 hours, long enough for a large number of measurements during flight (Friedl-Vallon et al., 2014) (Piesch et al., 2015).

2.3 IR Detectors

To perform thermal emission measurements, an infrared detector is needed. There are a variety of different detectors available, used in different systems. A description of different detectors and their uses are described here. The detector chosen is described in Section 2.3.2, and the characterization of this detector is the second aspect of this thesis. The background of aspects of the detector that are characterized, the non-linearity of the signal as well as the signal responsivity, are both described in this section.

2.3.1 IR Detector Types

At the highest level, there are two types of infrared detectors: Thermal type and Quantum/Photon type. Thermal type detectors operate by using a surface where incident radiation is absorbed to change the material temperature. There are four types of thermal type detectors: First, the thermopile, which uses a metal or semiconductor junction. When heat is absorbed by one of the metals, it creates a thermoelectric motor force due to the thermoelectric effect which is measured. These are not as sensitive as other methods but are very reliable and cost effective. The most popular option is the bolometer, which is a large resistive element that has a large temperature coefficient and a small heat capacity, and the resistance change can be measured. This was originally considered for the LIFE instrument but it was determined it would not fit requirements. The third thermal type is the pyro-

electric, where a small capacitor polarization is changed due to incident radiation, with the magnitude dependent on the radiation. These can be used in high-responsivity applications. Finally, the Golay cell consists of a container filled with gas (typically with low thermal conductivity), and incident radiation will cause the gas to expand slightly, which moves a membrane on the side of the container, and the movement of this membrane is measured. While this has a relatively slow responsivity, it is extremely sensitive (Rogalski et al., 2018).

A difference between thermal type and photon type detectors is that thermal type detectors rely only on the energy of the radiation, or heat. This means that they do not have a precisely defined wavelength range, like photon type detectors. While this is a positive of thermal type detectors, they also have a low detection capability as compared to photon type detectors. Photon type detectors are overall better than thermal type detectors but are more expensive, and must be chosen based on wavelength range. Different detector materials all correspond to different wavelength ranges, and must be chosen according to the wavelength range needed for the application. These detectors may also have to be cooled depending on the range measured (Hamamatsu, 2004).

Photon detectors operate by absorbing incoming radiation within the material by interactions with electrons, either bound to lattice atoms, free electrons or impurity atoms. The output signal results from a changed energy distribution of the material, and the physics behind this change is dependent on the type of detector. Generally, they can be split into two classes: photovoltaic (PV) detectors and photoconductive (PC) detectors. Photovoltaic detectors operate through the use of a p-n semiconductor junction and a strong internal electric field. When a photon is incident on the junction, free electron-hole pairs that are normally separated by the electric field cross the junction. This causes a change in voltage (or current, depending on the configuration) that can be measured. Photoconductive detectors are similar theoretically to thermal type bolometer detectors, where a large semiconductor is used as the detecting surface. When a photon is incident with this surface, an electron-hole pair is released, which increases the conductivity. This change in conductivity is measured in one of two ways depending on the configuration of the detector, either through 'constant-current' where the voltage will change, or 'constant-voltage' where there is a bias voltage across the conductor and the current change is measured. An advantage of PC detectors is

having a much higher responsivity, however a disadvantage is that these must be operated at low temperatures, which also causes a non-uniform detector element, leading to errors in measurements. This is a key issue with these detectors and is described in detail in Section 2.3.3 (Rogalski et al., 2018). Both PV and PC detectors are similar but are used in different applications. There are other designs for photon detectors but they are only used in very specialized cases.

The case of the photon detector where operation is based on measuring the release of a hole-electron pair or the excitation of an electron are known as intrinsic detectors. Another method of detection is through exciting electrons into the conduction band from impurity-bound states such as energy gap or quantum wells. These are known as extrinsic detectors. These detectors can have high wavelength detection bands, but are often expensive and need to be cooled to extremely low temperatures (Rogalski et al., 2018).

A key aspect of almost all photon detectors as compared to thermal detectors is the need for cryogenic cooling. Thermal generation of charge carriers happens easily for the semiconductor materials used in photon detectors, and the detector quickly becomes saturated, or at the very least extremely noisy. All extrinsic operating detectors and most intrinsic operating detectors must be cooled to achieve the advantage of longer-wavelength sensitivity. There is a relationship between the wavelength that can be detected (λ_c) and the highest temperature the detector must operate at (T_{max}), and this is given in Equation 2.13.

$$T_{max} = \frac{300K}{\lambda_c[\mu m]} \quad (2.13)$$

This maximum temperature is the highest temperature to achieve background-limited performance (BLIP), where the background noise does not saturate the detector. This relation is based on the variables that affect the detector performance such as electron excitation energy at lower wavelengths (Rogalski et al., 2018).

The main characteristics of IR detectors, as mentioned above, are the wavelength region (or temperature) to be measured, the sensitivity and signal to noise ratio needed, and responsivity. With these in mind, a detector can be chosen. For LIFE, a spectral range of 7-14 μm was needed, a high sensitivity/signal-to-noise ratio, and high responsivity. The high sensitivity and responsivity meant that thermal type detectors was not an option, leav-

ing photon type detectors. In the spectral range necessary, only a few types of detectors would meet requirements: the intrinsic type mercury-cadmium-telluride (MCT or HgCdTe) detector, which has a spectral range of 2-16 μm , extrinsic germanium which has a range of 2-14, 2-30, or 2-40 μm depending on the metal doped in the germanium, or extrinsic silicon, which has a range of 1-17 or 1-23 μm again dependent on the metal the silicon is doped with (Hamamatsu, 2004). Although the extrinsic type detectors have a high responsivity and large spectral ranges, they must be cooled to temperatures below 10K and as such are very difficult to use. Thus the MCT detector was chosen as the solution for the LIFE instrument.

2.3.2 MCT Detectors

Mercury-cadmium-telluride is currently one of the most popular detector materials for high-performance infrared detectors. There are numerous reasons why this material has become popular. The largest is its wide wavelength range at a temperature of 70-80K, much higher than materials with comparable wavelength bands. When producing the MCT material the molecular composition can be changed to slightly alter the wavelength range, making it versatile. MCT as a semiconductor material has many desirable qualities that make it ideal for its application as a photon detector: It has a high optical absorption coefficient, so it can absorb almost all incoming radiation, and has readily available doping techniques to improve the material. The reason for its operation at relatively high temperatures for its wide wavelength range is its low carrier generation rate and high electron mobility. As a result, there is less noise due to thermal carrier generation, and the detector can be operated at higher temperatures without compromising performance (Baker, 2010) (Baker, 1981). As with all PC detectors, it has a high responsivity and sensitivity, making it an ideal candidate for the LIFE application. The GLORIA instrument uses as very large 256-pixel MCT detector array for infrared measurements of the same species as LIFE, to great success (Friedl-Vallon et al., 2014). More detail and specifications for the setup of the LIFE MCT Detector are provided in Chapter 5. There are two main characteristics of MCT detectors that must be carefully studied before use, the non-linearity and responsivity.

2.3.3 Non-linearity

As described in Section 2.3.1, PC detectors operate by exhibiting a change in conductance when radiant photons are incident on the detector. When operating in constant-current mode, this change in conductance corresponds to a change in voltage, which is proportional to the radiant flux. However, it has been found in numerous experiments that this voltage change is not linear with a linear increase in incident flux, but is instead a non-linear curve that flattens towards the top of the detection range until it becomes saturated. This non-linearity must be minimized and characterized, as it leads to distortions in the resulting measured spectra (Novak and Eppeldauer, 1989) (Rahmelow, 1997).

Theoretically, the incident flux on the detector when used in an IFTS should linearly correspond with the amplitude of the resulting interferogram. For some detectors, this assumption holds, but with PC detectors this does not suffice. In addition to this issue, non-linearity can appear as out-of-band detection. In some situations, non-zero values can be seen in resulting spectra out of the wavelength band of the detector, where there should theoretically be no detection. This non-zero region is a result of non-linearity, and can distort spectral calibrations and analysis (Abrams et al., 1994).

There are several causes for this non-linearity, with one major reason being the result of high light flux on the detector, i.e. saturation. This is the cause of the non-linearity in the voltage change near the top of the operating region towards saturation. This saturation due to high flux occurs as a result of the decline in the lifetime of charge carriers in the semiconductor, a result of Auger recombination. In MCT detectors, one of the advantages is the high electron mobility relative to the hole mobility, which gives high responsivity. Due to the high electron mobility compared to the hole mobility, an equation can be written for the photoconductivity of the detector cells, shown in Equation 2.14.

$$\sigma_{pc} = q\mu_{\eta}n_e = q\mu_{\eta}(1 - R)\eta\tau\Phi/d \quad (2.14)$$

Here q is the electron charge, μ_{η} is the electron mobility, n_e is the excess carrier density, R is the reflectivity of the detector surface, η is the quantum efficiency, τ is the free-electron lifetime, Φ is the incident photon flux, and d is the thickness of the detector. Theoretically,

μ_η , R , η , and τ are independent of Φ . Thus, the conductivity is entirely dependent on the photon flux, as predicted. However, in the case of high photon flux, very large excess carrier concentrations cause a decrease in mobility due to the phenomena of electron-hole scattering (Scott, 1972). This has effects of reducing quantum efficiency as a result of free-carrier absorption, and can also change the reflectivity through the index of refraction. Finally, this will effect carrier lifetime, also having an effect on responsivity, as recombination happens more quickly (Bartoli et al., 1974).

In addition to high photon flux, there are other causes, such as the non-linearity of the semiconductor itself. Intrinsically, the exchange of electron-hole carriers across the band gap of a semiconductor may be non-linear due to the manufacturing process, which contributes to the non-linear voltage output. High bias voltage can also have an effect, contributing to saturation (Eppeldauer and Martin, 2001) (Novak and Eppeldauer, 1989). One of the major aspects of characterizing the MCT detector as part of this thesis is to take measurements and alter settings on the LIFE detector such that the non-linearity is minimized and well-known. This will make calibration and spectra from measurements more accurate.

2.3.4 Responsivity

Responsivity is an aspect of MCT detectors that must be determined and optimized, both for the best operation and to lower noise. Responsivity is the ratio of generated voltage (or current, depending on the setup) and incident radiative power of a detector. In other words, it is a direct conversion between the incoming radiation and the output voltage signal. A basic equation for this ratio is shown in Equation 2.15.

$$\mathcal{R}_s = V_s/\mathcal{P}_\lambda \tag{2.15}$$

Here \mathcal{P}_λ is the incident flux power, and V_s is the output signal voltage from the detector (Baker, 1981). Incidence flux power can be related to the photon flux Q_s and frequency ν through Equation 2.16.

$$\mathcal{P}_\lambda = Q_s Ah\nu \tag{2.16}$$

Ideally, this responsivity is maximized such that incident radiation causes a large change in voltage, and even very small amounts of incident radiation power is measured and can be seen in the voltage change. Therefore, for the most part, the higher the responsivity, the better the performance of the detector (Sha, 2013). However, it cannot simply be optimized for this maximum ratio, because as responsivity increases, so does non-linearity. This is a result of higher bias voltage being one of the causes of non-linearity and so if radiation causes a large voltage change, it will cause a non-linear change and may even saturate the detector. Characterization and optimization of the responsivity is essential to good measurements from the detector.

The responsivity of an MCT detector can be calculated theoretically from the conductance of the detector, based on the derivation in the text *Semiconductors and Semimetals, Volume 18: Mercury Cadmium Telluride*. The conductance of the detector is given by Equation 2.17.

$$G = (q/L^2)(\mu_e N + \mu_h P) \quad (2.17)$$

Here μ_e is the electron mobility, μ_h is the hole mobility, N is the total number of electrons, P is the total number of holes, the detector length is L , and q is charge. The photon flux per unit area at a wavelength λ results in change in conduction, given by Equation 2.18.

$$\Delta G = (q/L^2)(\mu_e \Delta N + \mu_h \Delta P) \quad (2.18)$$

Here ΔN and ΔP are the total excess carriers in the steady state regime. In good quality MCT detectors ΔN and ΔP can be assumed to be equal. Non-linearity can arise from here if these two values are not equal. The excess charge carrier lifetime, τ , can be defined as Equation 2.19.

$$\tau = \Delta N / [Q_s(\lambda)\eta(\lambda)A] \quad (2.19)$$

$\eta(\lambda)$ is the rate at which photons at wavelength λ are converted to electron-hole pairs in the detector material. Equation 2.18 now becomes Equation 2.20.

$$\Delta G = (q/L^2)\mu_h\tau[Q_s(\lambda)\eta(\lambda)A][1 + b] \quad (2.20)$$

Here $b = \mu_e/\mu_h$, and for most MCT detectors $b \gg 1$, so $b + 1 \simeq 1$. If the detector device is assumed to be in a circuit with a load resistor whose conductance is much lower than the detector, a change in the detector conductance as a result of incoming flux results in a signal change across the load resistor given by Equation 2.21.

$$\Delta V_L = V_b \Delta G / G \quad (2.21)$$

V_b is the bias voltage, which can be tuned for the detector. Combining this equation with Equations 2.15, 2.17, 2.16, and 2.20, the responsivity for steady state operation is found, in Equation 2.22.

$$\mathcal{R}_s = [\eta(\lambda)/Lwd](\lambda/hc)V_b\tau/n_0 \quad (2.22)$$

Here w and d are the width and thickness of the detector respectively, and n_0 is the average equilibrium carrier density. Finally, this equation describes how the responsivity of the detector is dependent on both the detector design ($\eta(\lambda)$ and dimensions) as well as the bias voltage of the detector (Baker, 1981). The bias voltage is the part of the detector that can be changed and tuned to alter the responsivity, and plays a large role in the optimization as described in Chapter 5.

In the ideal scenario at a macro scale, this equation can be simplified for the scenario of a basic circuit. Going back to the basic circuit consisting of a bias battery supply V , a load resistance R_L , and a detector, Equation 2.22 can be simplified to Equation 2.23.

$$\mathcal{R}_s = \frac{V_s}{Q_s h \nu A} \quad (2.23)$$

In the small signal approximation, the signal voltage V_s of this circuit is given by Equation 2.24.

$$V_s = V \frac{R_L}{(R_L + R_0)^2} (-\Delta R_0) \quad (2.24)$$

Here ΔR_0 is the change in resistance of the detector due to illumination (Gopal, 1998). This is a simple method of relating the voltage signal directly to the detector conductivity change as a result of incoming radiation.

The method used for finding the responsivity in the case of LIFE is more complex, as realistically an MCT detector uses a larger circuit to measuring incoming signal that involves amplifiers and converters. Another theoretical approximation for responsivity is developed for GLORIA. These are described in detail in Chapter 5.

2.4 Summary

In the background section of this thesis, three major topics were covered, one as the general background of the motivation for the LIFE instrument and two as the motivations for the main aspects of this thesis. First, a discussion was given on the atmosphere, including atmospheric layers and constituents. Specifically, the region of interest to LIFE and similar instruments was discussed, the UTLS. Following the atmospheric overview, techniques were discussed for atmospheric remote sensing, and particularly the technique that LIFE is based on, limb emission thermal imaging. Finally, an overview of two instruments that preceded LIFE in the thermal emission FTS imaging field is given. These instruments as well as an overview of the atmosphere and UTLS are given to motivate the use and measurements of the LIFE instrument.

The second section covers thermal design as a background for the first part of this thesis, the thermal-mechanical design. This covers methods of heat transfer as used in thermal design, as well as the balloon environment that atmospheric instruments must be designed for. Following, a description of self-emission gives motivation of the importance of thermal design in a thermal imaging instrument. Thermal control methods are discussed, and ending with the thermal requirements and design considerations of similar thermal imaging instruments.

The third section discusses infrared detectors and specifically MCT detectors, to provide motivation for the characterization and optimization of the LIFE detector, the second part of this thesis. For MCT detectors the two main considerations for characterization, the non-linearity and responsivity, are described. This provides a background into the importance of ensuring the LIFE detector is working correctly such that the non-linearity is minimized and the responsivity is optimized.

3 THERMAL-MECHANICAL DESIGN

3.1 Overview

This chapter discusses the first of two major aspects of the LIFE design that are the focus of this thesis, the thermal-mechanical design. With previous instruments designed by the Atmospheric Research Group in ISAS, the thermal-mechanical design has played a smaller role. These instruments were not thermal imaging instruments and so had less stringent thermal requirements, and also had less power consumption which would lower any thermal effects. However, due to the complexity of these aspects with LIFE, it was determined that the thermal-mechanical design and analysis would play a major role and would require more research and simulations than previous instruments. The requirements that lead to the design are described in Section 3.2, which gives an overview of both the optical and electronic thermal ranges as well as the requirements for the mechanical design. The thermal environment is described in terms of how it relates to the thermal requirements and the simulations in Section 3.3. The software used to develop both the design and perform the simulations is described in Section 3.4, which also includes an overview of Finite Element Analysis. The description of the preliminary design and thermal simulations are found in Section 3.5, and finally the construction and testing of LIFE is described in Section 3.6.

3.2 Requirements

Requirements always play a key role in any design, but may vary in how much they constrain the design process. Both the thermal requirements (set by the optical and electrical systems) and mechanical requirements (set by the CSA and CNES for the gondola) have had a large effect on the design. These requirements are described in detail in the following sections,

before the design is described in detail, to provide background behind the design considerations. The optical system, being the most thermally sensitive and driving much of the LIFE design and thermal simulations, is described first. Following is the electrical system, which also has constraining requirements due to the high amount of heat dissipated as well as narrow operating temperature ranges. Finally, the mechanical constraints as set by CSA and CNES for the gondola flight are described.

3.2.1 Optical Requirements

The optical system, as with any thermal imaging instrument, must be carefully designed so that the thermal effect of the instrument from self-emission and temperature variations throughout flight have a minimal effect on the measurements. Before describing the requirements for each component of the optical system, a Computer Assisted Design (CAD) model of the optical system is shown in Figure 3.1 to illustrate all important optical system components. This will be described in greater detail in Section 3.5. A table summarizing the optical system requirements is presented at the end of this section, in Table 3.1.

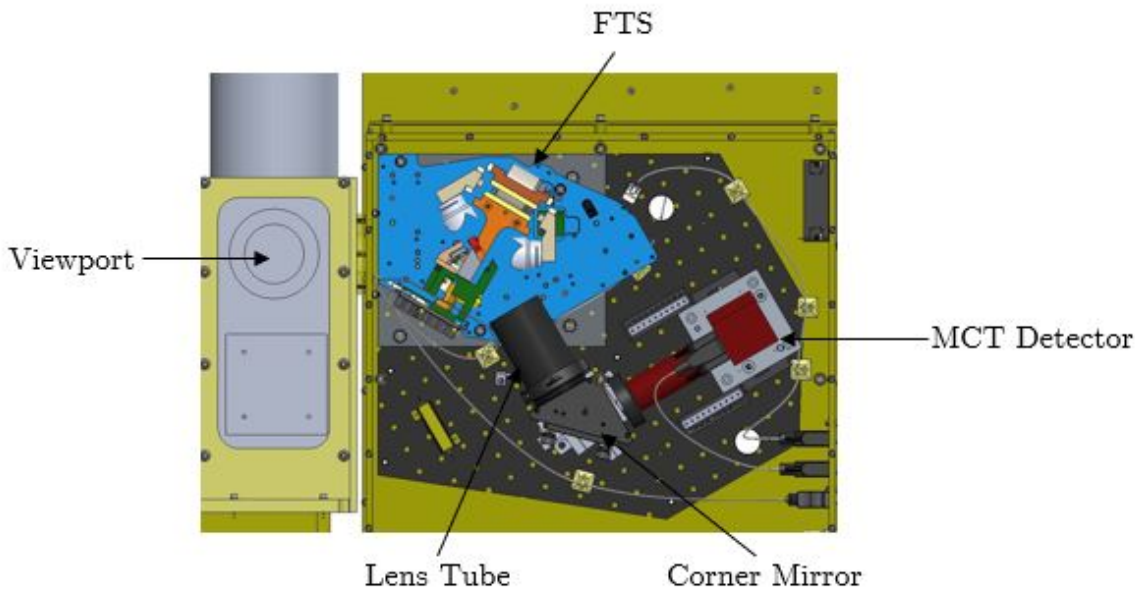


Figure 3.1: CAD model of LIFE optical system.

The optical system consists of the FTS, MCT detector, and imaging lens system between the FTS and detector. The FTS is a purchased commercial MB-3000 system from ABB, which was customized by ABB for this specific application. The MCT detector also came with the FTS as part of this purchase, specifically for the use in the LIFE instrument. The imaging lens system was designed in-house.

The first consideration is that the detector must be operated at 70K or lower as typical of MCT detectors. This requirement is already met by the pre-installed Stirling cooler that sits above the detector, so this requirement itself did not heavily influence the thermal design. However, something that still needs to be considered here is the removal of heat from this system. It must be ensured that the Stirling cooler is able to remove heat from the detector, either through conduction to the box walls or through sufficient radiation. Also, this removed heat will warm other components nearby, so must be designed for as well.

The lens array and FTS are the components that need to be most carefully thermally controlled. For this system, temperature requirements must be defined for environmental and mechanical reasons. Condensation in the lenses must be prevented during the ascent of the flight, where the instrument travels through the cold and humid troposphere. To provide a reasonable margin to avoid the optics dropping to 0°C or below when condensation can form, a minimum temperature limit of 5°C was set. When operating in a warmer environment, such as the lab, thermal expansion of the lenses can be an issue, which may change optical properties and cause alignment problems. To avoid this, the maximum temperature requirement was set as 25°C. In addition to this temperature range requirement, the temperature drift must be considered as well. This is required to avoid issues with self-emission and removing the self-emission signal in the data analysis. As the time frame for multiple images of an instrument view (i.e. a blackbody or limb measurement) is on the order of minutes, the drift must be as small as possible over this range. A requirement is set at less than 0.1°C/min temperature drift over the lens and FTS components.

The optical system mechanical requirements are to avoid any movement that could cause misalignment of the optics. It can be difficult to notice an issue with alignment as well as re-align the system, due to it being designed for non-visible light. The system must be as firmly built as possible to avoid any issues. There was originally also a mechanical requirement of

removing vibrations from the system; small vibrations from the Stirling cooler were initially planned to be dampened or removed through some mechanical design. However, through in-lab tests and the use of a uniform time sampling algorithm, it was determined that these vibrations would not have enough of a detrimental effect on the data to require a much more complex vibration dampening optics system design, and was removed from consideration.

System	Requirement
MCT Detector	Temperature at 70K
MCT Detector	Dissipate heat to avoid overheating
FTS/Lenses	Temperature range 5°C - 25°C
FTS/Lenses	Temperature drift < 0.1°/min
Mechanical	Minimize vibration

Table 3.1: Optical system thermal-mechanical requirements.

3.2.2 Electronics Requirements

The electrical components of LIFE have a wide variety of temperature ranges, which plays a large role in the design of the electronics box. There are a few particular components that have a narrow temperature range requirement, which must be placed accordingly in good locations and the temperature verified with simulations. The electronics are placed in a separate box from the optics; it is typical to place electronics in a separate box from the optical system, for both cleanliness and thermal reasons. The electronics in LIFE do not need to be as carefully controlled and kept as thermally steady as the optics, but it must be ensured that the temperature will not swing outside the required temperature range, especially during the ascent phase of flight through the tropopause. The most thermally sensitive components are the control board for the FTS system (BMXS Board), and the Ethernet interface boards (Pleora Boards) attached to the detector data acquisition (DAQ) boards. The thermal requirements for all major electronics in LIFE are detailed in Table 3.2.

An important consideration in meeting these requirements is for the instrument to be

Component	Minimum Temperature (°C)	Maximum Temperature (°C)
BMXS Board	5	35
CPU Stack (x2)	-40	85
DAQ Board (x2)	-40	60
DC-DC Converter	-40	85
Ethernet Switch	-40	70
Motor Driver	0	60
Pleora Board (x2)	0	40
Temperature Controllers (x5)	-40	85
VIPAC Power Supply	-40	95

Table 3.2: Temperature limits of the major electrical system components.

able to dissipate enough heat in the warm scenario, without freezing in the cold scenario. Overall the total dissipation of the instrument is upwards of 500 W, largely due to the two DAQ boards of 40 W each. The instrument must be designed to move this heat away from these boards efficiently, and played a large role in the design.

3.2.3 Mechanical Requirements

The LIFE prototype was tested on a high-altitude balloon gondola, and to do this the instrument had to meet mechanical requirements as outlined by CNES and the CSA. These requirements included volume, weight, bolt pattern, force and impact requirements. In addition to the gondola constraints, the instrument needed to be tested inside the ISAS Thermal Vacuum Chamber (TVAC), which provided further volume constraints.

CNES has multiple high-altitude gondola models of different sizes, and LIFE was designed to work with *Carmencita*, the smallest model. A CAD model of *Carmencita* is shown in Figure 3.2 (Vincent, 2019). The design requirements that this gondola imposed upon the LIFE design were the volume, mass and bolt pattern constraints. As it is the smallest CNES gondola, and the flight was being shared with a few other smaller experiments, the CSA gave

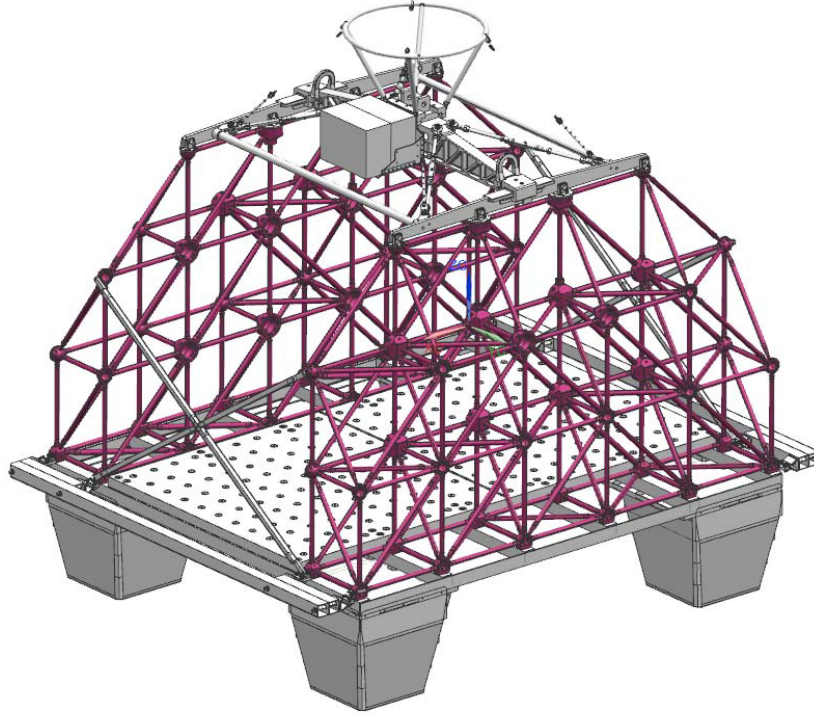


Figure 3.2: The CNES Carmencita gondola which carried LIFE for the test flight.

LIFE a maximum weight requirement of 100 kg. In terms of size, the gondola is a modular design, forming 'boxes' with corner nodes that can be connected to other boxes. The size of one of these boxes is 342 mm x 342 mm, meaning that the total height of the gondola is 1.026 m in the centre, sloping down to 342 mm on the edge. No part of the instrument could protrude past this limit as a thermal blanket would be placed over top as a cover. LIFE was planned to be placed towards the centre of the gondola to maximize height allowance, but the sloping cover still needed to be taken into account, which could affect the LIFE maximum height depending on the width of the instrument. The honeycomb base plate panels that the instrument would attach to led to requirements for length and bolt pattern. The instrument base plate must match a 100 mm x 100 mm M6 pattern, and avoid protrusions used to attach the base plate to the structure. This gave a base plate length requirement of 950 mm. The wall-to-wall length was slightly longer, at 1114 mm (Vincent, 2019). The TVAC chamber gives further volume requirements, with an internal size of 1006 mm x 813 mm x 794 mm. A more detailed overview of the TVAC chamber is provided in Section 3.6.2. Both these dimensions and the Carmencita dimensions provided an overall size requirement of 950 mm

x 813 mm x 794 mm.

LIFE had to meet numerous mechanical requirements as specified by the CSA. They provided an extensive Excel document which would calculate forces at each mechanical interface of the gondola to LIFE, as well as LIFE interfaces, to ensure it would survive a worst case force scenario. This was calculated at multiple angles from 0° to 315°, and calculated the maximum shear and tension forces based on the LIFE weight. A more detailed examination of these interfaces and forces calculated can be found in Section 3.5 as the survival requirements depended on the detailed design, including mass and bolt pattern. However, one of the defining values for survival was the maximum force due to acceleration or shock. For the weight and size of the Carmencita gondola, this was given as 15 g shock at ground impact. Other forces included rapid deceleration after parachute opening, at 8 g. As LIFE was relatively heavy, it had to be ensured during design and through simulations that the connection between the instrument and the gondola, as well as connections between various parts of the instrument would be able to survive a maximum shock of this magnitude.

3.3 Thermal Environment

In addition to the stringent requirements given for the electrical and optical systems, these requirements need to be met in numerous environments, subject to a variety of conditions. The instrument must be designed by simulating different scenarios to ensure survival. This section discusses the main three environments the instrument will see, and the plan for simulations: the lab, the ascent phase of the flight, and the main float part of the flight. These environments formed the basis of the simulation temperatures and environments.

Lab Environment

The instrument is most often operating in the lab environment. An air conditioning unit was installed in the lab to ensure that temperatures of both the instrument and the room would not increase substantially. The average temperature of the room was measured, so that the lab case for thermal simulations, known as the *warm* case, could be determined as having an atmospheric temperature of 20°C, and a baseplate temperature of 15°C (based on the surface

temperature of the table).

A difficult component of this environment to determine is convection. As described in Section 2.2.1, it is difficult just to estimate a reasonable starting point for values such as the convection coefficient, which has a large impact on the resulting temperatures. Since this would have caused too much uncertainty in the model, convection is ignored for the lab environment simulations. Although this does make the simulations inaccurate, it provides a worst case scenario, as convection will only cool the instrument when the instrument is at higher temperatures than the room which is being cooled via air conditioning. Thus the baseline for the simulations was to set the baseplate temperature to 15°C and meet temperature requirements without the use of convection to cool.

As a precaution for cooling, fans were installed in the instrument. The flow from these fans caused forced conduction upon the electronics and cool everything quickly. This could theoretically be modelled via the SolidWorks Flow Analysis package, which would allow the simulations to be more accurate for the lab environment. However the package was deemed too difficult to use for this purpose, and unless there were serious temperature issues with the radiation and conduction based lab simulations, it would not be used.

Flight Ascent Phase

Ascent is the most rapidly changing environment, and also provides a wide array of unknowns, making it difficult to simulate properly. Ascent covers the phase from when the instrument is launched to when it reaches float altitude, covering over 30 km. Both temperature and pressure change rapidly in this region, and for the LIFE flight from Timmins a pressure variation from 100 hPa to 3 hPa and a temperature range from 10°C to -70°C can be seen as a worst case scenario. This minimum temperature can occur for as long as 60 minutes (Vincent, 2019). These changes lead to difficulty in the simulation of convection, which depends on a number of variables, including temperature and pressure.

Due to the uncertainty in most simulation variables, this phase was chosen not to be modelled before flight. From previous instruments, it was found that although the temperature drop through the ascent has a noticeable effect, it is not in this region long enough to freeze and damage electronics. Further, there are no papers or materials on the change in convec-

tion in this pressure or temperature range; studies are typically done in warm environments at higher pressures, for the purpose of studying mechanical systems. It was decided that the instrument would be designed to withstand the worst case cold scenario at float altitude, and post-flight a simulation would be created based on the measured temperature through ascent, to inform future instruments and missions. This is presented in Section 4.4.

Flight Float Phase

At float altitude, the environment is fairly well defined and stable. Thus the instrument can be designed to survive and operate here with reasonable certainty in simulations. Although the measurements of the LIFE instrument do not depend on the time of day or night, it is chosen to fly at night to further define the thermal environment. It removes the possibility of seeing the sun, which presents issues such as solar heating and radiation, both of which are not well defined and are based on the viewing geometry of the instrument with respect to the sun, as well as what parts are shaded. In the night environment, the only external thermal impact on the instrument is due to conduction between the instrument baseplate and the gondola. As measured during the CATS flight and discussed in Section 2.2.2, the coldest the gondola will get is -40°C . This was used as the worst case cold scenario for the initial simulations. For the majority of the flight, the baseplate will sit between -20°C and -30°C , so the most common scenario, or the middle simulation case, was a baseplate at -30°C . In total, there are three initial simulation cases: 20°C (lab, warm case), -30°C (float, base case), -40°C (float, coldest case, following ascent).

During flight, due to the unavailability of a landing site, the landing was delayed until the afternoon, well after the sun had risen. So even though the sun case was not considered in the design, it played a role in the resulting thermal environment and should be described here. If a flight is planned to go past sunrise, sun shields are installed on the gondola to provide shade for the instruments to reduce solar heating. However since the daylight part of the flight was not planned, the sun had a significant effect on instrument temperatures. Solar heating at this altitude, due to the lack of atmosphere, can have a very strong impact on the temperature of an instrument if the absorptivity of a material is high. An example given from the CSA is a black anodized aluminum material, with an absorptivity α of 0.67,

will reach a surface temperature of 117°C in direct sunlight of 1400 W/m^2 solar flux at float ambient temperature (Vincent, 2019). Radiation will also be effected, as the object seen by the surface is at a very high temperature, as opposed to the cold atmosphere or deep space. The effects on LIFE of the part of the flight after sunrise is described and analyzed in Chapter 4.

Finally, the float component of the flight is good to simulate thermally as the simulations can be verified in the lab through the use of a Thermal Vacuum chamber (TVAC). With a vacuum environment and a cold plate that can reach -40°C through the use of liquid nitrogen, it can provide a good test of the actual flight float environment. Comparing results of the simulation to the actual results of a TVAC also helps to determine the answers to a number of questions, such as basic survivability, but also unknowns such as heat transfer coefficients across gaps. A more detailed discussion on the LIFE TVAC tests can be found in Section 3.6.2.

3.4 Thermal-Mechanical Design & Simulation Software

With previous instruments, the thermal requirements were not overly stringent, and the thermal design could be estimated with simple calculations and knowledge of previous missions. With the LIFE requirements it was determined that this would not provide enough accuracy for flight, and a full thermal analysis of the instrument was needed. A thermal model was to be created, based on the instrument mechanical model. It would analyze the thermal performance in different flight and lab environments, and determine the necessary methods required to keep the instrument above freezing as well as to dissipate enough heat. Both mechanical and thermal designs were iterated many times before coming to a final design solution. The software used to perform the analysis and design is described here. This section also explains the basis behind many design analyses, Finite Element Analysis, and relates this to how this is used in LIFE thermal simulations.

3.4.1 Computer Assisted Design Software

There are a wide variety of Computer Assisted Design (CAD) software available, and they are all used widely in industry. A large subset of these can also perform thermal analyses within the program. Research was done into different software to determine which would best suit the needs of the LIFE simulations. Two final options were found: Siemens NX and SolidWorks, both the most popular options in industry.

Siemens NX, developed by Siemens AG, is a CAD software heavily used throughout industry for advanced modelling of large designs, and particularly thermal simulations. It was recommended for the LIFE project by Honeywell Aerospace, who used the software to develop the thermal models of the CATS and ALI (Aerosol Limb Imager) instruments that the ISAS group has co-developed. NX thermal modelling software is widely considered the most advanced in the industry, particularly in aerospace design. However, downsides to NX are a very steep learning curve and price. Regardless, the thermal simulation software would likely be the best to suit the needs of LIFE.

SolidWorks, developed by Dassault Systems, is likely the most popular CAD software available. It is designed more for modelling of smaller designs and parts rather than large assemblies, and has overall less functionality. While this is a downside, it also has an easier learning curve and academic licenses are easily available, which cuts down on cost. Due to its popularity, there is a large amount of community support through forums and online tutorials on both its basic functionality and simulation abilities. Further, the early initial CAD model of LIFE had already been designed in SolidWorks; using the thermal analysis functionality of the program would be much simpler, not having to rely on exporting to another software. The thermal simulation suite, which comes built-in with an academic license, does not have the same depth as NX. This will lead to less accurate simulations. SolidWorks does have an electronics thermal modelling package as an add-on, which could be beneficial to the design. However the complexity of the package was larger than necessary, and is meant more for board-level electronics designs. As such it was not considered in the final decision. Overall however, due in large part to the much cheaper cost and prior experience in the software, SolidWorks was eventually chosen to be used for the simulations and to develop the CAD

model further.

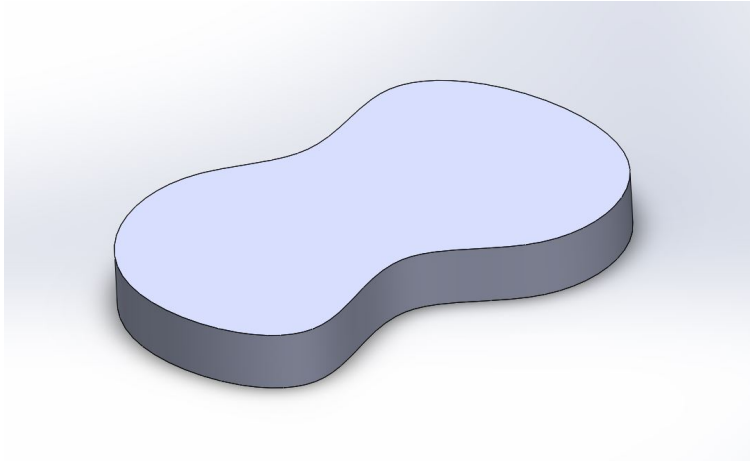
The mechanical model for LIFE, as is described in depth in Section 3.5, is designed entirely using SolidWorks. The thermal design is discussed in tandem with the evolution of the mechanical design, as they are heavily connected. Simulations were done with the aforementioned built in thermal software, and some structural simulations as well. The basis behind all SolidWorks simulations is an analysis technique known as Finite Element Analysis.

3.4.2 Finite Element Analysis

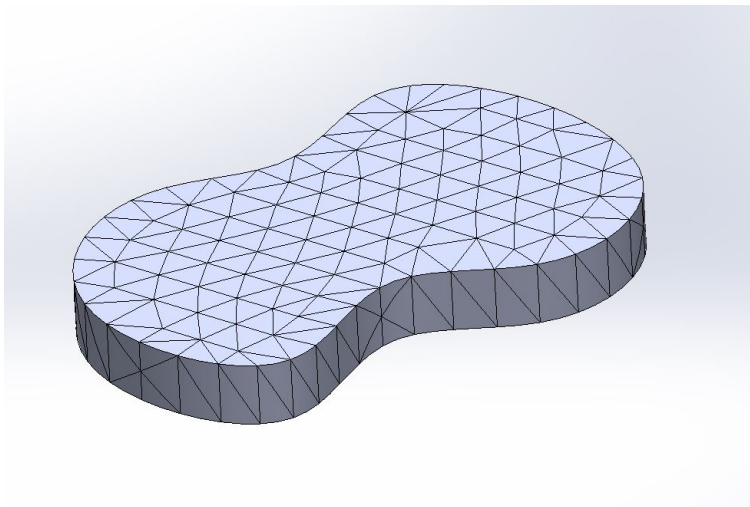
Finite Element Analysis (FEA), also sometimes referred to as the Finite Element Method (FEM), is one of the most important numerical analysis tools available for engineering design. It allows any arbitrary surface or shape in any number of dimensions to be analysed and simulated numerically. Almost all CAD software simulations utilize FEA at its basis. FEA, overall, is a process of converting any shape along with its sources and restraints that can be represented by differential equations to a system of matrices that can be solved to give an approximate solution (Ed Akin, 2009).

The basis of FEA is to replace any complex shape or model with simple shapes, that when summed together create the original shape. These simple shapes, which are dependent on the simulation but most often some type of triangle, are known as finite elements. These can be compared to the original model in the same way that finite elements of a sum can be compared to infinitesimal differential elements of integral equations. The elements can be altered in numerous ways, including shape and size, to work best for each simulation (Ed Akin, 2009). The array of elements when it is applied to a part is known as a mesh. An example of a shape being converted into both a coarse mesh and fine mesh with slightly different shapes is shown in Figure 3.3.

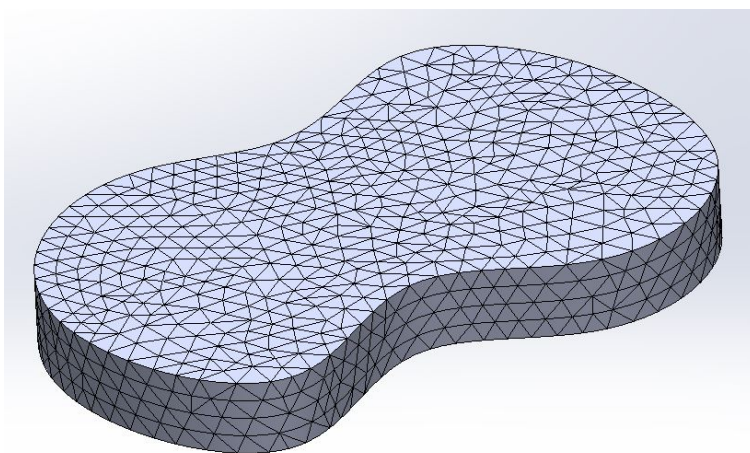
The volume of this part could now be easily calculated. The choice of element shape must be considered when creating the mesh; Computationally, the linear triangle, as shown in Figure 3.3b, is easiest to solve using a simple area equation for a linear triangle. All that is needed is the vertex components for all triangles to be able to calculate the area or volume. A quadratic triangle with curved sides, as shown in Figure 3.3c, is better at approximating curved shapes, however more advanced numerical integration is needed to solve for the area



(a) Example SolidWorks part, before elements applied.



(b) Example SolidWorks part, with coarse, regular elements.



(c) Example SolidWorks part, with fine, curved elements.

Figure 3.3: A shape being converted to finite elements, or a mesh.

or volume of a quadratic triangle (Ed Akin, 2009). It is a trade-off that must be considered between error and simulation solve time, but often there is no choice, especially working with a lot of curved components, that the latter and more computationally expensive option must be used. By default, SolidWorks uses quadratic triangles, but use higher polynomial shapes if necessary. Tetrahedral elements are always used for volume components in SolidWorks.

The evaluation of an FEA problem relies heavily on the mesh, and particularly its vertices. The mesh generates two arrays: The first is a list of all vertices, with their spacial coordinates, and is known as the nodal set. The second is known as the connectivity list and describes each vertex along with the vertices that it is connected to. This list is critical to solving analyses and simulations, as these inform the matrices and equations used for the solution (Ed Akin, 2009). For each vertex in the mesh, there is one simultaneous equation that describes every equation or variable that may impact the final values at that node.

For whatever type of simulation is being done, the general equilibrium matrix will always be the same. It is simplest to show this with the well-known spring system, following the example in the textbook *Finite Element Analysis Concepts via SolidWorks*. For the problem of a single spring that is generalized so that either side can be restrained or loaded with force, the equilibrium equations can be shown as the matrix form in Equation 3.1.

$$k \begin{bmatrix} 1 & -1 \\ -1 & 1 \end{bmatrix} \begin{Bmatrix} u_1 \\ u_2 \end{Bmatrix} = \begin{Bmatrix} f_1 \\ f_2 \end{Bmatrix} \quad (3.1)$$

Here k is the stiffness, u is the displacement, f is the force, and the subscripts correspond to each side of the spring. This can be used to represent a node of the matrix. However, in this form the equation cannot be solved; there is only information about this one node. Information must be given as an initial condition, i.e. displacement, and boundary conditions, i.e. force. If the initial condition is given as u_{given} and the force on one end of the spring is given as F , then Equation 3.1 can be written as Equation 3.2.

$$k \begin{bmatrix} 1 & -1 \\ -1 & 1 \end{bmatrix} \begin{Bmatrix} u_{given} \\ u_2 \end{Bmatrix} = \begin{Bmatrix} F \\ f_2 \end{Bmatrix} \quad (3.2)$$

This leaves the displacement of the other end of the spring and the reactionary force to be solved for. The two given values would be input into SolidWorks, say as the force on a

plate and its initial displacement, and it would calculate how far the next node would move based on its force and displacement from the initial node. This is calculated for all nodes in the mesh. This equation becomes much more complex as more nodes are added and as the shape of the elements becomes more complex, leading to more inputs on each node from other nodes. The general equation for the mechanical displacement problem is given in Equation 3.3.

$$\begin{bmatrix} \mathbf{K}_{uu} & \mathbf{K}_{ug} \\ \mathbf{K}_{gu} & \mathbf{K}_{gg} \end{bmatrix} \begin{Bmatrix} \Delta_u \\ \Delta_g \end{Bmatrix} = \begin{Bmatrix} \mathbf{F}_g \\ \mathbf{F}_u \end{Bmatrix} \quad (3.3)$$

Here, Δ_u are the unknown nodal displacements, Δ_g are the given boundary values of other displacements, such as a restraint on the edge boundary of a part. For a known part, all values of the \mathbf{K} matrices are known. The applied loads to the nodes is represented by \mathbf{F}_g , with \mathbf{F}_u as the unknown reaction forces from other nodes and their boundary conditions. As there are only two unknowns remaining, this general matrix can be solved.

Structural and thermal analysis have a number of analogous terms, making it simple to use Equation 3.3 in thermal simulations by changing a few variables. A table showing the conversion from structural analysis to thermal analysis is shown in Table 3.3 (Ed Akin, 2009).

Equation Component	Thermal Variable	Mechanical Variable
Unknown	Temperature, T [K]	Displacement, u [m]
Gradient	Temperature gradient, ΔT [K/m]	Strain, ϵ [m/m]
Flux	Heat flux, q [W/m ²]	Stress, σ [N/m ²]
Source	Heat source, Q [W]	Force, g [N]
Indirect restraint	Convection	Elastic Support
Restraint	Set temperature, T [K]	Set displacement, u [m]
Reaction	Heat flow, H or Q [W]	Force, F [N]
Material Property	Thermal conductivity, k [W/mK]	Stiffness, k [N/m ²]
Law	Fourier's Law	Hooke's Law

Table 3.3: Equivalents between thermal and mechanical simulations.

Thermal simulations with FEA all have a single equation governing each node, as in mechanical simulations. All above components of the equation are considered within this equation. This includes heat flux due to heat power, radiation, and conduction, the convection restraint, restraints on specified temperatures (for example, the base plate must be -40°C as a worst-case scenario), the reactions are the resultant heat flow that is necessary to maintain the specified temperatures, and the final unknown is the temperature. All other conditions add source terms, such as the dissipated heat power of electrical components (Ed Akin, 2009).

For thermal equilibrium, the resulting matrix equations have a general form as shown in Equation 3.4.

$$\begin{bmatrix} \mathbf{K}_{uu} & \mathbf{K}_{ug} \\ \mathbf{K}_{gu} & \mathbf{K}_{gg} \end{bmatrix} \begin{bmatrix} \mathbf{T}_u \\ \mathbf{T}_g \end{bmatrix} = \begin{bmatrix} \mathbf{F}_g \\ \mathbf{F}_u \end{bmatrix} \quad (3.4)$$

where \mathbf{T}_f represents the restrained vertex temperatures and \mathbf{F}_g represents the thermal heat power (heat flow) of the vertex. The \mathbf{K} values represent the thermal conductivity matrix for each node, where if the material is assumed isotropic is unit matrix. \mathbf{F}_u is unknown and represents the total heat flow in or out of a node that is necessary to maintain the given temperatures \mathbf{T}_g . \mathbf{F}_g is calculated with heat flux, which is where conduction and radiation equations are used in the solution. For thermal conductive heat flux, Fourier's Law is used, from Equation 2.1. Heat flux incident on the body and radiation from the body is from Equation 2.9. \mathbf{F}_u is thus calculated from adding the conductive flux from Equation 2.1 the radiation flux from Equation 2.9, and the flux resulting from \mathbf{F}_g . This allows to complete the goal of the equations which is to solve for \mathbf{T}_u (Ed Akin, 2009) (Bathe, 2016). An example solution equation for the temperature at a node would look like Equation 3.5.

$$\mathbf{T}_u = \mathbf{K}_{uu}^{-1}(\mathbf{F}_g - \mathbf{K}_{ug}\mathbf{T}_g) \quad (3.5)$$

In a simple example part in a vacuum environment, \mathbf{T}_g would be an array of constants as chosen for the simulation, k would be a constant material conductivity if the material was isotropic, and \mathbf{F}_g would be the conductive heat flow plus the radiative heat flow.

The size of the set of equations that is in general given by Equation 3.3 is the number of nodes. Thus, for an example of 100,000 nodes, there are 100,000 equations, and 100,000

temperatures calculated. Putting all these nodes together in the CAD model gives a solved thermal model necessary for thermal analysis. The model can be evaluated for both lab and flight conditions by including or neglecting convection respectively, and by specifying relevant boundary conditions.

3.5 LIFE Thermal-Mechanical Design Process

The preliminary design for LIFE was completed using SolidWorks, through a series of iterations of different components of the instrument. In all, the instrument can be split into four major parts: The blackbody system, the box containing the optical system, the main electronics box which contains electrical parts for the FTS and detector as well as the computers, and finally a smaller electronics box that contains the electronics used to control the blackbodies. To give an overview for how these parts are connected before going into detail of the design process for each, a block diagram of LIFE is provided in Figure 3.4.

Although there are fluctuations through the design process, it is helpful to give an overview of the purpose of each component. The blackbody assembly, which was procured from ABB, houses the three blackbodies that the instrument images during calibration and testing. The instrument also views the atmosphere through this unit, through a side viewport. This system is described in greater detail in Section 3.5.1. The optics box houses all the core components of the imaging system of the instrument: The lens array, the FTS, and the detector. These are all mounted to an optical breadboard plate, which is mounted to the side of the box interior for FOV purposes. The optical path goes out of the Optics Box and into the blackbody unit, where it is reflected into the atmosphere. The Electronics Box houses the parts necessary for operation of all components of the instrument, except for the blackbodies. This includes the data acquisition boards for the detector, the control board for the FTS, the computer system, multiple power supplies, and its own heaters and temperature controllers. As such, there are critical connections between the optics and electronics box that carry the sensitive data signals from the detector as well as control signals to and from the FTS. This box also interfaces with an external computer, which can be used if necessary to control and read data from the instrument during the development and testing phase,

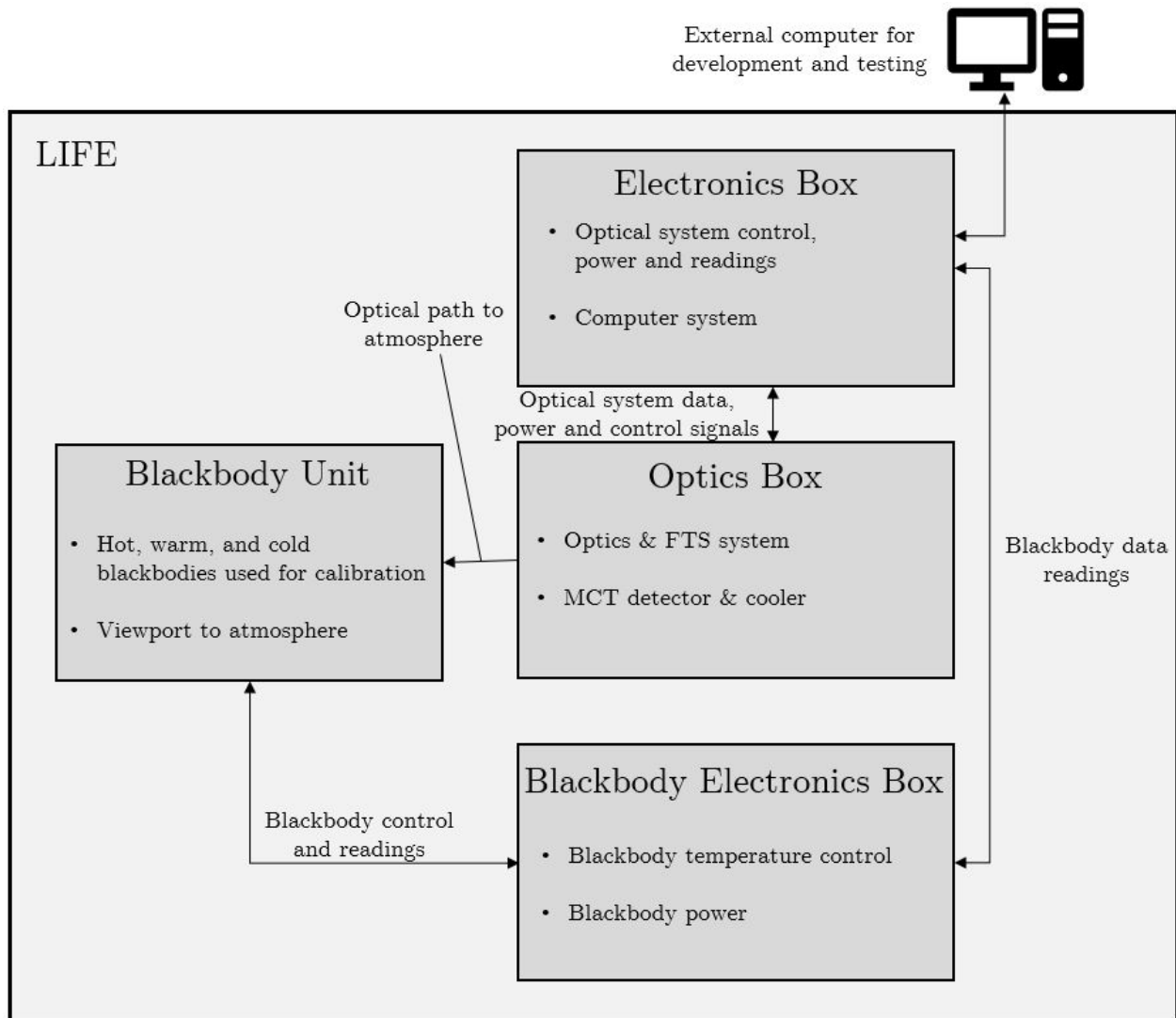


Figure 3.4: Block diagram of the LIFE instrument.

as well as troubleshooting. Finally, the Blackbody Electronics Box houses the electronics necessary for operation of the blackbodies, such as the temperature controllers and power supply. In early iterations, the electronics in this box were part of the main electronics box, until the size grew too large for the volume requirements of the CNES gondola. Cables allow communication between the electronics in these boxes.

The LIFE instrument went through a large number of design iterations before reaching the final design that was constructed and launched. Each subsection below, with the exception of the Blackbody Assembly (as it did not play a role in the design iterations), discusses a version of the design. This includes a detailed description of the optics and electronics boxes, which each went through a number of their own versions, and the thermal analysis done for each. The thermal analysis often formed the basis for a new version of the design. The final section goes into further detail about the final version and the detailed thermal analysis that was done to prepare it for TVAC tests and the flight.

3.5.1 LIFE Preliminary Design: Blackbody Assembly

The blackbody assembly, unlike the rest of the design, was not designed in-house. It was procured separately from ABB, to save the cost of designing and building or purchasing a new blackbody system. It still required work to characterize the blackbodies to ensure proper operation and to ensure that they would work properly with LIFE. They also play an important part in the overall LIFE design, so they will be described here.

The blackbody assembly has six blackbody surfaces that can be imaged. The original purpose of the instrument required two identical systems, so there are two entrance viewports, three pairs of blackbodies, and two exit viewports towards the atmosphere. LIFE only requires one system, so the other was used only for lab verification testing. Focusing now on one part of the system, there are three surfaces that can be imaged. The cold blackbody surface is connected to a thermoelectric cooler. This surface is capable of reaching set-point temperatures well below 0°C. However, in a lab environment, the surface temperature dropping below zero would lead to frost buildup on the surface, causing changes in the emissivity. With changes in the emissivity, the temperatures would no longer be measured properly, and in addition the frost buildup could cause dust and other materials to build

up on the surface, rendering it less accurate. Thus the lowest temperature this blackbody was set at was 5°C, and was set to 10°C for the majority of our testing. Another external blackbody, which was originally developed for pre-flight testing of the ACE instrument, was procured from ABB for the purposes of looking at a temperature well below freezing, in a TVAC environment. This is described in greater detail in Section 5.4.2.

The other two surfaces can theoretically be used interchangeably as the hot and warm blackbody surfaces, however it was discovered that the power of the heater inside one surface is much larger than the other, so to ensure enough power to reliably keep the temperatures steady, the former was chosen as the hot blackbody surface. During tests, the blackbody surfaces were interchanged, and in a cold environment there is not enough power to keep the temperature steady for the hot blackbody with the lower power heater. These surfaces can be set to temperatures as high as 225°C. In the LIFE configuration, most often the hot blackbody was set at 60°C and the warm blackbody was set at 30°C. These temperatures were chosen based on the needs of the detector calibration and are taken as requirements for the thermal-mechanical design. A CAD model of the system is shown in Figure 3.5.

The temperatures in the schematic show the temperatures from the original configuration, not the LIFE configuration. Also, for the final flight configuration of LIFE, it is noted that the bottom warm blackbody and the bottom hot blackbody are removed, as they are only used for lab verification and are unnecessary weight. Plates were built and installed to cover the openings into the system left by removing these two blackbodies, to ensure that the surfaces remained clean.

The blackbody system operates using a rotating mirror at the centre of each system. The optical path goes through the input window, and reflects off the mirror in whichever direction is necessary: Up for warm blackbody, right for hot blackbody, down for cold blackbody, or left towards the atmosphere. The optical properties of this mirror are unknown, which caused some uncertainty in the self-emission calculations. However as it has a gold coating and was used in a previous application where self-emission minimization was also important, it is assumed to be low. The operation of the mirror was done by rotating a stepper motor, which was one of the first parts of the system to be reconfigured for LIFE. Software needed to be developed to control the stepper motor; this was first done in the proprietary software

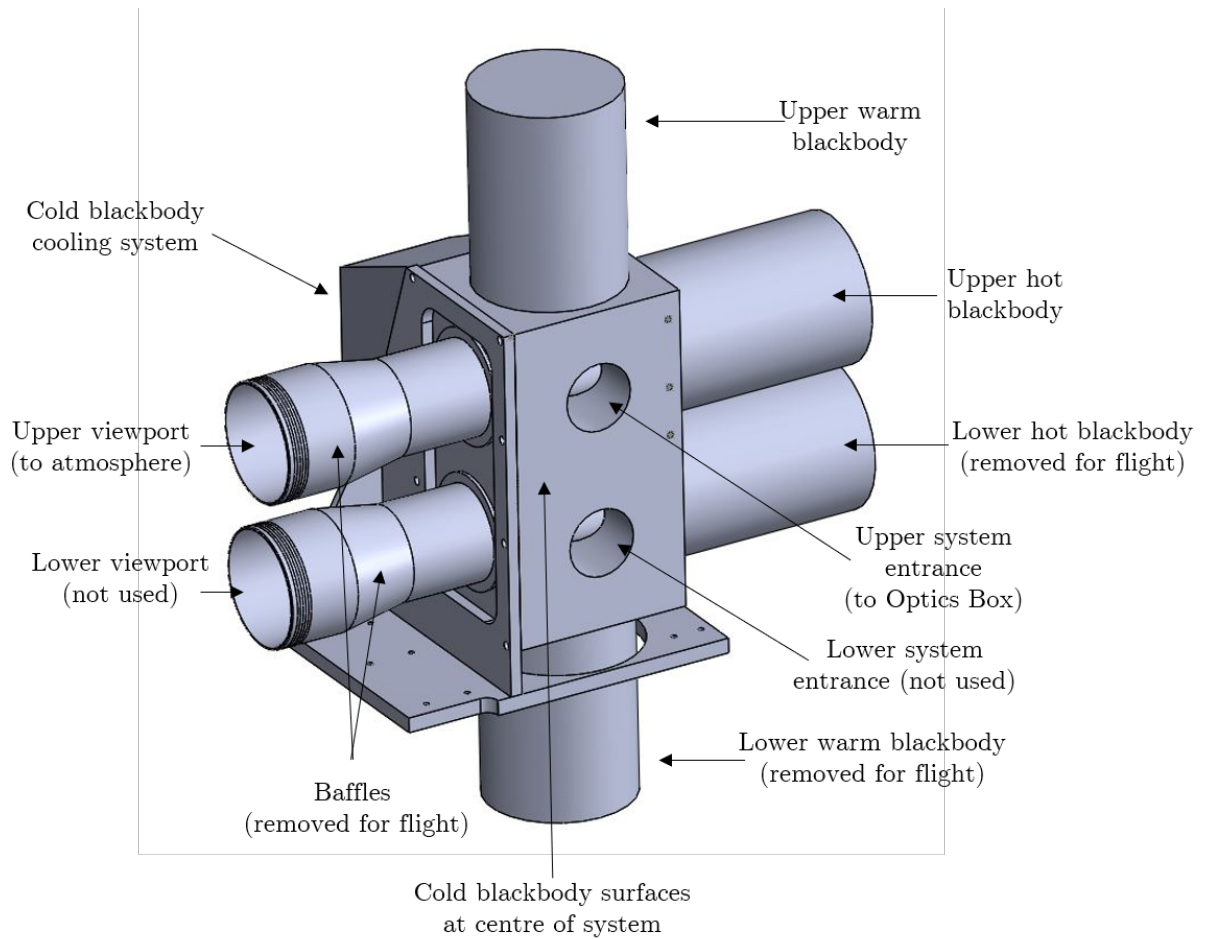


Figure 3.5: CAD model of LIFE blackbody system.

interface for the particular stepper motor, which was used for all testing and development. Later, in-house software was developed using C++ to allow more direct control and avoid the use of the interface.

The accuracy of the stepper motor also needed to be verified for proper data analysis after flight. To allow retrievals of the data, a very precise knowledge of the viewing angle of the instrument is needed, to within 0.1° . As there was no encoder for the stepper motor, it was impossible to tell through data feedback where the motor exactly was. Numerous measurements needed to be taken to see the variation in angle each time the mirror realigned itself to image a blackbody or the atmosphere. This also led to the discovery of a few systematic errors, such as the motor overshooting its required stopping position by a certain number of steps. Through testing and development of the motor, this systematic error was corrected, and the error in angle was deemed to be within the 0.1° required.

The largest issue with the blackbody system that required correction were the surface temperatures. Although the accuracy of the surface temperatures of the blackbodies were not important to the detector characterization, as long as they were well known and replicated in all images, the temperature drift over time of the surface was important. The LIFE FTS system requires 2.3 seconds to take a full image; if the temperature of the imaged surface changes significantly during this time, there are significant errors in the spectral data and the results are meaningless. The blackbody temperatures must be kept as steady as possible during the image capture time, ideally less than 0.1°C of drift. Temperatures of the blackbodies were controlled via Team Wavelength proportional–integral–derivative (PID) temperature controllers, which were able to withstand a vacuum environment with small modifications, and had been used by previous atmospheric research instruments developed by ISAS. It was discovered that when using these controllers with defined setpoints, the temperature would oscillate around the setpoint indefinitely. PID controllers reach their setpoints by oscillating around a setpoint making small corrections, with the oscillations becoming smaller until the steady setpoint was reached. In the LIFE design the setpoints were never reached, and a different size of oscillation occurred for each blackbody: The hot blackbody oscillated by roughly 4°C every ten minutes, while the cold blackbody could oscillate by as much as 25°C in the same time frame. A temperature reading acquired by the

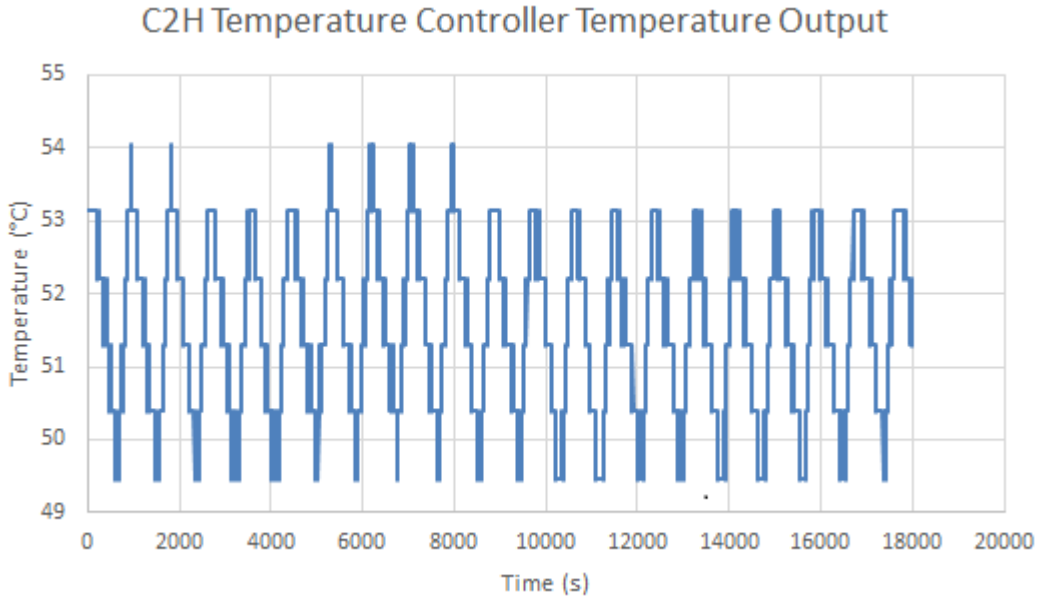


Figure 3.6: Oscillation of hot blackbody temperature over 5 hours.

hot blackbody temperature controller is shown in Figure 3.6 to demonstrate this oscillation.

Often, in a PID system, the oscillation and setpoint overshoot can be minimized by selecting optimized P, I, and D values. In the chosen temperature controller, the only value that allowed direct control was the proportional gain, P. Tests with various values of proportional gain found it to have very little effect on the oscillation error. Eventually it was found through examining documentation and contacting the manufacturer that the integration constant can be changed by changing a specific capacitor. The manufacturer could not provide any guidance on what a better capacitance would be, only that it should be lower. Starting with a capacitance of 0.05 μF , different capacitors were tested with decreasing capacitance. With each decrease in capacitance, the oscillation decreased, but it was not until a 1 nF capacitor was used that the error in temperature oscillation was within the required 0.1°C, for the warm and hot blackbodies. However, even at this capacitance, the cold blackbody temperature continued to oscillate by at least 2°C. This problem was eventually solved by using a different temperature controller. This option was not easily available for the other two controllers as they had to be used during flight, needed to be remotely controlled, and be able to survive a vacuum environment. The cold blackbody was only to be used for verification in the lab, so the controller did not have the same requirements. An external controller

was sourced, in which the PID values could be easily configured. Through further testing, the values were optimized such that the oscillation of the cold blackbody surface was 0.1°C . With the temperature drift requirements met for all three blackbodies, the blackbody system was fully ready to be used for LIFE.

3.5.2 LIFE Preliminary Design: Version 1

Prior to the beginning of this thesis, Ethan Runge had planned to develop the thermal-mechanical design himself as part of his MSc. Eventually, it was decided that due to the required amount of work for the design, it should be a separate thesis. However, prior to this decision and prior to this work, a first preliminary version was developed. A large part of Ethan's MSc. thesis was the development of the LIFE optical system, and a CAD model of this system had already been developed in SolidWorks partly through some of Ethan's work and partly from models sent by ABB. This was placed into two early versions for the optics and electronics boxes, both known as Version 1. Though these models would be eventually redesigned from the ground up (besides the core optical system) as part of this thesis, it is helpful to examine this initial design as it would inform the basic concept of future designs. A model of LIFE Version 1 is shown in Figure 3.7.

The layout of this design is the basis of the layout of all subsequent designs: a baseplate with the blackbody at the front, a box containing the core optical system, and an electronics box that contains the optics electronics. However, this is the only aspect of the design that does not change through the subsequent iterations and updates. This footprint is heavily based on the requirement that the MCT Detector be tilted 90° relative to the horizontal, which is described in the next section.

Optics Box Design: Version 1

The driving requirement behind the Optics Box design where the optical system is mounted perpendicular to the baseplate is the orientation of the MCT detector pixels. To vertically profile the atmosphere as required, the pixel array needed to be vertical. However, the detector that is supplied with the FTS system has a horizontal 1×16 pixel array. As a result, it needed to be mounted on its side, such that the horizontal array would be turned

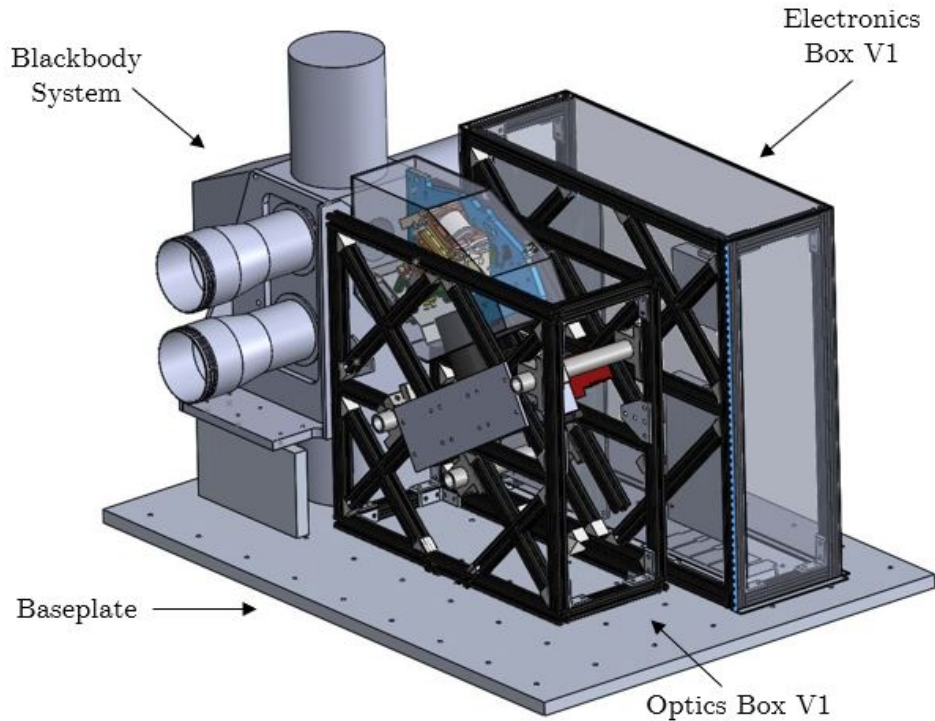
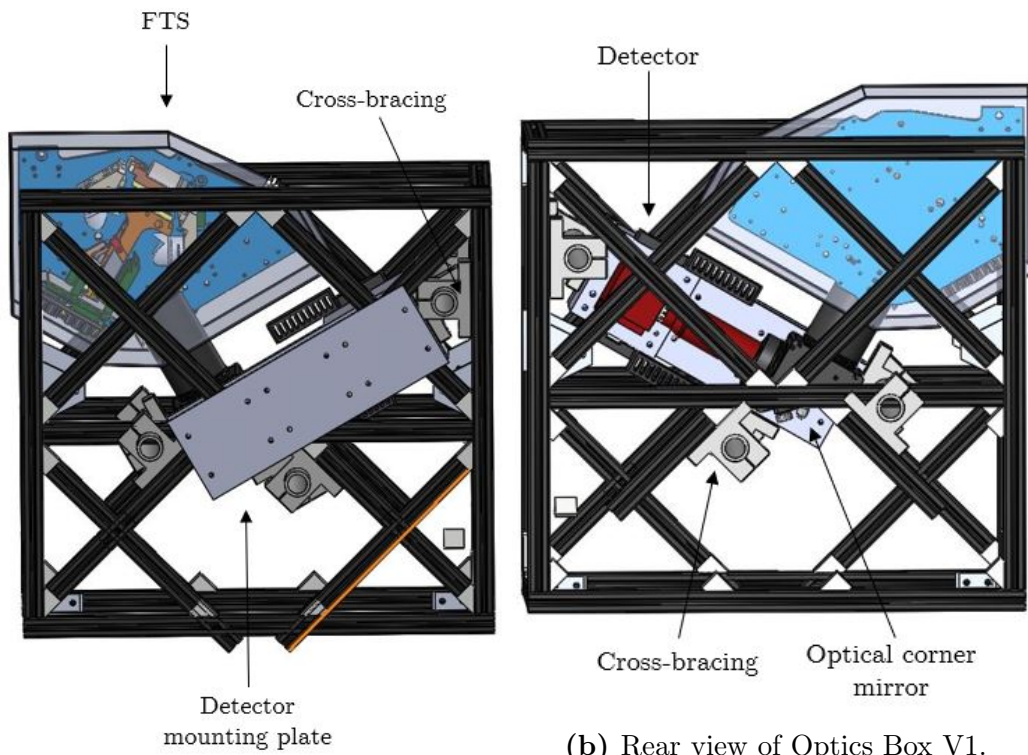


Figure 3.7: LIFE Version 1.

vertical, and the atmosphere could be vertically resolved. Mounting the optical system perpendicular to the baseplate was a departure from all previous instruments that the ISAS atmospheric research group had designed, and led to increased complexity in development. This complexity would lead to issues such as needing to be mounted to the wall, yet have all parts be free to move if necessary for alignment, and still be sturdy enough to avoid any shaking causing misalignments during the flight. Version 1 of the Optics Box, designed to meet the requirement of tilting the optical system, is shown in Figure 3.8.

The initial design used a construction material known as *T-frame*. It is an inexpensive, off-the-shelf component made from aluminum that is designed to easily fit together and also comes with fasteners and connectors, all readily available and easy to build. Being able to order this material and build in-house would save a large amount of the construction budget. It also still allowed freedom in the design, as all components could be cut to length as necessary. Using a CAD model of this material taken from a suppliers website, a model for the box could be quickly designed. However, downsides to this material are that although easy to build, it is not entirely secure, as a result of manufacturing tolerances. Connecting



(a) Front view of Optics Box V1.

(b) Rear view of Optics Box V1.

Figure 3.8: Original design of the Optics Box.

things to this frame would also be a challenge, as there was no easy way to mount any parts, such as the FTS, to the wall, without having either an interface plate or to install it prior to putting the box together, which meant a significant amount of time could be necessary for repairs.

Initially, as described in Section 3.2.2, vibration needed to be dampened as much as possible. Vibrations from the Stirling cooler could potentially cause vibrations in the FTS, which would cause errors in the data. The solution to this was to use a spring system between the detector and the wall of the box, which would dampen the vibrations enough that they would not travel to the FTS system. These springs cannot be seen in Figure 3.8 but are between the detector mounting plate and the detector. The box was further stiffened through the use of rods connecting the two walls of the box, to try to avoid vibrations propagating freely through the T-frame structure, either from the detector or from the gondola.

When this thesis work started, one of the first design decisions made was that the vibrations were not a driving requirement as originally thought. As a result, the spring system and cross-braces were removed. A Version 1.1 was developed, which was a simplified version of the original design with the optics attached to the walls through an interface plate, and other unnecessary stiffening and dampening components removed. An updated model of this design is shown in Figure 3.9.

One of the main issues of this design is that it is open; the optics must be kept as clean as possible, and need to be well protected when not in a clean room. In addition, thermal control of the optics would be easier if the entire temperature environment inside the box could be kept steady. Therefore, the main requirement of the next version of the optics box would be to design an enclosure for the optics, in a way that would enclose the optics and FTS while not directly attaching to these components to avoid vibration propagation and to be easier to install around the optics.

Electronics Box Design: Version 1

The design of the Electronics Box changes throughout the design process largely due to two reasons: The thermal requirements, and adding more components. As the mechanical design progressed, so did the electrical design, completed by lab engineer Paul Loewen. This

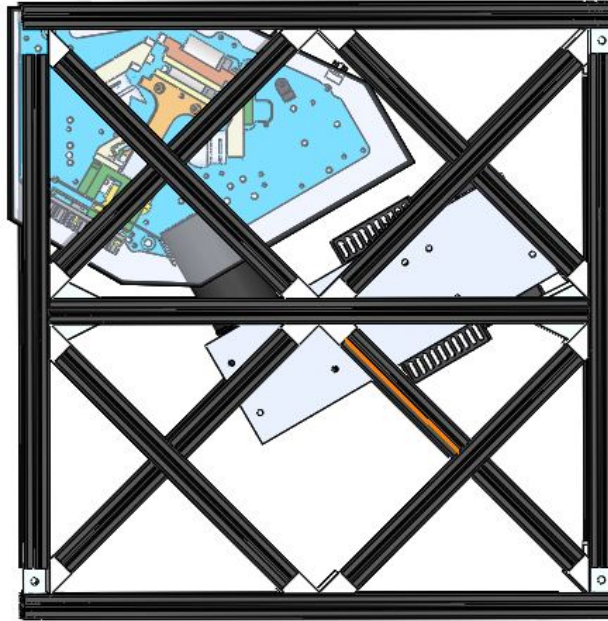


Figure 3.9: Version 1.1 of the Optics Box, with dampening and cross-bracing components removed.

required room for more components, which led to the need for a larger box and a better layout. However, for the first design, the only electronics that were of concern were the components necessary for the operation of the optical system: The FTS control board, known as the BMXS board, the two data acquisition boards, with the Pleora Ethernet interface boards attached, an Ethernet hub to allow the data acquisition boards, BMXS board and the external computer to all communicate, and a power supply for the system. An image of Version 1 of the Electronics Box is shown in Figure 3.10. Similar to Version 1 of the Optics Box, the original version of the Electronics Box used T-frame as its basic structure. Aluminum panels on all sides, including on the back to which the electronics are bolted, are transparent in the figure so the T-frame and inner electronics can be seen. This is a simple design, and like the Optics Box T-frame, would be easy and inexpensive to build.

Although later in the process the design of the electronics box would be driven by the thermal analysis, the initial design was driven by the cable length connecting the detector and the data acquisition boards. Sixteen cables (one for each detector pixel) sent signals from the detector to these boards, to be amplified, digitized and sent to the computer. These cables were extremely delicate and could not be lengthened; due to the signals being

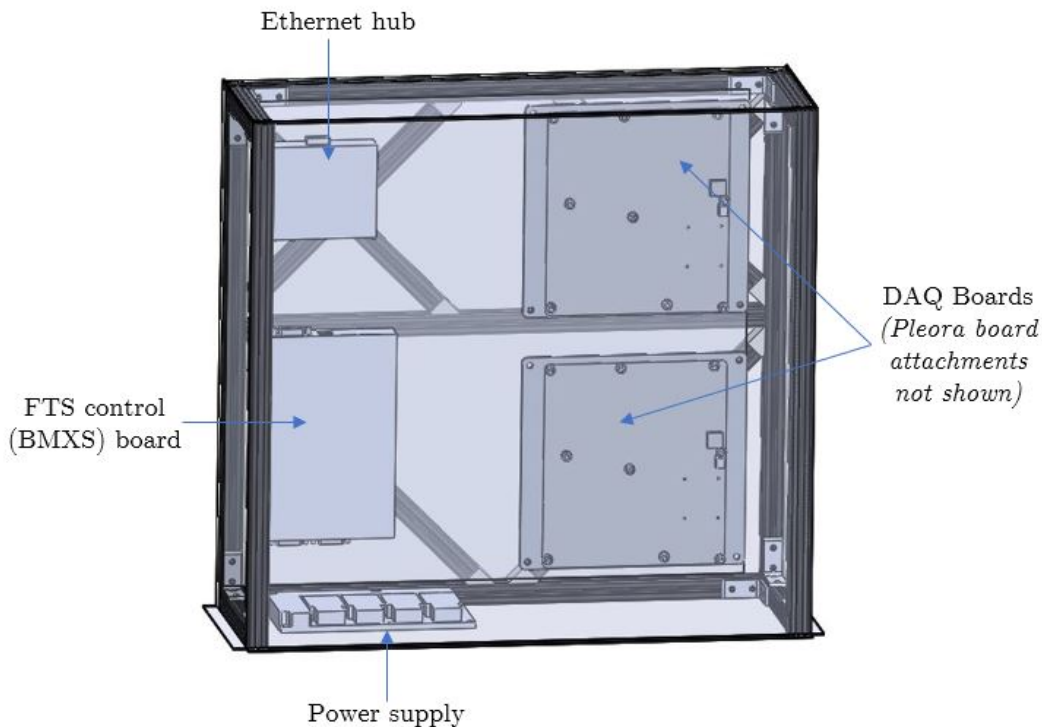


Figure 3.10: CAD model of Version 1 of the Electronics Box.

unamplified coming from the detector, they would have to be fed directly from the Optics Box to the Electronics Box. Thus these boards were placed and oriented in the Electronics Box to minimize distance to the detector. The rest of the components were placed around arbitrarily in the rest of the box. The thermal analysis of this box is completed when the first computer stack was developed and added to the design, during the development of LIFE Version 2.

3.5.3 LIFE Preliminary Design: Version 2

The second iteration of LIFE was largely based around a thorough update of the optics box. This was the first major design iteration that was developed as part of this thesis, and was more heavily based on thermal constraints. Design changes are largely based on the results of thermal analyses. The Electronics Box remained largely the same for this iteration, with the exception of adding the computer stack component. However, the initial thermal simulations of the Electronics Box were done in this version as well, and would inform updates of the

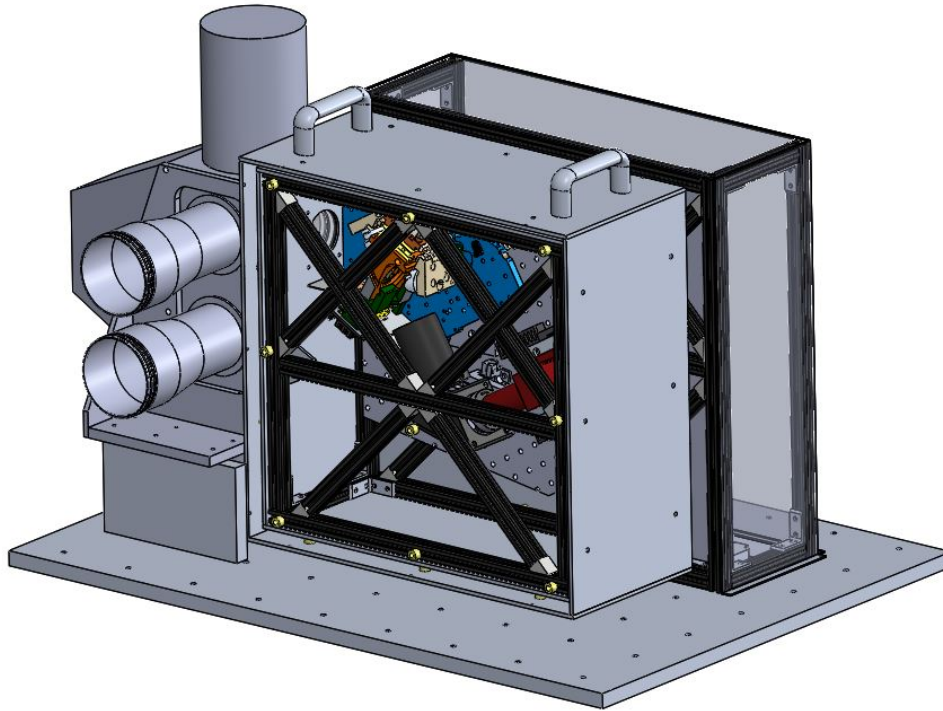


Figure 3.11: LIFE Version 2

Electronics Box in future LIFE versions. A full model of LIFE Version 2 is shown in Figure 3.11.

Optics Box Design: Version 2

To allow the optics temperatures to be more easily controlled, and to protect the optics when outside of a clean room, a box was designed around the T-frame. It consists of six panels that are bolted directly onto the T-frame structure. In addition to this, the optics system was redesigned to be attached to a single optical breadboard. This breadboard could be attached directly to the T-Frame, so the placement, alignment and testing of all optical components could be done externally outside the box, before a simple installation. In addition, all components would be on one plane inside the box, making final alignment much easier. Having all components bolted to this breadboard also allows a more uniform temperature across all components. With the previous design, different components were mounted on different parts of the frame, meaning multiple heaters, temperature sensors,

and controllers would be necessary to ensure that each optical component would remain at the same temperature. Constraining the optical system to one baseplate means easier temperature control, as they are all on one surface, the temperature of which could be more easily controlled. A further change to this design was to make it smaller and cut out unnecessary empty space inside. The height of the FTS is the constraint, as it must align with the entrance of the blackbody system, so there will be an empty area towards the bottom of the box; however the extra space on all sides of the optical system were made smaller.

Beyond this improvement in the optics and surrounding box, there was still a potential to improve it further. With the components enclosed in a box, external radiation, either from the environment (e.g. sun) or from nearby components (e.g. Electronics Box), could warm the box and cause the system to overheat. An idea was taken from the CATS instrument design, which had similar requirements for temperature: External walls, known as radiation plates, can be placed as an outer layer over the inner box. To prevent any thermal path between the internal and external walls, titanium spacers are used as a connection between these plates, which have a low thermal conductivity. Thus, in a vacuum environment, heat can only be transferred through radiation from the exterior plates to the interior plates, and through conduction through the spacers. Heat transfer through both of these paths are very slow. This allows the inner box to stay at a steadier temperature, minimizing any external temperature variations that may occur. This design also added titanium spacers as an attachment between the Optics Box and the baseplate. The gondola temperature can swing as low as -50°C , and this limits large temperature oscillations and temperature drops as a result inside the optics box. Smaller heaters can then be used to keep the optics above the minimum temperature requirements. The finalized model for the Optics Box Version 2 is shown in Figure 3.12.

This was the first component of the instrument to be studied with thermal analysis. As this design was created with thermal properties in mind, it was important to see the results of using these various design methods to help with the thermal analysis. There are four main heat loads for the thermal analysis of this box: The dissipated heat of each electrical component, the temperature of the base of the box (i.e. gondola temperature), the temperature of the side wall caused by the electronics box, and the power of the resistive

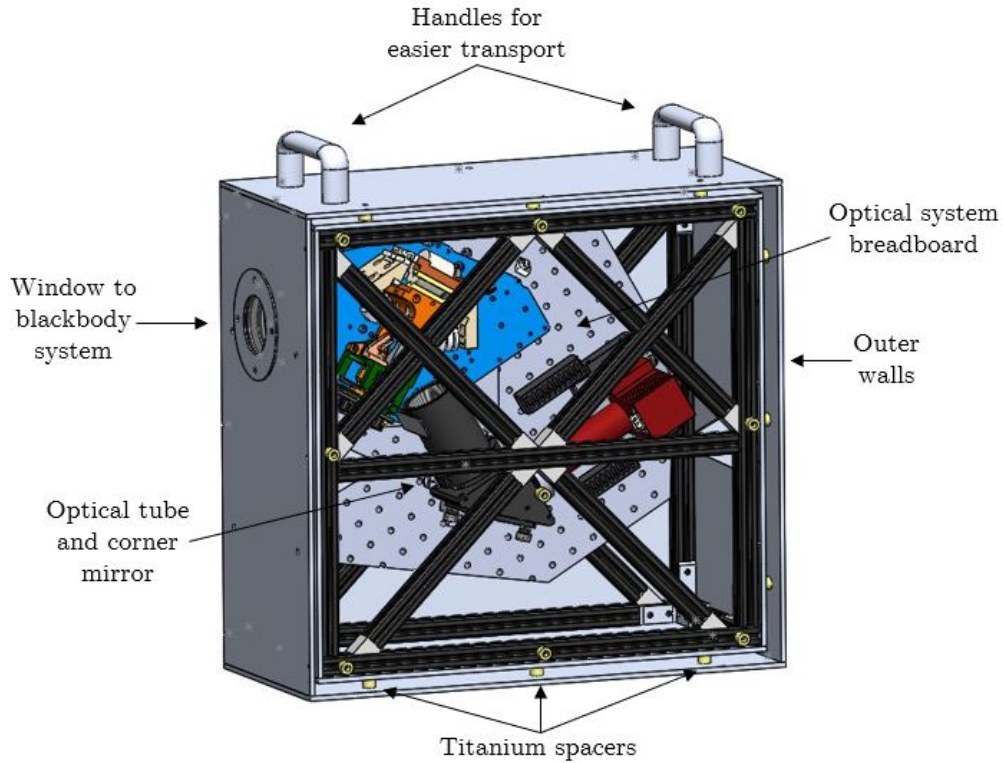


Figure 3.12: Version 2 of the Optics Box, which incorporates external radiation plates.

heaters applied to the plate. The dissipated heat of each electrical component is known, and given by ABB: The FTS generates a negligible amount of heat (1 W chosen for study) and the MCT generates 8 W. The baseplate temperature was changed between -30°C and -20°C . The side wall heat load was assuming a thermal connection between the electronics box and optics box, as a way to dump heat from the electronics box and warm the optics box. The final heat load, the heaters, is unknown and iterated through the design to meet the temperature requirements. A total of 17 designs were simulated, each with a different amount of heaters, placement of heaters, and power dissipated from the heaters. For each simulation, temperatures of various components were measured, such as the FTS, different parts of the breadboard, the lens system, and an average temperature of the breadboard, outer and inner walls. These were recorded in a spreadsheet describing the results of each simulation to track the changes through simulation iterations. Only a few of these iterations will be described here.

It is noted that the majority of the initial simulations, until later in the design process,

were steady-state. SolidWorks has the ability to perform transient analysis, and is utilized for the final designs, but to perform these simulations it must complete a simulation for each time step. As a result, the time to solve a transient analysis can be very long, and it was not realistic to perform this for rapid prototyping. Through some transient analysis tests, it was found that many hours were required to actually reach steady state temperatures (>12 hours), longer than the time of flight. As such, the steady state temperatures are the maximum or minimum temperatures that will be reached, and can be treated as worst-case scenario results. If the temperatures from a steady-state simulation fit within the temperature requirements, it will certainly reach those requirements for the transient analysis and during the flight time frame.

The initial simulation involved no heaters, as a test to see how cold the optics would get with a -30°C baseplate. The majority of the heat comes from the Electronics Box, based on an idea that the Electronics Box and Optics Box could be thermally connected, as a way to use the waste heat from the Electronics Box and make the instrument more efficient. The result of this simulation is shown in Figure 3.13.

A key takeaway from this simulation is that the titanium spacers are accomplishing their task of minimizing the cold travelling through the bottom of the box into the optical system. With a spacer of roughly 1 cm in height, there is a temperature change of almost 20°C . The temperatures of the optical system are in a range of $12\text{-}15^{\circ}\text{C}$, on the low end of the required temperature range, and is dependent on heat coming from the Electronics Box. As a way to increase the temperature for the next test, the outer radiation plate between the optics and electronics boxes is removed. This allows a more direct heat path between the boxes with the removal of the titanium spacers, and will further warm the optics box. The results of this simulation is shown in Figure 3.14.

The result, as expected, is that the optical system is much warmer. With a direct path to a 25°C source, much of the optics come close to 25°C . The temperatures of the optics are at the high end of the required temperature range, and ideally should be more towards the centre. However, the biggest issue with this design is that the temperature of the optics are based heavily on the temperature of the Electronics Box, which cannot be controlled as it is simply heat being dissipated from the electronics. So as not to rely on this, heaters

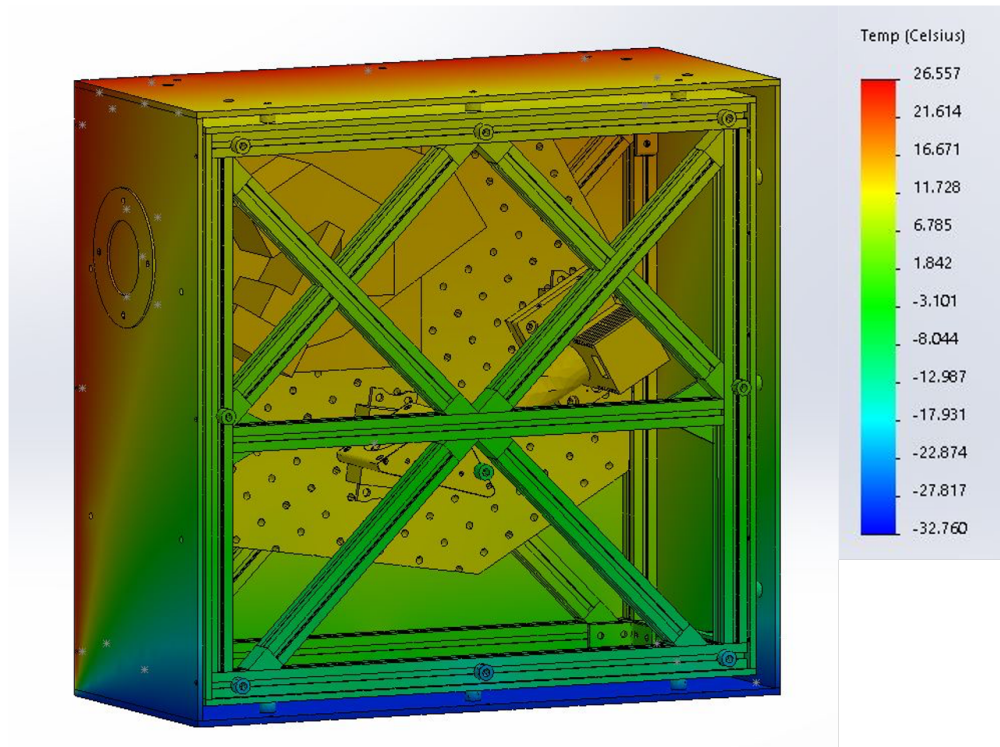


Figure 3.13: Initial temperature simulation of Optics Box V2, with no heaters and a direct connection to the Electronics Box.

were added to the design. For the next simulation, the outer wall is added back, so the temperature from the Electronics Box will be closer to what is seen in Figure 3.13. For this test, the heaters are all set to 30 W, and the resulting simulation is shown in Figure 3.15.

The results for this configuration show that the temperatures of the FTS and lenses are now roughly 23°C. It is on the high end of the temperature range but the power to the heaters can be controlled by turning them off if the temperature of the optics gets too high; thus the maximum temperature they will reach is 23°C. This design satisfies the temperature requirements. However, these temperatures are still assuming a constant temperature of 25°C from the Electronics Box. If the electronics were not dissipating as much power as expected, this temperature would fall, potentially causing the optics to fall below 5°C. To see what would happen if this temperature connection was removed, thus allowing full control of the optics just through heaters, a simulation was done with no temperature condition on the side wall. To compensate, an extra heater was added on the optics plate. Through a few iterations, the heat powers also had to be increased to allow the optics to stay within their

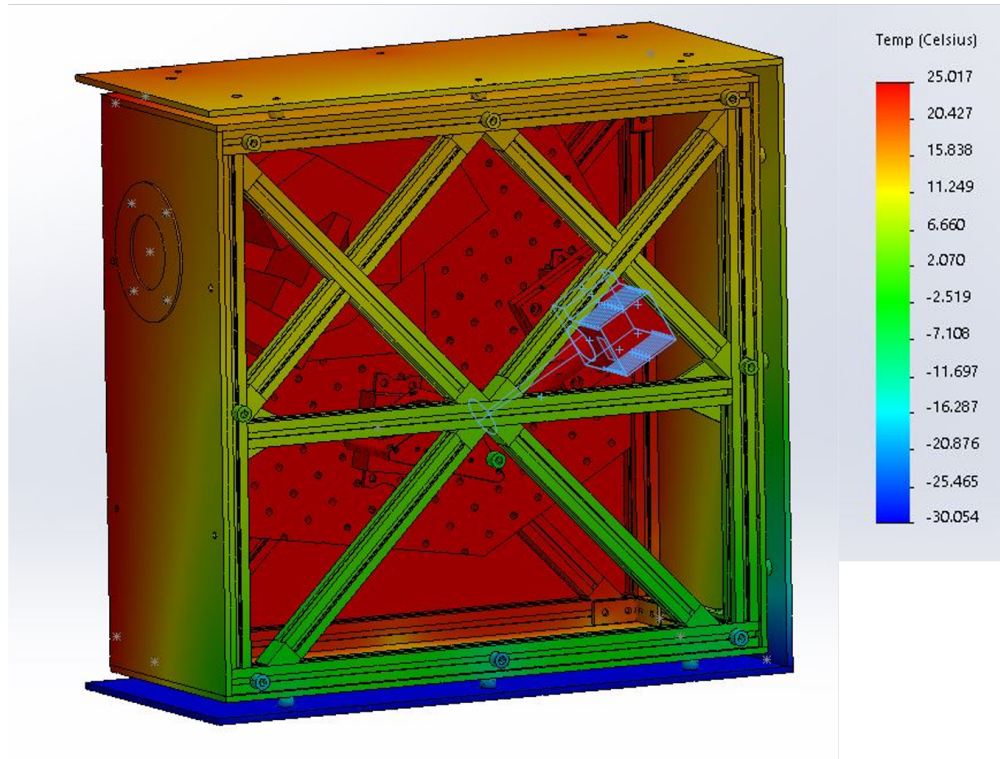


Figure 3.14: Simulation of Optics Box V2 without an outer wall between the Optics Box and Electronics Box.

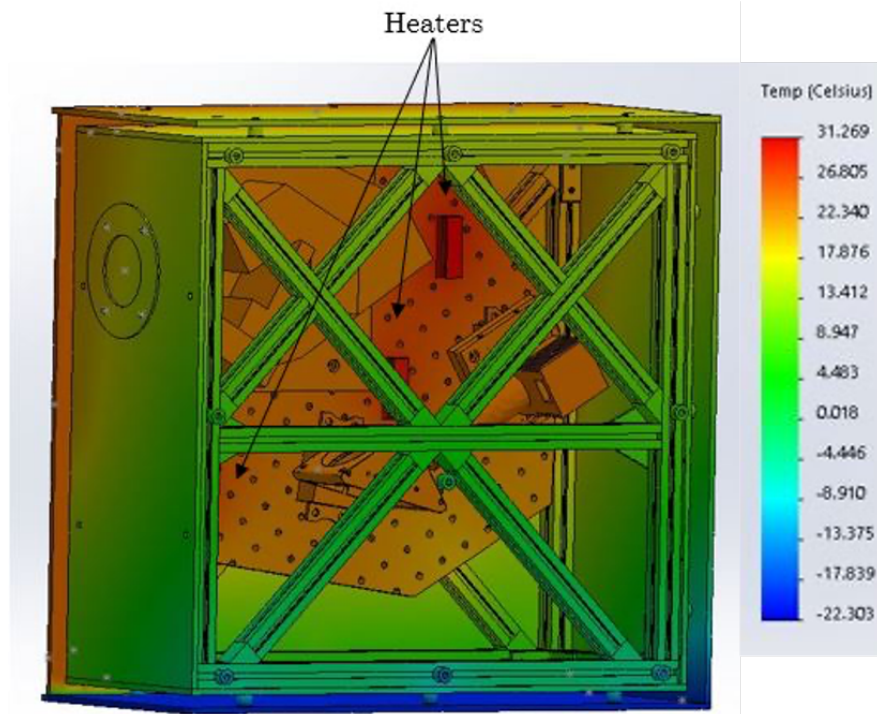


Figure 3.15: Simulation of Optics Box V2 with three heaters at 30 W.

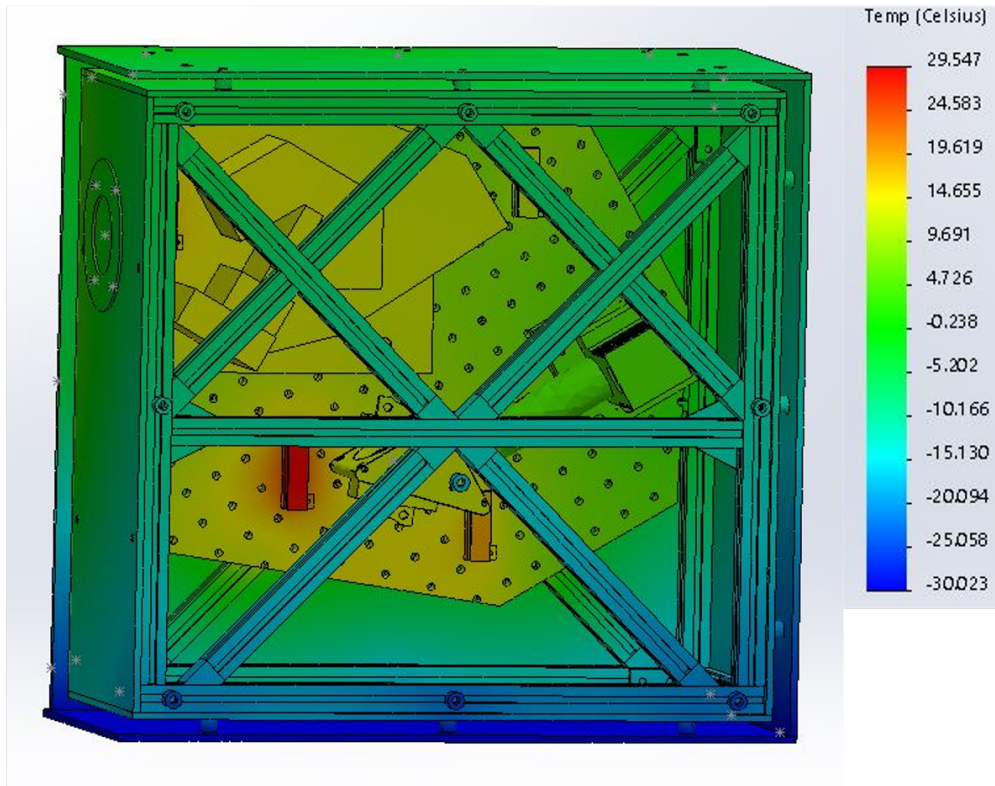


Figure 3.16: Simulation of Optics Box V2 without any heat flow from the electronics box, and four heaters.

required ranges: 25 W for the heater attached to the FTS, and the three heaters attached to the breadboard are 100 W, 50 W, and 25 W. The results of this simulation is in Figure 3.16.

These temperatures are in the required temperature range. However, just to maintain minimum allowable temperatures, the total power for the heaters was 200 W, which is far beyond the reasonable power limit to just heat the Optics Box. To ensure a more reasonable power draw, the best option would be to transfer heat from the Electronics Box. However, another method to better control the optics temperatures is explored in the next version of the Optics Box.

In addition to the issues with trying to maintain proper Optics Box temperatures, there is an issue with the mechanical design. It will be difficult to align all connections properly after building the T-frame, due to its loose tolerances, and in addition it is difficult to attach the plates to the frame, where a special screw attachment is needed, and attaching it through various panels could prove difficult. A new version of the Optics Box was developed that removed the T-frame structure, to allow for easier construction.

Electronics Box Design: Version 1 Thermal Analysis

This Electronics Box overall design remained largely unchanged in Version 2 of LIFE, but the initial thermal simulations were completed here, after the thermal simulations of the Optics Box Version 2 as described above. The main change before simulations was the addition of the LIFE *Computer Stack*, the computer control centre of the instrument. This does not have stringent temperature requirements and does not dissipate a large amount of heat so does not have a large affect on the design, but must be considered for the purpose of space. As discussed in Section 3.2.2, most electronics have narrow temperature ranges and simulations must be completed to ensure that they will stay within these ranges during flight and in the lab.

Initial simulations were completed with each part dissipating typical heat power, and the baseplate temperature was kept at -20°C and is changed to more extreme temperatures in later tests. The first thermal test of the Electronics Box with these constraints is shown in Figure 3.17. The main issue with this design is that there is not enough heat being dissipated from the DAQ boards, and the temperature reaches 51°C in the top right corner, which is above the maximum operating temperature of 45°C . The design must be altered so that more heat can be dissipated to the gondola deck. To do this, the baseplate which the electronics are mounted to was made larger, extending out to the edge of the T-frame. This allowed more thermal contact with the structure so that more heat could dissipate into the frame, which could dissipate into the gondola deck. The results of this change are shown in Figure 3.18.

In this model, the temperatures of the upper DAQ board is improved to be within a reasonable range, but now the lower DAQ board (on the bottom right) and the BMXS board are now dangerously close to their minimum temperature limits, as the cold from the gondola makes better contact with the electronics baseplate. This would be a recurring problem with the design of the electronics box; the DAQ board dissipate a high amount of power, and to avoid overheating, this power needs to be dissipated to the gondola baseplate. However, with a large thermal connection to the baseplate, the electronics become too cold, as the minimum temperature value of the DAQ board is 0°C and the minimum value for the BMXS

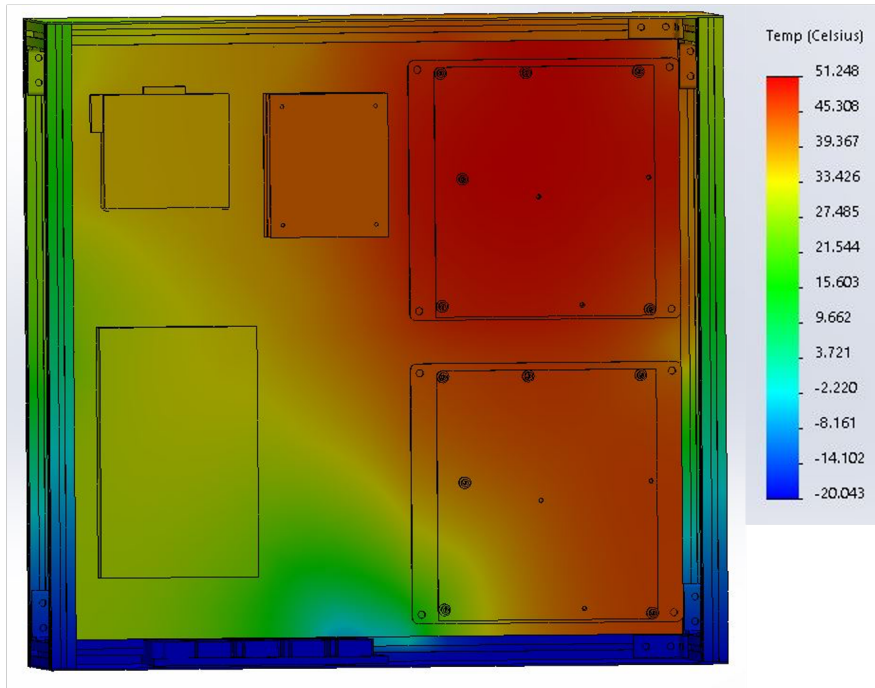


Figure 3.17: Initial thermal simulation of Electronics Box V1, with a base temperature of -20°C .

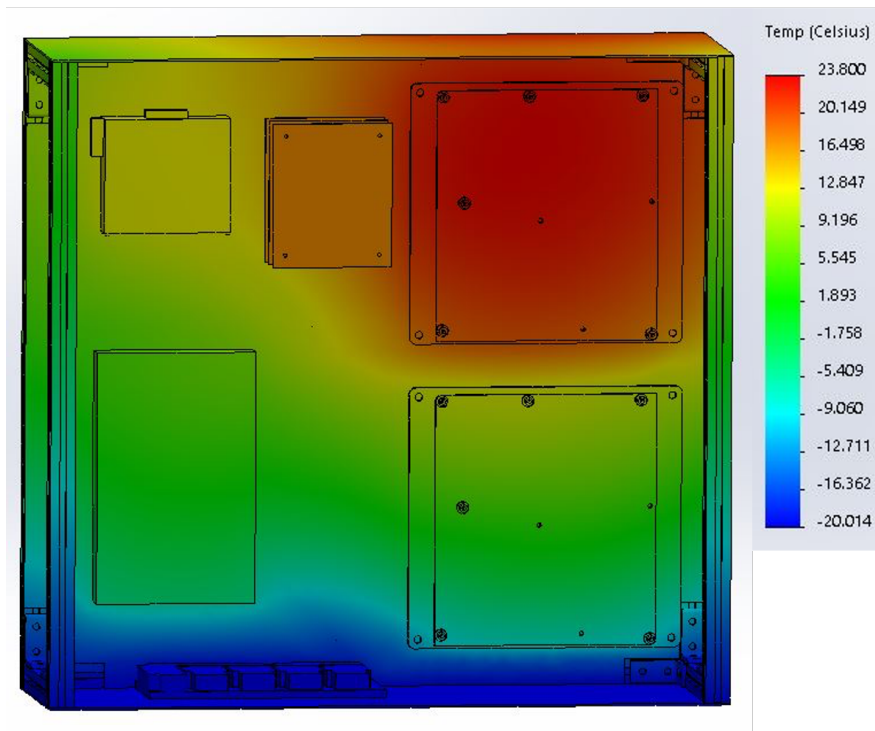


Figure 3.18: Second thermal simulation of Electronics Box V1, with an expanded electronics mounting plate.

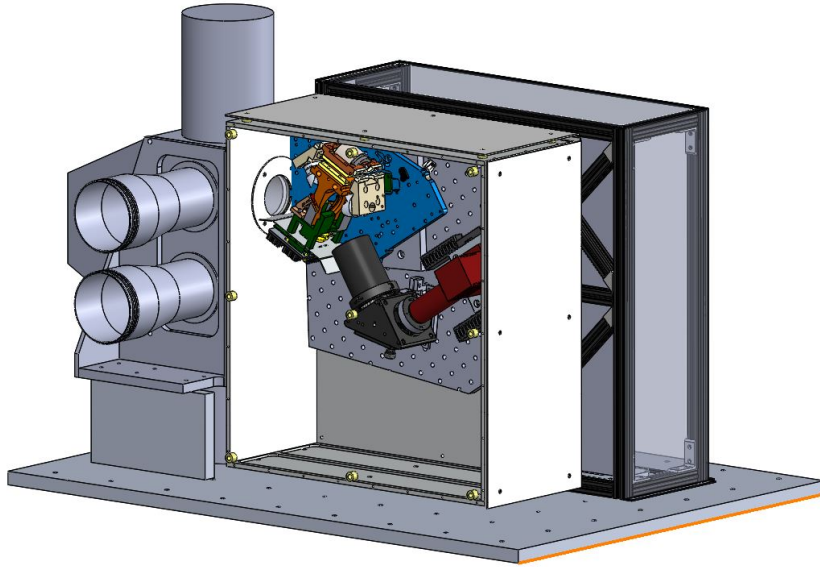


Figure 3.19: Third version of LIFE, with an updated optics box.

board is 5°C . It is unlikely that this design would have survived the extreme temperatures of the ascent. The further development of this thermal model to address these issues is done alongside the development of the Optics Box thermal model, and in subsequent chapters are discussed together.

3.5.4 LIFE Preliminary Design: Version 3

Similar to Version 2, the main change in Version 3 of LIFE was a large change to the design approach of the Optics Box. It was designed around the need for something easier to build, and is further based upon the CATS design. On the other side of the instrument, the Electronics Box received minor updates, adding electronics and further altering the design to improve the thermal properties of the instrument. A more thorough update of the electronics box occurs in Version 4 of the instrument. A model of Version 3 of LIFE is shown in Figure 3.19.

Optics Box Design: Version 3

Although the previous version of the Optics Box met most of the requirements, such as the proper temperature range in different scenarios and holding a steady temperature, there were

still some downsides to the design. Chiefly, there was the issue of it being very difficult to assemble. Although the costs were kept low by buying a number of off-the-shelf components and keeping the cost of having the components made by the machine shops low, it would be tough to maintain. With the T-frame design, all walls would have to be bolted to the T-frame, which would be a more difficult task once the instrument was more fully enclosed. It would be even more difficult when attaching the outer radiation plates through the inner walls, where the bolts would have to be connected blindly. In addition to attaching plates, it would be difficult to attach the optics breadboard baseplate to the wall, as it would need to be done from the optics side (hence the bolts could not be in the optical path, and would also lead to a risk of bumping the optics). Finally, the largest issue would be the need to perform fixes, alignments and maintenance to the optical system when it was fully built. The T-frame would need to be removed from one side of the box to allow access, which would be difficult, time intensive, and difficult to reinstall without altering the optical setup.

It was determined that a trade-off of higher cost would be reasonable for a design that was easier to build and access. Thus, a new design was developed from the ground up, only keeping the core optics system the same. The new design was further developed from CATS: The walls would be thicker and all walls could be directly bolted together, thus only needing six parts for inner walls, and removing the need for any inner structure. The outer radiation plate design would be kept the same, but would be easier to install as the outer plates could be attached directly to the inner plates. The optical system baseplate could be directly bolted to the wall from the opposite side of the optics. If the optics needed to be aligned or otherwise worked on, the entire baseplate could be disconnected from the other side and lifted out, or only one side of the box would need to be removed to have access, rather than one side plus the T-frame bracing. A model of the third version of the Optics Box is shown in Figure 3.20.

The two main drawbacks to this new design was expense and weight. The weight was minimized by milling cavities from the thicker panels, and the cover plate was chosen to be as thin as possible (the backplate was thick and not milled out to be able to hold the weight of the optics system). All parts for this new design would need to be built by the machine shops, which caused a threefold increase in price.

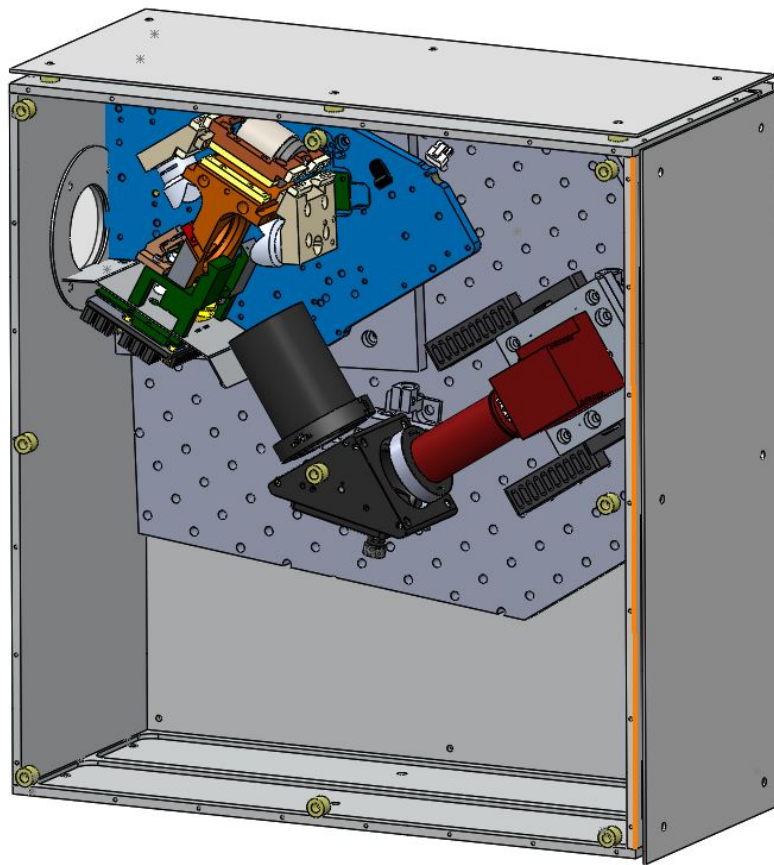


Figure 3.20: Third version of the Optics Box, based on the CATS design.

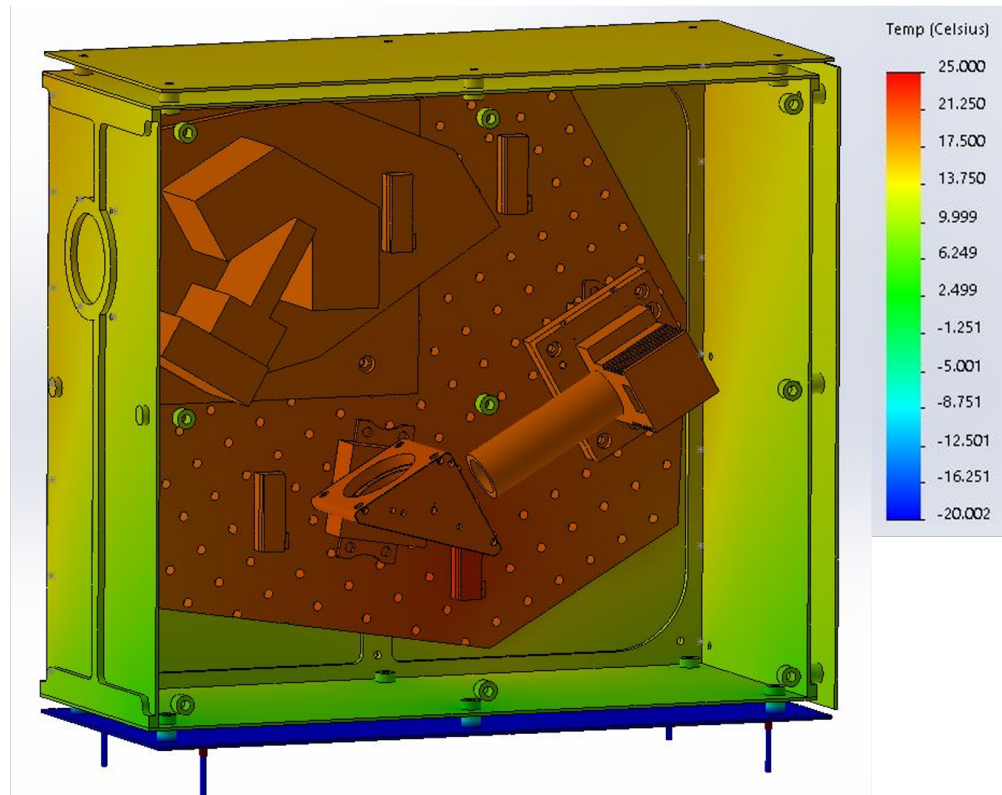


Figure 3.21: Simulation of Optics Box V3 with a heater and thermal connection to the Electronics Box.

For the thermal analysis of this version, the core aspects of the thermal design are still present: The titanium spacers and radiation plates. However as the walls are rigidly connected together and there is no frame, heat would flow differently. Another change from the previous design is leaving gaps between the radiation plates, which removes heat flow between these plates and better isolates the interior. Once again, there were a large number of thermal simulation iterations, and only a select few will be discussed here.

Initial simulations for this box still assume a thermal connection between the Optics Box and Electronics Box, so the outer radiation plate that faces the Electronics Box is set as 25°C. In this simulation, although all heaters are still in the model from Optics Box Version 1, only one is dissipating power (the bottom right), at 12.5 W. The bottom plate is set at a temperature of -20°C. The FTS and MCT Cooler are dissipating their normal heat loads. The results of this simulation can be found in Figure 3.21.

The most important outcome of this simulation is it shows the effect of heat flow compared to the previous version. With a 12.5 W heater and heat dissipated from the electronics box,

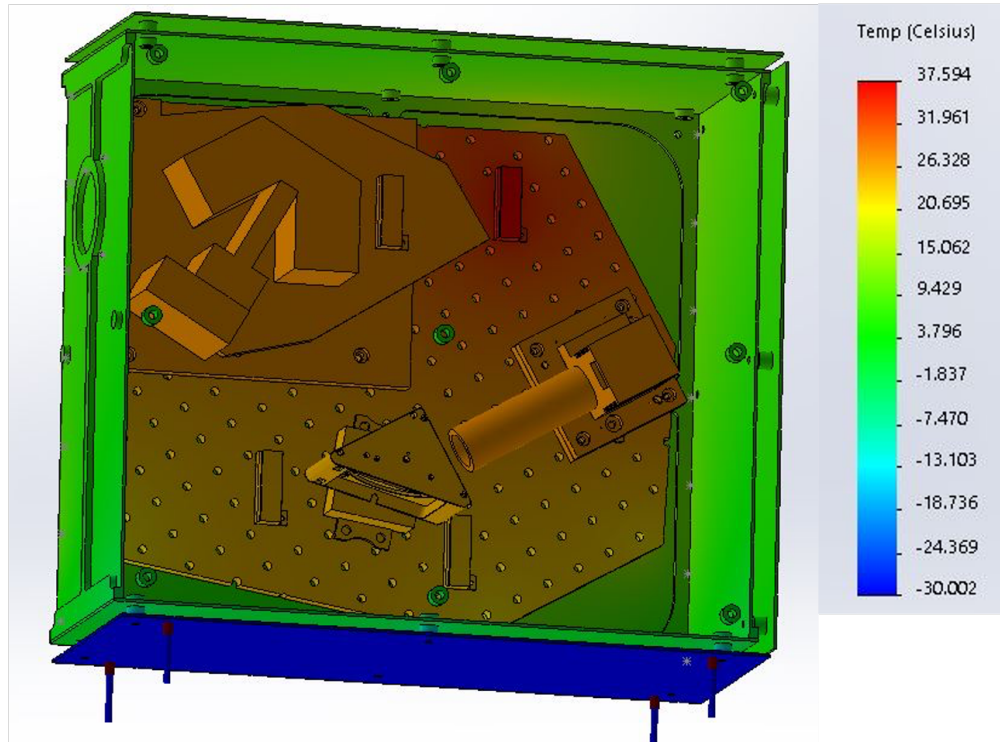


Figure 3.22: Simulation of Optics Box V3 with no thermal connection to the Electronics Box.

the temperatures are staying within their required limits, as compared to heat power of over 100 W needed for the last simulation with T-frame. The titanium spacers are still performing well in maintaining steady temperatures and isolating the inner box from the gondola baseplate. The next simulation shown is with no thermal connection between the Electronics Box and Optics Box, to allow better thermal control without relying on heat coming from the electronics, which cannot be actively controlled. With only the top right heater being used with a power dissipation of 35 W, Figure 3.22 shows the resulting simulation with a baseplate temperature of -30°C (extreme cold case).

The temperatures are above their temperature ranges, even with the -30°C baseplate, which is good. Although the temperatures are too high, with a properly controlled heater this will stay within its temperature limits. Further iterations can be completed to see exactly what heater power is required. However, although this system works, one more thermal control method is implemented. Currently, although the inner Optics Box stays at a relatively uniform temperature due to the titanium spacers and outer radiation plates, it

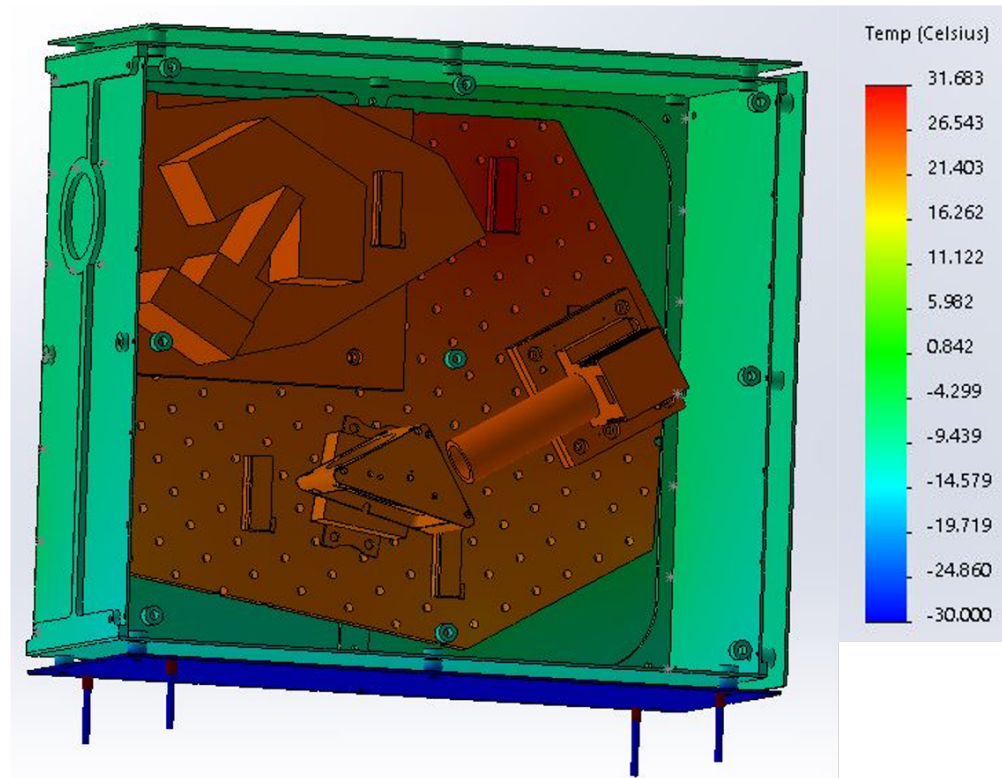


Figure 3.23: Simulation of Optics Box V3 with titanium spacers added between the optics breadboard and the side wall.

can still incur larger temperature oscillations than required for good optical operation. To prevent this and better isolate the optics, titanium spacers are added between the optics breadboard and the Optics Box wall. This is one of the most important parts of the thermal system to ensure a steady temperature in the optics, as it further decreases temperature oscillations as a result adding another thermal insulation layer. Also, it allows for a more uniform temperature across the whole system, allowing for further ease in removing the self-emission, and also lowers the necessary heater power as the heat can only escape through radiation. With the titanium spacers in place, a simulation is performed with a heater power of 20 W and a baseplate temperature of -30°C , shown in Figure 3.23.

This model shows that the titanium spacers do have a significant effect. The temperatures of the optics are similar to the previous simulation, but with 15 W less heater power necessary. The temperature of the optics has less dependence on the gondola baseplate temperature as well. Overall this design is much improved over the previous design, using much less heater power while keeping temperatures more steady, and also being easier to build.

This is the last major update for the Optics Box overall design, but further temperature simulations are done as part of the larger LIFE assembly, which includes the Electronics Box. This begins in Version 4 of the instrument.

3.5.5 LIFE Preliminary Design: Version 4

The next version of LIFE is largely based around a thoroughly redesigned Electronics Box. This is also the first version to simulated both the Optics Box and Electronics Boxes together as a full assembly. As there is no major updates to the Optics Box, there will only be a discussion of the redesigned Electronics Box before going into the full assembly thermal simulations.

Electronics Box Design: Version 2

The previous version of the Electronics Box had the same design issues as the first two versions of the Optics Box, which was the use of T-frame. As in the Optics Box, the use of T-frame to build the Electronics Box, although inexpensive, would have been difficult to build well, and the thermal design more difficult. As a result, the Electronics Box was redesigned from the ground up using a similar design to the Optics Box, using CATS as inspiration. The box would now be made from machined aluminum panels, which would connect to each other directly, so that an inner frame did not need to be used. To save weight, the side panels had milled cavities. The heaviest part of this new design was the mounting plate for the electronics, the thickness of which was based on both the strength needed to mount the electronics securely, as well as dissipate heat effectively. This version still only contains the core electronics at this point; the next version of the box contains the rest of the necessary components. The layout of the electronics remains the same as the previous version, with the exception of the power supply, as a result of the mounting holes on the bottom plate. This model is shown in Figure 3.24.

The thermal analysis of this box was done as a full assembly with the Optics Box. However it is noted that there is now a better thermal connection between the box and the gondola deck. As a result, the heat from the DAQ boards can dissipate easily into the gondola deck, but in the cold case the BMXS and DAQ boards can go below minimum required

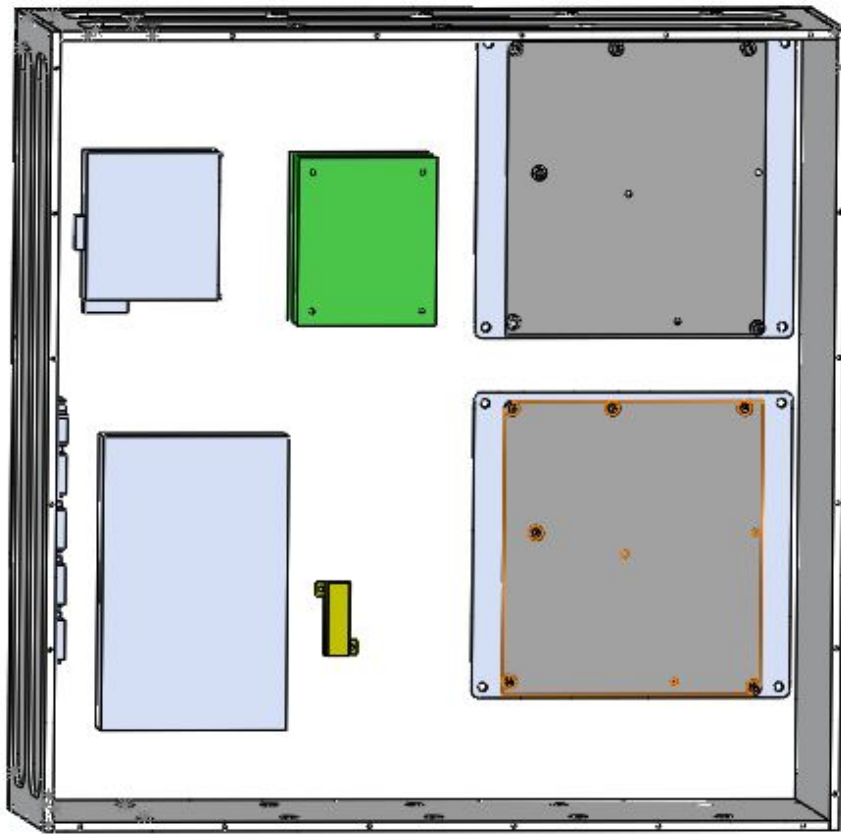


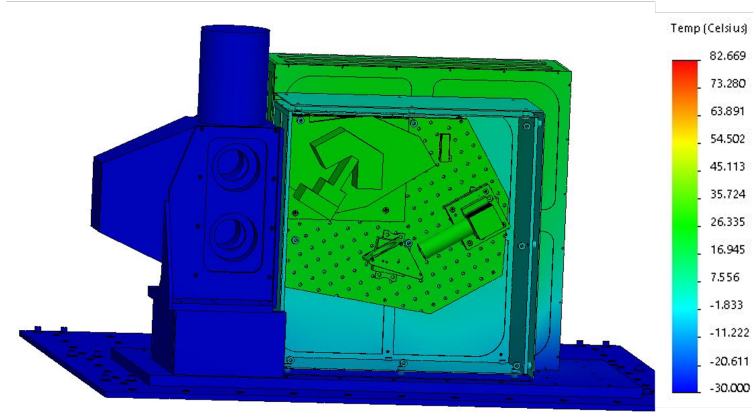
Figure 3.24: Second version of the electronics box, following the design of the Optics Box.

temperatures. To ensure this doesn't happen, a heater is placed next to the BMXS board to help warm it in the cold case, and the power supply (which dissipates 45 W) is placed nearby to maintain a temperature above 5°C.

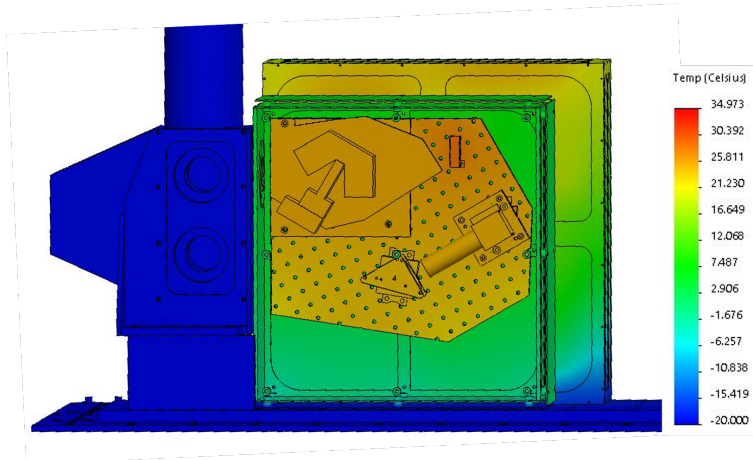
LIFE Version 4 Thermal Analysis

Version 4 was the first model to be simulated as a full assembly, i.e. with the Optics Box and Electronics Box simulated in the same thermal model. In terms of changes to the model, excluding the Electronics Box (changes of which are discussed previously), the unnecessary heaters are removed from the optics breadboard. This leaves one in the top right part of the breadboard, to maintain the FTS temperature. Initially, the boxes are flush with each other, allowing heat to transfer between them. Now that simulations are being performed for the entire model, tests for all three temperature cases will be performed: The cold case with a gondola deck temperature of -30°C, the average case with a gondola deck temperature of -20°C, and a warm (lab) case with a gondola deck temperature of 15°C. The Optics Box heater is set at 14 W, 12 W, and 0 W for the cold, average, and warm cases respectively, and the Electronics Box heater is set at 150 W, 60 W, and 0 W for the same respective scenarios. The results of these three simulations are shown in Figure 3.25 (Optics Box view) and Figure 3.26 (Electronics Box view).

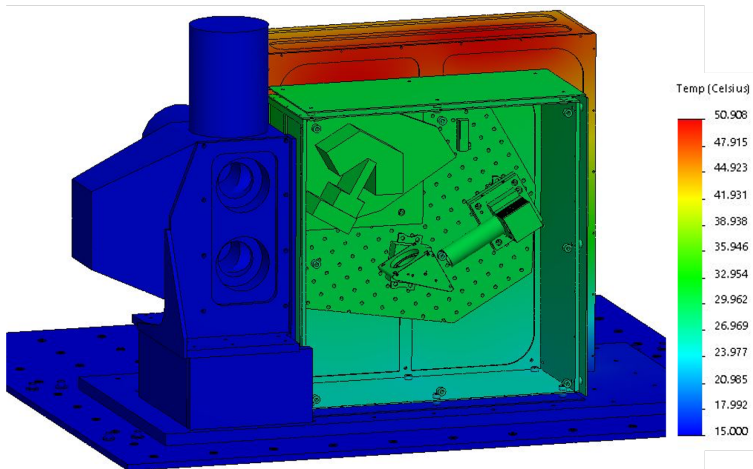
Overall, the results from these simulations are positive, but show areas needing improvement. Both boxes, with the exception of part of the BMXS board, survive the cold case well, and everything is operating well in the average case. In the warm case however, the optics components and some of the electrical components are overheating. This is not as much of an issue for the Electronics Box, which will have fans to keep things cooler in the warm case (although this is still something that needs to be minimized if possible), but the Optics Box needs to be running at least 10°C cooler than these simulations show. The main reason for the high temperatures in the Optics Box is due to the connection between the outer wall and the Electronics Box wall. Although it will cause an increase in temperatures in the Electronics Box, the thermal connection between the boxes is removed, so that the optics do not exceed their required temperature limits. The design was changed to have a 5 mm gap between the boxes. The same three scenarios are run as simulations, with the



(a) Cold temperature case simulation for Optics Box, boxes connected.

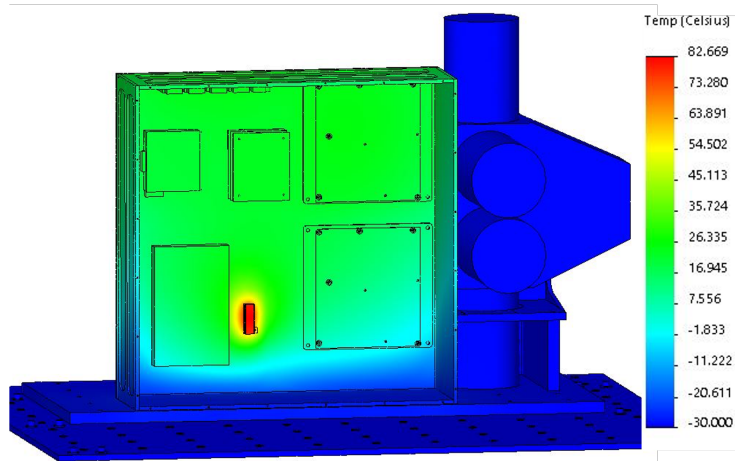


(b) Average temperature case simulation for Optics Box, boxes connected.

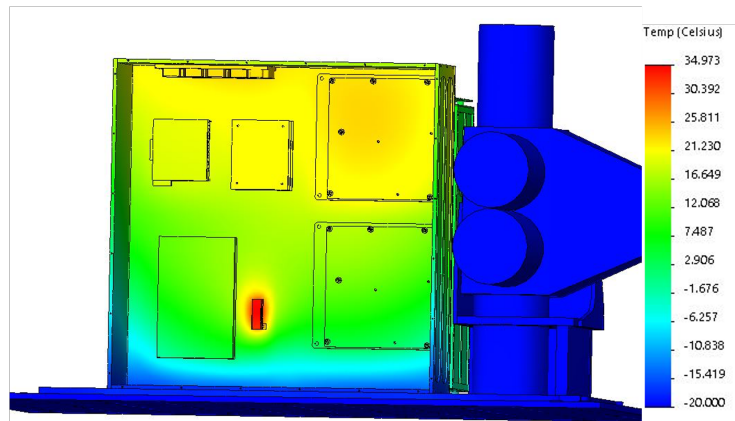


(c) Warm temperature case simulation for Optics Box, boxes connected.

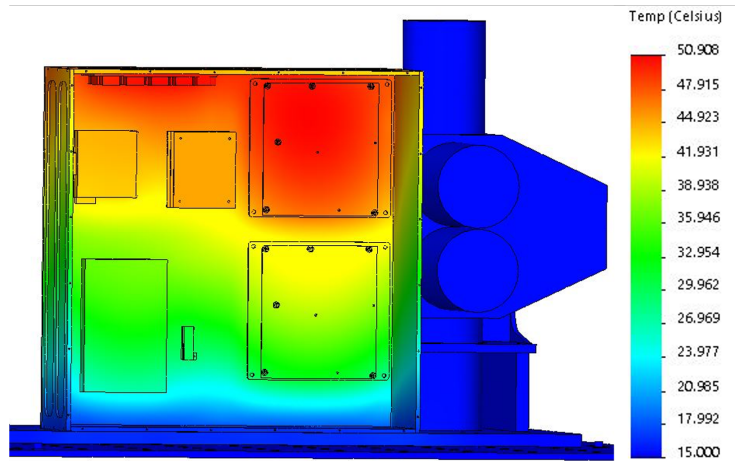
Figure 3.25: Simulations for LIFE V4, Optics Box view, boxes connected.



(a) Cold temperature case simulation for Electronics Box, boxes connected.



(b) Average temperature case simulation for Electronics Box, boxes connected.



(c) Warm temperature case simulation for Electronics Box, boxes connected.

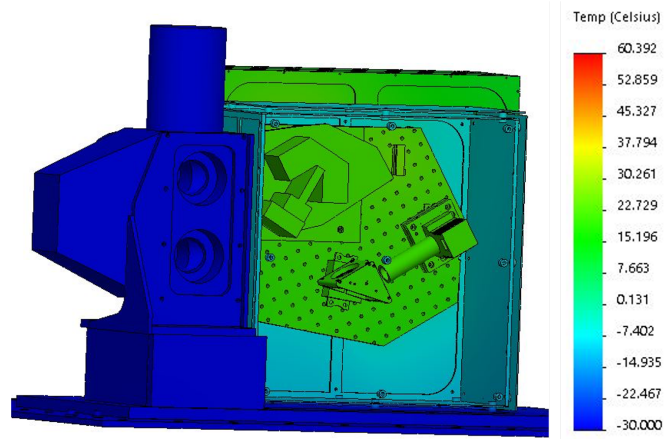
Figure 3.26: Simulations for LIFE V4, Electronics Box view, boxes connected.

Optics Box heater now set as 18 W, 14 W, and 0 W for the cold, average, and warm cases respectively, and the Electronics Box heater now set as 100 W, 50 W, and 0 W. The results are presented in Figure 3.27 (Optics Box view) and Figure 3.28 (Electronics Box view).

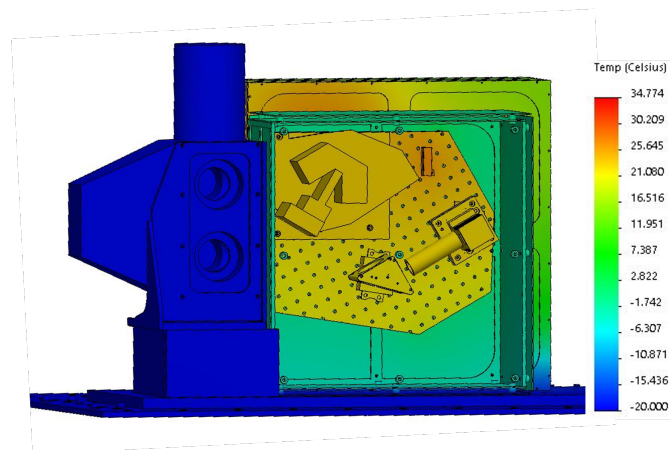
With no thermal connection between the boxes, the Optics Box temperatures are now well within their required ranges. With a moderately sized heater, optical components maintain a temperature of 20°C in the cold case and warm case, and roughly 18°C in the warm case. However, with less heat being dissipated elsewhere, many components in the Electronics Box are now too warm. In the cold and average case, the components are well within their limits, and a smaller heater is required as the heat is no longer transferring the Optics Box. However, in the warm case, the DAQ board is reaching temperatures in excess of 52°C, well beyond the temperature maximum, and cooling fans may not be enough to keep it cool through continuous operation in the lab. There are also more components that will be installed in this box, which will generate more heat. A complete redesign of the electronics layout within the Electronics Box would be necessary, both for thermal reasons and space reasons. With the Optics Box requirements met for all cases, the new design only effects the Electronics Box. This leads to the third version of the electronics box, in LIFE Version 5.

3.5.6 LIFE Preliminary Design: Version 5

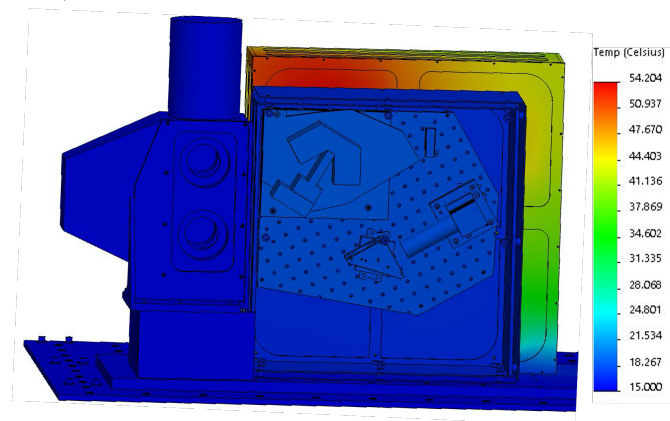
Towards the end of the thermal-mechanical design cycle of LIFE Version 4, the electronics design for LIFE was nearing completion. It was now known what other electronics components would need to be added: DC-DC converters (power supplies to interface with the gondola power supplies), filters for the power lines, temperature controllers, a second computer stack, and the controller for the motor within the blackbody system. After a few different iterations of the design, it was determined that there was no good way to put all electronics into one box. The box would have to be too large for the volume requirements of the gondola, or components would have to be installed very close together. This leads to difficulty in building and repair of the electrical system, and also makes meeting the thermal requirements difficult. Thus for the the next version of LIFE, Version 5, a new box would be added to the design, holding some of the instruments electrical components. The new electrical components that were placed in this box were all components necessary to operate



(a) Cold temperature case simulation for Optics Box, boxes not connected.

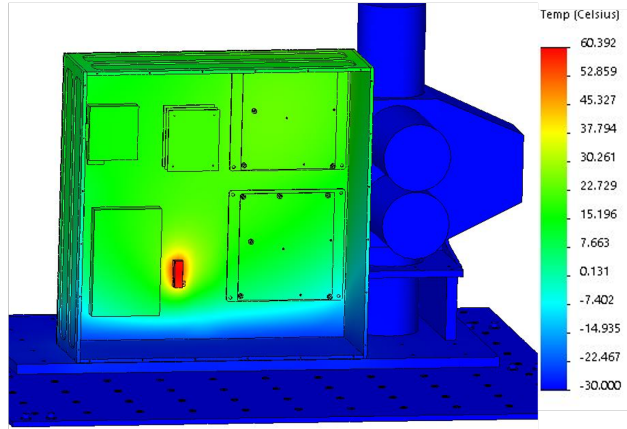


(b) Average temperature case simulation for Optics Box, boxes not connected.

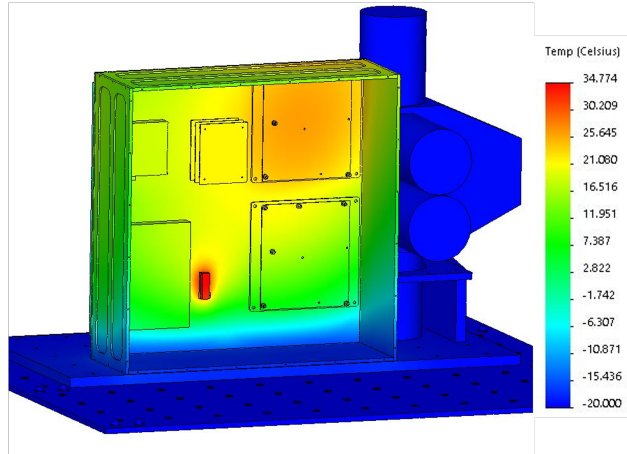


(c) Warm temperature case simulation for Optics Box, boxes not connected.

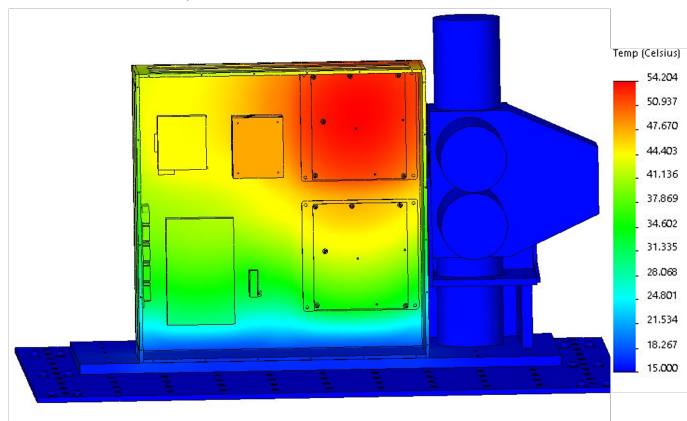
Figure 3.27: Simulations for LIFE V4, Optics Box view, with no direct thermal path between boxes.



(a) Cold temperature case simulation for Electronics Box, boxes not connected.



(b) Average temperature case simulation for Electronics Box, boxes not connected.



(c) Warm temperature case simulation for Electronics Box, boxes not connected.

Figure 3.28: Simulations for LIFE V4, Electronics Box view, with no direct thermal path between boxes.

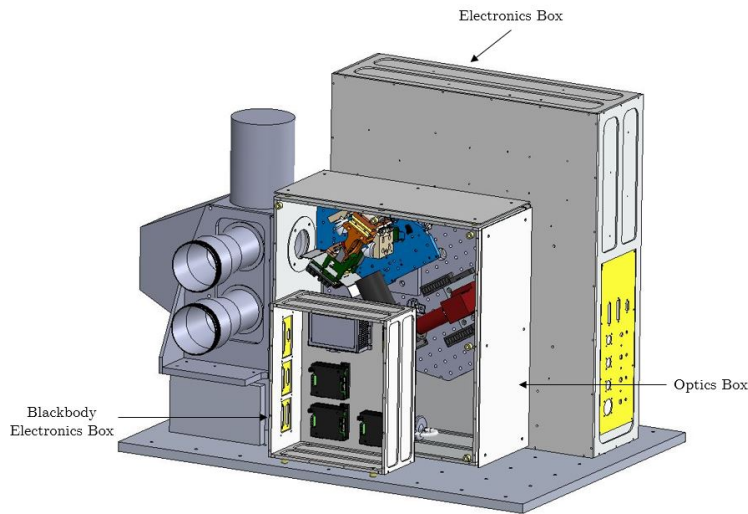


Figure 3.29: Initial version of LIFE Version 5, with the new Blackbody Electronics Box.

the blackbody system, and it was thus named the *Blackbody Electronics Box*.

Outside of this addition, there were a few other changes. The Optics Box remains largely unchanged, except for the addition of smaller components such as the purge and desiccant system, which allows the box to be purged with nitrogen and kept dry before launch. The full model of LIFE V5, including this new box, is shown in Figure 3.29.

Electronics Box Design: Version 3

Version 3 of the Electronics Box saw the addition of many new electronics components, which prompted a redesign of the layout. However, the main design for the layout was based upon a few requirements, from thermal simulations. The first was the location of the BMXS board. In the previous design, it was placed in the bottom right of the box, arbitrarily. As it has the most stringent minimum temperature of any component in the electronics box, it should not be placed close to the bottom of the box, which can become the coldest. As a result, it was placed near the top of the box. The issue with placing it in this position was the potential for overheating, as it is more difficult to dissipate heat and the BMXS also has the most stringent maximum temperature, but it was less of an issue than the freezing problem. The components which had low minimum temperatures, such as the DC-DC converter, Ethernet

hub, and power supply, were all placed near the base. In addition, the DC-DC converter and the power supply both dissipated a high amount of power, and placing these close to the baseplate mitigated overheating.

In addition to the BMXS, the other parts that had a large effect on the layout were the DAQ/Pleora boards. These boards dissipated the most heat, while also having the second smallest temperature range, after the BMXS. It took many simulations to be able to place them in the correct location. First, their location was limited by their connection to the MCT Detector. Sixteen cables connect the DAQ board to the detector, and are at a finite length of less than half a meter. They had to be placed at somewhat the same height as the detector in the Optics Box to minimize distance. Beyond this constraint, the power and thermal requirements would need to be balanced for the ideal location. If the boards were too high, they would not be able to dissipate enough heat in the hot case, and would overheat. However, if they were placed too low, they would freeze in the cold case if the Pleora board attachments fell below 0°C. These boards were moved up and down and placed in various orientations through many thermal simulation iterations until they would be able to meet the minimum temperature requirements in the cold case and the maximum temperature requirements in the hot case. The final location for these boards had only 5 mm of error in moving up and down to continue staying within the required range. The heaters used and the resulting temperatures are described in the thermal section. Beyond these boards, the remaining components of temperature controllers and computer stacks could be placed somewhat freely, as they had wide temperature ranges and had relatively low heat dissipation. The result of these layout iterations and thermal simulations is Version 3 of the Electronics Box, shown in Figure 3.30.

Another addition to this box beyond Version 2 was the first version of the breakout board, or the wall through where external connections would be made. This was designed using a third party software outside SolidWorks and ordered independently, outside of the machine shops. There was also planned to be a protective cover placed over the DAQ boards as they were the most electro-static discharge (ESD) sensitive components in the instrument, to stop any accidental contact with these boards during construction or repair. However it was decided later during the build that the implementation was not necessary.

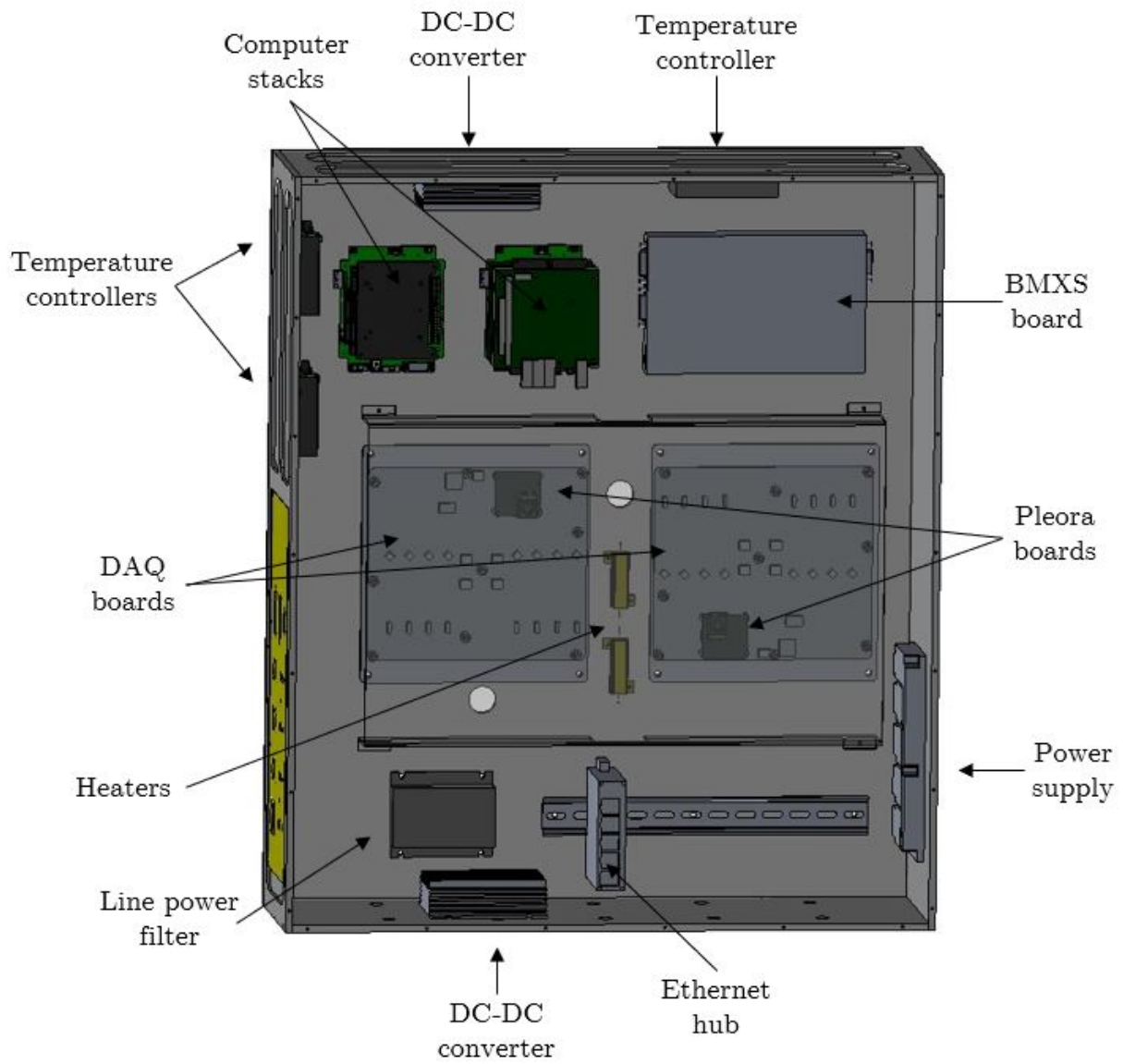


Figure 3.30: Electronics Box Version 3, with more components added.

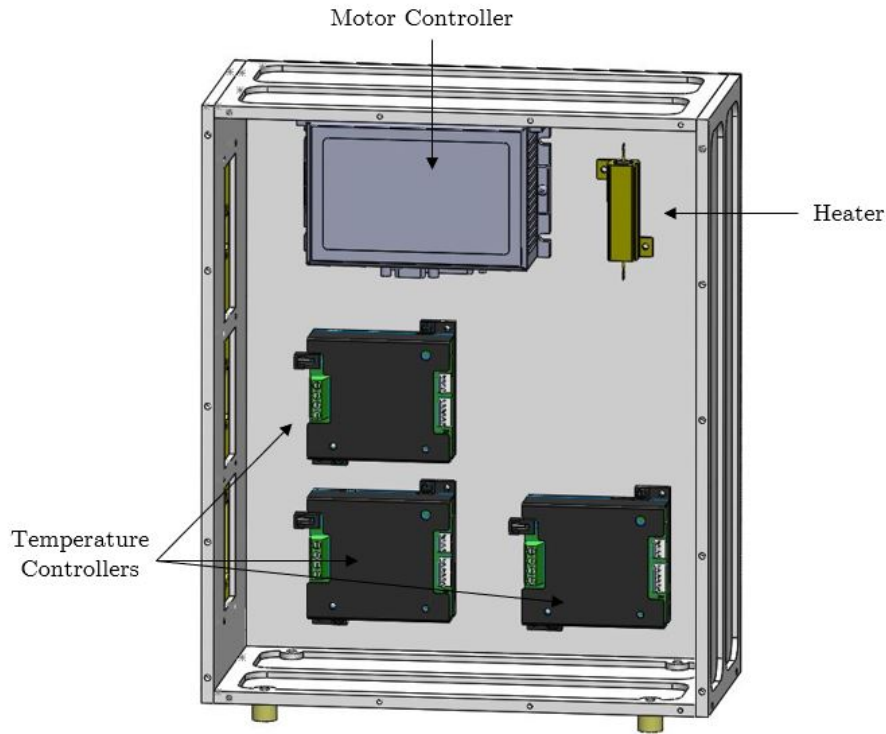


Figure 3.31: Initial model of the Blackbody Electronics Box, which contains components which control the blackbodies.

Blackbody Electronics Box Design: Version 1

This box housed components that were required to operate the blackbody system, and could not fit within the main Electronics Box while meeting size and space requirements. The core components of the new box are three temperature controllers and a motor controller. Two of the three temperature controllers control the blackbody temperatures, the third would control the temperature of this new box, and the motor controller is for the blackbody system. While less thermally sensitive than the other boxes, the thermal design of this box was still important due to the temperature range of the motor controller. As described in the thermal section, a heater was added to this box for the purpose of keeping the temperature of the box above 0°C . A few more components would be added later, but these were most important for the thermal design. A model of this box is shown in Figure 3.31.

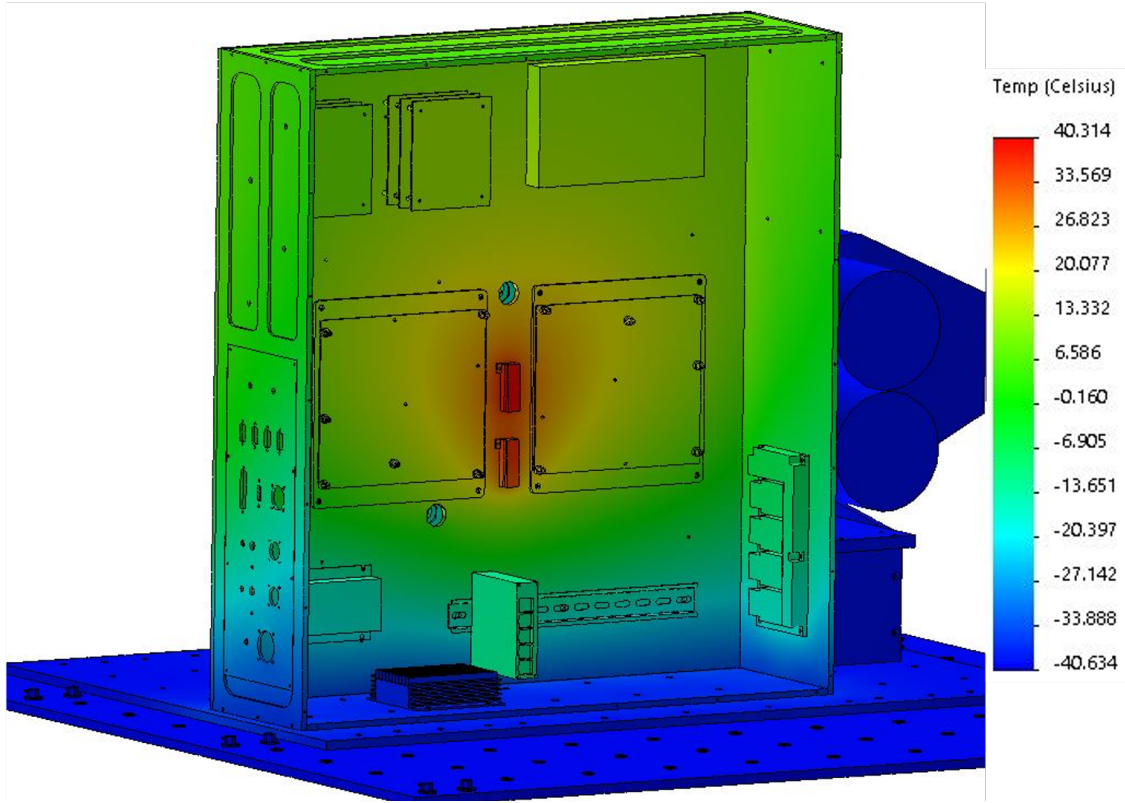
LIFE Version 5: Thermal Analysis

As with previous analyses, the simulations were split into the three major scenarios: The cold case, average case, and warm case. As the thermal design of the Optics Box from the previous thermal analysis met requirements, this will mainly focus on the Electronics Box and Blackbody Electronics Box. Numerous iterations were done with different heater values, heater locations, and electronics locations to ensure that the most critical components would meet requirements. The Electronics Box heater was split in two, becoming two resistors wired in parallel, which would aid in redundancy should one of them fail during flight. Spreading them out also means a better heat distribution to delicate components, and requires smaller heaters. For the cold case, the thermal simulation inputs were as follows: the minimum temperature was lowered to -40°C , to better simulate what could be experienced during the ascent, even for a short period of time. The heaters in the electronics box dissipated 60 W each, the optics heater dissipated 22 W, and the Blackbody Electronics Box heater dissipated 60 W. The model for the simulation is shown in Figure 3.32.

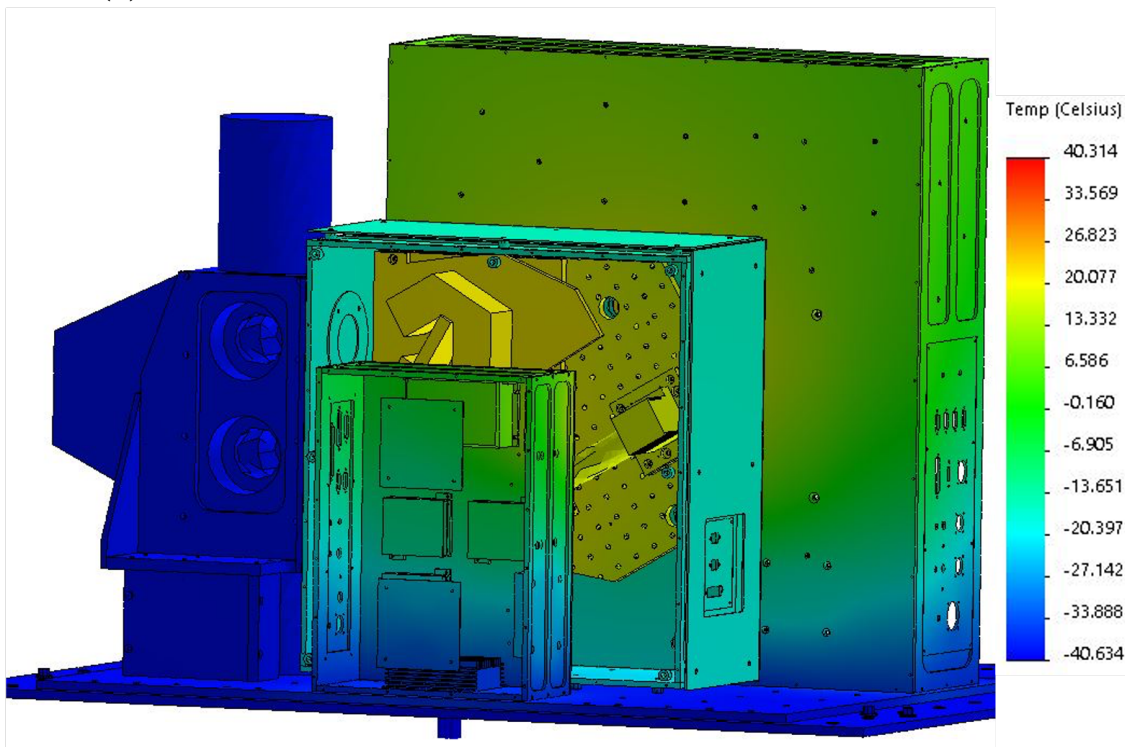
The component temperatures meet the required temperature ranges. Although the DAQ boards drop below 0°C in some areas, the locations where the Pleora boards are attached stay above 0°C , as required. For the average case, the inputs were as follows: the baseplate temperature set as -20°C , the electronics box heaters dissipate 40 W each, the Optics Box heater dissipates 14 W, and the Blackbody Electronics Box heater dissipates 40 W. The model for the average temperature scenario is shown in Figure 3.33.

The temperature requirements are met for the average temperature case. Finally, examining the warm case, it must be ensured that the Electronics Box, and specifically the BMXS board, will not overheat. For this final case, the baseplate temperature set as 15°C , and all heaters are off. The model for the warm (lab) temperature scenario is shown in Figure 3.34.

Here, the Electronics Box is close to overheating, but manages to stay within the required temperature range. Ideally, there is a margin of error from the simulation to the requirements, but this is the worst case scenario. This simulation assumes all electronics on full power, for an indefinite amount of time, with no fans. Most important will be the installation of fans, which will run while the instrument is in the lab, ensuring the components do not overheat.

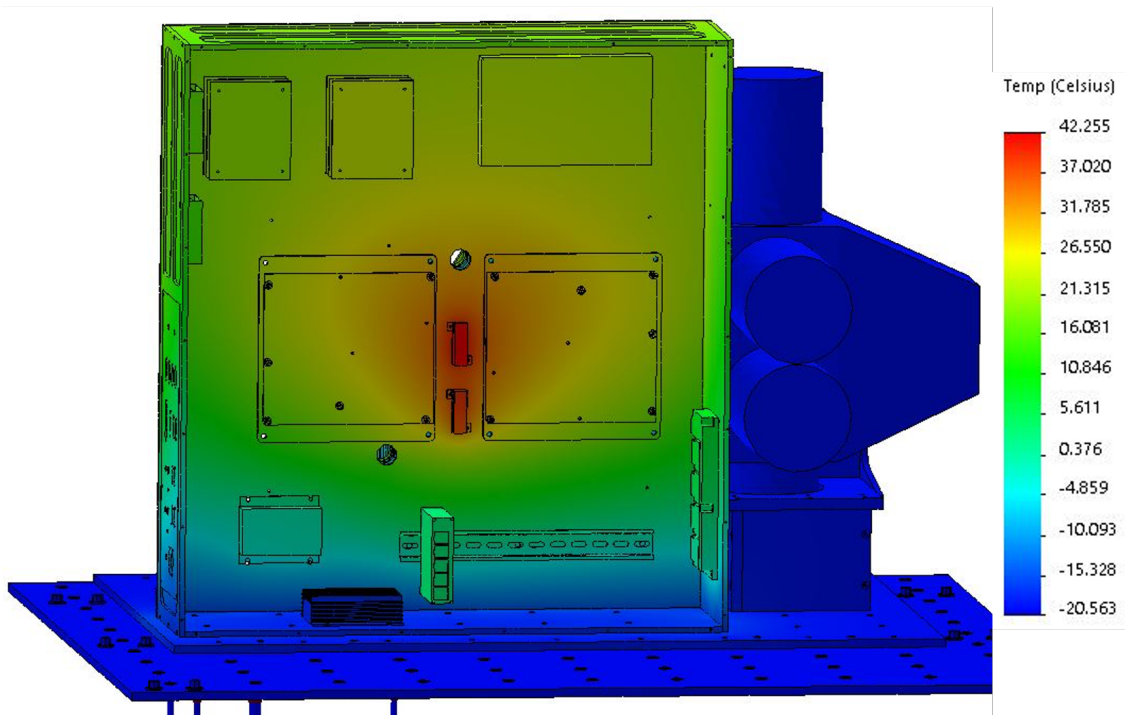


(a) Cold temperature case simulation for LIFE V5, Electronics Box view.

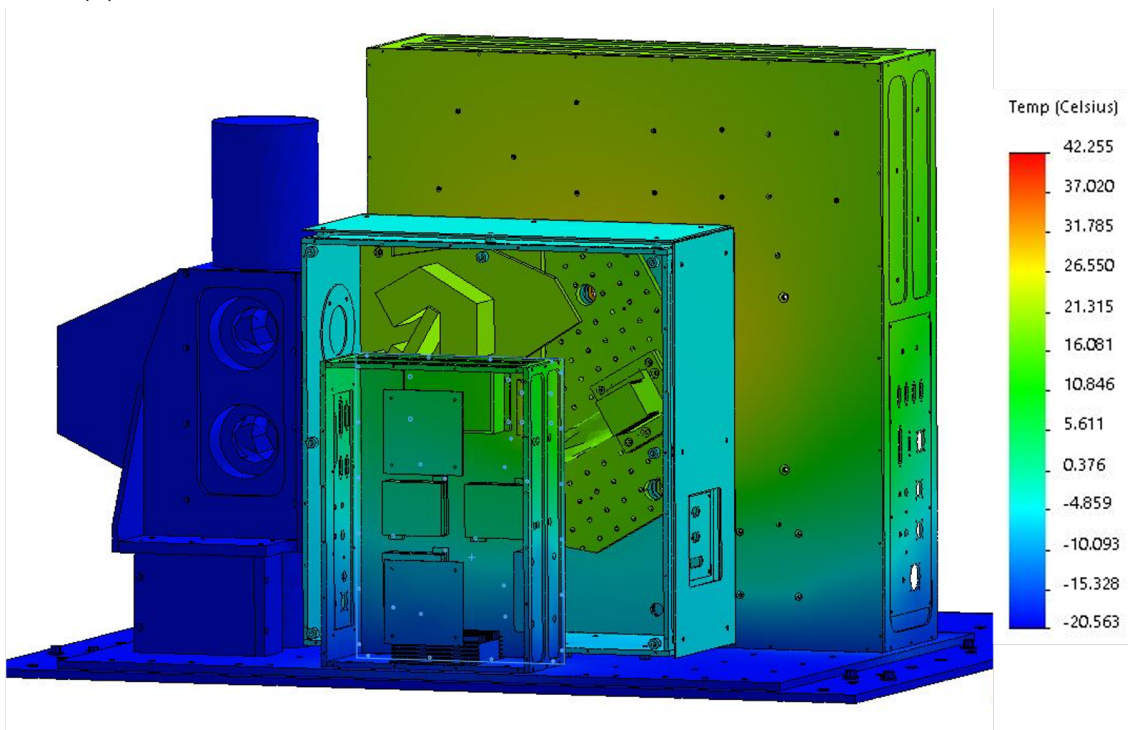


(b) Cold temperature case simulation for LIFE V5, Optics Box view.

Figure 3.32: Front and rear view of LIFE V5 cold scenario simulation.

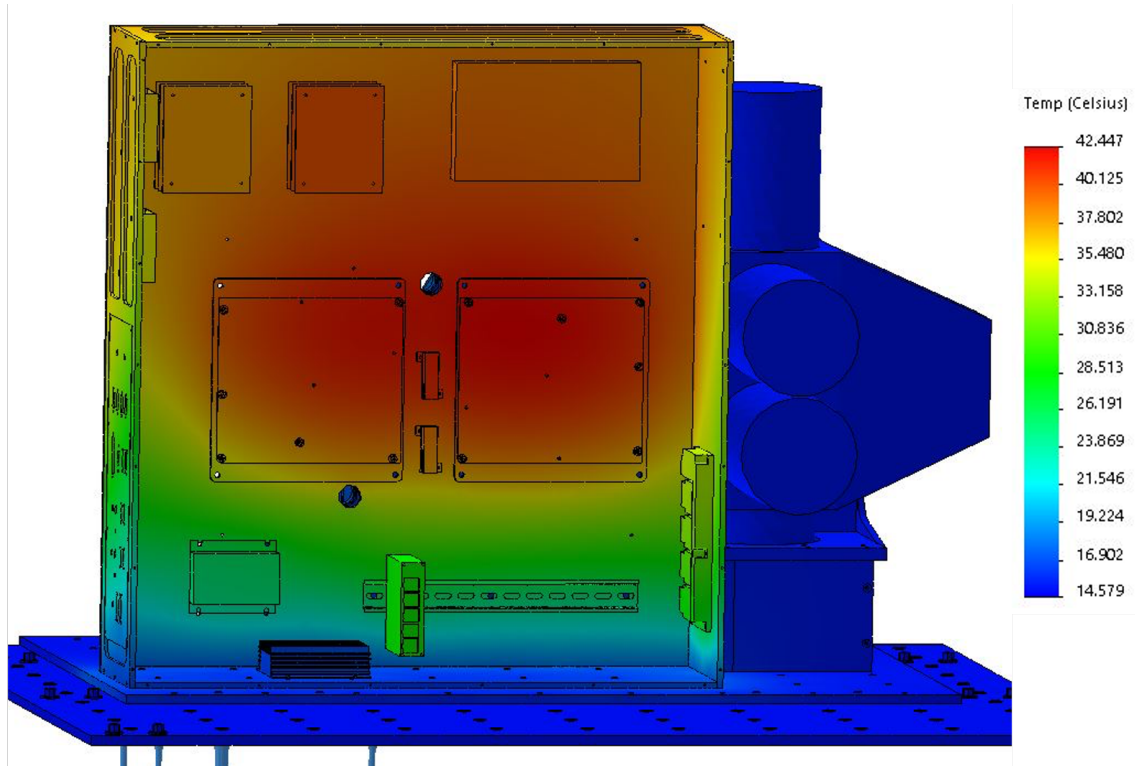


(a) Average temperature case simulation for LIFE V5, Electronics Box view.

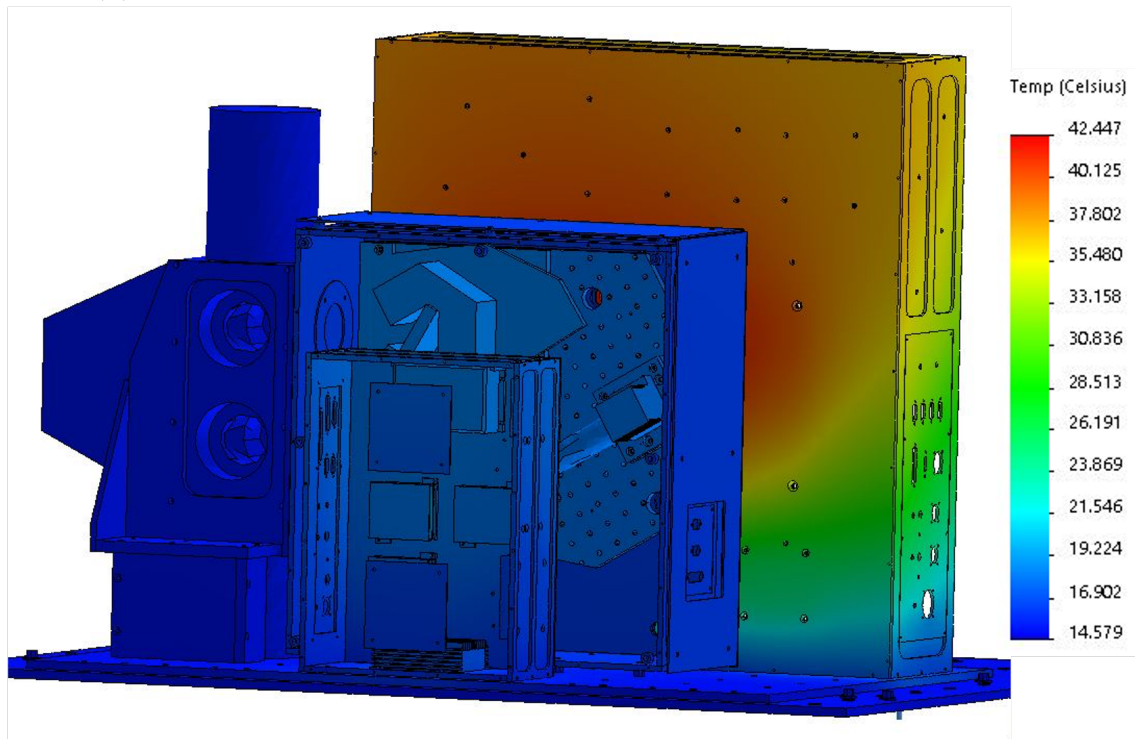


(b) Average temperature case simulation for LIFE V5, Optics Box view.

Figure 3.33: Front and rear view of LIFE V5 average scenario simulation.



(a) Warm temperature case simulation for LIFE V5, Electronics Box view.



(b) Warm temperature case simulation for LIFE V5, Optics Box view.

Figure 3.34: Front and rear view of LIFE V5 warm scenario simulation.

So, overall, this design meets all thermal requirements, and a final, detailed design can be created. However, one more version of LIFE was created, as an alternate to Version 5. It is described in the subsequent section.

3.5.7 LIFE Preliminary Design: Version 6

One issue with LIFE Version 5 is that although some components were moved to a separate Electronics Box, the main box still contains many components. Most importantly, it contains the electronics for the Optics Box system: the BMXS board, the DAQ board, and their power supply. The BMXS board and DAQ board are both highly ESD-sensitive components, and must be handled very carefully. Less time spent working around these components means a lower chance that they could be touched accidentally while working, causing potential damage to these components. An idea was raised of moving all non-optics related electrical components into their own box, leaving all the components necessary for the operation of the optical system in their own box. This would lower time spent working around sensitive components and lowering the chance of unintended damage to the electronics. The Optics Box would remain the same. This new design was named LIFE Version 6, and a model is shown in Figure 3.35.

The box that would contain all Electronics for the Optical System was named the *Optics-Electronics Box*. It housed the two DAQ boards with the Pleora boards, the Ethernet hub, BMXS board, power supply, heaters for for the DAQ boards and BMXS, and their associated temperature controllers. The connections to the Electronics Box would be for power to the temperature controllers and heaters, and the Ethernet connection from the Ethernet hub to the computer stack. A model of this is shown in Figure 3.36. The electronics box, holding the rest of the components, is shown in Figure 3.37.

An issue with this design is that the BMXS board now needs to be placed on the base, where the temperature changes can be much larger. This is why in Version 5 it was placed above the DAQ boards. The DAQ boards cannot be moved lower, as they would freeze if they were too close to the base as well. One option to improve the thermal characteristics would be to add more heaters around the BMXS board, but the instrument is already drawing a large amount of heater power, approaching the limit of what can be supplied by the gondola.

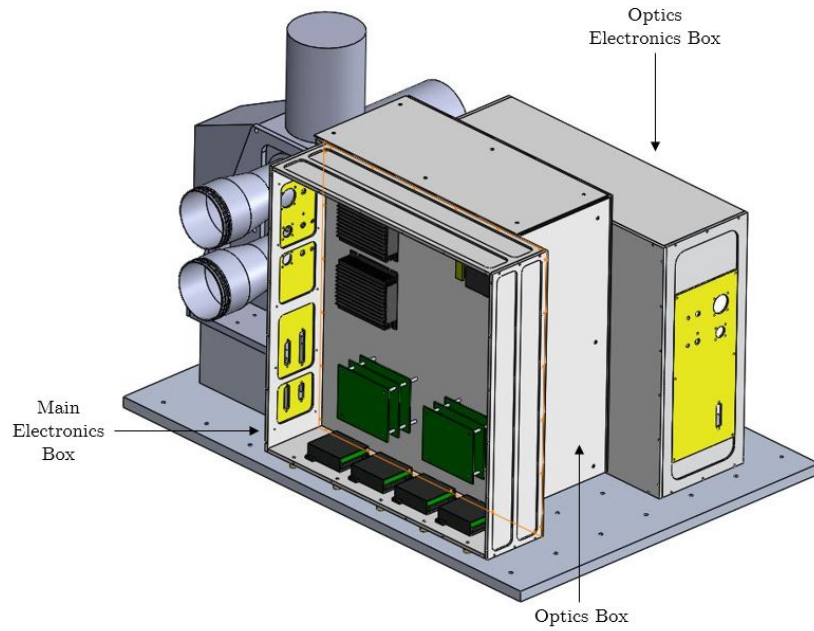


Figure 3.35: LIFE Version 6, which shifted components between electronics boxes to better protect the optics electronics.

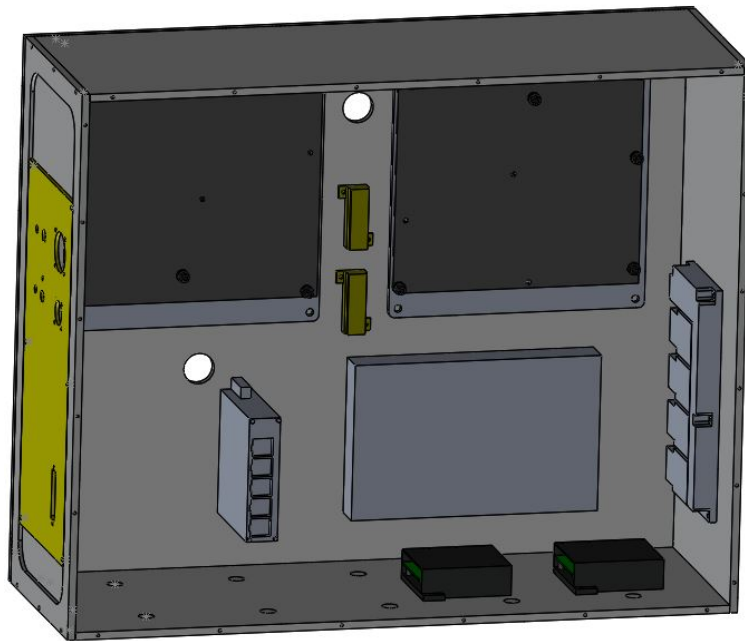


Figure 3.36: A new box, meant to replace the Blackbody Electronics Box, which houses only the optics electronics.

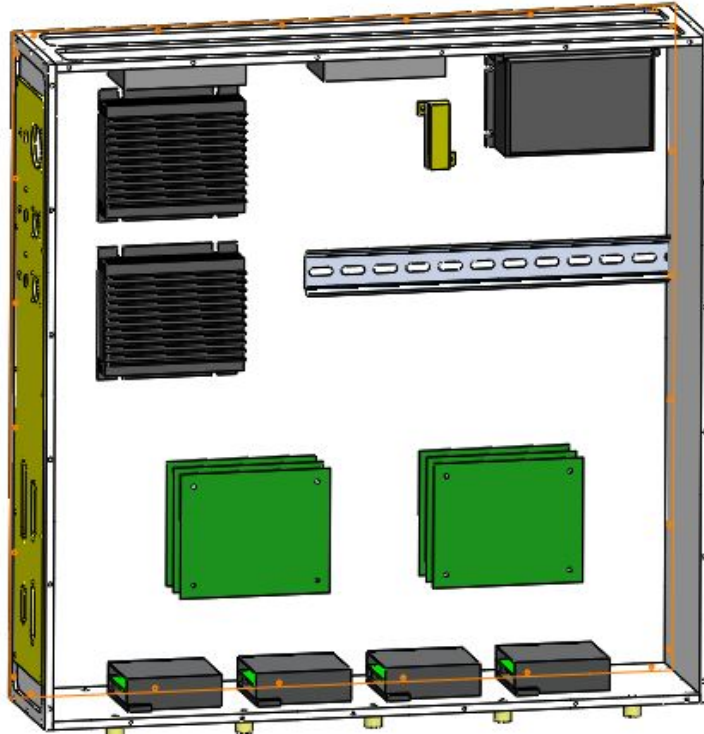


Figure 3.37: The fourth version of the Electronics Box, which here houses all electronics except the optical system components.

The other option would be to move the BMXS board above the DAQ boards, however this would make the box almost as large as before, adding weight, which is also almost at the required limit.

There were no detailed thermal analysis done for this design. After redesigning, it was determined that it was not worth the time to perform many new thermal iterations and to redesign the connections between boxes and components, which had already been designed to a large extent for the previous design. The solution for the original problem, the ESD-sensitive components, was to place a cover over them, as discussed previously (this was added after Version 6, but was still part of the Version 5 design). Thus this new design was scrapped, and the final design chosen was Version 5. The next section goes into the detailed design of this model.

3.5.8 Final LIFE Design: Version 5 Revisited

The design chosen to go ahead with the detailed design was Version 5. The detailed design includes a number of changes to the mechanical design, such as adding components that are not necessary to the thermal model. These components include connectors and fasteners, cables, and components that were omitted from thermal designs due to their complex shapes, including detailed board models. The blackbody design is also changed to show alterations made specifically for its use in the LIFE instrument. The final LIFE design also includes a more detailed thermal analysis, including radiation and other factors, which will have effects on characteristics such as the material coating. When the detailed design is complete, the model can be sent to be manufactured.

Final Thermal Simulations

The thermal analysis was re-examined in more detail first. A notable exception to the previous thermal analyses was the exclusion of radiation. Through some initial tests, it was found that radiation would have a small effect on the final thermal model. It also exponentially increased the simulation solving time, and as iterations needed to happen quickly in the initial designs, it was ignored. As this is now the final design, it was included in the analysis. The initial assumption was correct, in that for a typical bare aluminum surface, the emissivity is very low, at roughly 0.1. Adding radiation to the design cooled components slightly, but a negligible amount. However, bare aluminum is not a good surface, especially for high altitude balloon applications, due to rust. Typically, the boxes are painted or anodized to mitigate this.

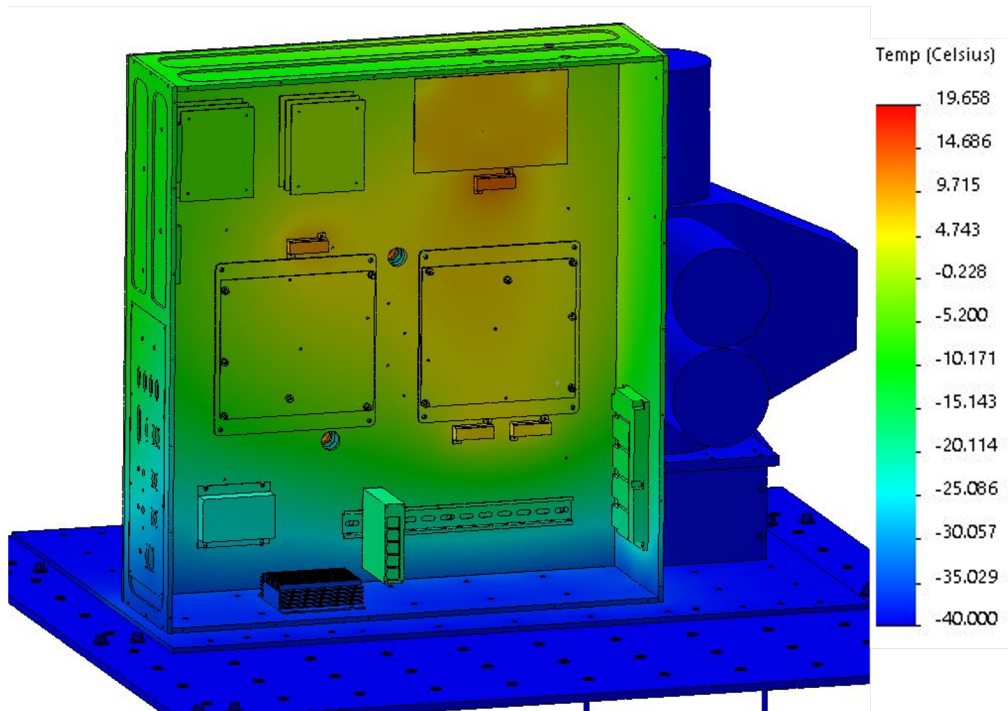
Both painting and anodizing have a large effect on radiation. Painting, depending on the color and type of paint used, can increase emissivity to as much as 0.9. Anodization typically increases emissivity of aluminum to 0.77. This would dramatically reduce temperatures, especially in the Electronics Box, where temperatures are high. The box would get much too cold with an emissivity of 0.9, with some temperatures reaching 20°C below their recommended temperature ranges. The only option was to use anodization, and to improve heating. The Blackbody Electronics Box and Optics Box remained in good temperature

ranges even with anodization, so the only changes needed to be made were in the Electronics Box. This was done by changing the number of heaters from two to four, and moving them to locations as close as possible to delicate components, specifically the Pleora Boards and the BMXS board. Two heaters were placed close to the Pleora Board on the right side, which was closest to the bottom of the box. This would help counteract the cold temperature that resulted from being closer to the gondola deck. Another heater was placed close to the other Pleora board, which as it is higher did not get as cold. The final heater was placed next to the BMXS board. This is not shown in the following temperature simulations, as this change was made just prior to construction.

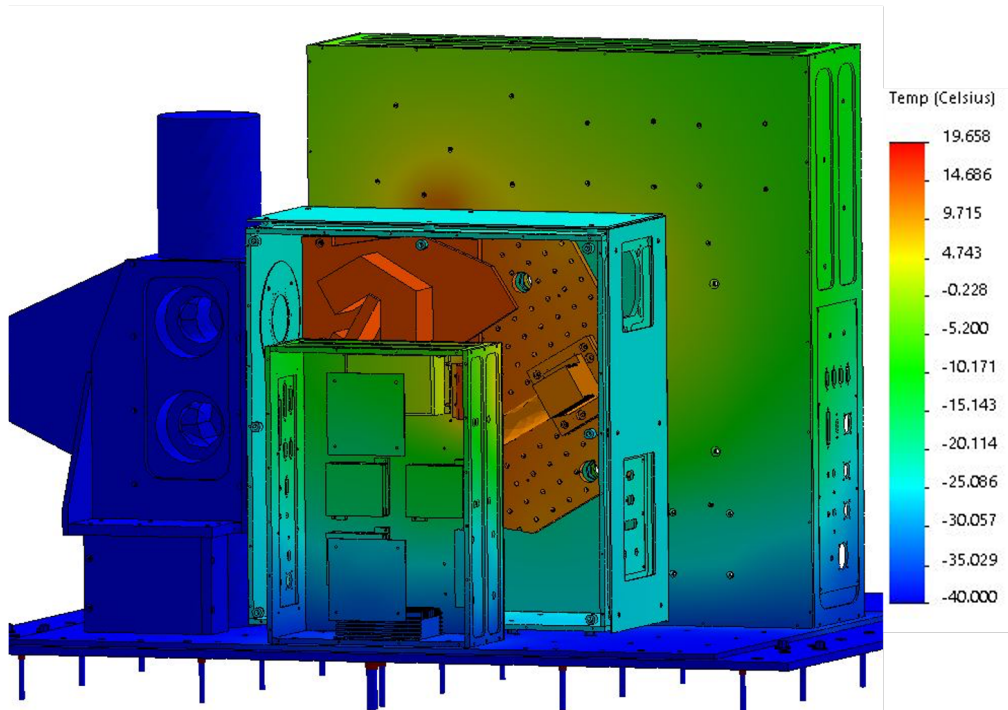
A final change made to the thermal design was the addition of a garolite spacer between the Optics Box and Blackbody system. To ensure the stability of the Optics Box during flight (as it was sitting on spacers and therefore not as sturdy as the other boxes), the Optics Box was to be bolted directly to the Blackbody system. This would help with stability as well as help align the optical path between the two systems. However, a metal spacer could not be used as that would introduce a new thermal path to the Optics Box. To ensure thermal insulation, a spacer was machined out of garolite, an epoxy material which has good thermal insulation properties while also having low off-gassing properties.

With these changes to the surface coating and the addition of the garolite spacer, another set of thermal simulations were completed. This consisted of radiation on all box surfaces, with an emissivity value of 0.77, and 30 W for each heater in the Electronics Box, 55 W for the heater in the Blackbody Electronics Box, and 22 W for the heater in the Optics Box. The resulting simulations are given in Figures 3.38, 3.39, and 3.40 for the cold, average, and warm scenarios respectively.

These simulations show that with the anodization, all components fall within their temperature limits. The closest components are the Pleora boards, but the heaters are well placed to heat them even if the rest of the DAQ board falls below 0°C . The only part of these board that must be above 0°C are where the Pleora boards are connected, as the DAQ board minimum temperature is much lower at -40°C . The final choice to be made was what color anodization should be chosen. Ideally, white would be the best choice, to lower the absorptivity, so in the case that the instrument did see the sun it would not be highly affected.

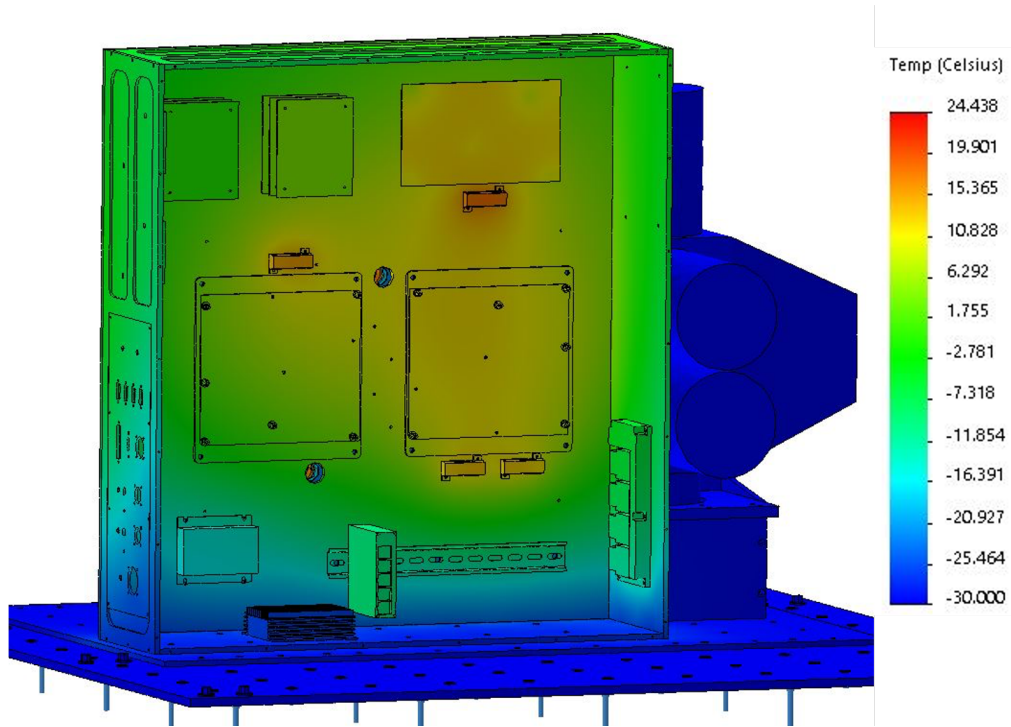


(a) Cold temperature case simulation for final LIFE model, Electronics Box view.

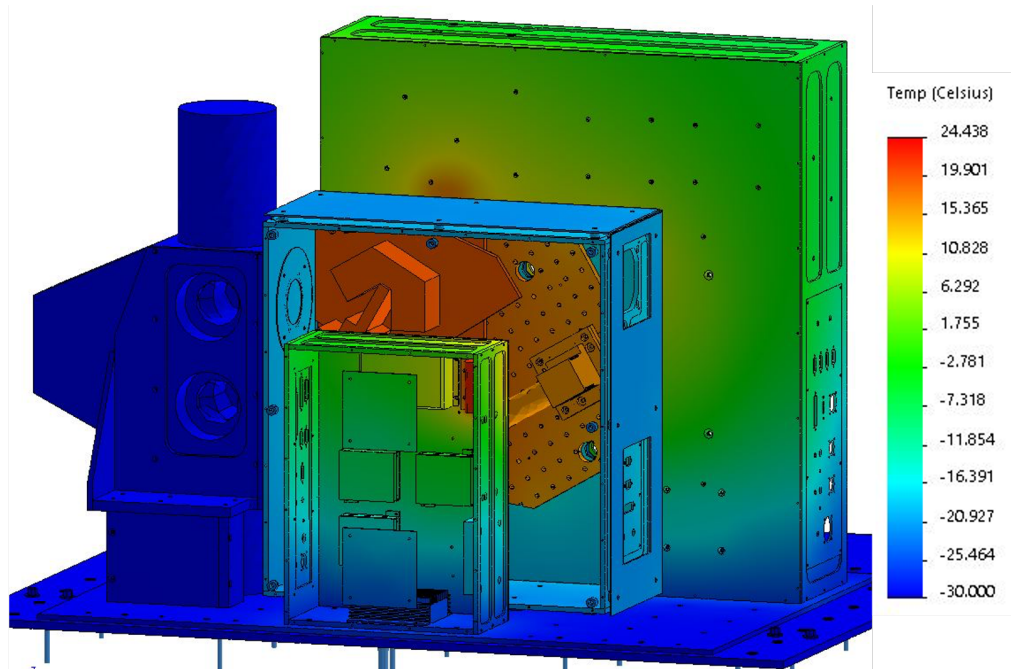


(b) Cold temperature case simulation for final LIFE model, Optics Box view.

Figure 3.38: Front and rear view of the final LIFE model cold scenario simulation.

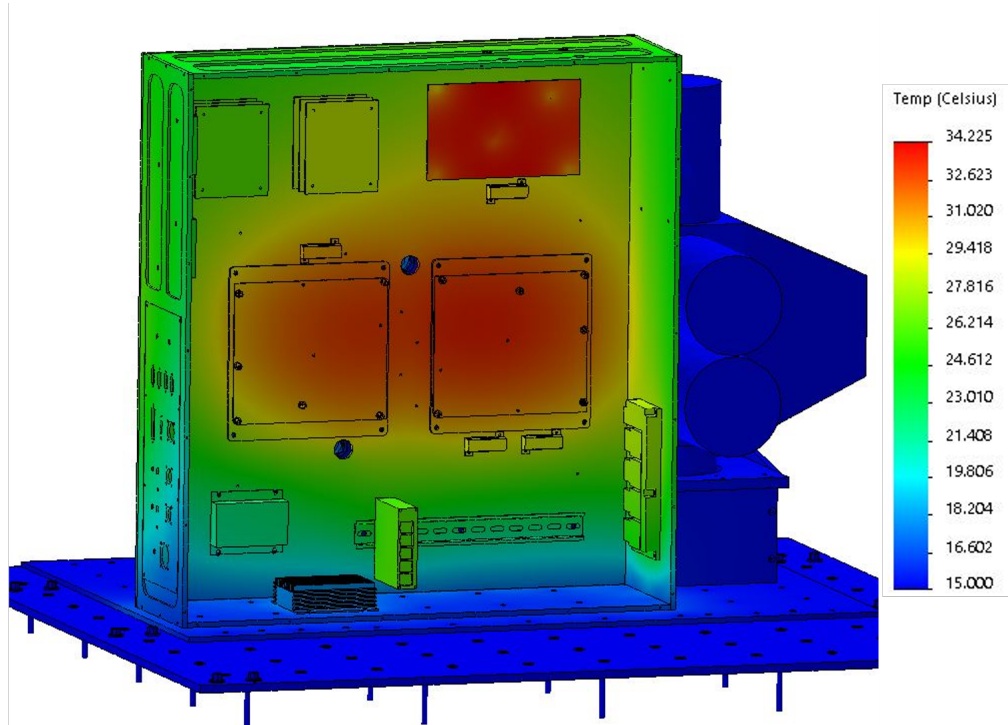


(a) Average temperature case simulation for final LIFE model, Electronics Box view.

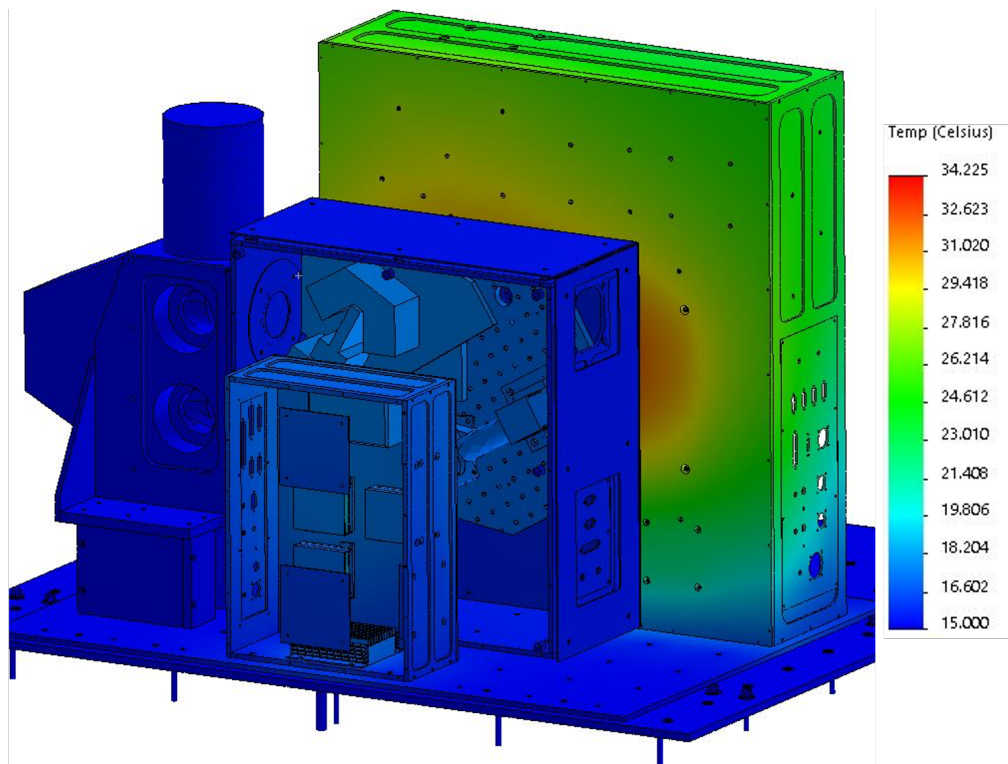


(b) Average temperature case simulation for final LIFE model, Optics Box view.

Figure 3.39: Front and rear view of the final LIFE model average scenario simulation.



(a) Warm temperature case simulation for final LIFE model, Electronics Box view.



(b) Warm temperature case simulation for final LIFE model, Optics Box view.

Figure 3.40: Front and rear view of the final LIFE model warm scenario simulation.

However, white is not an option for anodization as a result of the manufacturing process. The next lightest options were a clear anodization coat, or a gold anodization. Gold was chosen for its high reflectivity, lowering the absorptivity if it sees the sun. This was the final change made to the thermal model before manufacturing, although as described later, a few fixes were needed following the results of the TVAC tests to align the model with what was seen during tests.

Final Mechanical Changes & Models

Another part of the design that is updated is the Blackbody system. The bottom hot and warm blackbodies are removed, as they are not useful to the instrument in the LIFE flight configuration, and are heavy. Also removed are the viewport baffles. These are taken off because the instrument needs to view downwards at a slight angle of 2.86° . This is done by tilting the mirror downwards, rather than tilting the optical system or the optics box, which was deemed too difficult. With the mirror tilted downwards the FOV may clip the edge of the baffle, so to ensure a full FOV it is removed. It is also noted that the cold blackbody will not be used during flight, so the electronics to control and operate this blackbody are not present in the instrument; it is connected to an external system in the lab for operation.

A number of mechanical changes are made. First, fasteners are added to the model. This includes all bolts, washers, nuts, and spacers needed to connect boxes together and to fasten electronics. This is done to ensure that all holes are in the correct location in regards to other parts or the connection locations of the electronics, so that everything fits together as expected after manufacturing. The next step of the design was to add connectors and cables to the electronics design. The connectors were to ensure that the holes on the breakout boards were the correct size, and that there was enough room to make connections; if the connector of a component was too long it may overlap with a nearby component, which would need to be accounted for. Also added in conjunction with this were models of the cables and wires, using the SolidWorks Routing tool. This allowed cable lengths to be determined in the model, to ensure that no wires are wasted and to ensure clean and efficient cable routing inside the boxes, keeping them out of the way of any sensitive components.

The final model of the LIFE instrument before construction is shown in Figure 3.41. The

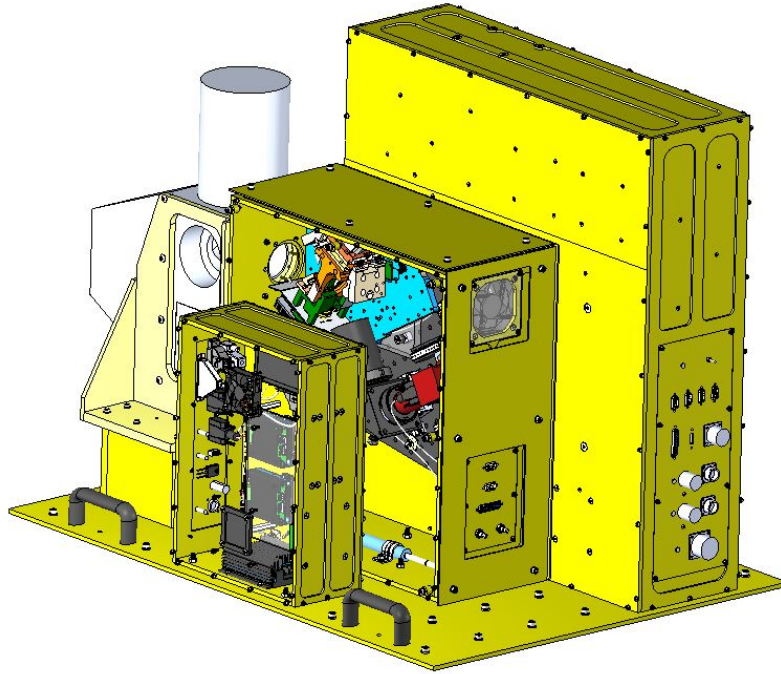


Figure 3.41: The final model of LIFE.

model for the final model of the Optics box with the detailed design of the Optical system, purge system and wiring design is shown in Figure 3.42. The final models for the Electronics Boxes which includes wiring and connectors are shown in Figures 3.43 and 3.44.

To minimize weight of the final design, mechanical simulations were completed of some of the more load-bearing surfaces, such as the wall of the Optics Box which holds the optics breadboard, or the baseplate of the instrument. Using the instrument baseplate as an example, the plate needed to be as thin as possible to minimize weight, but also strong enough so that when the instrument was lifted and moved, it would not deform. A mechanical analysis was performed using a SolidWorks mechanical simulation, which operates similarly to the thermal simulation solver. It shows the deformation of the plate based on the force upon it. A figure of this study is shown in Figure 3.45.

This study makes two assumptions: The weight is uniformly distributed, with a total force on the baseplate of 1 kN. Also, rather than the fixtures being at the handles, they are at the two edges of the plate (highlighted by green arrows). A few studies were completed with various thicknesses until a suitable option was chosen that was a compromise between

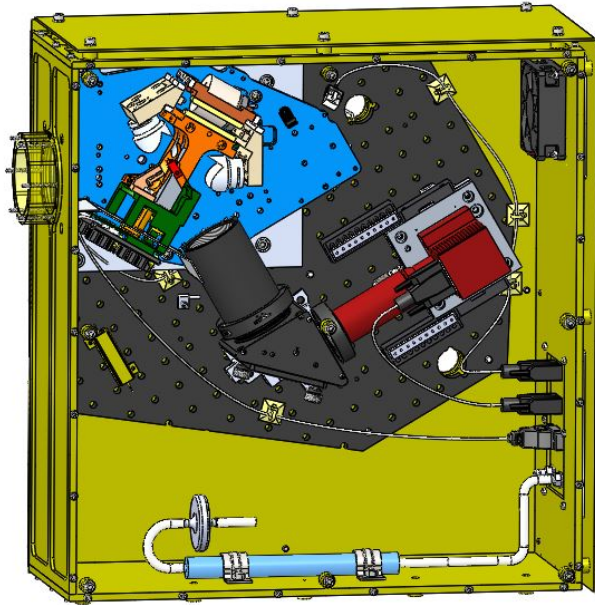


Figure 3.42: Final version of the Optics Box.

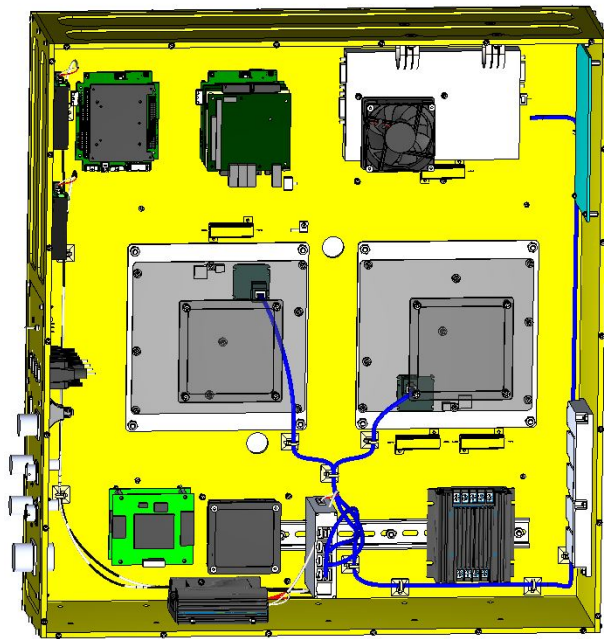


Figure 3.43: Final version of the Electronics Box.

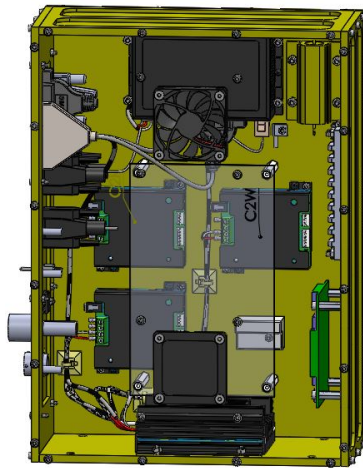


Figure 3.44: Final version of the Blackbody Electronics Box.

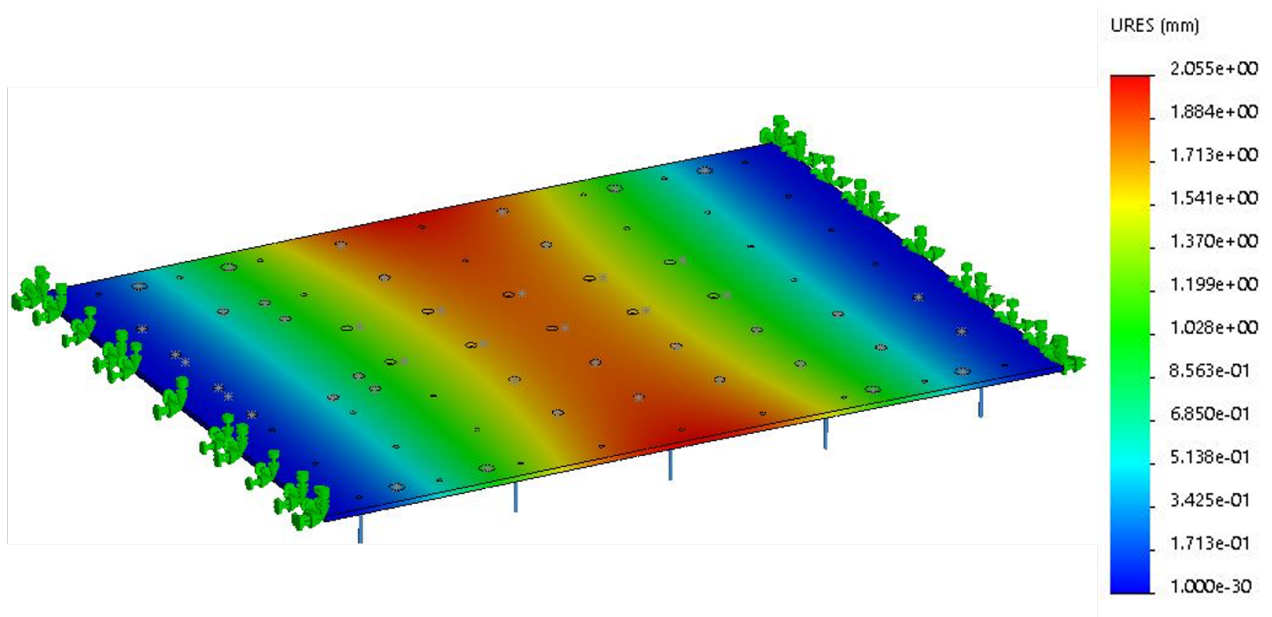


Figure 3.45: Mechanical simulation of instrument baseplate, to minimize thickness and weight while maintaining strength.

strength and lightness. In this final simulation, the thickness of the plate was chosen to be 6.35 mm. With these as the load and fixture, respectively, the worst case deformation is 2 mm. With the fixtures on the sides, and no connections in the centre, this would be a worst case scenario. In the actual case the boxes would help strengthen the centre, leading to less deformation. As a result this was chosen as the best compromise between weight and strength.

This design also had to meet the mechanical requirements set by the CSA. To ensure that major mechanical connections of the instrument would withstand some of the possible forces seen during flight, the CSA sent a spreadsheet that could calculate if a mechanical interface would survive worse case scenarios of force, at multiple angles. To do this, for each mechanical interface, the bolt locations with respect to the centre of the interface were measured and input into the spreadsheet. Further information about the model, such as the total weight and centre of gravity, were also added. The force upon each bolt connection could be calculated. Finally, the bolt type/size (e.g. M6) was input, and the theoretical limit of the different types of forces the bolt could withstand (shear, tension) were calculated and compared to what was expected. If they were within the margin of safety to the actual value, the connection would either pass or fail.

Calculations for interfaces were done for the six major connections: The blackbody system to the blackbody frame, each box to the LIFE baseplate, the optics system to the Optics Box wall, and the entire LIFE instrument to the gondola base. As an example, the LIFE instrument interface is provided. An image of the CAD model from above with bolt locations highlighted is shown in Figure 3.46, and a figure provided for the spreadsheet with bolt locations compared to the centre is shown in Figure 3.47. From the latter figure, the X and Y coordinates of all bolts are input into the spreadsheet.

The bolt type, M6, is also input into the spreadsheet. The bolt survival in tension for this type of bolt in this configuration is calculated to be 9.1 kN. The worst case scenario that will be seen on flight for this interface is 983 N. Thus this connection will easily survive the flight, and the test passes. This study is done for each interface, for each bolt, at all potential angles and forces seen for flight, such as the parachute opening or the landing. With all test passed the CSA then approves the mechanical design as ready for flight.

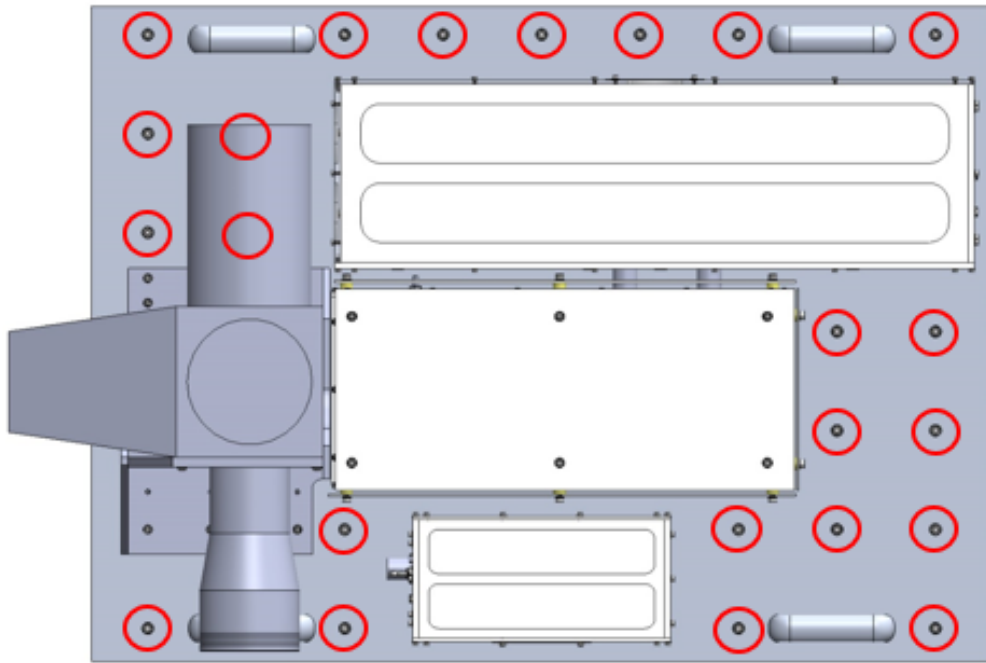


Figure 3.46: A top down view of LIFE V5, with bolt locations to the gondola highlighted.

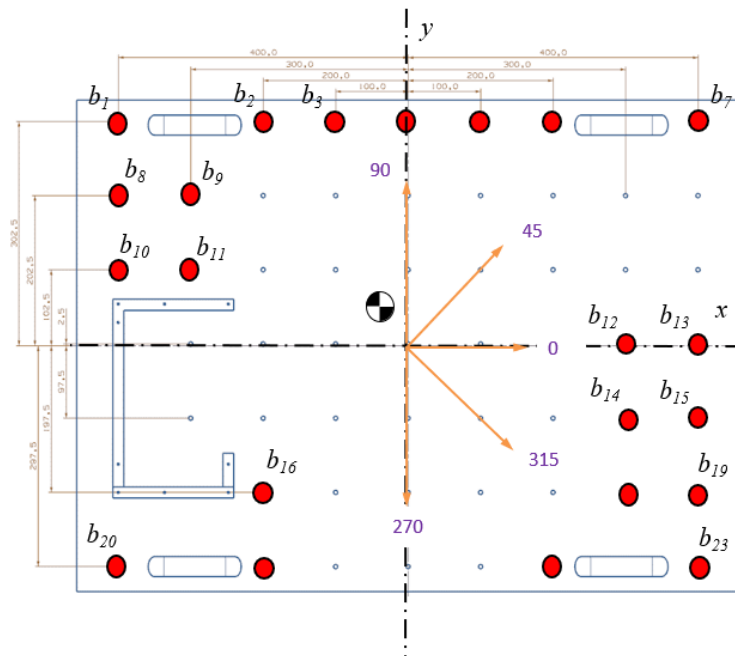


Figure 3.47: An image provided for the spreadsheet which shows distances to all bolt locations from the centre of the plate.

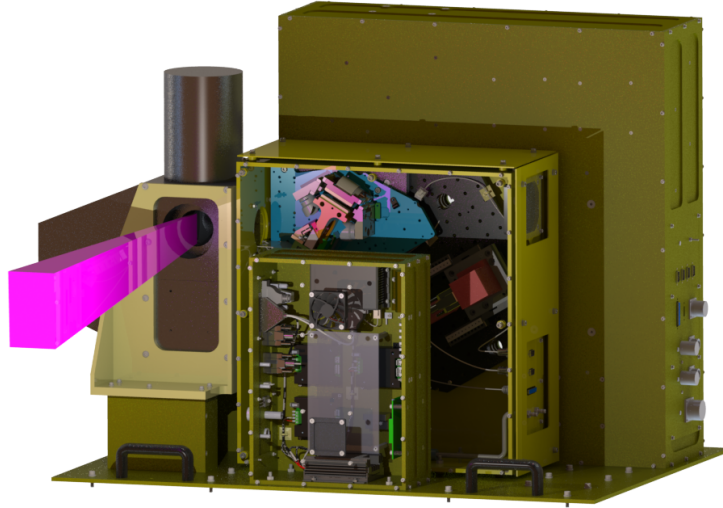


Figure 3.48: A render of the LIFE final model, from SolidWorks.

Renders were also completed of the final model, with the FOV included to show what the instrument would realistically look like once built. The FOV is shown as the pink shape coming from the instrument viewport. This render can be seen in Figure 3.48. With these models complete, parts were sent to be manufactured, which between the manufacturing and anodization, took roughly two months. The next section describes all steps from manufacturing until the high-altitude balloon launch in Timmins.

3.6 Pre-flight Construction & Analysis

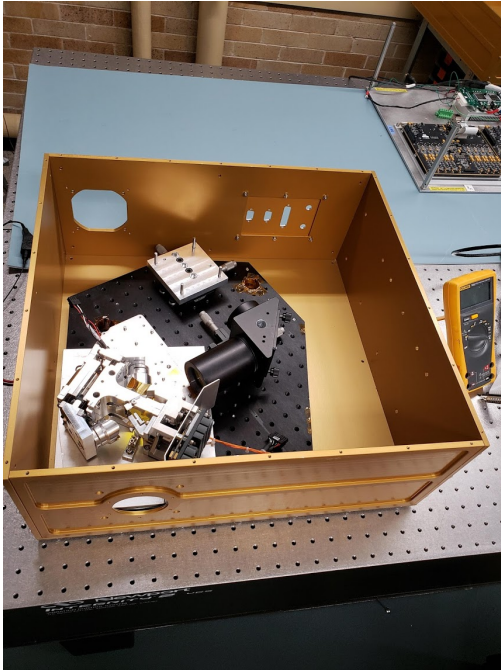
With the instrument being fully modeled and analyzed, and all requirements met, construction could begin. All components were manufactured by the Physics Machine Shops, but the full construction afterwards was done by the LIFE team. The first subsection here discusses the construction process, and lessons learned from the construction phase that should be applied to further designs. Once the construction was complete and the instrument was up and running, Thermal Vacuum tests took place, to verify the thermal design and operation. Data is presented here on what was found during these tests. Following, the thermal model was updated using results of the thermal vacuum tests, to more closely align simulation temperatures with actual temperatures.

3.6.1 Construction

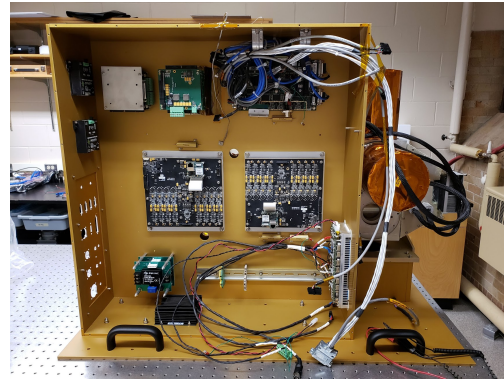
The instrument was built through the Spring of 2019. The construction went smoothly, with the boxes being fully constructed through the course of a month, and the electronics being installed shortly after, and wired inside the ISAS clean room. A few images of the build process are shown in Figure 3.49, and the final completed instrument is shown in Figure 3.50.

The most important issue that came up during the construction was an unexpected issue with the anodization: it is non-conductive. This is a well-known property of anodization, but was a forgotten consideration in the design. To properly install the electronics, they need to be grounded through the box to the baseplate, which is grounded to the gondola. However, due to the anodization being non-conductive, as the components were originally installed they were all floating grounds, which was not permissible by the CSA for the flight. Thus the instrument needed to be disassembled, and the anodization removed in areas where each component would be placed. Anodization was also removed on the edges of parts of the boxes, so that all boxes were electrically connected. Finally, the anodization layer was removed around bolt holes near the bottom, so an electrical connection was formed through the bolt to the gondola baseplate. Another issue this would cause, that was only realized after manufacturing, is that anodization also has an effect on the thermal conductivity. All electronics in the thermal model were assumed bonded to the mounting plates, which was a good assumption as thermal paste was applied between the components and the wall to maximize thermal transfer. However, anodization can lower the thermal conductivity between the component and the wall. There are no studies that show any definite numbers, with a thermal conductivity decrease anywhere in the range of 5-20%. Fortunately it was found later through the thermal tests that this would not cause any issues.

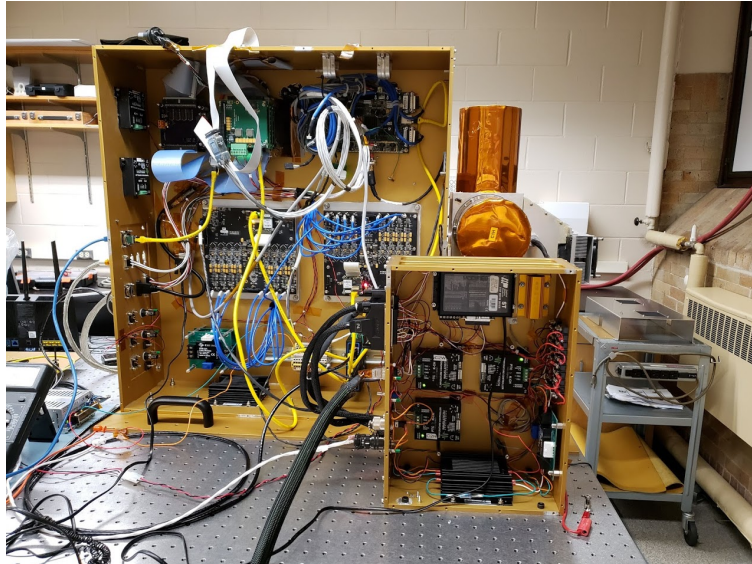
Another aspect of the build that caused difficulties, that should be improved upon in the future, were the different bolts necessary. While there were not many different types of bolts used, different lengths were needed for a variety of different parts of the instrument. This made construction and repairs difficult. In future designs, the length of bolts used should be attempted to be kept the same, and at least minimized. This saves on cost and time to



(a) Initial construction of the Optics Box.



(b) The Electronics Box during construction, with initial components installed.



(c) Electronics and Blackbody Electronics Boxes fully wired, performing initial testing.

Figure 3.49: A few images through the LIFE construction process. Images courtesy Paul Loewen.

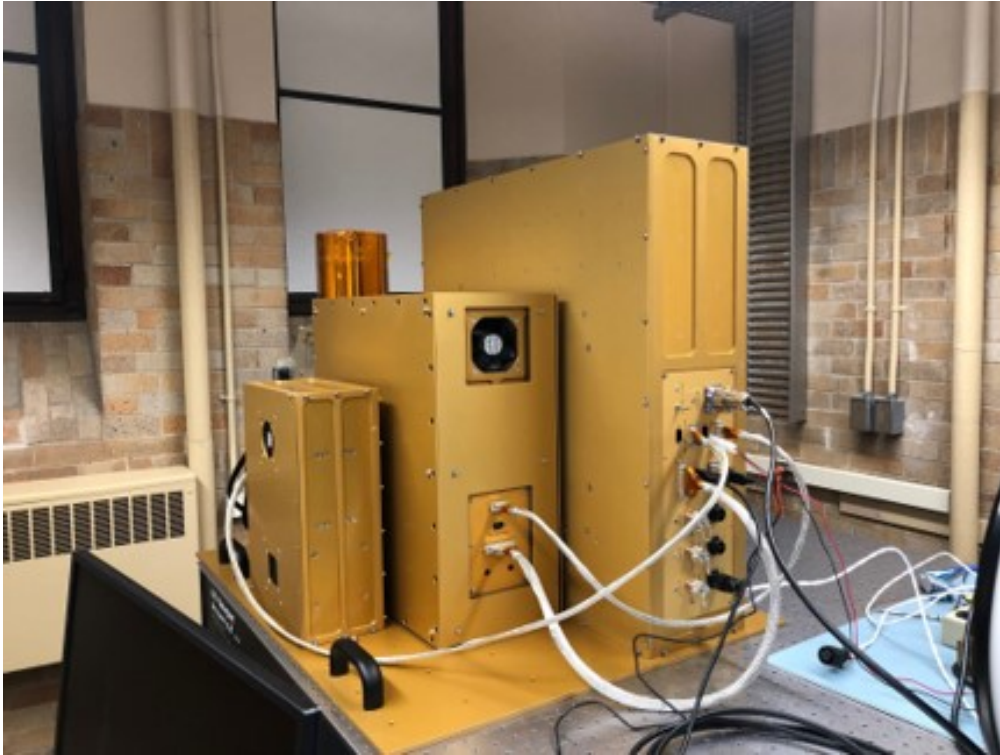


Figure 3.50: LIFE after completion, performing initial tests in the lab.

assemble and disassemble.

3.6.2 TVAC Tests

The first verification of the thermal model would take place during the TVAC chamber tests. Each instrument from the Atmospheric Research Group that will fly on a high-altitude balloon is subjected to these tests, to ensure that it will survive the flight. The vacuum environment and cold baseplate of the TVAC attempts to simulate as closely as possible the environment that the instrument will face. The TVAC chamber itself consists of a roughly 1 m^3 interior cavity into which the instrument is placed. Liquid nitrogen runs through the bottom baseplate to cool, and the temperature of this baseplate can be set. Most often during tests, it is set as -40°C , the lowest that the gondola baseplate will get during the float phase of the flight. The vacuum pump decreases the pressure to 3-4 torr.

Two TVAC tests were performed on LIFE, the first of which was used as a verification for different components and for some imaging tests, the second was used more for thermal tests. Each test ran the instrument as it would during flight, taking measurements and

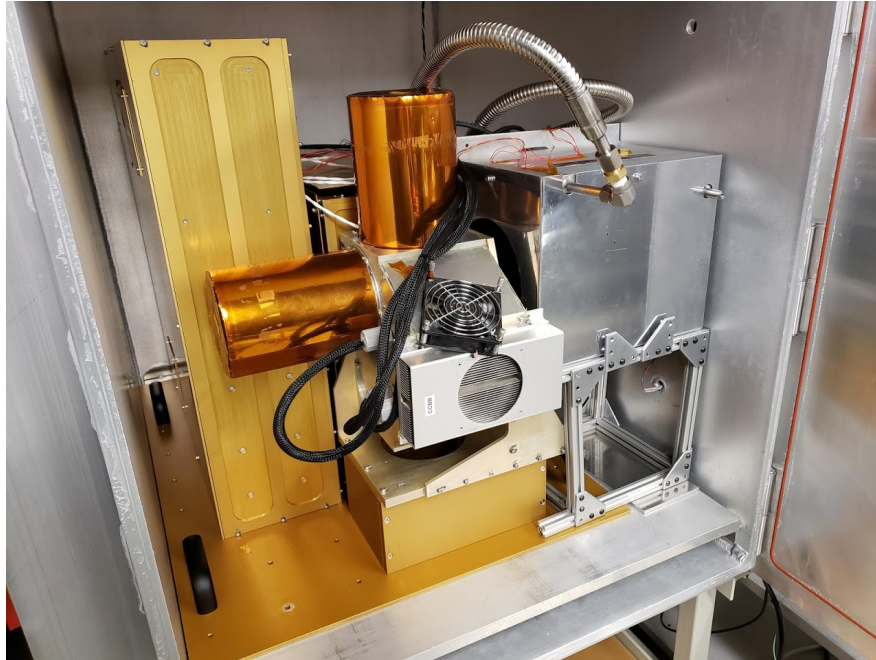


Figure 3.51: LIFE in the TVAC tank for testing. The silver box beside LIFE is the external cold blackbody used for self-emission tests.

operating from a nearby computer. Temperatures were measured both from the internal temperature sensors and from added external temperature sensors that were fed through the wall of the chamber to an external computer for measurement. An image of LIFE inside the TVAC tank is shown in Figure 3.51. The instrument ran well for all tests, and stayed within the required temperature limits. As the first TVAC test was used more for instrument operation verification, not thermal verification, only the second test will be described here. The temperature data from this test is shown in Figure 3.52.

Overall, it was a success. The test took place over the course of eight hours, the maximum expected length of the flight. The first four hours of the test was cooling down the TVAC baseplate to -40°C . The rest of the time until the instrument was turned off overnight was the core of the test, which the thermal model is compared against. Some anomalies in the data were due to testing, and were expected. For example, the temperature spike seen around the optics area at around 23:00 UTC was due to a heater being installed here, and power supplied during this time. The purpose of adding this heater was not for the purpose of cold survival, but for testing the effect of temperature change in the optics on the self-emission. The second day was for instrument verification, as the supply of liquid nitrogen was exhausted early into

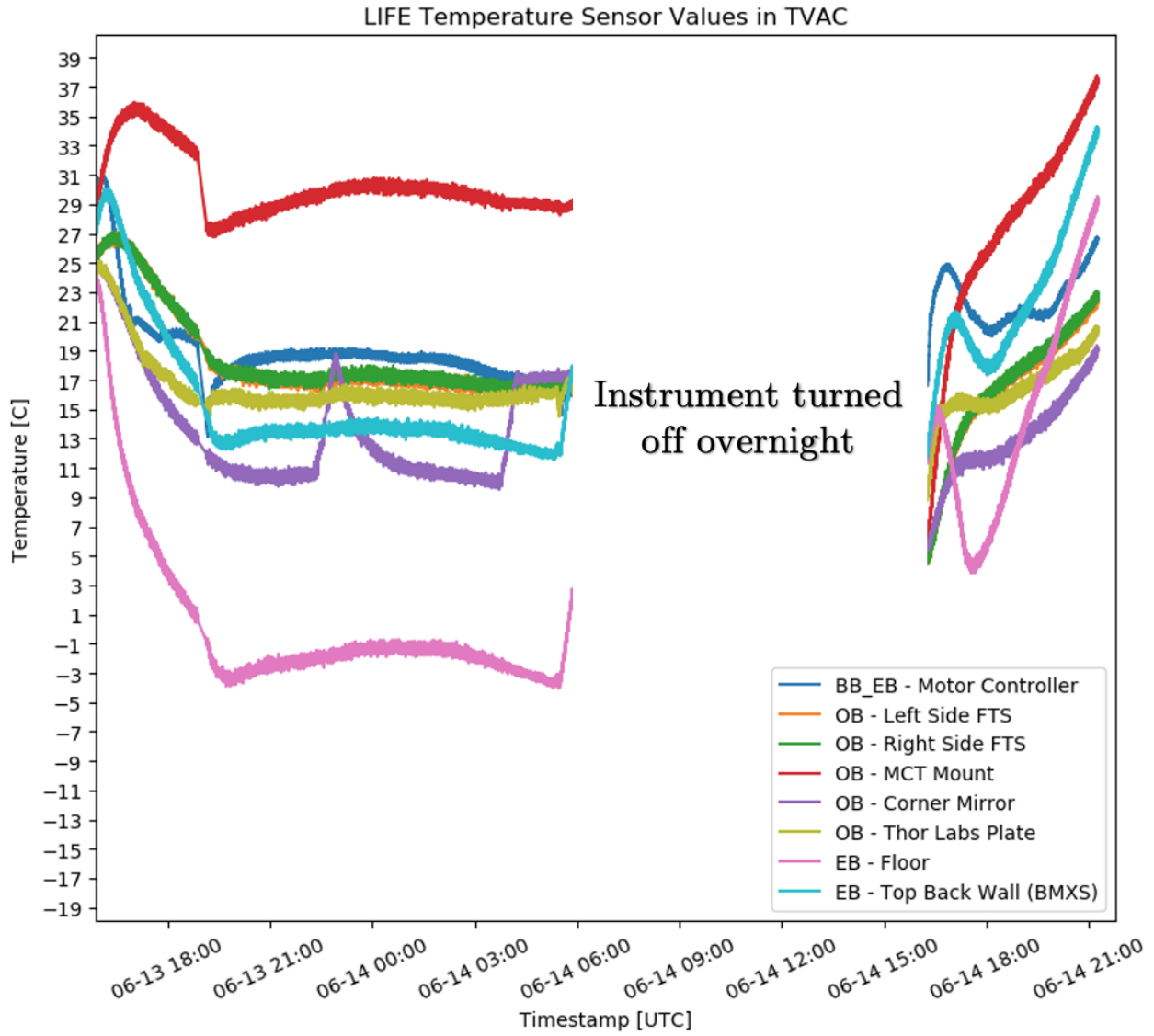


Figure 3.52: Temperature measurements throughout the second TVAC test.

the second day and cold temperature tests could not be completed. This test succeeded in verifying the thermal design works; the temperatures of core components, specifically the optics, stays in the required operating range, and very steady. Although the temperatures were within their required ranges however, temperatures were not quite what was expected from the thermal model. The results of the TVAC tests provided data for the improvement of the LIFE thermal model, removing assumptions and making the model more accurate. This is described in the next section.

3.6.3 Final Simulations

As the second TVAC test most accurately simulated what the instrument was expected to experience during flight, the thermal model was compared to these values. The largest difference between the TVAC test data and what was expected from the model was not the temperatures, but the heater power required to keep the instrument at those temperatures. The power supplied to the heaters was up to 40 W less than the expected power of 60 W for the electronics, and 20 W less for the Blackbody Electronics power. The Optics Box needed 10 W less than expected.

The reason behind this was determined to be the thermal resistance between the baseplate and the boxes. As described in Section 2.2.1, heat flow across a gap is very difficult to calculate. The error is so large that it was recommended by a consulted CSA expert to just determine this through tests, and apply what is learned to the model. That is exactly what happened with LIFE. In the pre-TVAC simulations, the joint connection between the baseplate and boxes is assumed to be bonded, or have a thermal resistance of 0. This was a large assumption that was expected to be wrong. Specifically, with an anodized surface, the thermal resistance will be high, as the roughness of anodization decreases the surface contact through which heat can flow. So, with a range of possible power values for the heaters from the current readings, and known temperatures, a number of iterations were completed of the thermal model to estimate a value for this thermal resistance. This was also done for other important thermal connections, such as the interfaces between the optical components (FTS, corner mirror, MCT) and the optics breadboard.

These tests used transient analysis, as the tests in the TVAC chamber were a finite length.

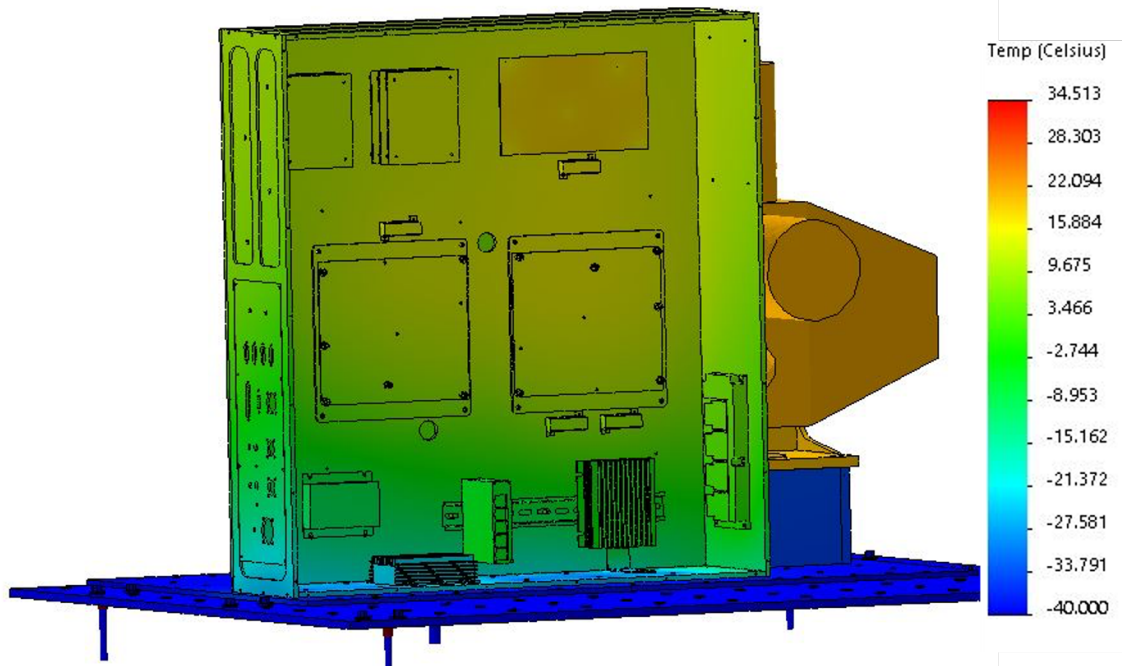
A time was chosen towards the end of the test to compare temperature values, which was well after the temperatures were steady. The temperatures of all internal temperature sensors at 700 minutes into the test are described in Table 3.4, these would try to be matched in the simulation.

After 22 iterations of different heater values and thermal resistances, a model was created wherein the heater powers were in the expected ranges from the current, and the critical temperatures were matched to within 1°C of what was seen in the tank. The thermal model for the final iteration is shown in Figure 3.53. A summary of the resulting temperatures, compared to what was seeing during the test, is provided in Table 3.4.

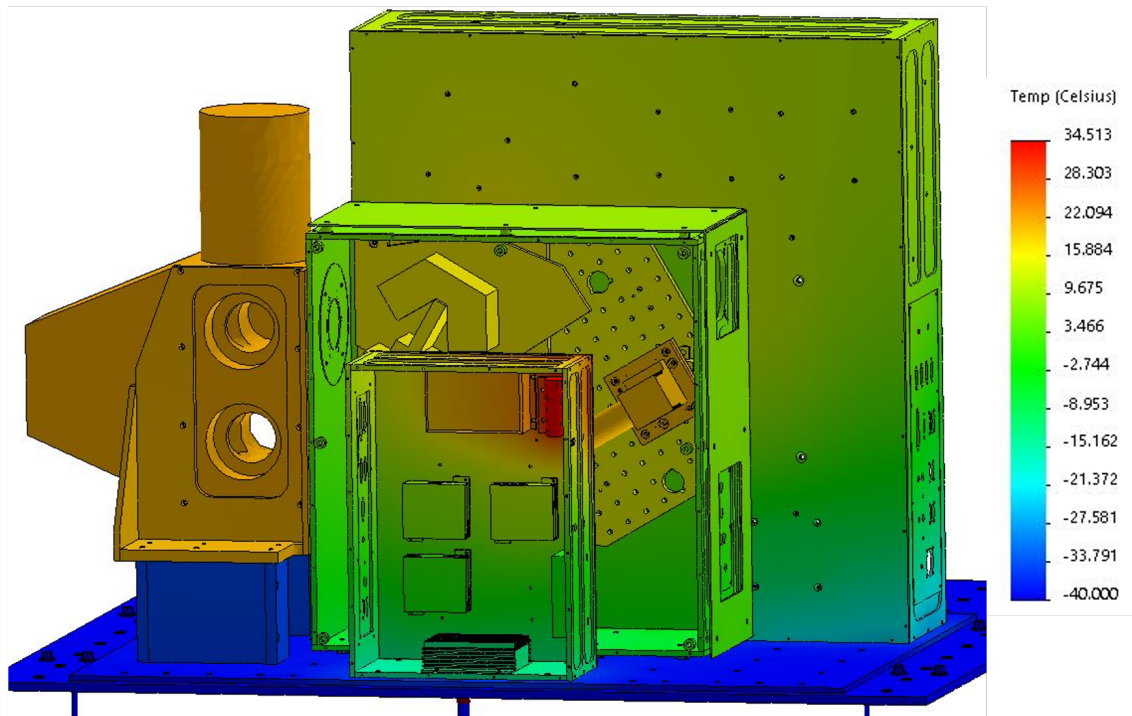
Sensor	Simulated Temperature (°C)	Actual Temperature (°C)
BB EBox - Floor	-13.5	-13.5
BB EBox - Motor Controller	17.7	17.6
Optics Box - FTS Left Side	16.7	16.7
Optics Box - FTS Right Side	16.6	16.6
Optics Box - MCT Mount	20.5	29.4
Optics Box - Corner Mirror	9.1	10.1
Optics Box - Thor Labs Plate	16.6	15.6
Optics Box - Floor	-7.3	-9.7
EBox - Floor	-2.3	-2.2
EBox - Top Back Wall	13.8	12.4

Table 3.4: Temperature sensor values 700 minutes into the updated SolidWorks simulation and TVAC test.

The final values used for this simulation are 5 W per heater in the Electronics Box (a total of 20 W), 49 W power for the heater in the Blackbody Electronics Box, and 10.6 W for the heater in the Optics Box. These all fell within the ranges expected by the currents. The final value for the thermal resistance was 0.16 W/mK, which is in the expected range for a compressed gap between two anodized aluminum panels. Throughout the test, the base temperature was set to -40°C (as the TVAC baseplate was), and the initial temperature was



(a) Final simulation of LIFE thermal model, based on updates from TVAC data, Electronics Box view.



(b) Final simulation of LIFE thermal model, based on updates from TVAC data, Optics Box view.

Figure 3.53: Front and rear view of the final LIFE model after updates to the thermal model based on the TVAC test data.

25°C for all components. One other aspect that required some iteration was the ambient temperature, as required for the radiation simulation input. For the TVAC test, this ambient temperature would be the temperature of the walls of the TVAC chamber, which was estimated to be 5°C (as these are not actively cooled, and not thermally connected to the liquid nitrogen cooled baseplate).

With updates to the simulation, most of the critical temperatures are within 1°C of the actual temperature, with some close as 0.1°C to the actual temperature. A notable value to point out, which is the largest difference between actual and simulated, is the MCT Mount sensor. This would turn out to be an error with a connection in the simulation, which was fixed after the flight for flight comparisons simulations, as was not an error with the simulation inputs. With a model of the thermal model instrument now updated and accurate, and the instrument successfully completing the thermal tests, the instrument was ready to fly in Timmins.

3.7 Summary

This chapter covers the largest aspect of this thesis, the creation of the thermal-mechanical model. An overview of the requirements for the model was given first, for the three major aspects of the instrument: The optical system, the electrical system, and the overall mechanical system. These requirements were taken from the known thermal ranges of instruments, taken from survivability constraints for flight from the CSA, or developed using knowledge of our system for the optics. An overview is then given of the thermal environment that will be faced, to help put these requirements and the design into perspective.

The next section of the chapter discussed the software used for the design, SolidWorks. A high-level explanation of the software was given as well how the simulations work at a core level, using Finite Element Analysis. FEA is described as it relates to the two types of simulations that were performed for the LIFE instrument, thermal and mechanical, and related these simulations back to the fundamental equations that explain thermal and mechanical phenomena.

The many versions of LIFE and its different components are described in Section 3.5.

After an overview of the third-party blackbody system, and the work done to prepare it for LIFE, each version of LIFE is described in detail. There were a total of six versions of LIFE, each with different versions of the core Optics Box and Electronics Box system designs. Each of these designs are described in terms of the components and the thought behind the designs. Thermal analysis, being a core part of the design, is also described in each version as it was developed. Finally, the final design chosen was Version 5, and a detailed design was created that included wiring diagrams and fasteners. A more detailed thermal analysis was done on this model to ensure that it would survive the atmospheric environment, before it was built and tested.

The final section here describes the construction and analysis completed prior to the Timmins flight campaign. A few images and a description of the build process is given, as well as some notes for the construction of future instruments. Tests were completed on the instrument once it was built to ensure survivability, by placing it in the TVAC chamber. The data collected here was used to improve the thermal simulation model, and once this was complete the instrument was ready for flight.

4 POST-FLIGHT ANALYSIS

4.1 Overview

This chapter discusses the post-flight analysis of the thermal-mechanical model of LIFE. In the first section, an overall summary of the stratospheric balloon flight campaign in Timmins, Ontario is presented, including work done while in Timmins and the overall results of the flight. The next section describes the mechanical results, in terms of how the mechanical design performed and some modifications for the future. The rest of the chapter discusses the creation of a full flight thermal profile of the instrument. Split into four subsections, different parts of the flight are examined in terms of the thermal results, and a thermal model is created to match these results. This will help to inform future instrument thermal models, as very little information on the flight environment is currently available. All post-flight analysis regarding the MCT Detector is presented in the next chapter.

4.2 Flight Campaign & Results

The campaign took place over three weeks in Timmins, Ontario, at the CSA/CNES high-altitude balloon base. The work required prior to flight included initial checks of the instrument, ensuring proper operation after transport. Once this was complete, the instrument was integrated onto the gondola. This required ensuring that it could be properly fastened to the gondola deck, and that it would operate properly while connected to the gondola power supplies and computers. An image of the instrument integrated into the gondola is presented in Figure 4.1.

The integration and checks all went well. The instrument operated properly both through initial tests and while connected to the gondola. With this completed, the instrument was

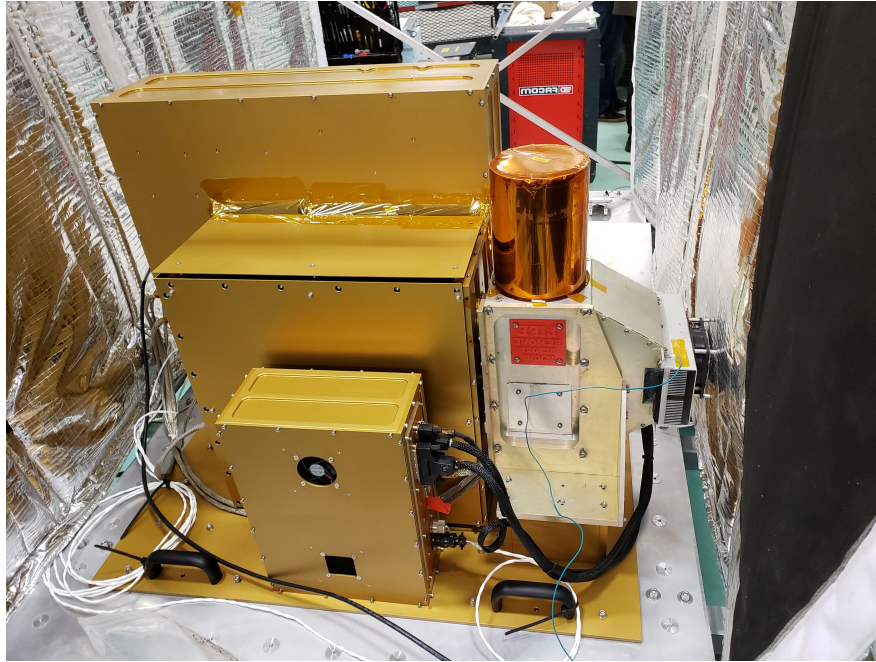


Figure 4.1: LIFE integrated into the CNES gondola.

ready to launch, and would wait until the weather was clear and the CSA was ready to launch. This occurred on August 31st. The instrument was loaded onto the gondola at 7pm, initial checks and boot up was completed, final closures and connections to the instrument were made, and the instrument launched at 10pm local time. An image of the instrument sitting on the gondola waiting for launch and the inflation of the gondola balloon is shown in Figure 4.2.

The instrument reached a float altitude of approximately 36 km at 1am. Measurements were taken throughout the ascent, but the science quality observations were made from stable float altitude. The instrument operated without issue through the entire float phase. At about 5:30am, the sun rose, and the instrument began to warm. Initially, the CSA had no plans to operate the instrument in daylight, with the gondola to be brought down prior to sunrise or shortly after. With this as the expected plan, LIFE was shutdown at around 6am. However, CNES was having trouble finding a proper landing location that was not close to any water, which lengthened the flight. As the flight was extended, LIFE was rebooted, so that more measurements could be taken and thermal data could be taken while the sun rose. The sun has no effect on the physics of the instrument, and as long as it is not directly looking at the sun the instrument can be operated at any time. The decision was made to operate



(a) LIFE on gondola, on launchpad prior to launch.



(b) The gondola balloon being inflated shortly before launch.

Figure 4.2: LIFE being prepared for launch.

the instrument until components reached their temperature operating limits. Normally, if sunlight was expected, this would not be as much of an issue. CNES, if the gondola will fly during the day, installs sun-shields to shade the instruments to minimize the effect of the sun, but as this was planned as only a night flight these were not added. Thus the sun shining directly on the instrument contributed significantly to the heating of the instrument. The flight continued well into the morning, only coming down shortly after noon. Thermal data and measurements were successfully taken for an extra 6 hours past sunrise. This provided more data to attempt to model what the instrument would see when the sun rose, as is described later in this chapter. The instrument landed safely in the early afternoon. An image of the instrument at its landing sight is shown in Figure 4.3.

The instrument was recovered and was brought back to base by the next morning, and the team left the base shortly afterwards. All images and measurements for the instrument were taken successfully, and thermal data of the instrument was successfully saved so that an accurate thermal model of the instrument based on this data could be created.



Figure 4.3: Gondola after landing.

4.3 Mechanical Results

Although the flight overall was successful, the landing did not go as planned. For all gondola flights, the landing is where the gondola has the greatest shock, with a force of typically around 10-15 g. This force is designed for and tested in the CSA mechanical verification spreadsheet, as discussed in Section 3.5.8. However, out of the planned three parachutes used during descent, only two opened properly. This caused two problems: one was that the gondola was descending much faster than was planned for. The second was that in addition to the descent speed, the gondola was falling at an angle, due to the three parachutes normally forming a triangle. Without the third, the weight was offset, and the edge of the gondola (towards the LIFE side) hit the ground first, rather than the bottom of the gondola which was cushioned for the landing. The gondola eventually hit the ground with a shock that saturated the on-board force sensors at 20 g.

This unplanned force did not cause any significant structural damage. Even though the mechanical interfaces were tested to 15 g, the safety factor helped the instrument survive over 20 g. However, there was some evidence of the impact. The largest was that the bolts holding the Electronics Box to the instrument baseplate were stretched out, meaning that



Figure 4.4: A gap between the Electronics Box and baseplate, due to bolt stretching caused by the shock of landing.

the interface was very close to breaking. This would have caused the LIFE instrument to be totally destroyed, as the crucial connections between the electronics in this box and the detector in the Optics Box would have been destroyed as well. An image of the result of the impact on this interface is shown in Figure 4.4.

This is one of the first things that needs to be fixed prior to LIFE being used again. However, this was not the only damage caused. When the instrument was taken back to the university lab from Timmins to perform post-flight tests, it was found that the detector could not reach the necessary measurement temperature of -198°C , only reaching -185°C . In addition, although images taken at -185°C are noisy but often usable, the images taken during these tests were much too noisy to be useful. There was an issue with the detector as a result of the landing impact. Through some data analysis on the noise during flight, and eventually removing the detector to send it to the manufacturer, it was discovered that the cold stop of the detector was now no longer attached to the Stirling cooler. Thus it was not being cooled properly and could not be used. There is a very high cost in repairing the

detector so that the instrument may be able to be used or modified for further missions, and it is unsure whether it will be fixed. As a result, no post-flight tests could be done to perform further verification and testing of the instrument.

4.4 Flight Temperature Model

After the flight was completed, the temperatures measured during flight were compared to the model. The most important aspect from the thermal-mechanical design was that all components stayed within the required temperature limits for the float part of the flight, when everything was operating as needed. However, the temperatures did not exactly match the measurements made pre-flight in the TVAC chamber, mainly because there are so many variables in high-altitude balloon flights. It is difficult to make an accurate model, even for just the simplest parts of the flight, because there are a number of variables that may effect the temperature, and next to none are documented or studied. For example, there is no information on how convection changes as altitude increases, especially at altitudes above the troposphere. There is no information on the precise amount of solar heating on an instrument that is dependent on altitude. A number of other questions also remain.

In this part of the thesis, a thermal model of LIFE was created for the entire balloon flight. This includes all phases, not just the float, which is the easiest and was modeled prior to flight. This model could then be a basis for future high-altitude balloon instruments to draw from, for thermal simulations and what to expect during a flight. This will help to ensure better survivability in future instruments.

Of course, there are too many variables to use this thermal model for all future instruments in entirety. It is meant to provide a starting point, and can help to plan for what to expect beyond ensuring that it will survive during the float phase. It can help to plan for the temperature decreases seen through the ascent, and help to design for better protection of the instrument should it be running in daylight. And through future missions, the model can be improved through new thermal data, until a thermal model with multiple sets of temperatures and improvements has been made can be used for future instruments with little changes. This will help to reduce the workload on future instruments and reduce costs

and engineering time.

Before going further into the temperature simulations, the flight temperature profile as a whole is examined in more detail. A plot of the flight temperatures measured by both the LIFE temperature sensors and a temperature sensor on-board the gondola baseplate is shown in Figure 4.5. The altitude of the gondola is also shown in this figure.

Described here at a high level, with more detail in subsequent sections, the different phases of the flight are seen here. The initial linear increase in temperature is from the instrument heating up as it sits running and waiting for launch on the launchpad. It increases quickly due to the lack of fans, which needed to be turned off and covered prior to flight. Immediately following launch at 2:00 UTC, the temperatures drop dramatically. This is the result of the cold region of the tropopause quickly cooling the instrument; on the night of the LIFE launch, the tropopause region was at approximately -50°C , which the gondola travelled through for almost half an hour. The instrument begins to warm once it reaches the warmer stratosphere. The gondola stabilizes just above 35km at roughly 5:00 UTC, where measurements are taken.

Through the main measurement phase of the flight, from 5:00 to 10:30 UTC, the temperatures are extremely stable. The required temperature drift is maintained through this time frame, only changing once the instrument begins to heat from the sunrise. All temperatures are also within required limits, with the optics staying just below 15°C and the electronics staying in the $5\text{-}10^{\circ}\text{C}$ range. This is slightly cooler than expected, which is due to the initially cold temperatures from the ascent. At the end of this phase, the sun begins to rise, and temperatures begin to rise as well. A small dip shows where the instrument was momentarily turned off, and the flight was expected to end. When it was turned back on, the instrument had cooled slightly, but began to rapidly warm due to the electronics and sunlight, until everything was finally turned off at 14:30 UTC.

The goal for the thermal model is to match the simulated temperatures to what is seen in Figure 4.5 through a series of iterations. For the purposes of the simulation, the flight was split into three major phases: The ascent through the troposphere and tropopause, the float period when the instrument is at altitude and taking measurements, and the sunrise, when the sun begins to shine on the instrument and have a major effect on the temperatures. Each of these simulations were completed separately, and the final temperatures of each

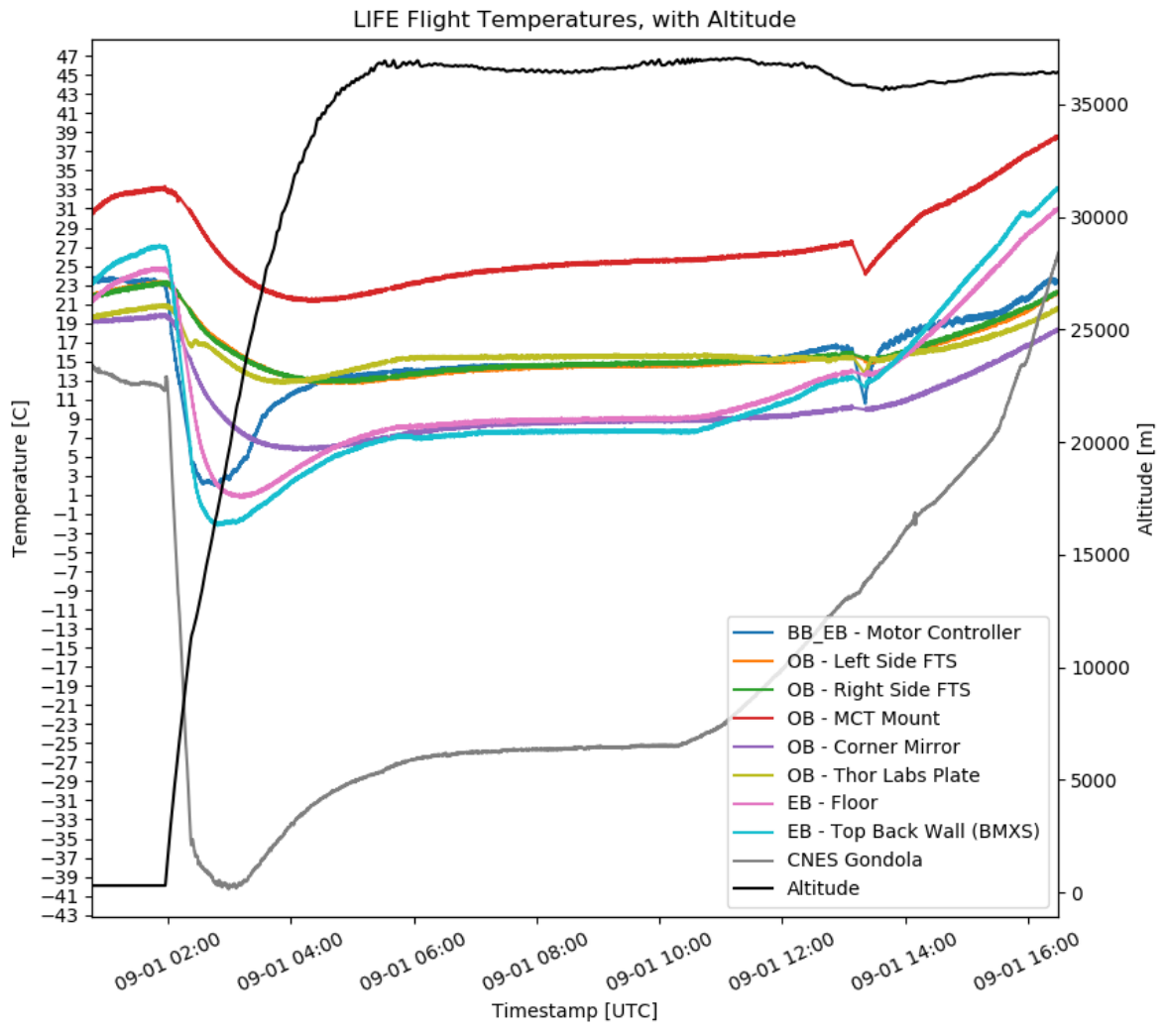


Figure 4.5: Temperatures over the course of the August/September 2019 Timmins flight.

simulation made to match precisely what was seen during flight. The final temperatures of a simulation would be used as the initial temperatures of the next simulation, so it was important that they were very close to the actual temperatures to avoid propagation errors. Once the final temperatures were met, the temperature curve of each section was compared to the temperature curve of the flight to ensure it fit.

4.4.1 Ascent

The first part of the flight was the ascent. This included the rise from ground level, up through the tropopause, and reaching the float level of 35km in the stratosphere. This was the most difficult part of the flight to simulate, due to having the most variables and the most significant change in temperatures. Convection only plays a role in this part of the flight, and is the biggest unknown that will need to be determined. Radiation, conduction, and forced convection as a result of the speed of the rising balloon gondola all need to be considered for this part of the simulation. As a result, it is likely the least accurate part of the entire thermal model, and also required the most iterations to model correctly.

Measured Temperatures

The simulation was split into two halves: The ascent up until the troposphere, and the ascent past the troposphere up to the stratosphere. The centre of this split is the temperature minimum for all components. The time of the launch was 2:00 UTC. The time until the temperature minimum, or when the gondola left the tropopause and began to warm up again, was approximately 3:00 UTC. The second part of the ascent, which ended when the gondola stabilized at the float altitude of 35km, was from 3:00 to 5:00 UTC. The temperature measurements of the entire ascent phase of the flight along with the altitude during this time is shown in Figure 4.6.

For the hour leading up until launch, the instrument is sitting on the launchpad, powered on and waiting; this is where the temperatures are slowly increasing. The most important part of this phase is the temperature drop shortly after launch. The cold air has the largest affect on the gondola baseplate, which drops to -40°C by the end of the tropopause, and overall it drops 50°C in as little as half an hour. This is the result of the cold air and the

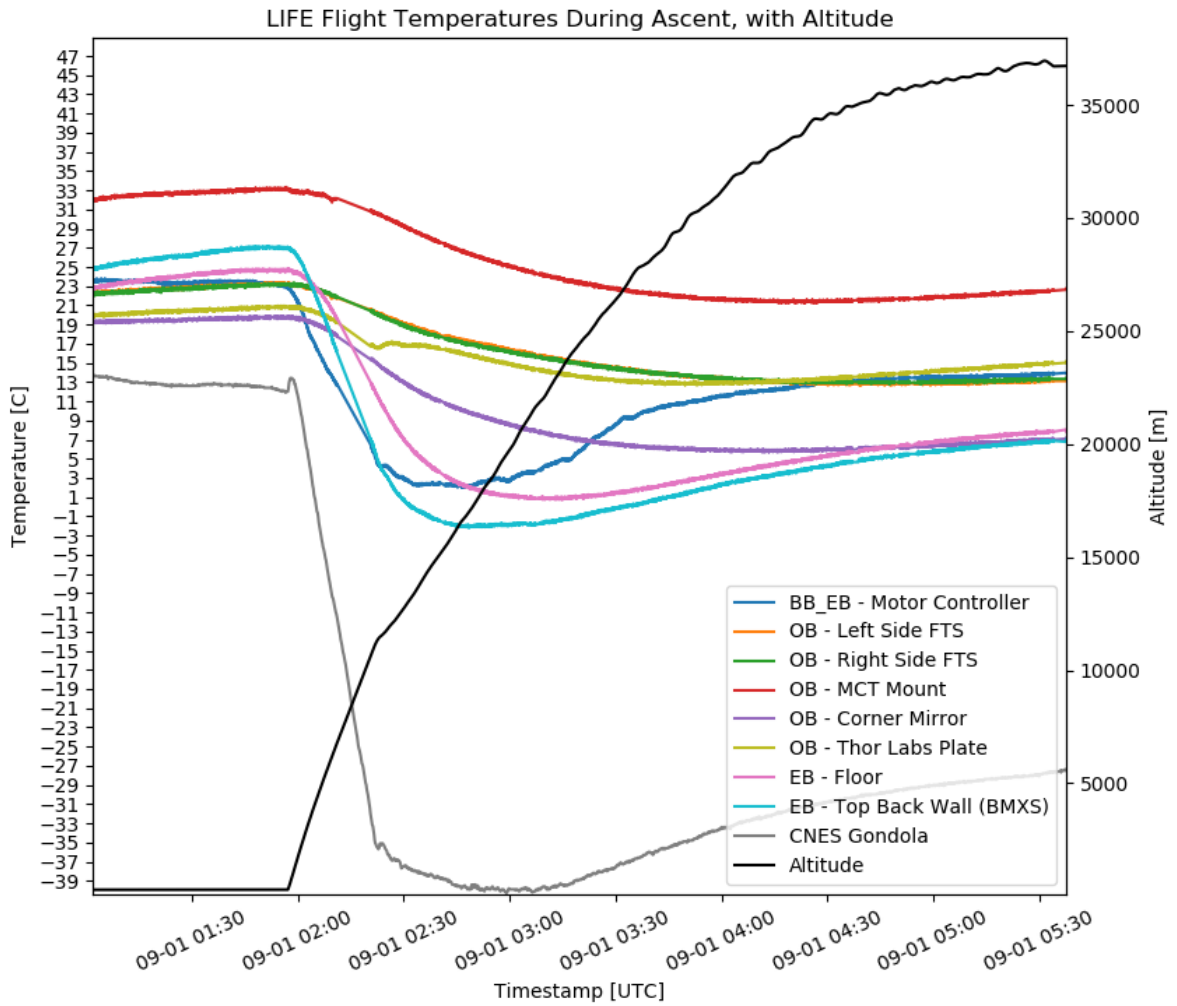


Figure 4.6: Flight temperatures through the ascent, the first three hours of the flight.

forced convection at these speeds and altitudes. As the LIFE temperature sensors are inside the boxes, the temperature changes are slightly delayed. The effects of the isolation of the Optics Box is evident here. The three sensors that show the largest and quickest temperature drop are in the Electronics Box and the Blackbody Electronics Box, which are not insulated from the baseplate. The lowest temperature seen anywhere on-board LIFE is just below 0°C, where the top of the Electronics Box dips due to the effect of convection on the largest open plate in the instrument. This was one of the few parts of the instrument that dropped outside of its required temperature range, but quickly warmed again from the heaters powering on, and no cold damage was sustained. Once the environmental temperature warmed and the heaters fully powered on, the temperatures quickly increased back to nominal.

All optics components show a much slower temperature decrease, as they are slowly cooled through the two layers of thermal insulation of the titanium spacers. Instead of dropping quickly and warming from the heaters, these components slowly decrease until they begin to stabilize from the warmer temperatures outside the box and the optics plate heater maintains the required temperatures inside the box. These temperatures were monitored closely through this phase of the flight to ensure temperatures were not dropping too quickly and the temperatures were being maintained towards the end of the ascent.

Simulations

With the ascent temperatures fully described and understood, a thermal model was then developed to attempt to match these temperatures. All thermal loads are described here, and the decisions and iterations behind each. Through 30 iterations for the first half of the ascent and another 31 for the second half, each thermal load was examined and tweaked. There are a total of 41 thermal loads in these simulations.

An important and difficult aspect of this first stage were the initial temperatures. Because the instrument had been running on the launchpad for an hour prior to launch, different components were at different temperatures as a result of the electronics. For example, the MCT detector dumps a large amount of heat as it cools, and this was sitting at above 30°C as the instrument was launched. In a SolidWorks thermal simulation, it is very difficult to choose initial temperatures for different components. Most often, the entire instrument has

one initial temperature, and if not then each component of the entire assembly must have its own initial temperature. In the LIFE model, this is upwards of 1000 components. One of the motivations for creating the ascent temperature model was to provide accurate initial temperatures for the float component of the flight without having to choose each of these separate initial temperatures. To avoid having to simulate the instrument sitting on the launchpad to get these initial temperatures, an average of the core component temperatures was taken, which was 23°C. This temperature was then applied to all components.

Conduction is the easiest heat transfer property to model, as the environment has no effect, unlike radiation or convection. Discussed previously in Section 3.6.3, the biggest unknown with conduction is the thermal conductivity across mechanical interfaces. A large aspect of the TVAC simulations and thermal comparisons were determining the actual values for these conductivities. Through these tests the conductivity for the boxes to the baseplate (two anodized surfaces) was found to be 0.16 W/m²K, and the conductivity for the optics components to their mounts, and their mounts to the baseplate (anodized to bare aluminum surfaces), was 0.20 W/m²K. These conductivities were not changed for the flight, and are used in all flight simulations.

Radiation from various surfaces of LIFE is a large problem in the simulations. To be able to simulate radiation, three values are needed: The view factor to other surfaces, the emissivity of the surface, and the temperature of nearby surfaces. The emissivity is the most well known property of these three values, and does not need to be tweaked. The three most common materials and surfaces all have well known emissivities: Anodized aluminum, which is the majority of the box parts as well as the optics breadboard, has an emissivity of 0.77. For circuit boards, the emissivity of silicon is 0.6. Bare aluminum, such as outer surfaces of the blackbody assembly, has an emissivity of 0.05.

The other two properties needed for radiation are much more difficult to determine. However, the view factor was slightly easier as it stayed constant through all simulations, so once good values were found in the initial ascent phase simulations they did not need to be changed again. As described in Section 2.2.1, the view factor can be calculated automatically through the simulations, but due to the complexity of the view factor integral equation, it dramatically increases the solve time. It is quicker if the values are estimated and entered

manually. Each radiative surface must be assigned a view factor to another surface at a certain temperature, and the view factor is a number representing the percentage of the surface that can be seen, from 0 to 0.99. Some of these estimations were simple, such as the outer surfaces of the boxes to the inner gondola walls. As there was nothing obstructing the view between these two surfaces, they would have a high view factor, above 0.9. Similar estimations could be made between the electronics surfaces in the Electronics Box to the box wall.

However, many surfaces proved more difficult. For example, a difficult surface to estimate was the optics breadboard. Different parts of the breadboard are in view of different components, such as the Optics Box wall, the FTS, or the detector. The best estimation was to choose the component that had the highest view factor, which for the breadboard would be the wall of the Optics Box. Similar decisions needed to be made for interfaces between box walls, and the inner surfaces of boxes where electronics are mounted.

The most variable component of the radiative heat loads was the ambient temperature. For all previous tests, such as the TVAC and initial test simulations, these temperatures were constant, as the environmental constraint temperatures were held constant. However, with the rapidly changing environment for the ascent, the ambient temperatures also rapidly change. Thus, a temperature curve must be created and input into SolidWorks. This had to be done for all major components, and the curve was approximately modelled after what was seen during flight, and the known temperature of the atmosphere at increasing altitudes. This could be accomplished easiest for the outer surfaces of the instrument, especially those that viewed the atmosphere, as this temperature was well known. More complex were the outer surfaces of the instrument that viewed the insulated walls of the gondola, which were a reflective insulation material which would have different temperature effects. The ambient temperatures for interior components and surfaces needed to be chosen based on both measured flight temperatures and what the temperatures were from previous iterations of the simulations. One of the most difficult parts of choosing these temperatures was that if the ambient temperature was changed, to reflect a temperature change from the latest version of the iteration, it could have rippling effects causing more temperature changes in future iterations. In short, changing the ambient temperature of one part to reflect another could

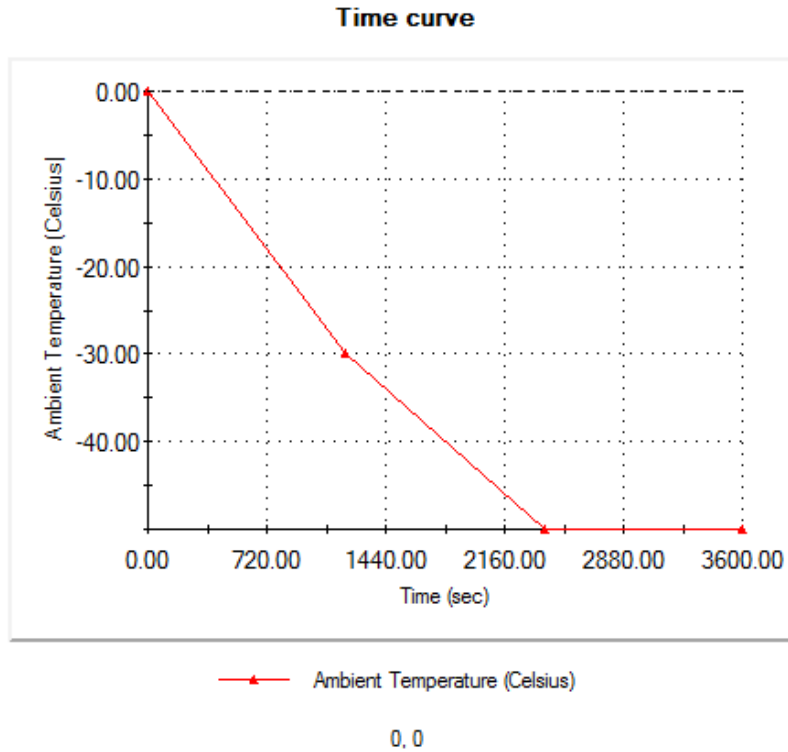


Figure 4.7: An example of creating the ambient temperature curve for the radiation of a component, specifically for the top surfaces of the boxes for the first half of the ascent.

change the ambient temperature of that component, and it would need to be updated again for the next iteration. This is one reason why so many iterations were necessary. An example ambient temperature curve is shown in Figure 4.7, for the first hour of the ascent for the external box surfaces. A curve like this is created for almost every radiating component in the model.

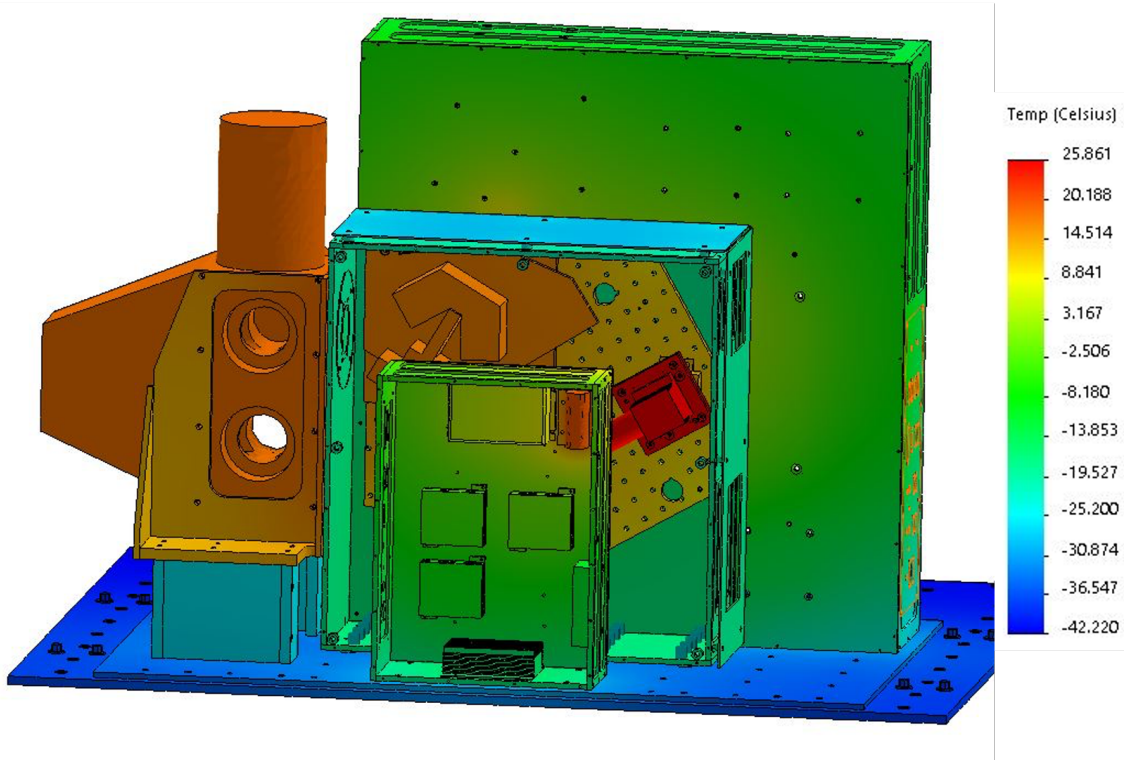
Finally, the last remaining and likely most difficult heat load is convection. This is the most complex and hardest part to model because it has two unknown features, that both change with time. The first is the convection coefficient, i.e. how quickly heat is flowing to or from the surface as a result of the convection. It is extremely difficult to calculate, and even if a value is calculated the error is much too large to be able to use confidently. In addition to the convection coefficient, the ambient temperature must also be varied throughout the simulation, in the same way as it is for radiation. This value was at least partially known, through the temperature sensors from flight and from the

known temperatures of the atmosphere. The convection coefficient however would be roughly estimated and changed numerous times.

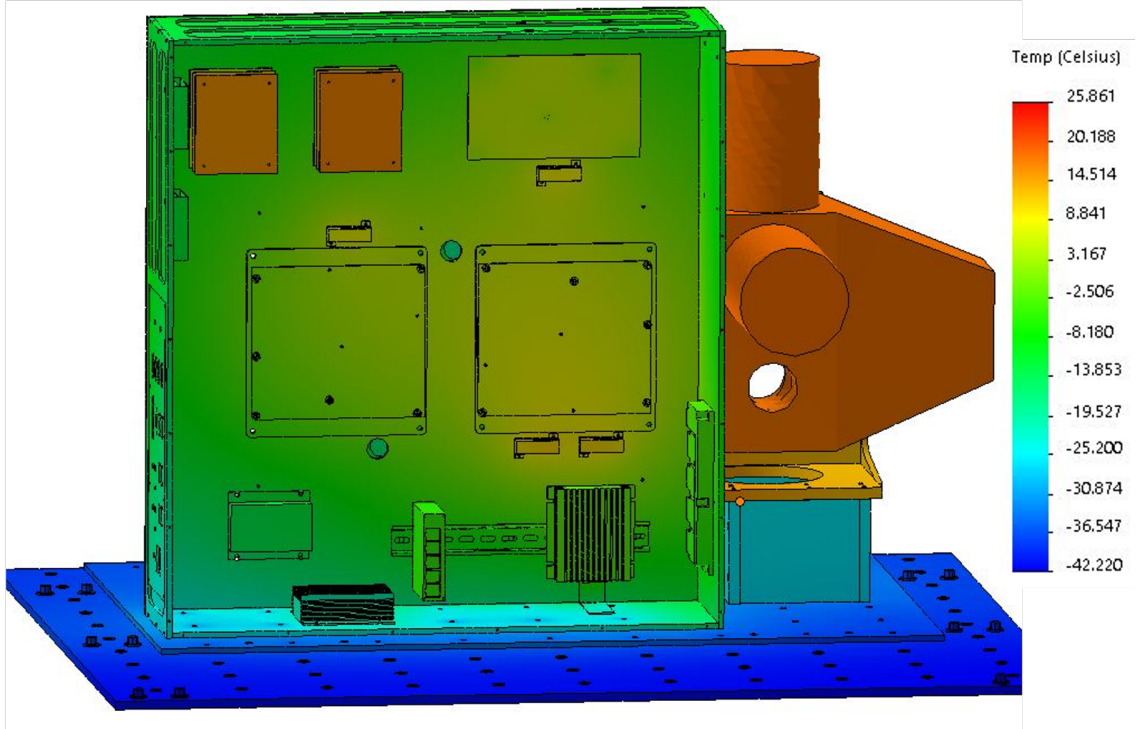
The convection coefficient of air can be anywhere from 1-10 W/m²K for free flowing air, and anywhere from 1-100 W/m²K for forced convection. It also drastically changes with pressure, as there is less density of fluid to be able to transfer heat. As discussed in Section 2.2.1, there are very few studies of the effect of pressure on convection, and only for the purposes of high heat industrial processes. As there was no information for a high-altitude balloon scenario, information was taken from the forced convection scenario, and steadily decreasing as a result of the decreasing pressure. For the exterior parts of the instrument, forced convection would be the most prevalent. However, as the gondola was mostly covered, the forced convection would not be overly strong. An estimation of 10 W/m²K was made as an initial value, and steadily decreasing to zero by the end of the first half of the ascent. The pressure past the tropopause is estimated to be too low for convection to have any effect past this point. Convection was estimated inside the boxes to be between 1-5 W/m²K, as the enclosures would limit any forced convection due to moving air from the ascent. Overall, these convection loads only played a part in the first part of the ascent, with the exception of some small convection on the bigger surfaces for the second part of the ascent. The ambient temperatures were kept the same or similar as the values used for radiation, to make the iterations simpler and for continuity across all components.

There are too many components and loads to be able to accurately describe all values chosen and all iterations here. A list of all loads, components and plots can be automatically downloaded from SolidWorks after a simulation, and this is added as an appendix for the final simulation, in Appendix A. After a total of 61 iterations, the final temperature models for the end of the first phase of the ascent and the end of the second phase of the ascent are shown in Figures 4.8 and 4.9, respectively. A plot showing the simulated temperature curves of the thermal model, measured at the same locations as the on-board temperature sensors, is shown in Figure 4.10 as a verification of the model.

From the plot in Figure 4.10, the model now fits the ascent very well, with the largest error being 1°C. Errors in the first part of the ascent are due to the generalized initial temperatures, but they begin to match the actual temperatures early in the ascent. It was

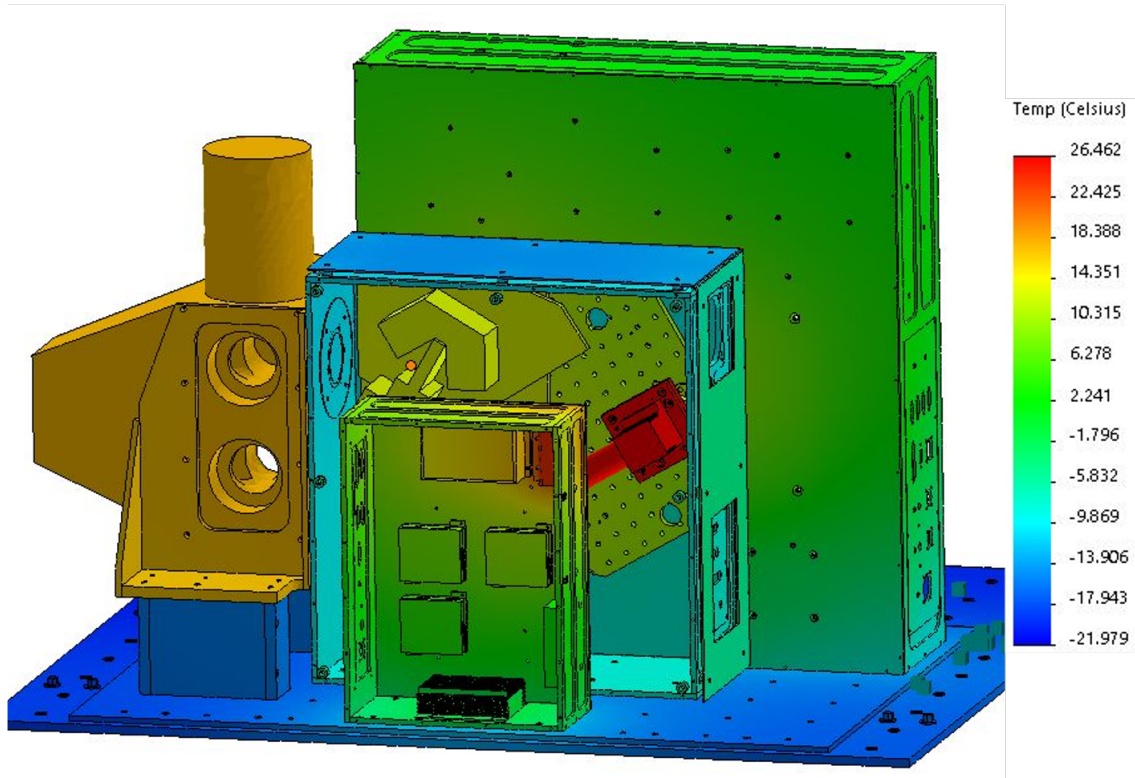


(a) Thermal model of LIFE instrument after the first hour of flight, Blackbody Electronics Box view.

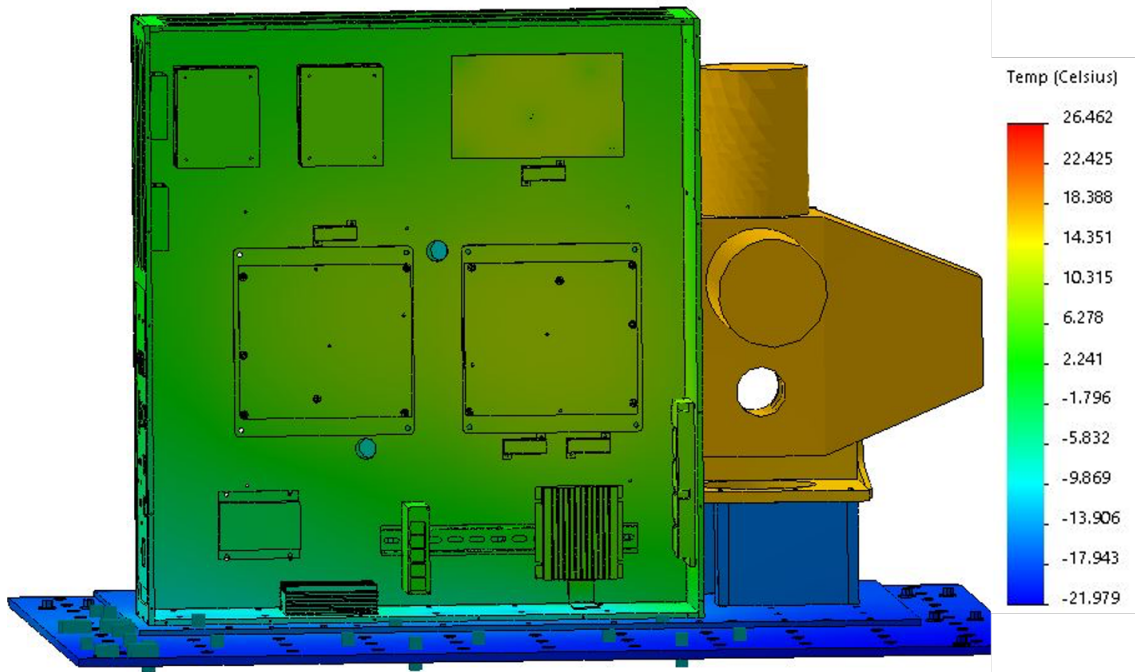


(b) Thermal model of LIFE instrument after the first hour of flight, Electronics Box view.

Figure 4.8: LIFE thermal model following first half of the ascent.



(a) Thermal model of LIFE instrument at the end of the ascent, Blackbody Electronics Box view.



(b) Thermal model of LIFE instrument at the end of the ascent, Electronics Box view.

Figure 4.9: LIFE thermal model, as the instrument is reaching the float altitude.

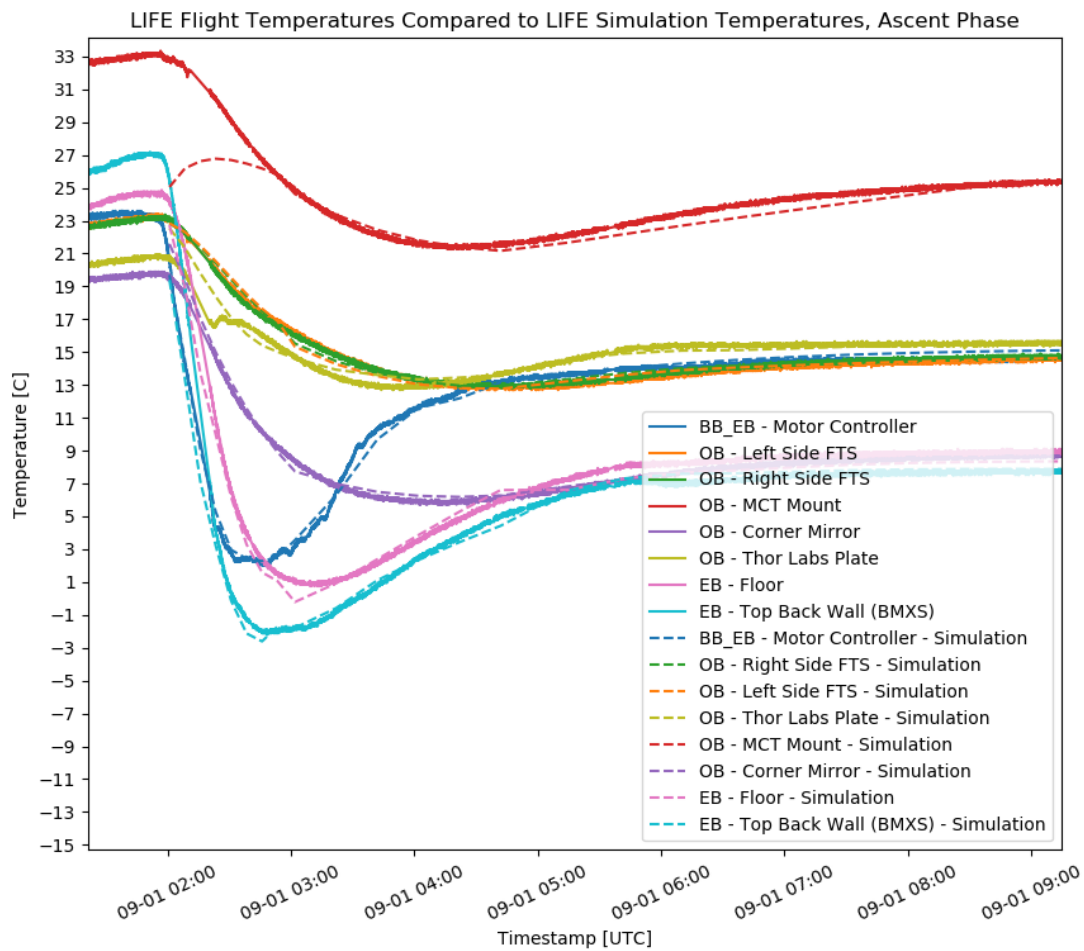


Figure 4.10: Flight temperatures through the ascent, compared to the simulated temperature curves after model updates. The corresponding actual and simulated temperature data is the same colour, with the simulated data shown dashed.

ensured that the temperatures were as close as possible to the actual temperatures at the end of the simulation, so the initial temperatures of the next phase are as close as possible. The error between actual and simulated temperatures for the end of the ascent are within 0.2°C for the critical components, which is well within the goal of 1°C.

4.4.2 Float

The next phase of flight was the *float* phase, or the phase where the instrument stayed steady at 36km altitude, operated nominally and took measurements. This was the simplest part of the flight to simulate, as the environmental effects were constant throughout this stage, and convection no longer played a role. Some transient temperatures are still used for some ambient radiation temperatures, but for the most part all heat loads stay steady. This was also the part of the flight that was simulated in the TVAC chamber, and as a result no issues were expected. This stage continues until the sun rises.

Measured Temperatures

The beginning of this phase of the flight was when the ascent was officially over, and the gondola had stabilized at the required altitude. This occurred at 5:00 UTC. The sun rose just after 10:00 UTC, and began to have an affect around 10:30 UTC. When the solar flux needed to be included, a new simulation was created. This was characterized as the *sunrise* phase of the flight, and is described later. The temperature measurements of the float phase, along with the gondola altitude, are shown in Figure 4.11.

The temperatures fully stabilized around 6:00 UTC. After this point, the temperatures remain very stable, until the gondola deck begins to heat at around 10:30 UTC. The warmest component was the MCT detector mount, which was expected as the detector was dumping heat to its surroundings. All optics were kept within a couple degrees, which is ideal. The double isolation of this plate helped to keep the temperatures constant across the entire plate, which will help to remove self-emission from the resulting data. In addition, the temperature drift requirement is met; over the course of almost 6 hours, the critical optical temperatures of the corner mirror and FTS changed less than half a degree. Thus there is no problems seen in any of the Optics Box temperatures, and it ran nominally for this stage.

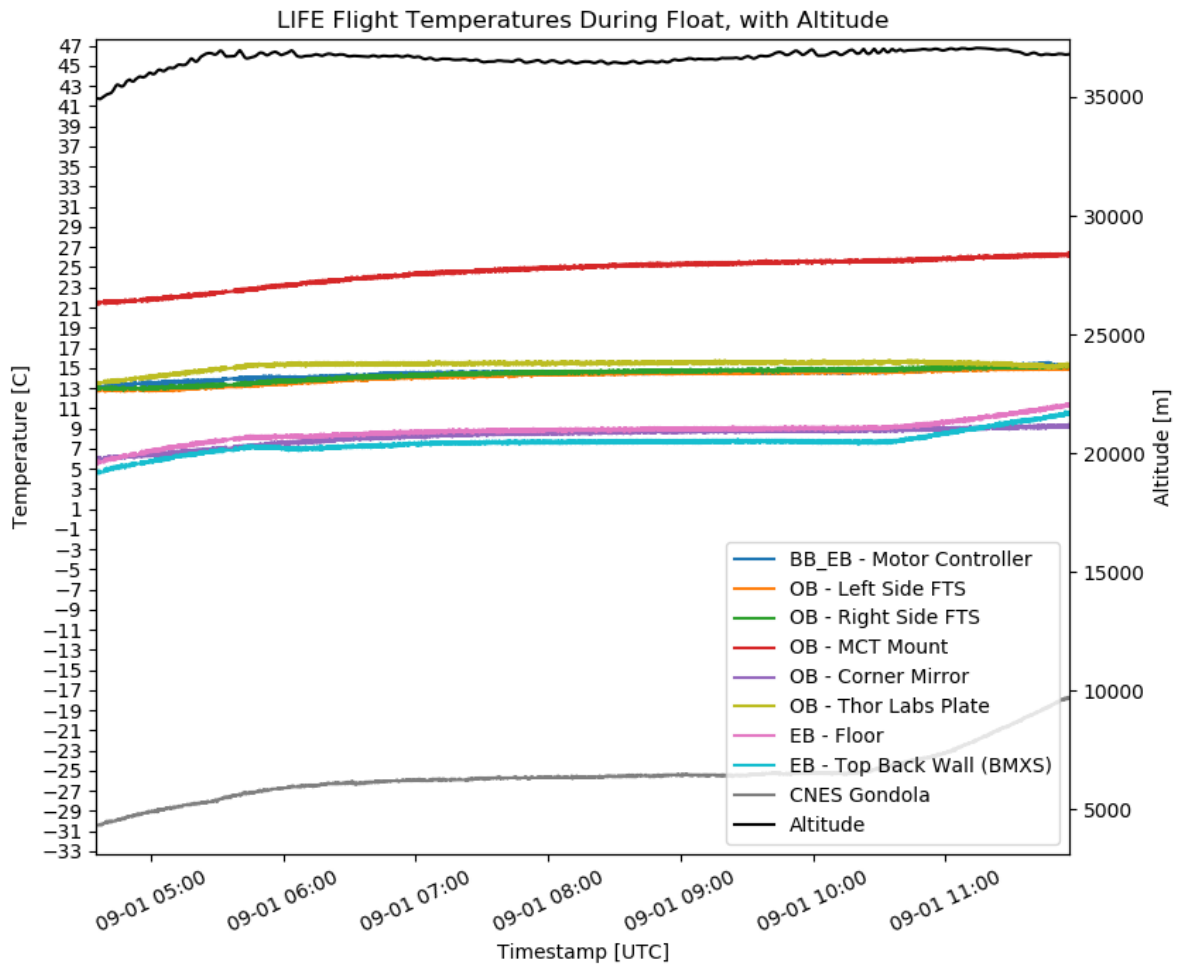


Figure 4.11: Flight temperatures through the float phase, five and a half hours where most measurements were taken.

The Electronics Box temperatures were cooler than expected. This was due to the initial temperatures for this stage of the flight; the temperature shock of the ascent had a larger effect than was expected. Also, in comparison to the Optics Box, there is less insulation and is larger; as a result, this box would be cooled faster through both convection across the back plate and conduction in the baseplate. However, when the heaters powered on and the instrument reached the warmer stratosphere, the temperatures steadied. Something to note was the temperature setpoint of the temperature controllers was higher than the actual temperatures, above 10°C. Through most of the flight, the temperatures were slightly below this. It was found that the setpoint of the temperature controller drifted, and as a result the amount of power sent to the heaters in the Electronics Box was lower than needed. The electronics temperature requirements were still met, but if this had happened to the temperature controller for the Optics Box, more serious issues could have occurred. A correction for this issue needs to be researched for future instruments, to ensure that temperatures stay nominal. The gondola baseplate temperature of roughly -27°C was in the range of simulated tests, and is good to know for future instrument simulations.

Simulation

With only conduction and radiation to include in the simulation, and with a steadier external environment, the simulations for this phase would be simpler. A total of 17 iterations were required to produce a model accurate to what was seen during flight. This was partly due to the initial temperatures from the previous simulation, which allowed an exact starting point for this simulation, following very precise initial temperatures compared to the flight. The conductive properties for this simulation were also all kept the same from what was determined from the TVAC tests and the ascent tests.

Much of the work of the radiation was already finished as well. The view factors were determined from previous simulations, and to maintain continuity between the simulations could not be changed. The only other value that needed to be determined was the ambient temperature. Due to the constant temperatures of both the instrument and the environment, they could be kept the same for the entire simulation, instead of attempting to determine a time curve. This made the iterations and determining the appropriate temperatures much

easier. The majority of the ambient temperatures were taken from what was seen during the flight.

With no convection to be determined, the only other aspect of the model that could be changed apart from the ambient temperatures was the power of the heaters. These were chosen, as with the TVAC test, from the measured instrument currents. More discussion into this is given in the full model discussion, in Section 4.4.4. As with the ascent simulations, after a number of iterations, a thermal model was created that very closely matched the flight temperatures. Images of the final simulation are shown in Figure 4.12, and a comparison of the flight temperature curve to the simulated temperature curve is shown in Figure 4.13.

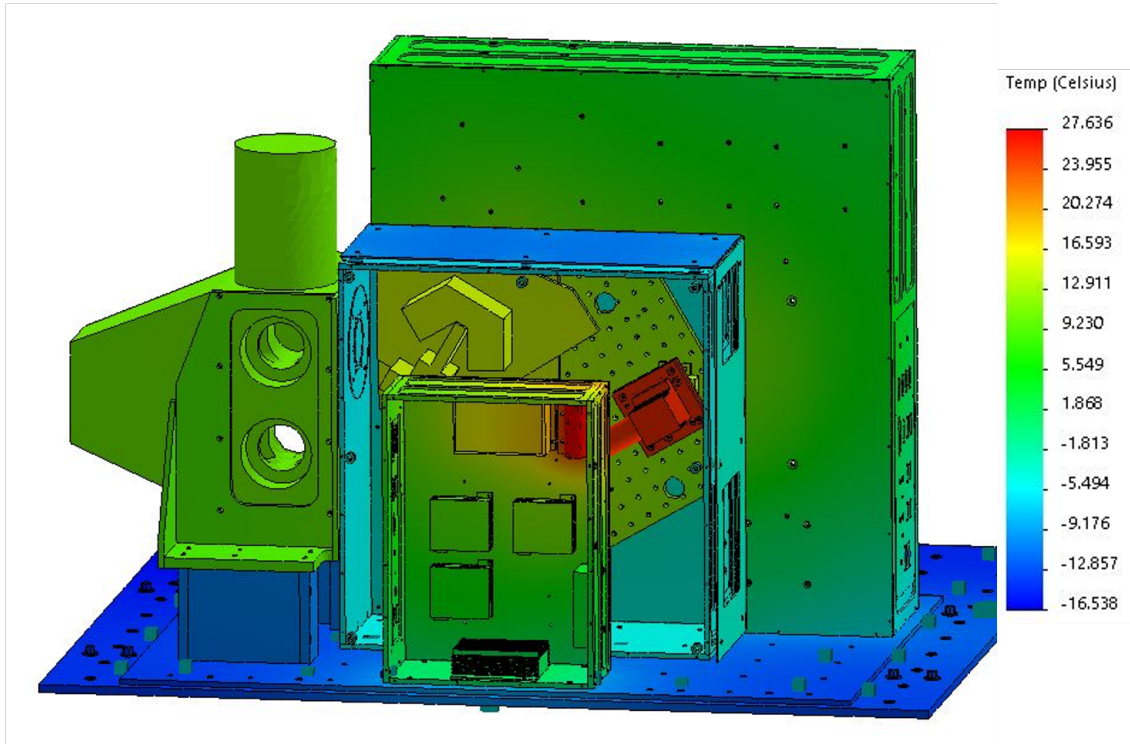
In Figure 4.13 the model now matches the actual temperatures very well. All temperatures match with a maximum error of 1°C, and the error on critical components less than 0.2°C. Once again, the final temperatures of this stage were very carefully simulated to match the actual temperatures as closely as possible, so the initial temperatures of the sunrise simulation match as closely as possible. Thermal loads for this simulation as well as the iterated thermal values can be found in the appendix.

4.4.3 Sunrise

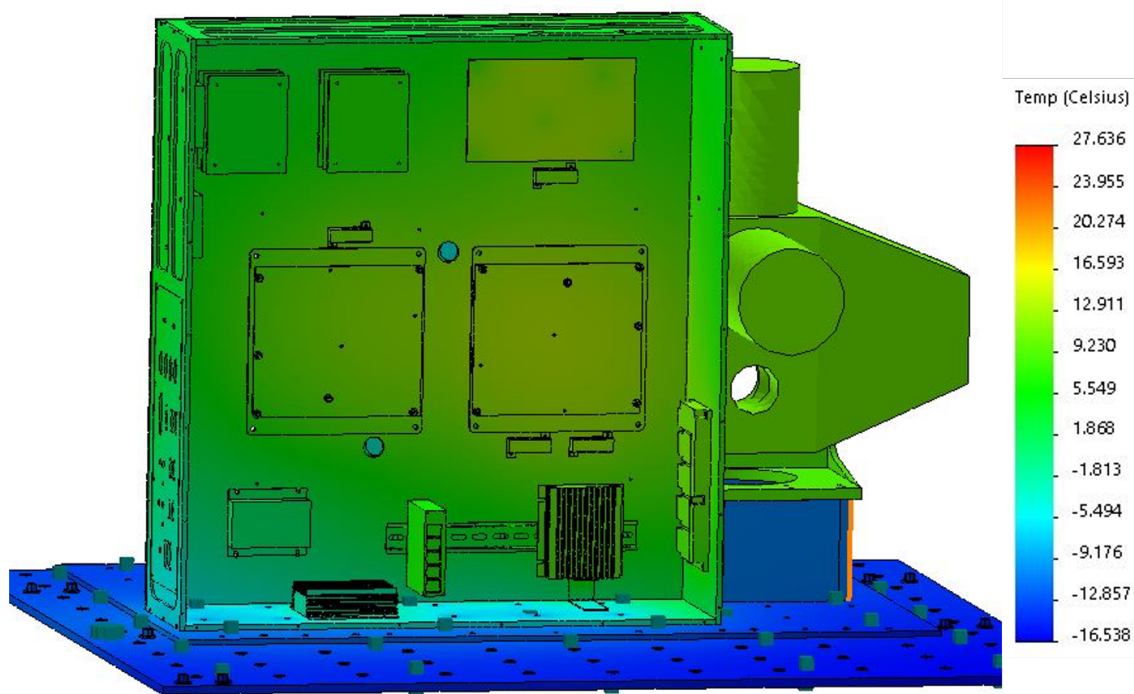
The final part of the flight, known as the *sunrise* stage, took place from 10:30 UTC to when the instrument was turned off prior to the descent, at 14:30 UTC. As mentioned previously this stage was not expected to occur, however there was difficulty in finding a landing zone for the gondola and the descent was delayed. While the instrument was originally planned to be turned off, it was decided that this was an opportunity to see how the instrument operated thermally in the sunlight. As there was time to create the thermal model for the sunlight and data was saved, this could be added to the atmospheric instrument thermal model.

Measured Temperatures

This stage of flight began as soon as temperatures began to increase after sunrise. They steadily rose throughout the remainder of the flight. While temperatures would be expected to begin levelling out again at some point, it is not surprising that the temperatures increased so quickly. The sun at high altitudes has a dramatic thermal effect, and no fans in the



(a) Thermal model of LIFE instrument at the end of the float phase, Blackbody Electronics Box view.



(b) Thermal model of LIFE instrument at the end of the float phase, Electronics Box view.

Figure 4.12: LIFE thermal model at the end of the nominal float stage of the flight.

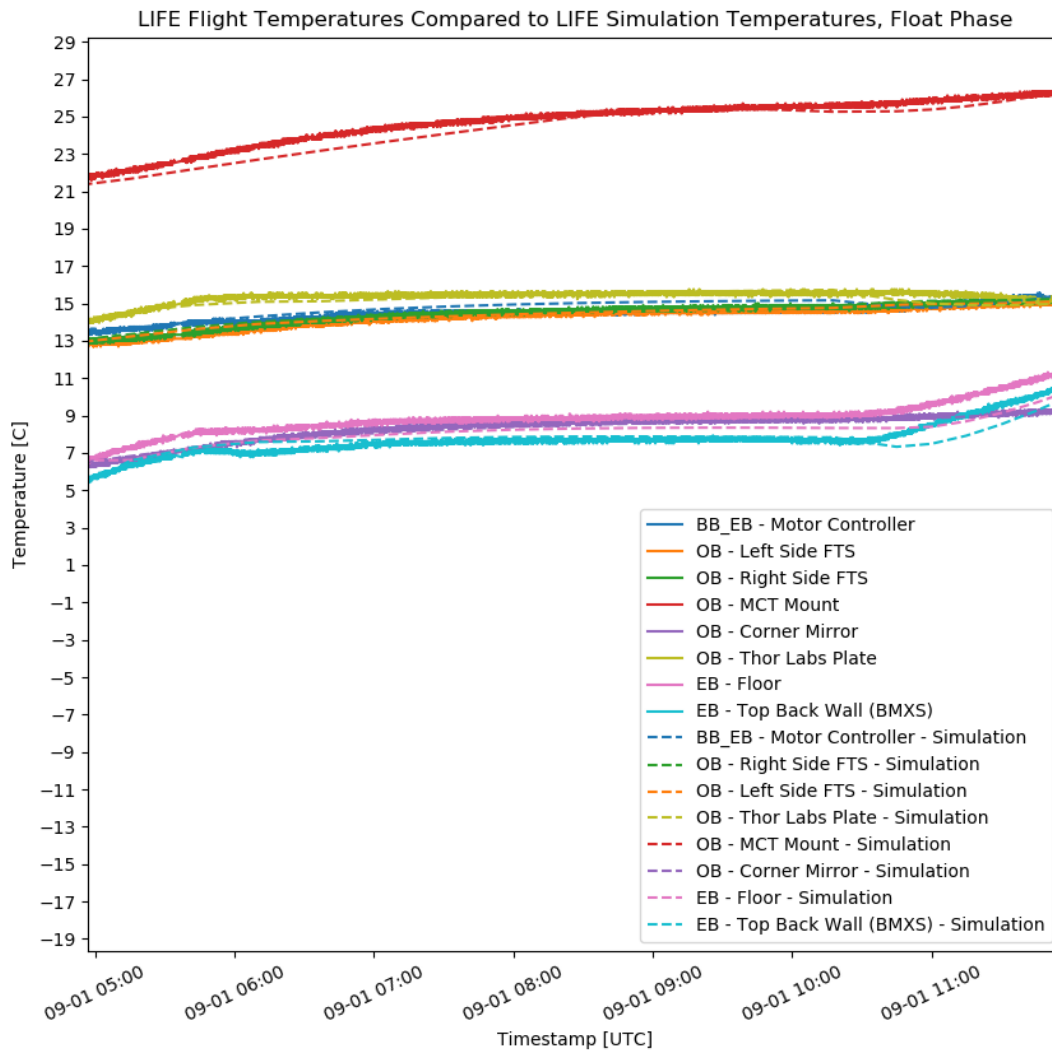


Figure 4.13: Flight temperatures during the float phase, compared to the simulated temperature curves after model updates. The corresponding actual and simulated temperature data is the same colour, with the simulated data shown dashed.

instrument were operating. There were also no vents anywhere either, as these were all enclosed to prevent any damage or intake to the inside of the boxes during the ascent. As a result the electronics steadily increased in temperature until they began to reach maximum allowable temperatures, and the instrument was turned off. A plot of these temperatures for this stage is shown in Figure 4.4.4.

The first aspect of the figure to point out is the drop around 13:00 UTC. This was due to an initial shutoff of the instrument, when the descent was expected to begin. When it was determined that the flight would continue for at least another hour after, the instrument was turned back on to take more images as well as to gather temperature data. However this drop does show the effect of turning off the electronics, and the amount of power that they generate. Most temperatures dropped by at least 2°C in just a few minutes. When power was restored the temperatures increased again quickly.

As with the previous stages of the flight, there is a large difference in behaviour between the electronics boxes and the Optics Box. With the sun shining directly on the rear plate of the Electronics Box, temperatures climbed very quickly in the last few hours of flight. However, even with the same sun shining on the Optics Box, the temperatures remained very steady until the last few hours. This shows that the outer radiation plates were operating as expected; while the outer plate was absorbing the flux of the sun, very little of that heat was being transferred to the inner box, and then to the optics. Only after the outer box was heated for a considerable amount of time did the effect of sun begin to show on the interior components. This shows that if the instrument was expected to operate in daylight, the addition of similar radiation plates to sensitive areas of other boxes (the top of the Electronics Box for example, where the temperature-sensitive BMXS board is mounted) would allow the instrument to be used without issue. In addition it is noted that for most daylight flights extra shielding is used over the gondola to mitigate sun-exposure. This may have helped maintain the LIFE temperatures in their required range even with no other changes to the instrument. Finally, the temperature of the gondola baseplate is noted; this shows how quickly the temperature of the gondola itself rose, and that the rise in temperature of LIFE was expected.

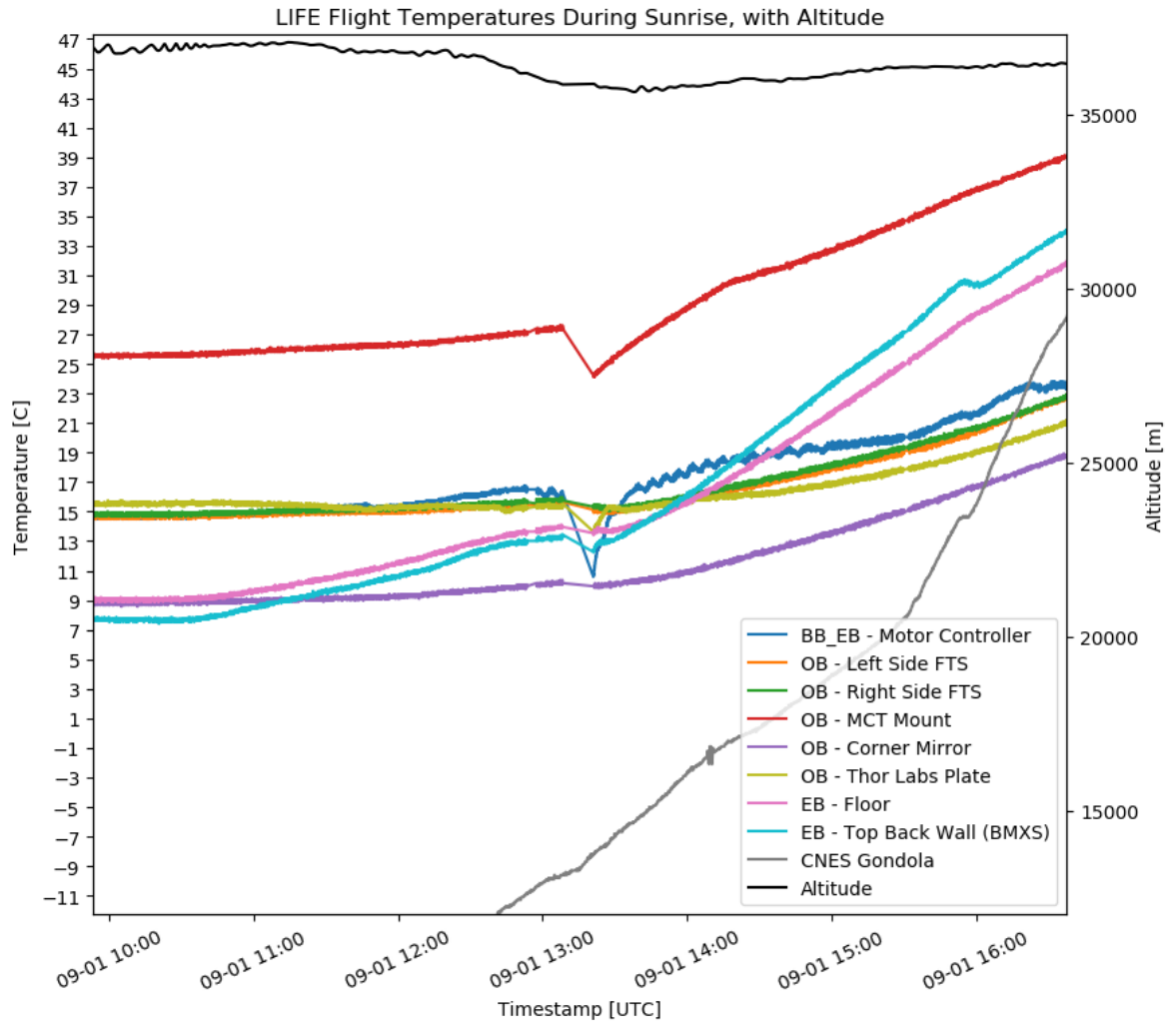


Figure 4.14: Flight temperatures as the sun rose and shone on the instrument, up until the end of the flight.

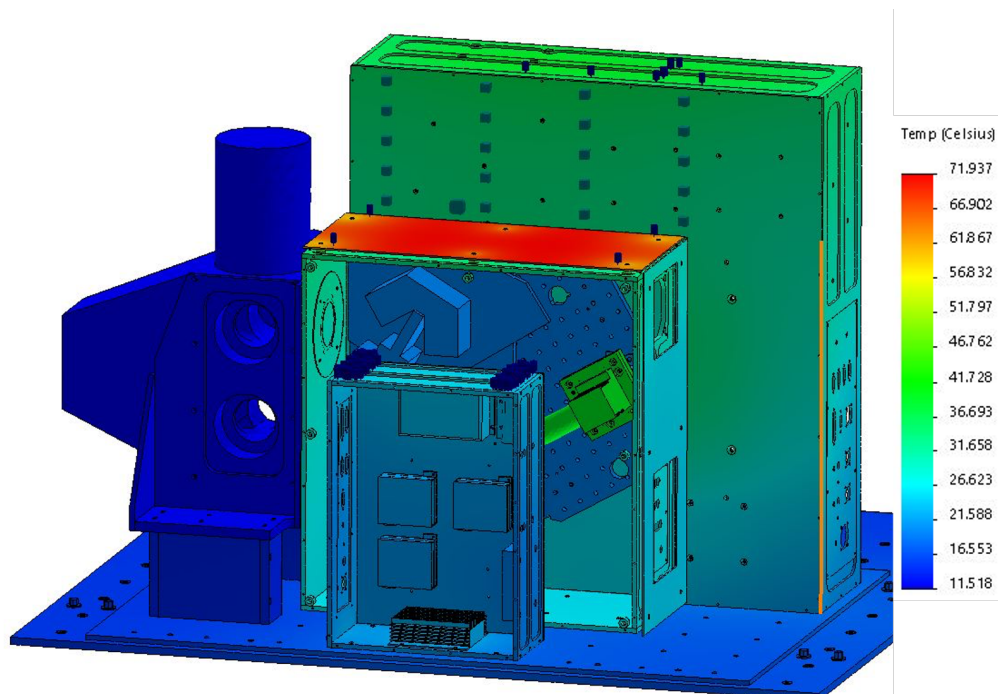
Simulation

This simulation does not have the quick changes in temperature and environment of the ascent, nor does it have convection. However the environment is not nearly as steady as the float portion of the flight. Most importantly, the effect of the sun must be included in this simulation. As with the float, the conductive properties and initial temperatures are already well known. The main properties that must be iterated through for the final stage is the solar flux effect and the ambient temperature of the radiation.

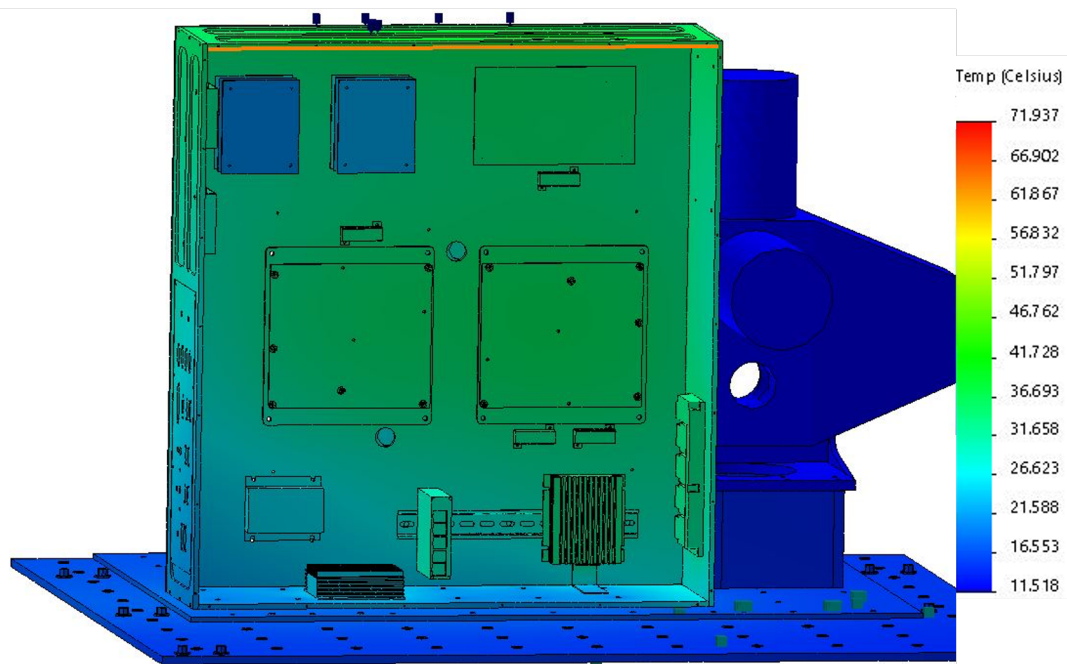
The heat flux from the sun was more difficult to simulate than expected. The solar flux from the sun is well known in orbit to be 1400 W/m^2 . However, this heat flux decreases through the atmosphere, as some of this flux is absorbed by atmospheric molecules. Beyond this, the sun was not shining directly on the instrument for the entire stage of the flight, nor with its full intensity. Only part of the sun could sometimes be seen, or sometimes it may have been shining on the side of the gondola. Unfortunately adding the solar flux was not as easy as adding a 1400 W/m^2 heat load to the side of the instrument. Through simulation iterations, it was eventually determined that a somewhat exponential flux curve led to the desired temperatures. Starting at 0 W/m^2 for the beginning of the phase, it increased to 800 W/m^2 . It is believed that the sun did not shine directly on the instrument, and was warmed either through the wall of the gondola or through reflections. More data on the effect of sunlight is needed to verify this.

The final changes were made for the radiation ambient temperatures. It was similar to the previous simulations, which was changing the ambient temperatures to what was seen from the flight data. In addition to this, the ambient temperature was increased for the outer parts of the instrument that may have been warmed by the sun or from parts of the gondola which were warmed. The ambient temperature of radiation for the top of the boxes as well as the sides was chosen to increase to upwards of 30°C by the end of the flight.

After 16 iterations a satisfactory thermal model for this stage was created. Images of this model are shown in Figure 4.15, and the comparison of the simulated temperatures to the actual temperatures is shown in Figure 4.16. A interesting note from the thermal simulations, the effect of the solar heating on the top of the Optics Box is very obvious,



(a) Thermal model of LIFE instrument at the end of the entire flight, Blackbody Electronics view.



(b) Thermal model of LIFE instrument at the end of the entire flight, Electronics Box view.

Figure 4.15: LIFE thermal model at the end of the sunrise stage of the flight, shortly before descent.

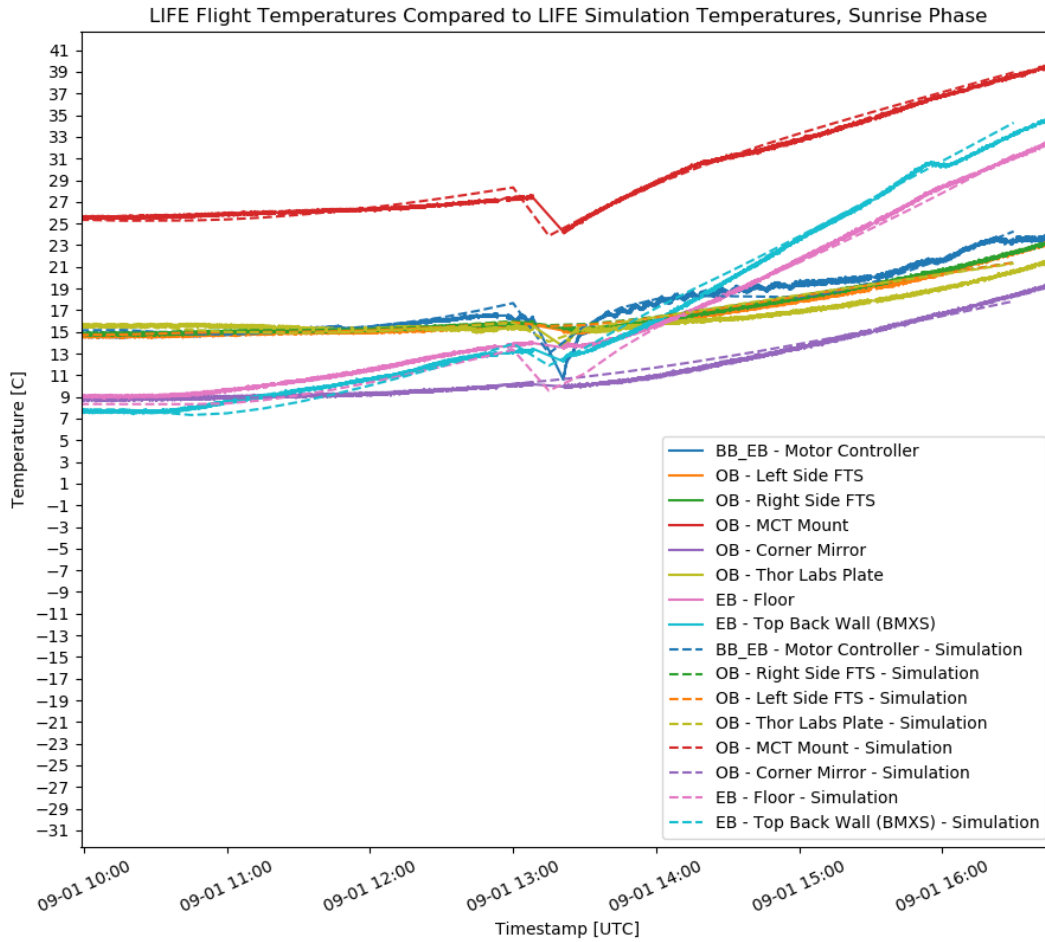


Figure 4.16: Flight temperatures during the sunrise phase, compared to the simulated temperature curves after model updates. The corresponding actual and simulated temperature data is the same colour, with the simulated data shown dashed.

heating the top plate to upwards of 70°C. The rest of the box still maintains a much cooler overall temperature.

Overall the model simulates the sunrise well. There is some error around the shutoff of the instrument, and this is due to the time step of the simulation. The power off time is roughly 10 minutes, and the entire phase of the flight is four hours. It would take a very long time to be able to run the simulation with steps of 10 minutes, so a coarser step is chosen. As a result the power off time in the simulation is slightly longer than the actual time. However, the temperatures still match in this region reasonably well. The temperatures are within 1°C of the actual temperatures, and as such the model is deemed successful. As before, more information about the thermal loads and temperature values can be found in the appendix.

4.4.4 Full model

With all sections simulated separately, they can be brought together as one full model. A comparison of the actual and simulated temperature curves for the entire flight is shown in Figure 4.17. The simulated temperatures overall now match very well with what was measured during flight. However, all thermal loads used still need to be verified with a thermal model of another instrument. Still, this provides a starting point for future thermal simulations.

Another way that this model can be verified is by comparing the heater currents used in the simulation to what was seen during the flight. The power sent to the heaters was tweaked in the simulation to help match the flight temperatures, but it must be ensured that the power curves that were used still match the measured current during flight. A current curve for the Optics Box/Electronics Box heaters and a current curve for the Blackbody Electronics Box heater is shown in Figure 4.18.

A margin of error is required for each system, for different reasons. In the Blackbody Electronics Box, this is to take into account that the measured current is also being used to power the blackbody system, not just the heater. This is known to be roughly 1.2 A, however it can vary depending on the external environment temperatures, but it could not be measured directly. An error is included of 0.5 A, to take into account the oscillation that could occur from the operation of the blackbody system. With the other boxes, the heater

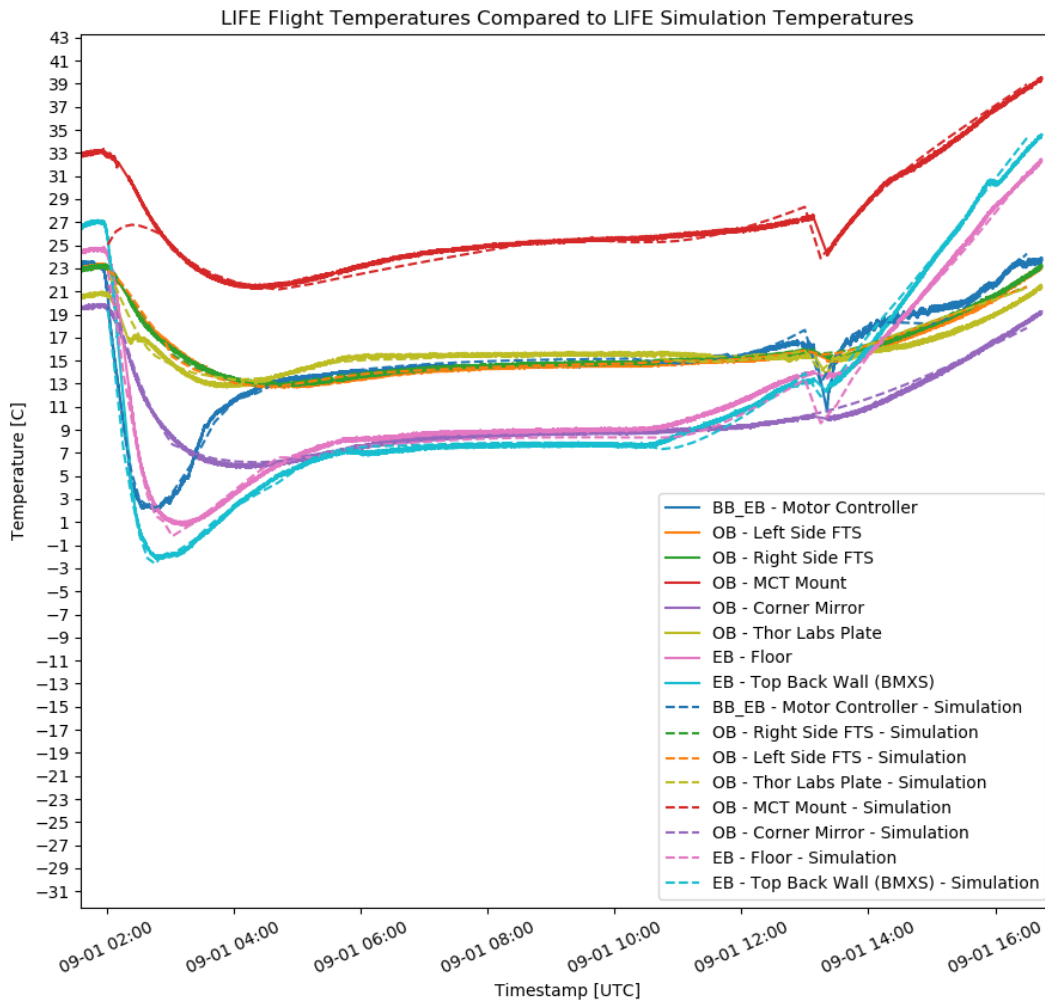
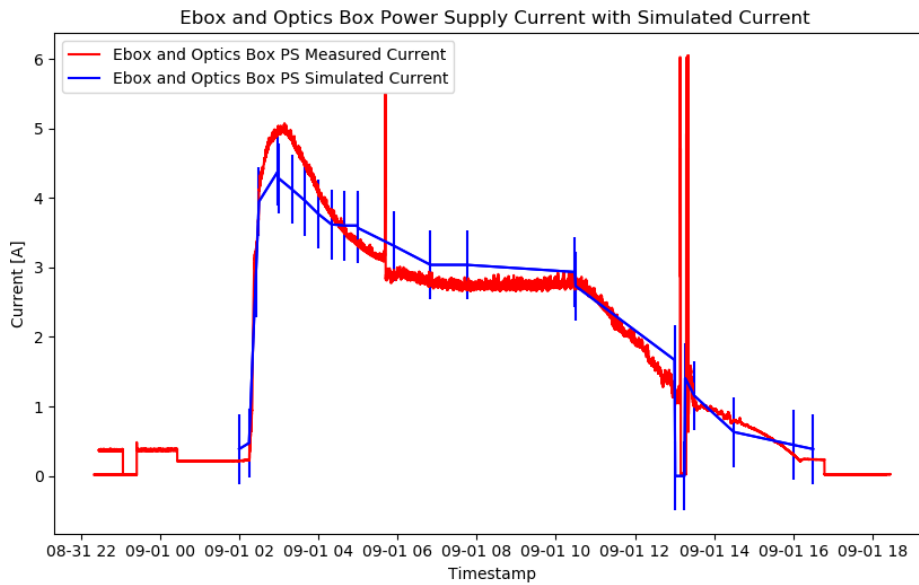
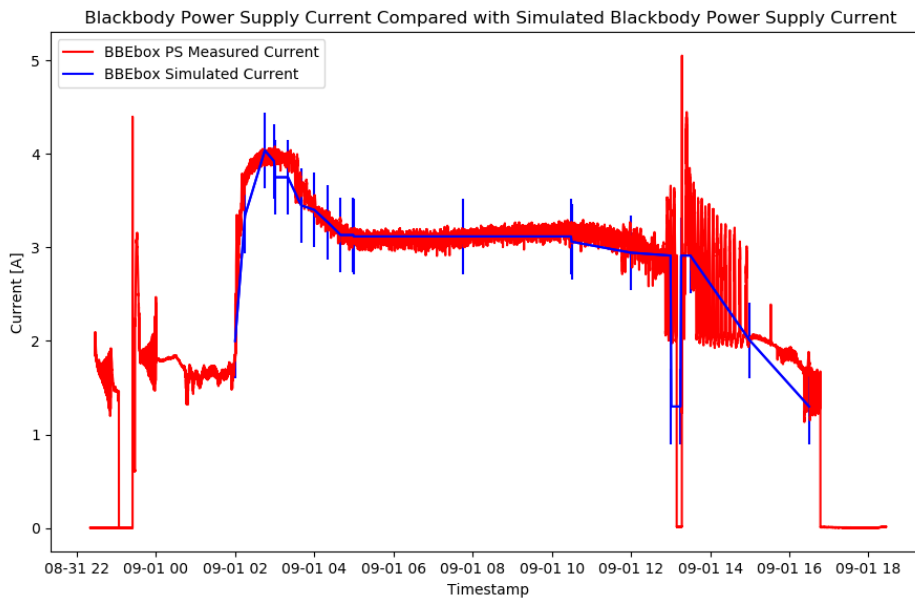


Figure 4.17: The actual and simulated temperature curves for the entire flight. The corresponding actual and simulated temperature data is the same colour, with the simulated data shown dashed.



(a) Actual and simulated current for the Optics Box and Electronics Box heater current.



(b) Actual and simulated current for the Blackbody Electronics Box heater current.

Figure 4.18: A comparison between the current curves of what was measured during flight, and what was input into the simulation.

power is also running a few smaller systems, which is not directly taken into account by the simulations, with a current of 0.3 A. As with the blackbody system power, these could oscillate, so the error is included to account for this.

Overall, the simulated temperature curve matches, within error, what was measured during flight. The overall shape is expected, with most of the power needed at the beginning to counteract the steep drop in temperatures through the ascent, leveling out around the float, and slowly turning off as the sun begins to heat the instrument. With this helping to verify the thermal model, there is more confidence that the thermal values chosen in the simulation accurately model high-altitude atmospheric conditions. This model can be used as a baseline in other thermal models of similar atmospheric instruments, which will help to gain confidence in future models and ensure those instruments will survive the flight environment.

4.5 Summary

In this chapter, all post-flight progress was discussed. The campaign and the overall results of the flight were discussed first. The flight was a success, with all thermal requirements being met, and the instrument operating nominally. Many measurements were taken over the course of the 14 hour flight, and temperature data was measured that could be used to help verify the thermal model. The mechanical results were also discussed, with the instrument surviving the harsh landing well but with some damage. The damage reviewed, and next steps for the instrument are being determined.

The main aspect of this chapter was the creation and discussion of the flight temperature model. With the temperatures well simulated for a survival test of the float portion of the flight, a more detailed model of the entire flight would be created. The temperatures measured were used to create a thermal model of all stages of flight that would match the temperatures measured for the ascent, float, and sunrise phases. Each of these phases were created and simulated in turn in SolidWorks, using some data from the flight and some known information about the flight environment. However, there is very little research on some of the more specific thermal properties of the atmosphere, such as convection. This model was created to gain some insight on these properties, by iterating through estimations of these

properties until the simulation matched the flight. It is hoped that in the future this model can be used for other atmospheric instrument flights and the model can be improved through more flight data.

5 DETECTOR CHARACTERIZATION

5.1 Overview

One of the core aspects of the LIFE instrument, along with the Fourier Transfer Spectrometer, is the Mercury Cadmium Telluride infrared detector. This detector images the atmosphere and blackbodies through the optical system and the FTS to create raw interferograms, which are saved to the computer. There are various parts of MCT detectors that must be carefully characterized so that the data is as optimized. The task of characterizing and optimizing the LIFE MCT detector forms the second part of this thesis. This chapter provides an overview of the MCT detector specific to the LIFE instrument in Section 5.2, as well as the work originally done to verify the detectors nominal operation in Section 5.3. Afterwards, various measurements were taken in the lab to optimize a number of different components of the detector, which is described in Section 5.4. This was all done prior to flight to optimize the data; Detailed post-flight analysis of the detector and the measured data is outside the scope of this thesis.

5.2 LIFE Detector

The LIFE MCT infrared detector was a custom purchase with the FTS from ABB, and is designed to function optimally with the LIFE system. It is manufactured by InFraRed Associates, and interfaces with the two custom amplification and digitization data acquisition (DAQ) boards also provided by ABB. The linear array of the MCT detector is 16 0.25 mm^2 square pixels, which respond to incident radiation from 2-14 μm , as is expected from an MCT-type detector. As described in Section 2.3.1, MCT detectors must be cooled to low temperatures to avoid saturation. The InFraRed Associates MCT Detector comes with an

attached Stirling cooler manufactured by Ricor, which cools the pixels to 77K. The 16 pixels provide 16 interferograms, which are split into two groups of eight and sent to the two DAQ boards where the signals are amplified. The two boards are connected to a computer where the data is then stored. These specifications are all given directly to the LIFE research team by ABB. An image of the LIFE detector is in Figure 5.1.

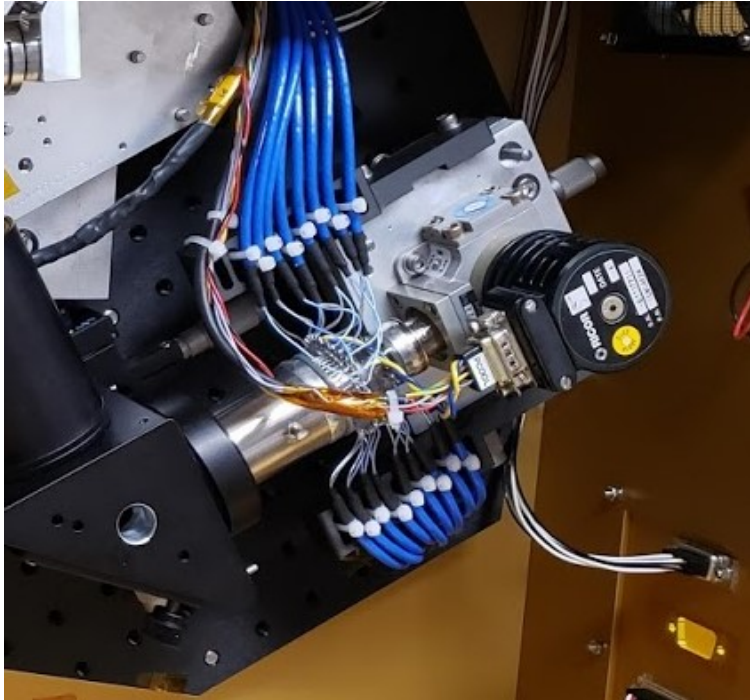


Figure 5.1: Image of the MCT Detector in the LIFE instrument.

5.3 Detector Verification

Before the detector could begin to be characterized, work was done to ensure that the detector was operating as expected. This work, and other optimization work, needed to be done in-house as the detector was originally designed and programmed to run in a different mode than in the LIFE application, known as *constant current* mode. In this mode, a constant current flows through the detector and a change in voltage is measured. In the ABB application in conjunction with the FTS, *constant voltage* mode is used. Here, the a constant voltage known as the *bias voltage* flows through the detector, and a current change can be measured. Also, verification tests allowed familiarization with the detector and its various settings before

attempting optimization. These tests were completed with the lab version of the instrument; i.e. they were completed with the MCT and FTS mounted on an optical bench rather than in the flight configuration. This was not ideal, as the system was not as well aligned as in the flight configuration, but it suffices for the optimization necessary. Tests were planned to be completed in flight configuration as well, but due to troubleshooting leading to the launch and damage sustained during the descent, these were not able to be completed.

To perform all verification and optimization work, there are two particular settings that can be changed via software for the LIFE MCT detector: The bias voltage, as described previously, and the offset current. The offset current raises and lowers the baseline of the measured current, and should be altered so that it does not dip below zero or saturate. These settings are related to the raw ADC output value of the detector through Equation 5.1 and 5.2, which are specific to the LIFE system as provided by ABB.

$$ADC_{raw\ value} = \frac{(I_{detector} + I_{offset})(-G)(2^{24} - 1)}{ADC\ Voltage\ Reference\ Range} \quad (5.1)$$

$$I_{detector} = \frac{V_{bias}}{R_{detector}} \quad (5.2)$$

For the case of the LIFE MCT detector, the ADC Voltage Reference Range is 4.096 V, and $R_{detector}$ is a function of the incident infrared optical signal flux. This function is typically linear, and for the LIFE detector over the expected operating range can be assumed to be a constant 50 Ω as recommended by ABB. However, as this is only an approximation, it is a source of some non-linearity that must be considered. G is the combined gain of all amplifiers, given as 195.65 V/A by ABB. As much of Equation 5.1 is made up of constants, it is easier to look at the proportional relationship between the ADC values and the bias voltage and offset current, shown in Equation 5.3.

$$ADC_{raw\ value} \propto - \left(\frac{V_{bias}}{R_{detector}} + I_{offset} \right) \quad (5.3)$$

With this simplified equation it is easier to see the dependencies. This forms a simple slope formula, with the bias voltage as the slope and the offset current as the y-intercept. Thus the operation of the detector can be verified by taking various measurements with

changing bias and offset settings. Numerous measurements were taken with the detector of blackbodies, and python software was developed to read these measurements to determine the output of the MCT system. It is noted that the output data presented in these tests is known as the *DC Component*, or the mean of the data, over an entire scan of the blackbody. This DC Component value is the same as the theoretical ADC raw value from Equation 5.3.

Before changing the bias and offset settings, a simple test was done of taking images of a blackbody with a temperature changing from 25°C to 60°C in 5°C increments. This was done to see the ADC output change based on blackbody temperature, giving an idea of the ADC range with different temperatures and the general output of the system. The result is shown in Figure 5.2.

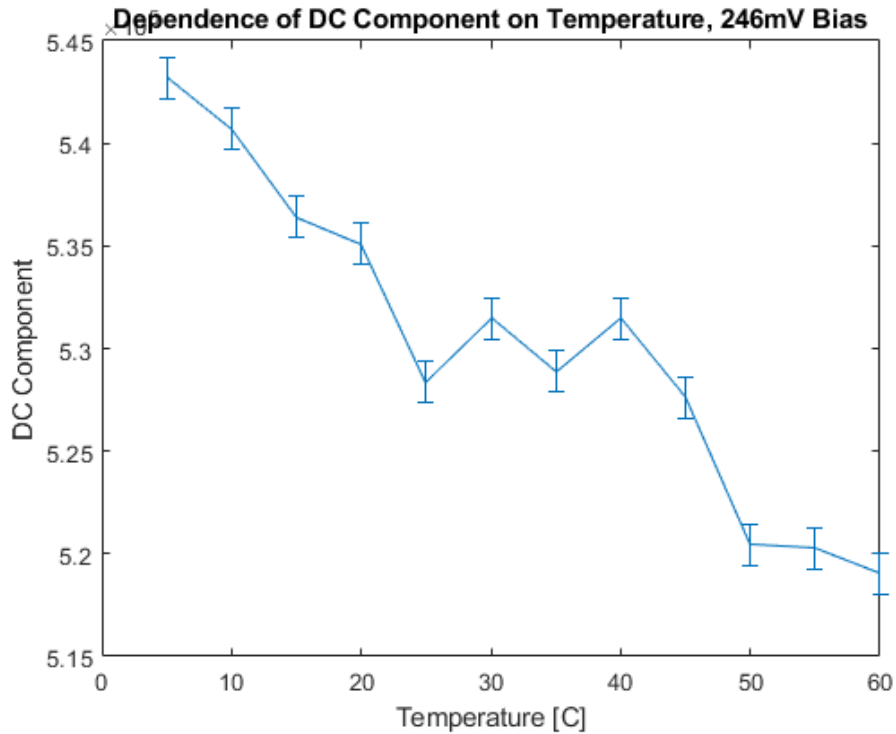


Figure 5.2: The result of changing the blackbody temperature on the raw detector signal.

This plot shows that there is a negative temperature dependence in the output data, which is a feature of the detector to avoid detector saturation at high temperatures. This allows the interferogram and detector to avoid saturation while more of the detector temperature range can be used. This result was helpful, as it also led to explanations of values for responsivity,

which is described in Section 5.4.1.

Beyond the overall decrease in the plot, ideally this should be much more linear. It was theorized that during the tests, the ambient temperature of the room had an effect on the output data. An air conditioning unit in the lab room and near the instrument cycled often, which would cause differing ambient temperatures throughout a test. This ambient temperature could affect the blackbody surfaces that were being imaged, as well as the surface of parts of the instrument that were possibly being imaged due to misalignment. A test done by taking images of the blackbodies at a constant temperature over a period of a few hours confirmed that the ambient temperature changes were having an affect on the output data, the results of which is shown in Figure 5.3.

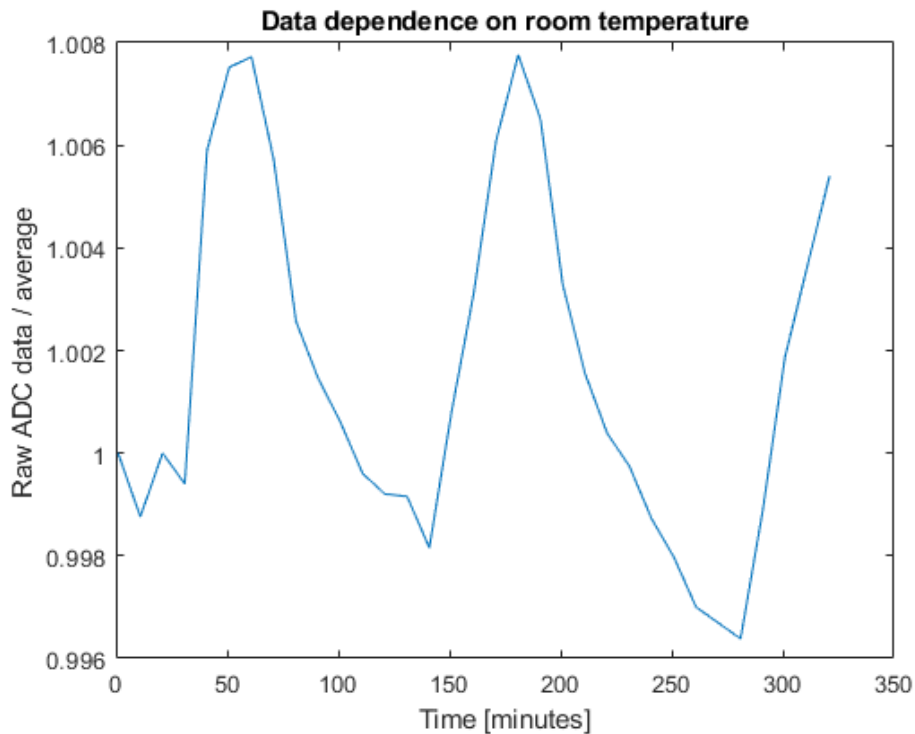


Figure 5.3: The result of the ambient room temperature changing throughout a longer term test, causing temperature changes in the blackbodies.

Although this is an issue that affects the lab data, it is unlikely to occur in the flight configuration of the instrument, as it was designed to be better thermally controlled as well as properly aligned. Ideally this would have been tested further after flight but as mentioned previously there was no opportunity.

Once these initial measurements were taken, further verification using the bias and offset settings could continue. Two main tests were done, one with constant bias voltages and incrementing offset current, and vice versa. For both tests, specific values were chosen for the constant bias voltage or offset current, respectively. These values were taken from a calibration spreadsheet provided by InfraRed Associates. As stated previously, the calibration would not work for the LIFE application due to it operating in a different mode, but there were specific values chosen for the bias voltage and offset current for all calibration tests; these are shown in Table 5.1. As there were a very wide range of possible settings, it was assumed that these values would be reasonable to begin with as they had been chosen by the manufacturer.

Bias voltage V_{bias} [mV]	Offset Current I_{offset} [mA]
246	4
431	6
625	8

Table 5.1: Bias voltage and offset currents as used in the factory calibration, used here as a baseline.

Measurements were done by taking images of a hot blackbody at 50°C and a cold blackbody at 10°C for both tests. For the first test, the offset was chosen as three constant values based on the factory calibration, and the bias voltage was incremented over a range chosen as 0.1 V to 1 V in 0.1 V steps. The resulting data is shown in Figure 5.4. It is noted that the detector was not constrained to the voltage range above, this was based on calibration values. It was noted by ABB that the range was much larger and there was no danger of destroying the detector with different values, but it was found that beyond this range there was no useful data and all tests were completed with these values.

The resulting dependence is expected. For each bias there is a small change in slope in the linearity of the data, as is expected from Equation 5.3. It is also downward sloping due to the negative proportionality, which results from the negative gain in the equation. The lines are all separated by the offset current chosen, also as expected. For each offset current, the cold

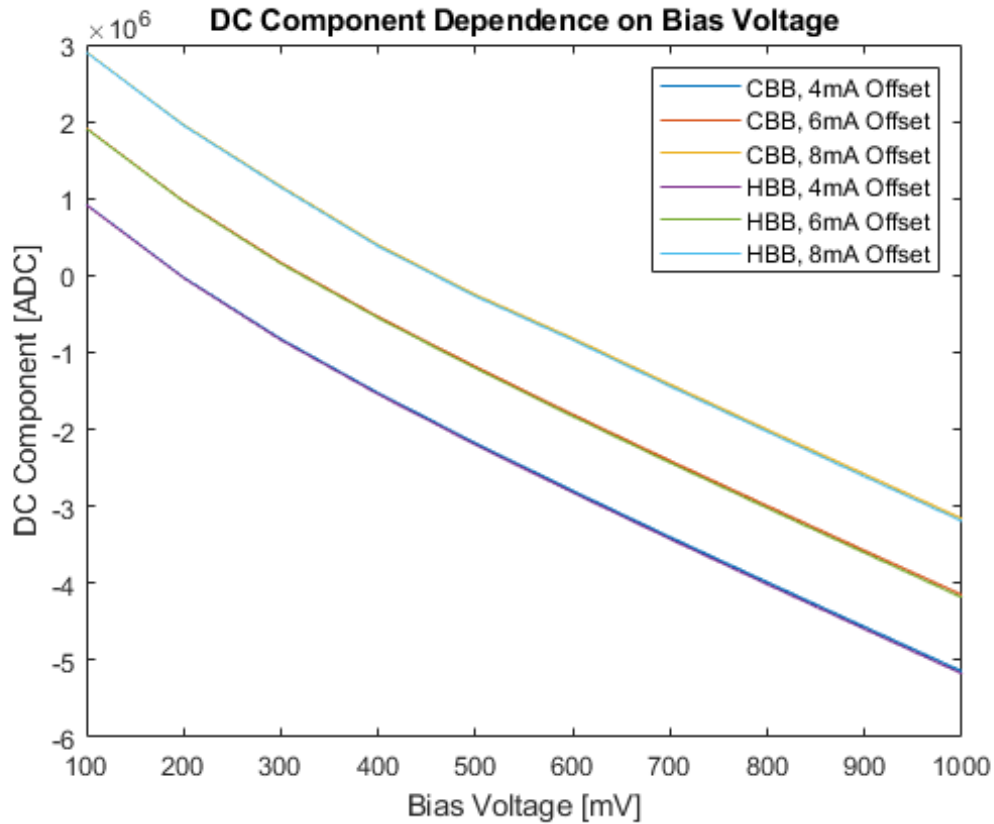


Figure 5.4: Detector raw data output dependence on bias voltage.

blackbody measurement and blackbody measurement appear to overlap. However, if the plot is magnified, the cold blackbody data is slightly higher than the hot blackbody data, which matches what would be expected from 5.2; the cold blackbody produces a higher ADC signal due to the signal inversion as described previously. The fact that the lines overlap shows the major effect that altering these settings have on the data; the change in ADC measurements from looking at two different blackbody temperatures is an order of magnitude smaller than the change in ADC measurements from altering settings. Overall, this plot confirms Equation 5.3. Figure 5.5 shows the second test, where the offset current is incremented over a range of 1 mA to 10 mA, with three bias voltages set according to factory calibration values. As with the bias voltage, the range of the offset current is much larger, but the aforementioned range was chosen to match the range of calibrated values.

The results shown in Figure 5.5 are also as expected. The data is very linear with increasing offset current, and are split by different bias voltages. The slope is also slightly

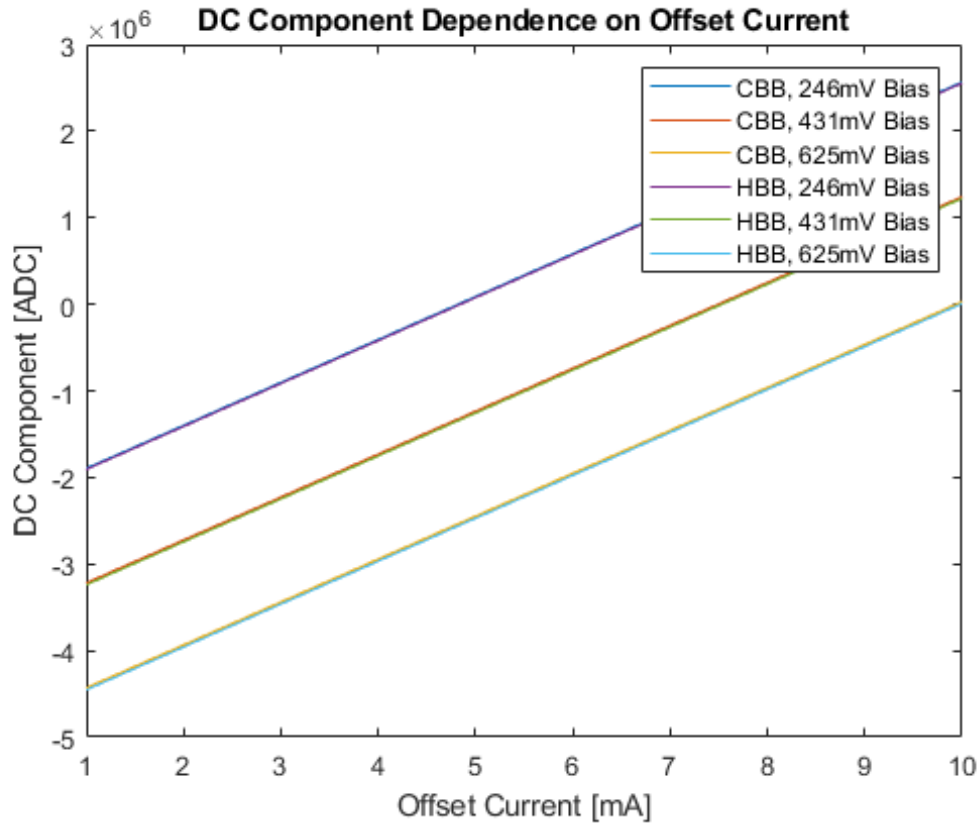


Figure 5.5: Detector raw data output dependence on offset current.

different for each plot, showing that the bias voltage does not have as large an impact on where the data is in the DC Component range. This would make sense as the function of the offset current is to move the baseline of the data, and the bias voltage is used to tune the responsivity; the results of changing this become more clear when tuning for responsivity. This is the topic of Section 5.4.1.

Overall, the results of changing the bias and offset settings on the output data match the equation provided by ABB that describes the system. Thus, the detector is verified to be working properly and as expected, and there is a greater understanding of the effect of altering the settings. Higher level optimization of the detector can now take place.

5.4 Characterization

To be able to produce the most accurate data possible, the MCT detector needs to be optimized to reduce common problems with MCT detectors such as non-linearity, and to detect incoming signal as well as possible. The latter corresponds with responsivity, which is discussed first and is the main characteristic to be optimized. A discussion of the calculation method, based on the GLORIA method, is described. A discussion of non-linearity follows, and the methods used to determine this, but the measurements and post-flight calibrations of non-linearity are out of the scope of thesis.

5.4.1 Responsivity

Responsivity is the measure of how sensitive, or responsive, the detector is to incoming signal. It is typically in units of ADC/Wcm^{-1} , with the length component coming from the spectral dependence, but the spectral dependence can be integrated out if the wavelength limits are known, which they are for a known detector and measured temperatures. Thus the units of responsivity for the case of LIFE are ADC/W , which gives a direct conversion from the input photon counts to power, i.e. the change in power from the input photons, which can easily be converted to the change in current that is measured. Theoretically, a higher responsivity would mean better performance, as the counts measured by the detector cause a larger change in the output current and giving a more accurate reading (Sha, 2013). However, if this change is too large, it can lead to non-linearity.

The responsivity is determined from an equation developed for the GLORIA instrument, which gives another equation for the raw output signal, similar to Equation 5.1 from ABB. The GLORIA equation is based on measurement results from hot and cold blackbody systems. A blackbody system consisting of three blackbodies, one at a hot temperature, one at a warm temperature, and one at a cold temperature, was procured for this purpose. It is on-board the LIFE instrument so these can be used to calibrate the FTS during flight, as described in Chapter 3. The DC signal measured by the detector is given in Equation 5.4.

$$DC = A_{pix}\Omega_{pix} \int_{\sigma_{min}}^{\sigma_{max}} \tau_{EW}(\sigma)\mathcal{R}_D(\sigma)L(\sigma,T)d\sigma \quad (5.4)$$

Here σ_{min} and σ_{max} are the lower and upper cutoff wavenumbers, $A_{pix}\Omega_{pix}$ is the throughput of the system, τ_{EW} is the transmittance of the detector window, \mathcal{R}_D is the detector responsivity, L is the spectral radiance, and T is the temperature of the blackbody. Whereas Equations 5.1 and 5.2 are given by ABB and based on the detector and its design only, giving raw output data, Equation 5.4 shows a theoretical output of the entire system, including both detectors and optics. In addition, the method for calculating responsivity using Equation 5.1 was not given by ABB and would require more work and characterization to determine a method. As the GLORIA system is similar to LIFE, Equation 5.4 applies to LIFE as well and is an accurate way of determining responsivity.

Using this equation at hot and cold temperatures, assuming the transmittance of the detector window to be unity, and rearranging, the detector response can be calculated from Equation 5.5.

$$\mathcal{R}_D = \frac{DC_{hbb} - DC_{cbb}}{A_{pix}\Omega_{pix}(L(T_{hbb}) - L(T_{cbb}))} \quad (5.5)$$

Here DC_{hbb} is the DC component of the interferogram signal from the hot blackbody, DC_{cbb} is the DC component of the interferogram signal from the cold blackbody, $L(T_{hbb})$ is the Planck function integrated over the range of wavenumbers for the hot blackbody, and $L(T_{cbb})$ is the Planck function integrated over the range of wavenumbers for the cold blackbody (Sha, 2013).

Now that there is an equation for the responsivity of the detector that can be related to the signal output, it can be tested with different inputs and settings on the detector. For all tests, the cold blackbody temperature was set to 10°C and the hot blackbody temperature was set to 50°C. Thus the responsivity between tests was entirely dependent on the DC signal from the hot and cold blackbodies, which the behaviour of is known from tests done in Section 5.3. The same bias voltage and offset ranges were used as the verification tests, and the first test of the responsivity dependence on offset current is examined. The results of these tests as calculated by Equation 5.5 are shown in Figure 5.6.

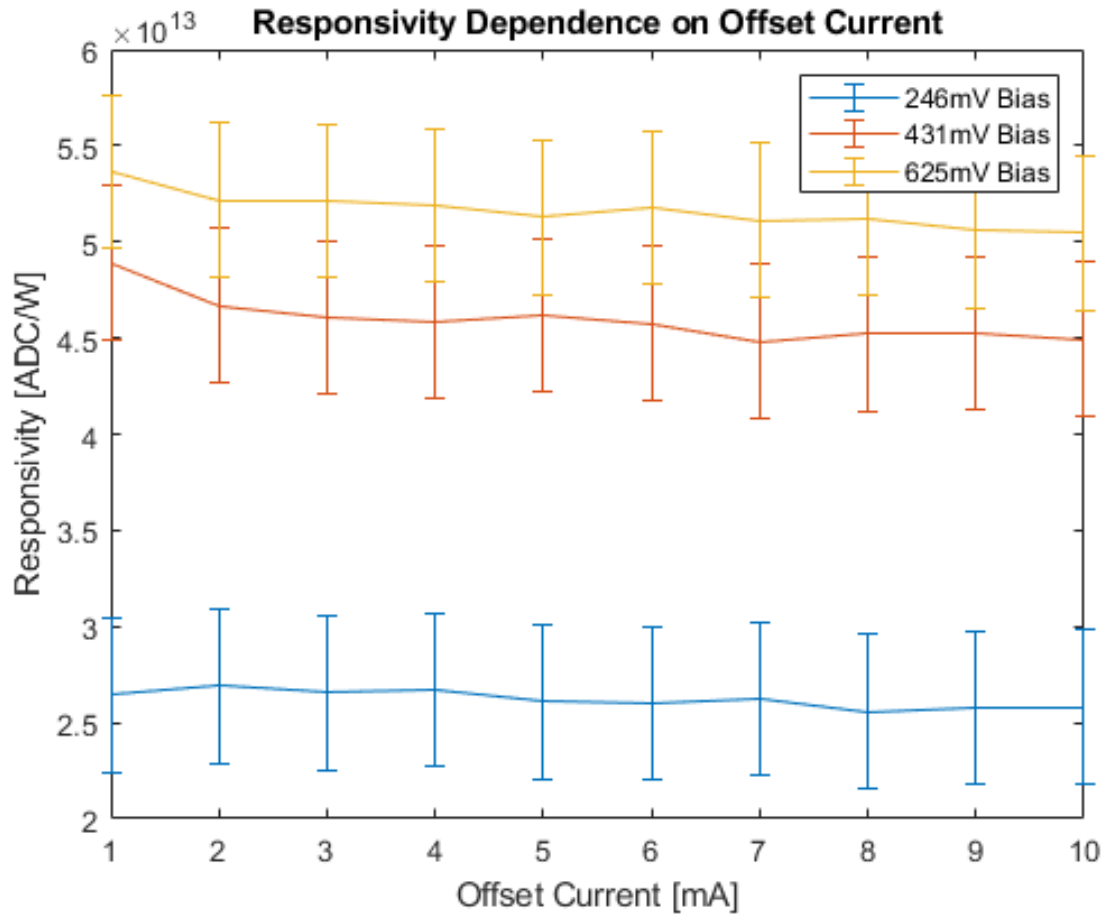


Figure 5.6: Detector responsivity change with different offset settings.

Figure 5.6 shows that the offset current has little effect on responsivity, with data for each bias voltage being effectively linear. The spacing between each set of data shows the large effect that changing bias has on the data. Now that it is known that the offset current only has the effect of changing the baseline of the data but not the responsivity, the result of changing the bias voltage will be examined. It is done over a range of 100 mV to 1 V and is shown in Figure 5.7.

This plot shows what is theorized; as the bias voltage increases, the responsivity of the detector increases. Also, the lines all effectively overlap, confirming Figure 5.6, showing that the offset current will not have an effect on the final value for responsivity. As mentioned before, theoretically, the responsivity should be as high as possible for the best detector performance, meaning that the bias voltage should be chosen to be at least 1 V. However, there is a saturation limit on the bias voltage, where the detector will not operate correctly.

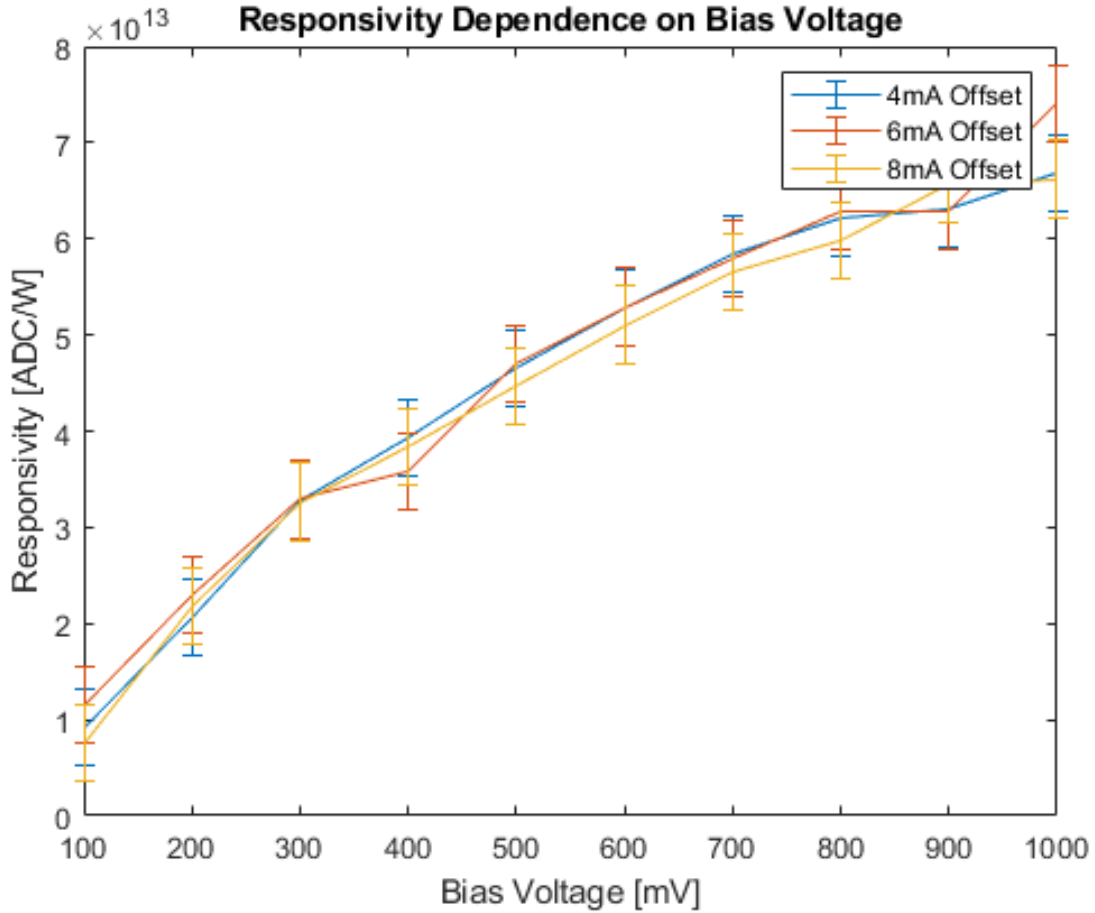


Figure 5.7: Detector responsivity change with different bias voltage settings.

This leads to non-linearity, which can be seen in this plot. The increase in responsivity with bias voltage begins linear but slowly begins to decline as it reaches saturation levels. Further tests in the thermal vacuum environment would show that if the bias voltage became too high, leading to a high responsivity, the detector would not be able to dump enough heat to keep the temperature to 77K. Even after lowering the bias voltage, the detector took almost 2 hours to cool back down to its previous temperature. Thus the final value for bias voltage must be chosen so that is not so close to the non-linear range as to saturate and effect the data.

After examining the data, it was determined that with a bias voltage any higher than 500 mV, there is a risk of non-linearity due to bias voltage having a large effect. Thus a bias voltage of 431 mV was chosen, one of the values originally given by the manufacturer. The gains in responsivity past this point were not worth the chance of saturation, and as

it was in the middle of the manufacturer's calibration range it seemed to be a good choice. Similarly, the offset current was chosen to be 6 mA, in the middle of the manufacturer's calibration range. As the offset current had little effect on responsivity, this was set more to choose a middle baseline for the current range. These two settings were used for all pre-flight calibration measurements as well as the flight itself.

Further examination into the responsivity was planned after the instrument was in full flight configuration as well as after the flight, to research more closely the responsivity of the detector for each pixel and to examine the effect of non-linearity further. It would also help to inform the design for future versions of the instrument. However, due to the damage the instrument and particularly the detector sustained upon landing, this will not be possible. It is an important aspect of the instrument to examine if a second version of the instrument is planned or if the detector is fixed.

5.4.2 Non-linearity

The non-linearity of the LIFE system must be determined to allow for its correction and removal from the data. The non-linearity will have an effect on Equation 5.3, as based on the structure of this equation the results should be linear. There are a number of ways to determine the non-linearity of the system, which must be utilized to allow for its removal. There are two main sources of non-linearity in the LIFE system: Electrical, based on the electronics of the MCT and its settings, and optical, which is more dependent on the characteristics of the MCT itself as well as the design of the optical system.

The non-linearity due to the electrical system is characterized and removed through the altering of the bias voltage and offset current settings, which is largely described in the previous section. The non-linearity of this nature comes from the non-linear bias voltage of the detector, as well as the non-linear amplifier response in the amplifying circuitry of the data acquisition system. Nothing can be done about the amplifier non-linearity, but the settings can be chosen to remove the effect of non-linear bias voltage as much as possible. As described in Section 5.4.1, the responsivity curve is highly non-linear, due to the increasing bias voltage. This should be set as low as possible while still maintaining a high responsivity to mitigate this effect. The electrical non-linearity was minimized through these verification

and responsivity characterization tests.

Non-linearity due to other parts of the system is more complex, making it more difficult to measure and more difficult to remove. A method of measuring the effect of non-linearity due to the optics is to measure the out-of-band spectral response. Here, signal can be seen in the resulting spectra outside of the cutoff wavelengths, where the measurement should be zero. There are different methods for characterizing this response, one of which is to examine a very cold blackbody. Theoretically, with a cold enough blackbody, there should be effectively zero signal measured by the detector. This was accomplished by examining a blackbody surface with a temperature dropped via liquid nitrogen to -100°C . This test needed to be done in a thermal vacuum chamber, so that frost would not build up on the blackbody surface; this would have changed the emissivity of the surface. Even though it was done in a vacuum environment frost was still an issue, but measurements were taken. The signal that was measured from the cold blackbody is the non-linearity, or the out-of-band response (Bakan et al., 2005). This also helped to determine if any part of the system was being imaged due to misalignment which would cause a higher temperature than expected. This self-emission and out-of-band signal could be then be removed from the data. No further work could be done to optimize the instrument prior to flight, and the non-linearity signal would have to be removed from the flight data. Post-flight, the data is being analyzed by Ethan Runge for his PhD thesis, which includes further research into removal of the non-linearity from the flight data.

5.5 Summary

This chapter discusses the second part of this thesis, the characterization of the MCT detector. The detector used in the LIFE instrument is first described in detail, with the information given from the manufacturer. The initial work done for the verification is then described, which involved multiple tests to ensure that the detector was working properly prior to the characterization tests. The two main settings for the detector, offset current and bias voltage, were changed both for verification and to examine the detector responsivity and non-linearity, before attempting to improve these.

The characterization of the detector involved working with these settings to optimize the responsivity of the detector to provide the best measurements possible, while avoiding any non-linearity in the resulting data. A number of tests were done with different settings to find the best responsivity, and once a value was chosen it was used for all future tests. Non-linearity was examined in more detail, however most of this work is outside the scope of this thesis, along with the post-flight analysis.

6 FUTURE WORK

6.1 Overview

With the first official version of LIFE complete, updates and changes for a potential future version of LIFE are now examined. With the results of the thermal-mechanical design in comparison with the simulated model, as well as examining the measured data, insights into how the instrument can be improved for the next flight can be created, should an opportunity arise. Changes to the thermal-mechanical design is discussed first, if there were less constraints on the time and budget of the design. Second, the MCT characterization is re-examined. This section discusses what other tests could be completed with the detector, and any issues with the detector that arose. Finally, a discussion on the atmospheric instrument thermal model is presented, and what needs to be improved.

6.2 LIFE Thermal-Mechanical Design Changes

The first version of LIFE had a number of constraints that led to the instrument being designed and built as it is. In future versions of the instrument, this may not be the case. A few changes to the instrument are examined here that should be considered should another version of LIFE be approved, and incremental changes could be made. These changes aim to fix a few of the initial issues of the instrument, and also to make it easier to design, develop, and build. In addition these changes could help to provide better measurements and also better data analysis post-flight.

The first component that is planned to be fully updated in the next version of LIFE is the blackbody system. High-quality blackbody systems, as are needed for the calibration of highly sensitive thermal imaging systems, are expensive. This is why LIFE retrofitted an

older blackbody system taken from a previous instrument. While the one used on LIFE was a high-quality system in terms of the blackbodies themselves, it did not fully suit the needs of LIFE. There are a number of changes that would be made and design requirements for a new blackbody system that should be considered if a system is designed or purchased for a future instrument. A few of the issues with the current system that would be changed are described here.

An issue with the blackbody system that was used for LIFE was the size and weight. Having been used in an instrument that required two full systems, it was large and heavy, and required the entire optical system to be raised so the window of the system would be aligned with the FTS. The bottom system was not used, and was unnecessary weight on an already heavy and bulky instrument, even with the unnecessary blackbodies removed. Some issues with the core mirror system also had to be dealt with, as the lack of encoder on the stepper motor as well as its age led to errors in the pointing of the mirror that may have caused self-emission issues. Finally, a general lack of information about the system due to its age led to some issues in the mechanical design. The system had to be measured and recreated in SolidWorks, and errors in this model led to some manufacturing errors that needed to be corrected. Other missing information included the surface coating of the mirror, which would have helped in determining self-emission, and there was little information given on the electrical system. A new blackbody system would be able to solve these issues, by making it smaller and designing it with the rest of the instrument in mind, as well as having information that was not available with the current system. A new and more precise centre motor system could also be installed to remove any viewing angle errors.

In addition to these issues and potential fixes to the blackbody system, an important component that was missing was the lack of a deep space view. Ideally, during flight and also just for characterization on the ground, the instrument would be able to view vertically upwards to space. This would provide another cold characterization point that would be colder than any blackbody or atmospheric view. Images of this cold view would be very helpful in the post-flight analysis of the data and would assist in self-emission and non-linearity removal methods. A basic mirror system was developed for the purpose of taking deep space measurements while performing instrument testing on the ground, which provided

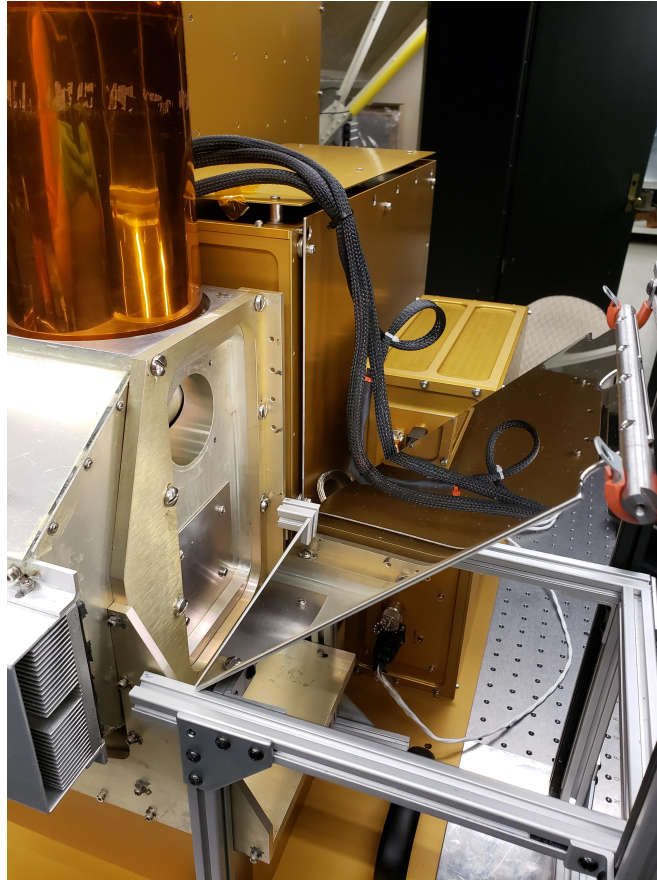


Figure 6.1: Mirror system for viewing vertically upwards towards space, for ground testing.

helpful data. A similar system could be implemented on a future flight instrument. An image of the temporary setup used for ground testing is shown in Figure 6.1. A better way to view a very cold blackbody, such as the blackbody used in the non-linearity characterization in the TVAC tank, could be combined with this new view to further improve characterization and post-flight analysis.

Now looking beyond the blackbody, one of the design constraints that led to a much more complex design was the MCT detector orientation. With the pixels in a 1x16 horizontal array on the detector but a vertical field of view needed, the optical system needed to be mounted vertically. This led to increased complexity in the optical system design, and also led to difficulties with aligning and repairing the optical system as needed in this orientation. If a new MCT detector could be sourced, a detector with a vertical pixel array should be chosen. This would allow the optical system to be mounted horizontally and would be easier to test

and align, as well as remain more stable during transport and flight. The remainder of the system could still stay the same, with the optical system being mounted to a breadboard and the system being thermally isolated still being design options with a horizontal optical system. The core optical system had issues with the field of view, which caused self emission errors, so this could be redesigned. However a more detailed discussion of an optical redesign is outside the scope of this thesis.

For more general mechanical updates, as mentioned briefly in Section 3.6.1, anodization should be considered more carefully, and it should be applied only to specific areas. The anodization caused issues with the grounding of electronics, and needed to be removed in some areas so that electronics would have a direct electrical path to the box, which was also connected to the baseplate as a ground. If possible, small areas where electronics are mounted would not have anodization applied, so that it would not need to be removed later. This would be similar to the process of taping over a small area if the box was being painted, so that upon removal the surface would still be unpainted. In addition, an effort should be made to choose more uniform bolts, both for the cost of purchasing a large variety and so that it is easier to construct.

Finally, the instrument could be made to fly in daylight without much added cost or time. It is unknown how much lower temperatures would have been with the added sun shields used for daylight flights of the gondola, but likely a significant amount. The addition of radiation panels to sensitive areas of the electronics boxes, such as the top of the Electronics Box, would decrease the amount of solar heating from direct sunlight on these components. The effect of these radiation plates is evident in the low temperatures of the Optics Box even after sunrise. However, the dissipation of heat from the more powerful components of the Electronics Box may still cause issues. Methods for mitigating this may require performing more simulations with a painted rather than anodized box, which would allow more heat dissipation, or by adding a thermal path via copper strap from these components to the base of the instrument. More simulations need to be completed to examine possible thermal designs, but based on what was seen for the flight of the current instrument, daylight flight would likely be an option with a slightly modified design.

With most of these proposed changes to the thermal-mechanical design, a thorough re-

design and rebuild of most of the instrument would be necessary. There are not many small incremental updates that could be done to the main instrument. Repairs need to be done to the current instrument, including reattaching the boxes to the baseplate properly, fixing the detector, and examining the optical system. However with a thorough update for a second version, especially with a new blackbody system, LIFE could be improved greatly for better measurements on future flights.

6.3 Further MCT Characterization

From the work that was completed on the detector prior to flight, the instrument performed well and took good measurements. The responsivity chosen limited the non-linearity, and the detector avoided saturation, so the settings chosen were good. However, further work could have been done to allow the detector to work better, which was not able to be completed. Beyond the verification and responsivity described in Chapter 5, other characteristics of the detector were planned to be tested. Unfortunately nothing beyond the responsivity could be tested prior to flight, due to other testing and electrical issues until the launch that delayed any further testing. This was then planned to be completed post-launch, but as the detector was damaged during flight, this was not possible either. Here, a few detector characteristics that need further testing are described, if the detector is repaired for a future flight.

The responsivity and characterization done prior to flight should be further verified. There is no direct way to do this, as the characterization was done by changing the detector settings and examining the effect. After the settings were optimized, they were not changed afterwards, and were kept the same throughout the flight. A measure of the quality of the measurements is the non-linearity and Johnson noise of the data, which can be examined. The non-linearity was optimized for the settings chosen, but can be examined for the flight data to see if it was really minimized, or if better settings could have been chosen. Johnson noise is another method of examining this, and is connected to the non-linearity. However, an examination of both of these characteristics of the data requires a large amount of data analysis, and is outside the scope of this thesis. Both of these should be examined in the future to determine if the MCT should be further characterized and optimized.

As a whole, more work should be done into the characterization of the non-linearity. The original approach to correcting non-linearity was based on a three-point blackbody correction, following a method developed by the GLORIA team. For LIFE, a very cold blackbody in the TVAC tank was used, along with the warm and hot blackbodies, allowing three points of reference for correction. However, it was discovered that there was still a non-linearity that could not be corrected using this method, that was also found by GLORIA. It is a result of the strength of blackbody measurements versus deep space or limb measurements, causing inconsistencies (Guggenmoser, 2014). To correct for this, more points of measurement must be taken with blackbodies. Before future flights, measurements should be taken at a number of blackbody temperatures, in the ranges of cold, warm and hot, that can be used to create more points of correction. The issue of non-linearity is a well known problem with MCT detectors, and the majority of remaining characterization of the detector involves the non-linearity, and its minimization and removal from the data.

6.4 Updates to Atmospheric Instrument Flight Thermal Model

As discussed in Section 4.4, there were many unknowns in the post-flight detailed simulations that were deduced through a combination of known values and trial and error. While the model in the end was able to accurately match what was seen during flight, there are likely errors in the values chosen and they could be tweaked to more closely match what was actually seen. However, to do this, more temperature data is needed. This section will describe what parts of the thermal model could be improved through more instruments gathering data and improving the model with these measurements.

The ascent portion of the flight is the part of the model that has the largest room for error. Particularly as a result of convection, there are a large number of unknowns that are iterated through to be able to create an accurate temperature model. Ideally, more convection information is known about an ascent through this part of the atmosphere, but that is more complex to gather. What is more likely is that further instruments gather temperature data through this part of the flight, and apply the current values of convection

to the new thermal model, and see how the temperatures match what was found during flight. Both the convection properties and the radiation properties may need to be altered to allow the temperatures to match correctly, but the original values will serve as a starting point for the new model. Although they may not be accurate, the properties for convection and radiation should be close to what is needed for the new model and through a number of instruments these properties will converge and can provide information for future instruments more accurately.

Similarly for the sunrise part of the flight, more information needs to be gathered on the affect of the sun on instruments of this altitude. The heat flux was included in the final part of the simulation and led to accurate temperatures, but there is little information known on how the sun was shining on the gondola. If possible it would be ideal to know this information for future daylight post-flight simulations, as it will allow more information for the thermal model. A longer time period of temperature measurements while the sun is shining on the gondola will provide this information.

The next instrument in the ISAS Atmospheric Research Group is currently being developed, and a full thermal model similar to LIFE is being developed for the flight. Although the instruments are different, the thermal model developed for LIFE will be able to inform some properties of the new simulations, and at the least provide good information on the environment. This will allow pre-flight simulations to go beyond the float portion of the flight and help to ensure better survivability.

6.5 Conclusion

The purpose of this thesis was to develop and prepare the LIFE instrument for an atmospheric balloon flight, where it would take measurements of greenhouse gases in the troposphere and stratosphere. A thermal-mechanical model of the instrument was developed, so that the instrument would be able to fly on a high-altitude balloon gondola, and be able to survive the environment of the flight. In addition, a core component of the instrument, the MCT detector, needed to be verified and characterized to ensure that it would operate and take good measurements during its flight.

Through 2018 and 2019, a model of LIFE was designed, developed, simulated, and built. It was flown at end of summer of 2019 on a gondola in Timmins, Ontario, to take measurements of the atmosphere and show that the instrument worked as expected. The flight was a success, all requirements of the thermal-mechanical design were met and the instrument took good measurements. Afterwards, from the data that was collected, a first iteration of a generalized thermal model for atmospheric instruments was developed, that could be used for future instruments as a starting point in the thermal design to save time and cost.

The purpose of creating the atmospheric balloon version of LIFE is to demonstrate that it can successfully operate and gather data on gases in the atmosphere. Information gathered from this flight, both its measurements and its operation, are used to inform future versions of LIFE, and eventually a satellite-borne instrument.

REFERENCES

- M. C. Abrams, G. C. Toon, and R. A. Schindler. Practical example of the correction of fourier-transform spectra for detector nonlinearity. *Appl. Opt.*, 33(27):6307–6314, Sep 1994.
- Stephan Bakan, Stuart Newman, and Lars Fiedler. Correction of detector nonlinearity in fourier transform spectroscopy with a low-temperature blackbody. *Applied Optics*, 44(25): 5332–5340, 2005.
- I. Baker. *MCT Photoconductive Detectors*. Academic Press, 1981.
- I. M. Baker. *MCT Photoconductive Infrared Detectors*. John Wiley and Sons, Ltd, 2010.
- F. Bartoli, R. Allen, L. Esterowitz, and M. Kruer. Auger-limited carrier lifetimes in hgcdte at high excess carrier concentrations. *Journal of applied physics*, 45:2150–2154, 1974.
- Klaus-Jurgen Bathe. *Finite Element Procedures*. Massachusetts Institute of Technology, Watertown, MA, 2016.
- P. Bernath. The Atmospheric Chemistry Experiment (ACE): An overview. In *The Atmospheric Chemistry Experiment (ACE): An overview*, Toronto, Ontario, 2002. IEEE International Geoscience and Remote Sensing Symposium.
- A. T. A. M. de Waele. Basic operation of cryocoolers and related thermal machines. *Journal of Low Temperature Physics*, 164(5):179, Jun 2011.
- D. P. Dee, S. M. Uppala, A. J. Simmons, P. Berrisford, P. Poli, S. Kobayashi, U. Andrae, M. A. Balmaseda, G. Balsamo, P. Bauer, P. Bechtold, A. C. M. Beljaars, L. van de Berg, J. Bidlot, N. Bormann, C. Delsol, R. Dragani, M. Fuentes, A. J. Geer, L. Haimberger, S. B. Healy, H. Hersbach, E. V. Hólm, L. Isaksen, P. Kállberg, M. Köhler, M. Matricardi, A. P. McNally, B. M. Monge-Sanz, J.-J. Morcrette, B.-K. Park, C. Peubey, P. de Rosnay, C. Tavolato, J.-N. Thépaut, and F. Vitart. The era-interim reanalysis: configuration and performance of the data assimilation system. *Quarterly Journal of the Royal Meteorological Society*, 137(656):553–597, 2011. URL <https://rmets.onlinelibrary.wiley.com/doi/abs/10.1002/qj.828>.
- D. Degenstein, A. Bourassa, C. Roth, and E. Llewellyn. Limb scatter ozone retrieval from 10 to 60 km using a multiplicative algebraic reconstruction technique. *Atmospheric Chemistry and Physics Discussions*, 8:11853–11877, 2008.
- Francis J. DiSalvo. Thermoelectric cooling and power generation. *Science*, 285(5428):703–706, 1999.

- Jan Doornink. Thermal design of the MIPAS instrument. Technical report, Fokker Space B.V. / SAE, Leiden, The Netherlands, 7 1996.
- J. Ed Akin. *Finite Element Analysis Concepts via SolidWorks*. World Scientific, Houston, 2009.
- M. Endemann. MIPAS instrument concept and performance. In *European Symposium on Atmospheric Measurements from Space*, pages 1–17, The address of the publisher, 1 1999. European Space Agency, ESA-ESTEC, P.O.Box 299, NL-2200AG Noordwijk, The Netherlands.
- George P. Eppeldauer and Robert J. Martin. Photocurrent measurement of pc and pv hgcdte detectors. *Journal of Research of the National Institute of Standards and Technology*, 106 (3):577–587, 2001.
- H. Fischer, M. Birk, C. Blom, B. Carli, M. Carlotti, T. von Clarmann, L. Delbouille, A. Dudhia, D. Ehhalt, M. Endemann, J. M. Flaud, R. Gessner, A. Kleinert, R. Koopman, J. Langen, M. Lopez-Puertas, P. Mosner, H. Nett, H. Oelhaf, G. Perron, J. Remedios, M. Ridolfi, G. Stiller, and R. Zander. MIPAS: An instrument for atmospheric and climate research. *Atmospheric Chemistry and Physics*, 1(8):2151–2188, 2008.
- F. Friedl-Vallon, T. Gulde, F. Hase, A. Kleinert, T. Kulesa, G. Maucher, T. Neubert, F. Olschewski, C. Piesch, P. Preusse, H. Rongen, C. Sartorius, H. Schneider, A. Schonfeld, V. Tan, N. Bayer, J. Blank, R. Dapp, A. Ebersoldt, H. Fischer, F. Graf, T. Guggenmoser, M. Hopfner, M. Kaufmann, E. Kretschmer, T. Latzko, H. Nordmeyer, H. Oelhaf, J. Orphal, M. Riese, G. Schardt, J. Schillings, M. K. Sha, O. Suminska-Ebersoldt, and J. Ungermann. Instrument concept of the imaging fourier transform spectrometer GLORIA. *Atmospheric Measurement Techniques*, 1(7):3565–3577, 2014.
- Stephane Gendron. Canadian space agency private communication, 7 2019.
- A. Gettelman, P. Hoor, L. L. Pan, W. J. Randel, M. I. Hegglin, and T. Birner. The extratropical upper troposphere and lower stratosphere. *Reviews of Geophysics*, 49(3), 2011.
- Vishnu Gopal. Responsivity modelling of hgcdte photoconductive detectors. *Semiconductor Science and Technology*, 1(13):887–889, 1998.
- Albert Greve and Michael Bremer. *Thermal Design and Thermal Behaviour of Radio Telescopes and their Enclosures*. Springer, Berlin, Heidelberg, 2010.
- S. Griessbach, L. Hoffmann, R. Spang, M. von Hobe, R. Muller, and M. Riese. Infrared limb emission measurements of aerosol in the troposphere and stratosphere. *Atmospheric Measurement Techniques*, 9(9):4399–4423, 2016.
- Tobias Guggenmoser. *Data Processing and Trace Gas Retrievals for the GLORIA Limb Sounder*. PhD thesis, University of Wuppertal, Wuppertal, Germany, 2014.
- Craig Haley. CATS thermal summary internal report. Technical report, ABB, 2018.

- Hamamatsu. Characteristics and use of infrared detectors. Technical report, Hamamatsu / CalTech, Hamamatsu, Japan, 11 2004.
- F. Hase, L. Wallace, S. Mclead, J. Harrison, and P. Bernath. The ACE-FTS atlas of the infrared solar spectrum. *Journal of Quantitative Spectroscopy and Radiative Transfer*, 111(4):521 – 528, 2010.
- A.E. Hedin. Msise model 1990, 1990. URL <https://ccmc.gsfc.nasa.gov/modelweb/atmos/msise.html>.
- M.I. Hegglin and S. Tegtemeier. SPARC, 2017: The SPARC data initiative: Assessment of stratospheric trace gas and aerosol climatologies from satellite limb sounders. Technical Report 8, WCRP-5, 2017.
- J. P. Holman. *Heat Transfer*. McGraw-Hill, 1981.
- James R. Holton, Peter H. Haynes, Michael E. McIntyre, Anne R. Douglass, Richard B. Rood, and Leonhard Pfister. Stratosphere-troposphere exchange. *Reviews of Geophysics*, 33(4):403–439, 1995.
- J W Kaiser, C von Savigny, K U Eichmann, S Noël, H Bovensmann, J Frerick, and J P Burrows. Satellite-pointing retrieval from atmospheric limb-scattering of solar uv-b radiation. *Canadian Journal of Physics*, 82(12):1041–1052, 2004.
- A. Kleinert, F. Friedl-Vallon, T. Guggenmoser, M. Höpfner, T. Neubert, R. Ribalda, M. K. Sha, J. Ungermann, J. Blank, A. Ebersoldt, E. Kretschmer, T. Latzko, H. Oelhaf, F. Olschewski, and P. Preusse. Level 0 to 1 processing of the imaging fourier transform spectrometer gloria: generation of radiometrically and spectrally calibrated spectra. *Atmospheric Measurement Techniques*, 7(12):4167–4184, 2014.
- Anne Kleinert and Olaf Trieschmann. Phase determination for a fourier transform infrared spectrometer in emission mode. *Appl. Opt.*, 46(12):2307–2319, Apr 2007.
- E. Kyrölä, J. Tamminen, G.W. Leppelmeier, V. Sofieva, S. Hassinen, J.L. Bertaux, A. Hauchecorne, F. Dalaudier, C. Cot, O. Korablev, O. Fanton d’Andon, G. Barrot, A. Mangin, B. Théodore, M. Guirlet, F. Etanchaud, P. Snoeij, R. Koopman, L. Saavedra, R. Fraisse, D. Fussen, and F. Vanhellemont. GOMOS on envisat: an overview. *Advances in space research*, 33(7):1020–1028, 2004.
- John H. Lienhard IV and John H. Lienhard V. *A Heat Transfer Textbook*. Phlogiston Press, Cambridge, Massachusetts, U.S.A., 5 edition, 2019.
- L. E. Mauldin, N. H. Zaun, M. P. McCormick Jr., J. H. Guy, and W. R. Vaughn. Stratospheric Aerosol And Gas Experiment II Instrument: A Functional Description. *Optical Engineering*, 24(2):307 – 312, 1985.
- M. McComrick, J. Zawodny, R. Veiga, J. Larson, and P. Wang. An overview of SAGE I and II ozone measurements. *Planetary and Space Science*, 37(12):1567 – 1586, 1989.
- K. Mohanakumar. *Stratosphere Troposphere Interactions: An Introduction*. Springer Netherlands, Dordrecht, 2008.

- L. Novak and G. Eppeldauer. Linear hgcdte radiometer. *SPIE: Imaging Infrared: Scene Simulation, Modeling, and Real Image Tracking*, 1110:91–96, 1989.
- C. Piesch, C. Sartorius, F. Friedl-Vallon, T. Gulde, S. Heger, E. Kretschmer, G. Maucher, H. Nordmeyer, J. Barthel, A. Ebersoldt, F. Hase, F. Graf, A. Klienert, t. Neubert, and H. J. Schillings. The mechanical and thermal setup of the GLORIA spectrometer. *Atmospheric Measurement Techniques*, pages 1773–1787, 2015.
- Kim Rahmelow. Electronic influences on an infrared detector signal: nonlinearity and amplification. *Appl. Opt.*, 36(10):2123–2132, Apr 1997.
- Henry E. Revercomb, H. Buijs, Hugh B. Howell, D. D. LaPorte, William L. Smith, and L. A. Sromovsky. Radiometric calibration of ir fourier transform spectrometers: solution to a problem with the high-resolution interferometer sounder. *Appl. Opt.*, 27(15):3210–3218, Aug 1988.
- M. Riese, F. Fiedl-Vallon, R. Spang, P. Preusse, C. Schiller, L. Hoffmann, P. Konopka, H. Oelhaf, Th. von Clarmann, and M. Hopfner. Global limb radiance imager for the atmosphere (GLORIA): Scientific objectives. *Atmospheric Measurement Techniques*, 1(7): 1915–1928, 2014.
- A. Rogalski, Malgorzata Kopytko, and Piotr Martyniuk. *Antimonide-based Infrared Detectors: A New Perspective*. SPIE, 2018.
- Ethan Runge. Limb imaging fourier transform spectrometer experiment (LIFE). Master’s thesis, University of Saskatchewan, Saskatoon, Saskatchewan, Canada, 2018.
- Murray Salby. *Physics of the Atmosphere and Climate*. Cambridge University Press, New York, NY, 2012.
- Walter Scott. Electron mobility in hg1xcdxte. *Journal of Applied Physics*, 43(3):1055–1062, 1972.
- M. K. Sha. *Characterization and Optimization of the new Imagining Fourier Transform Spectrometer GLORIA*. PhD thesis, Karlsruhe Institute of Technology, Karlsruhe, Germany, 2013.
- S. Solomon, D. Qin, M. Manning, R. Alley, T. Berntsen, N. Bindoff, Z. Chen, A. Chidhaisong, J. Gregory, G. Hegerl, M. Heimann, B. Hewitson, B. Hoskins, F. Joos, J. Jouzel, V. Kattsov, U. Lohmann, T. Matsuno, M. Molina, N. Nicholls, J. Overpeck, G. Raga, V. Ramaswamy, and J. Ren. Climate change 2007: the physical science basis. Technical report, Cambridge University Press, 2007.
- R. J. Thomas, C. A. Barth, G. J. Rottman, D. W. Rusch, G. H. Mount, G. M. Lawrence, R. W. Sanders, G. E. Thomas, and L. E. Clemens. Ozone density distribution in the mesosphere (50-90 km) measured by the SME limb scanning near infrared spectrometer. *Geophysical Research Letters*, 10(4):245–248, 1983.

- Larry W. Thomason and Ghassan Taha. SAGE III aerosol extinction measurements: Initial results. *Geophysical Research Letters*, 30(12), 2003.
- Philippe Vincent. Strato-science 2019 kick-off meeting presentation, 2 2019.
- Peter von Böckh and Thomas Wetzel. *Heat Transfer: Basics and Practice*. Springer, Berlin, Heidelberg, 2012.
- J. Wallace and P. Hobbs. *Atmospheric Science: An introductory survey*. Elsevier Academic Press, Burlington, MA, 2006.
- J. Wertz, D. Everett, and J. Puschell. *Space Mission Engineering: The New SMAD*. Micro-cosm Press, Hawthorne, CA, 2015.
- World Meteorological Organization. Atmospheric ozone 1985. Technical Report 16, WMO, 1986.

APPENDIX A

POST-FLIGHT SIMULATION THERMAL PROPERTIES

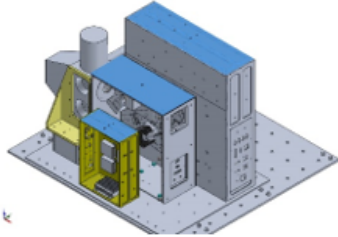
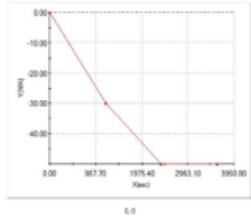
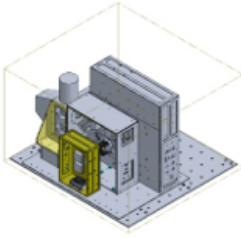
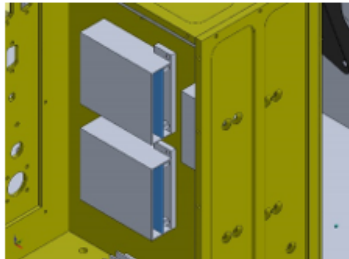
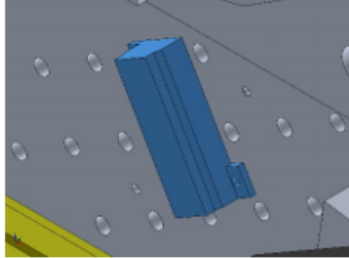
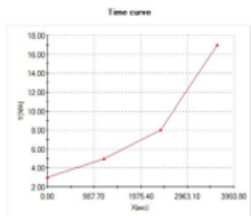
The purpose of this appendix is to provide all thermal inputs and settings used in the final simulations of the LIFE model. Using the following properties, the LIFE thermal simulations can be exactly reproduced, given the LIFE CAD model. These tables are output from SolidWorks automatically for this purpose. An explanation of these tables and how they are interpreted is described here.

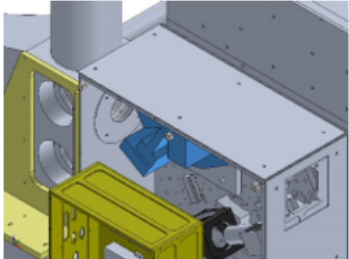
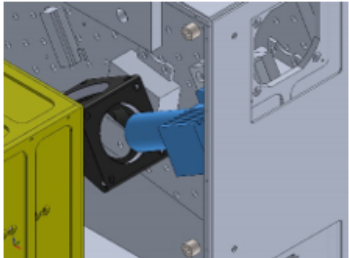
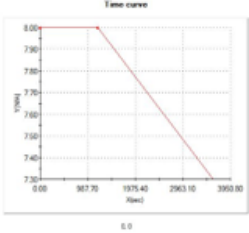
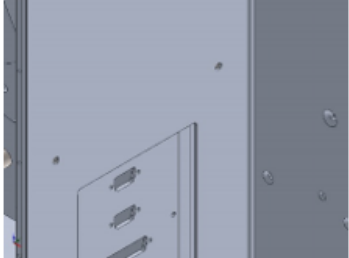
The tables are split into two colours, red and blue. The red tables describe all heat loads, such as radiation and power, and have four columns: load name, load image, load detail, and function curve. Load name describes the part in question as a variable name in the simulation, i.e. BB_Temp_Controllers would be the temperature controllers of the blackbody electronics box. The load image shows a screenshot of the model, with the affected areas (i.e. the surface of radiation, or the part emitting power) highlighted in blue. The third column, load details, describes all settings for that particular load set in the simulation. Finally, if applicable the fourth column is the function curve, which will show the radiation or heat power changing with time if it is a transient load. This box is blank if the load is steady-state.

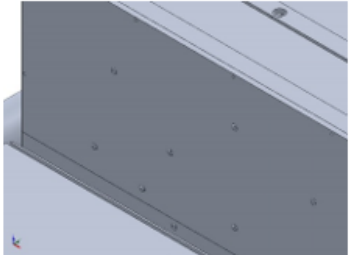
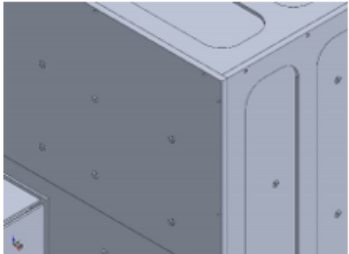
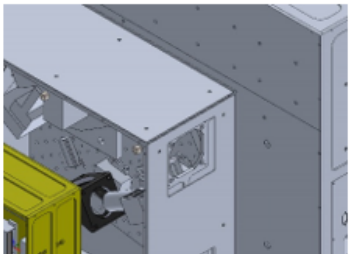
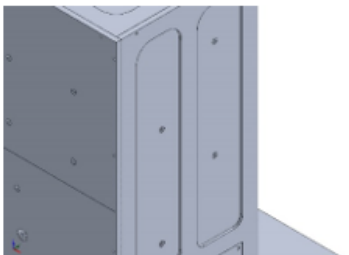
The blue tables describe custom contacts between parts, and are split into three columns: contact, contact image, and contact properties. The first column describes the name of the joint as a variable name. The second column is a screenshot showing the two surfaces that make contact, with one surface highlighted in blue and the other highlighted in purple. One surface may be hard to see in the image if it is facing away from view. The final column describes settings of the joint in question, most notably the thermal resistance value. For all part contacts not contained in the blue tables, it is assumed to be a bonded contact.

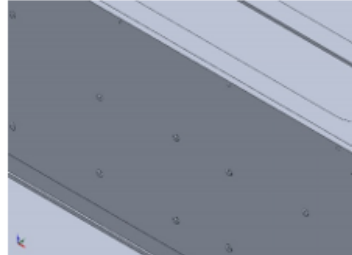
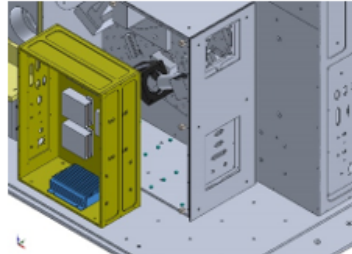
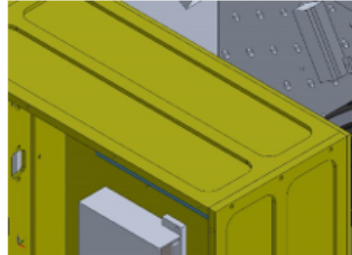
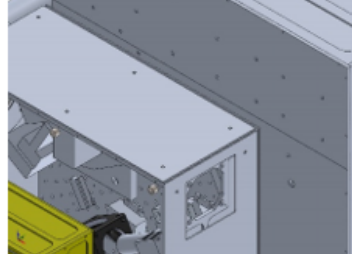
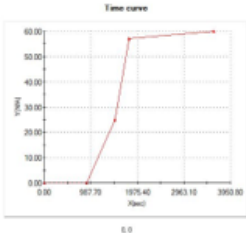
It is hoped that these heat loads will provide insight into the thermal simulations of LIFE and can be used to inform future instrument thermal models, and can also be used if anything happens to the thermal model file of LIFE.

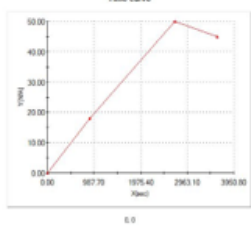
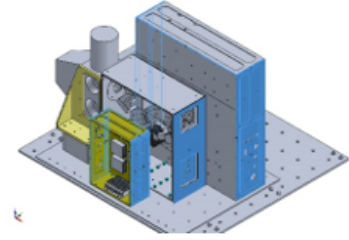
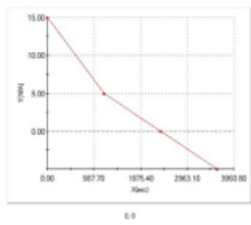
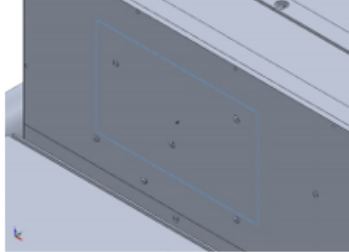
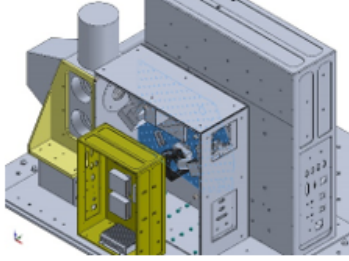
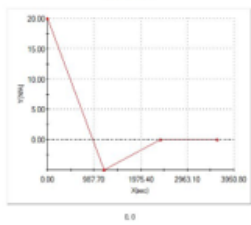
A.1 Ascent Phase: Part 1

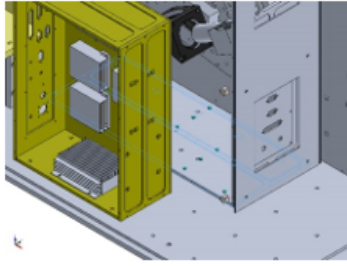
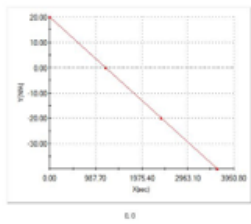
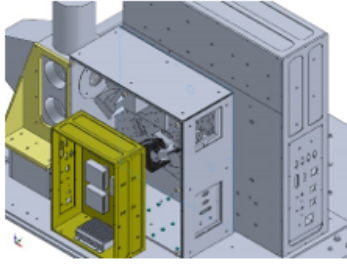
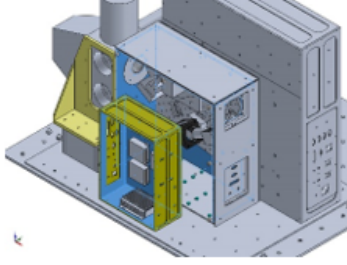
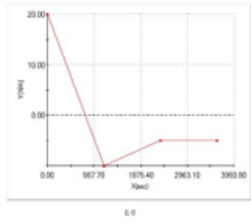
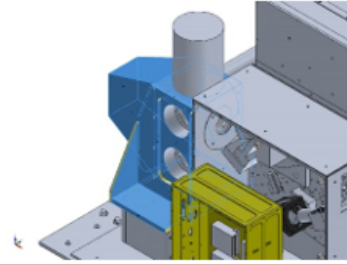
Load name	Load Image	Load Details	Function Curve
External_Atmosphere_Facing_Rad		Entities: 8 face(s) Radiation Type: Surface to ambient Ambient Temperature: 1 Celsius Emissivity: 0.77 View Factor: 0.8 Time variation: on	 <p>Time curve</p>
Initial_Temperatures		Entities: 1 component Initial temperature: 23 Celsius	
BB_Temp_Controllers		Entities: 3 components Heat Power Value: 1.2 W	
Optics_Heater		Entities: 1 component Heat Power Value: 1 W Time variation: on	 <p>Time curve</p>

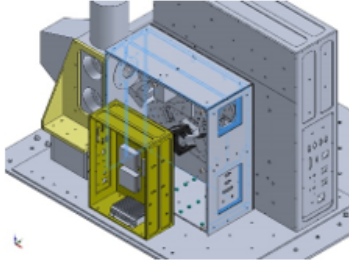
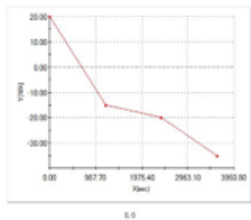
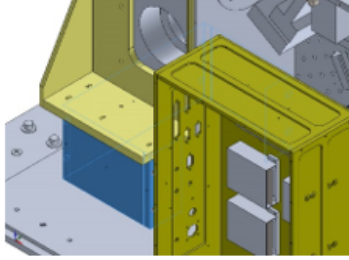
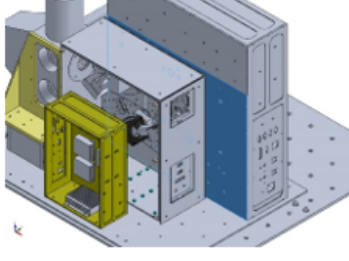
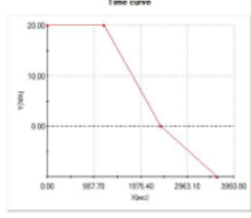
<p>FTS</p>		<p>Entities: 1 component Heat Power Value: 1 W</p>	
<p>MCT_Camera</p>		<p>Entities: 1 component Heat Power Value: 1 W Time variation: on</p>	 <p style="text-align: center;">Time curve</p>
<p>Ethernet_Switch</p>		<p>Entities: 1 component Heat Power Value: 6 W</p>	
<p>VIPAC</p>		<p>Entities: 1 component Heat Power Value: 24 W</p>	

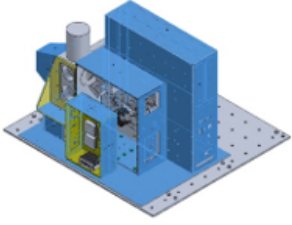
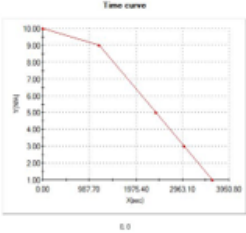
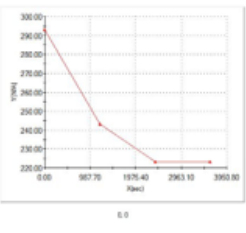
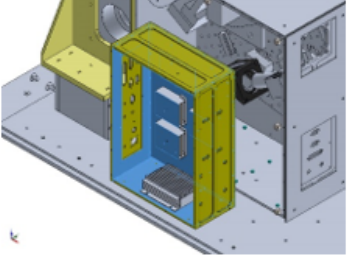
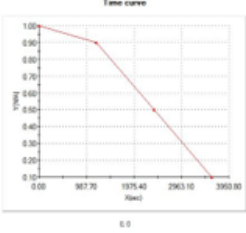
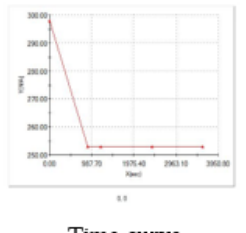
<p>FTS_Control _Board</p>		<p>Entities: 1 component Heat Power 5 W Value:</p>	
<p>CPU_Stack_ 1</p>		<p>Entities: 1 component Heat Power 1.25 W Value:</p>	
<p>DAQ_Boards</p>		<p>Entities: 2 components Heat Power 40 W Value:</p>	
<p>EBox_Temp _Controllers</p>		<p>Entities: 2 component(s) Heat Power 1.2 W Value:</p>	

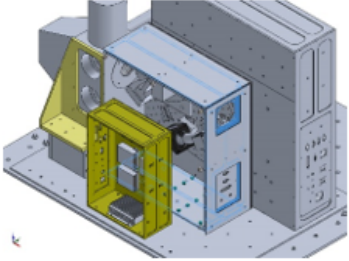
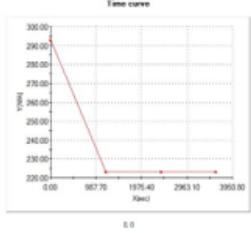
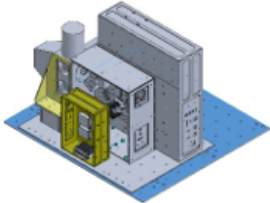
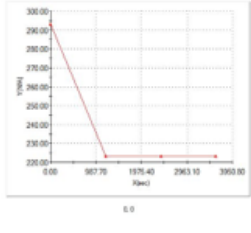
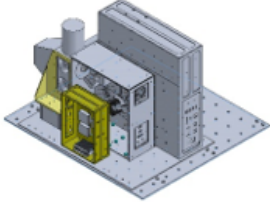
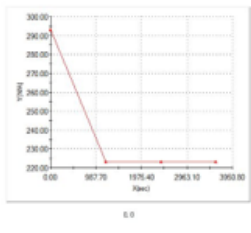
CPU_Stack_2		Entities: 1 component Heat Power Value: 13 W	
DC-DC_Converter		Entities: 3 components Heat Power Value: 15.6 W	
Motor_Controller		Entities: 1 component Heat Power Value: 1.5 W	
EBox_Heater_1		Entities: 4 components Heat Power Value: 1 W Time variation: on	 <p style="text-align: center;">Time curve</p>

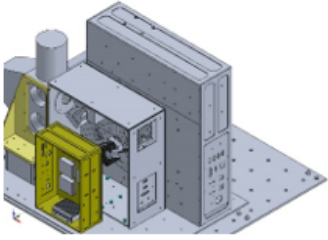
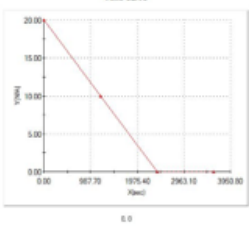
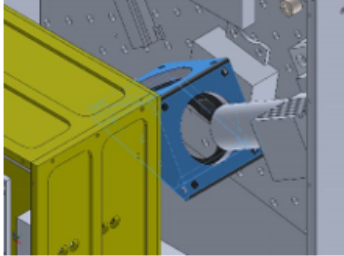
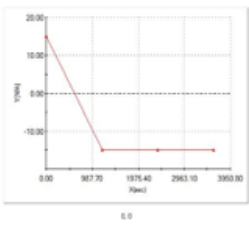
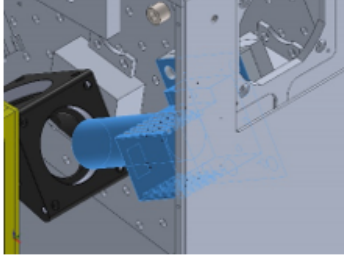
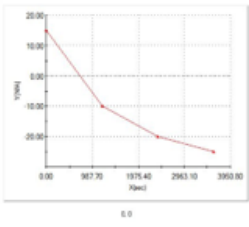
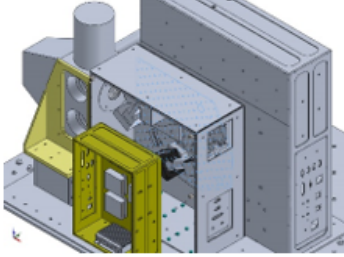
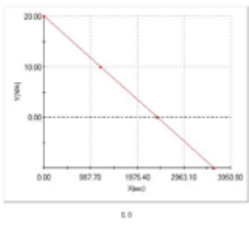
<p>BB_EBox_Heater</p>		<p>Entities: 1 component Heat Power: 1 W Value: on Time variation: on</p>	 <p>Time curve</p>
<p>External_Box_Rad</p>		<p>Entities: 28 face(s) Radiation Type: Surface to ambient Ambient Temperature: 1 Celsius Emissivity: 0.77 View Factor: 0.95 Time variation: on</p>	 <p>Time curve</p>
<p>BMXS_Rad</p>		<p>Entities: 2 face(s) Radiation Type: Surface to ambient Ambient Temperature: 10 Celsius Emissivity: 0.6 View Factor: 0.99</p>	
<p>Thor_Labs_Plate</p>		<p>Entities: 1 face(s) Radiation Type: Surface to ambient Ambient Temperature: 1 Celsius Emissivity: 0.77 View Factor: 0.4 Time variation: on</p>	 <p>Time curve</p>

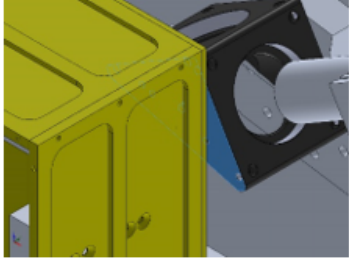
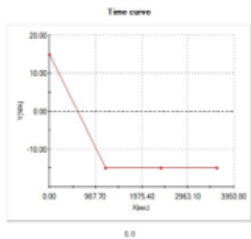
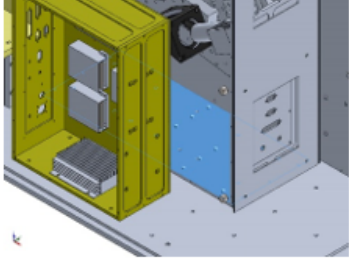
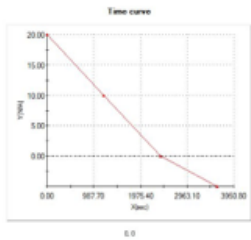
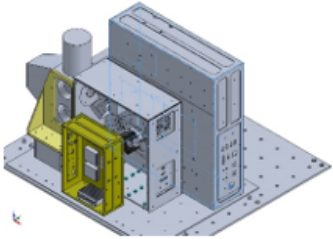
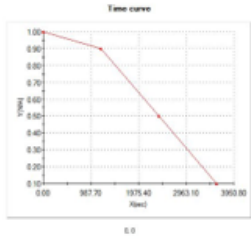
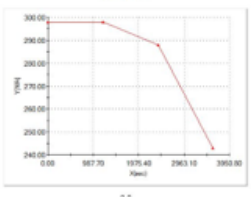
<p>OB_Bottom_Plate_Rad</p>		<p>Entities: 3 face(s) Radiation Type: Surface to ambient Ambient Temperature: 1 Celsius Emissivity: 0.77 View Factor: 0.99 Time variation: on</p>	 <p>Time curve</p>
<p>OB_EBox_Facing_Plate_Rad</p>		<p>Entities: 1 face(s) Radiation Type: Surface to ambient Ambient Temperature: 20 Celsius Emissivity: 0.77 View Factor: 0.99</p>	
<p>Internal_Box_Rad</p>		<p>Entities: 9 face(s) Radiation Type: Surface to ambient Ambient Temperature: 1 Celsius Emissivity: 0.77 View Factor: 0.6 Time variation: on</p>	 <p>Time curve</p>
<p>BB_Rad</p>		<p>Entities: 24 face(s) Radiation Type: Surface to ambient Ambient Temperature: 15 Celsius Emissivity: 0.05 View Factor: 0.9</p>	

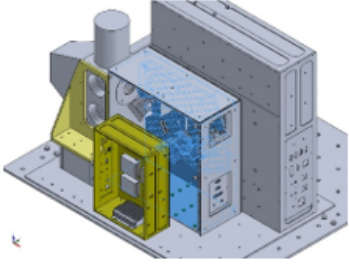
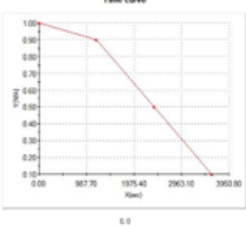
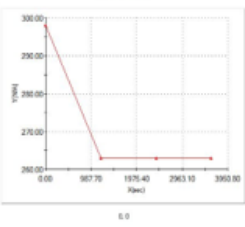
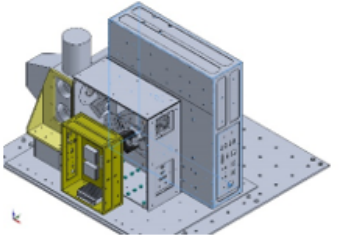
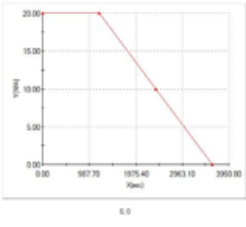
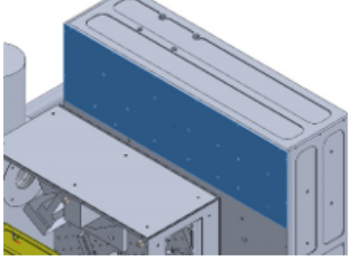
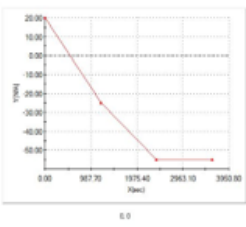
<p>OB_Inner_Box_Rad</p>		<p>Entities: 20 face(s) Radiation Type: Surface to ambient Ambient: 1 Celsius Temperature: 0.77 Emissivity: 0.95 View Factor: on Time variation:</p>	 <p>Time curve</p>
<p>BB_Support_Rad</p>		<p>Entities: 9 face(s) Radiation Type: Surface to ambient Ambient: 15 Celsius Temperature: 0.77 Emissivity: 0.9 View Factor:</p>	
<p>DAQ_Boards_Rad</p>		<p>Entities: 2 face(s) Radiation Type: Surface to ambient Ambient: 5 Celsius Temperature: 0.6 Emissivity: 0.95 View Factor:</p>	
<p>EBox_OB_Facing_Plate_Rad</p>		<p>Entities: 1 face(s) Radiation Type: Surface to ambient Ambient: 1 Celsius Temperature: 0.77 Emissivity: 0.6 View Factor: on Time variation:</p>	 <p>Time curve</p>

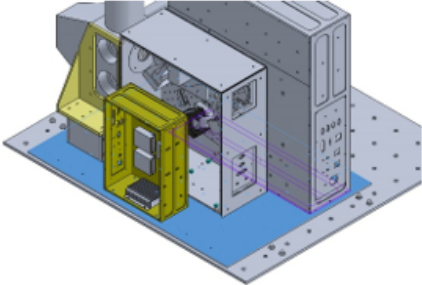
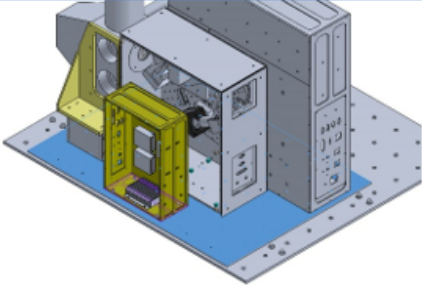
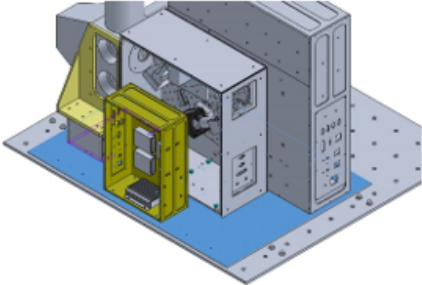
<p>Exterior_Convection</p>		<p>Entities: 40 face(s) Convection: 1 Coefficient: $W/(m^2.K)$ Time variation: On Temperature variation: Off Bulk Ambient Temperature: 1 Kelvin Time variation: On</p>	 <p>Time curve</p>
 <p>Time curve</p>			
<p>Interior_Convection</p>		<p>Entities: 9 face(s) Convection: 1 Coefficient: $W/(m^2.K)$ Time variation: On Temperature variation: Off Bulk Ambient Temperature: 1 Kelvin Time variation: On</p>	 <p>Time curve</p>
 <p>Time curve</p>			

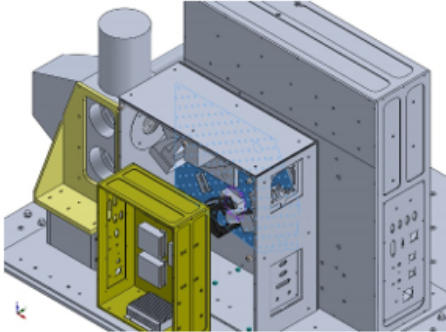
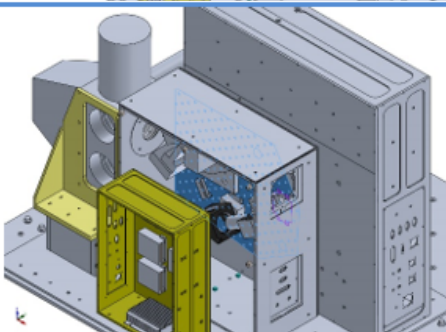
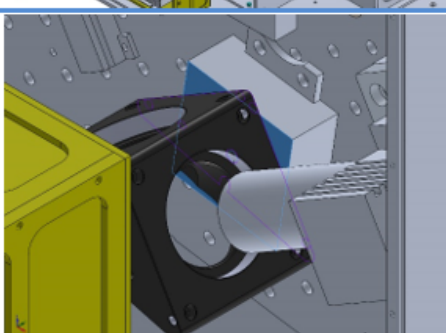
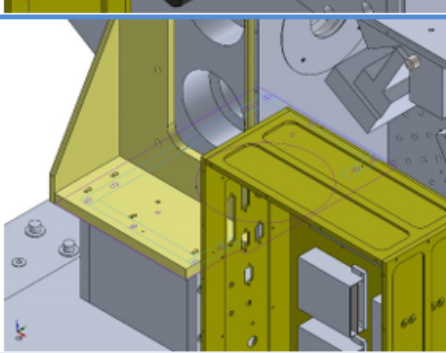
<p>Between_OBo x_Panel_Con vection</p>		<p>Entities: 9 face(s) Convection: 1 Coefficient: $W/(m^2.K)$ Time variation: Off Temperature variation: Off Bulk Ambient Temperature: 1 Kelvin Time variation: On</p>	 <p>Time curve</p>
<p>Convection-4</p>		<p>Entities: 1 face(s) Convection: 20 Coefficient: $W/(m^2.K)$ Time variation: Off Temperature variation: Off Bulk Ambient Temperature: 1 Kelvin Time variation: On</p>	 <p>Time curve</p>
<p>Convection-5</p>		<p>Entities: 1 face(s) Convection: 5 Coefficient: $W/(m^2.K)$ Time variation: Off Temperature variation: Off Bulk Ambient Temperature: 1 Kelvin Time variation: On</p>	 <p>Time curve</p>

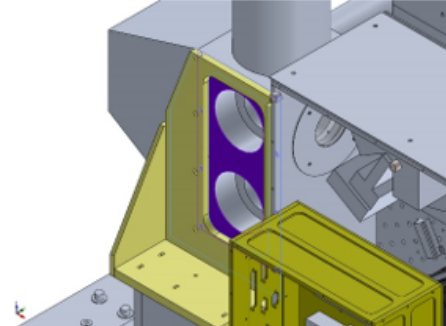
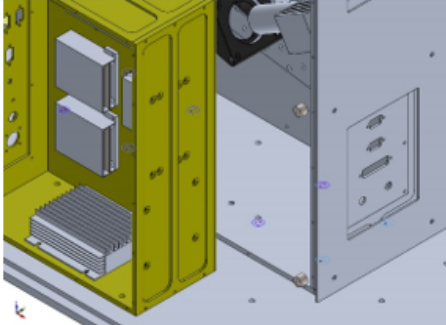
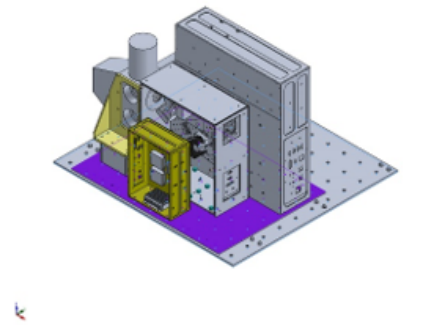
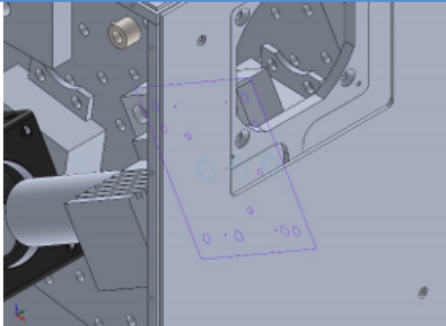
<p>Ebox_Cover_Plate</p>		<p>Entities: 1 face(s) Radiation Type: Surface to ambient Ambient Temperature: 1 Celsius Emissivity: 0.77 View Factor: 0.95 Time variation: on</p>	 <p>Time curve</p>
<p>Corner_Mirror</p>		<p>Entities: 7 face(s) Radiation Type: Surface to ambient Ambient Temperature: 1 Celsius Emissivity: 0.77 View Factor: 0.8 Time variation: on</p>	 <p>Time curve</p>
<p>MCT_Detector_Rad</p>		<p>Entities: 33 face(s) Radiation Type: Surface to ambient Ambient Temperature: 1 Celsius Emissivity: 0.95 View Factor: 0.95 Time variation: on</p>	 <p>Time curve</p>
<p>Thor_labs_rear_rad</p>		<p>Entities: 1 face(s) Radiation Type: Surface to ambient Ambient Temperature: 1 Celsius Emissivity: 0.77 View Factor: 0.75 Time variation: on</p>	 <p>Time curve</p>

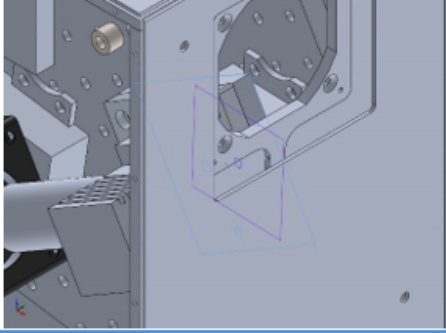
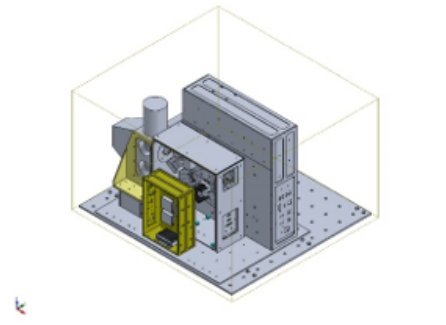
<p>Corner_mirror_top_rad</p>		<p>Entities: 1 face(s) Radiation Surface to ambient Type: ambient Ambient 1 Celsius Temperature: Emissivity: 0.77 View Factor: 0.95 Time on variation:</p>	 <p>Time curve</p>
<p>Radiation-21</p>		<p>Entities: 1 face(s) Radiation Surface to ambient Type: ambient Ambient 1 Celsius Temperature: Emissivity: 0.77 View Factor: 0.8 Time on variation:</p>	 <p>Time curve</p>
<p>Ebox_Interior_Convection</p>		<p>Entities: 8 face(s) Convection 1 Coefficient: W/(m^2.K) Time On variation: Temperature Off variation: Bulk 1 Kelvin Ambient Temperature: Time On variation:</p>	 <p>Time curve</p>
 <p>Time curve</p>			

<p>OB_Interior_ Convection</p>		<p>Entities: 42 face(s) Convection: 1 Coefficient: $W/(m^2.K)$ Time variation: On Temperature variation: Off Bulk Ambient Temperature: 1 Kelvin Time variation: On</p>	 <p>Time curve</p>
 <p>Time curve</p>			
<p>EB_Internal_ Box_Rad</p>		<p>Entities: 5 face(s) Radiation: Surface to ambient Type: ambient Ambient Temperature: 1 Celsius Emissivity: 0.77 View Factor: 0.6 Time variation: on</p>	 <p>Time curve</p>
<p>Top_EBox_ OB_Facing_ Plate_Rad</p>		<p>Entities: 1 face(s) Radiation: Surface to ambient Type: ambient Ambient Temperature: 1 Celsius Emissivity: 0.77 View Factor: 0.95 Time variation: on</p>	 <p>Time curve</p>

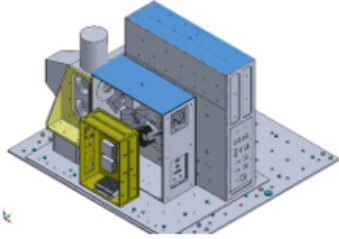
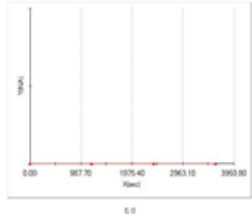
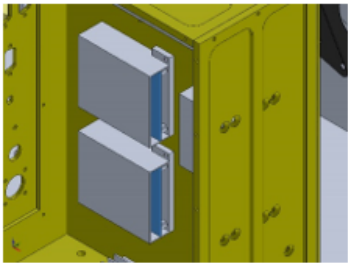
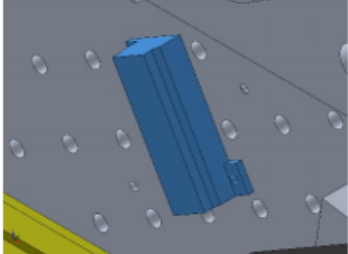
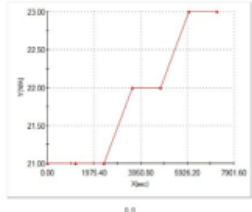
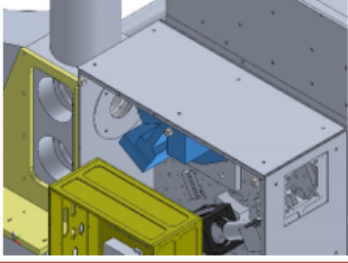
Contact	Contact Image	Contact Properties
Contact Set - Ebox to Baseplate		<p>Type: Thermal Resistance</p> <p>Entites: 6 face(s)</p> <p>Thermal Distributed</p> <p>Resistance:</p> <p>Value: 0.16(K.m²)/W</p> <p>Advanced: Node to surface</p>
Contact Set - BBEbox to Baseplate		<p>Type: Thermal Resistance</p> <p>Entites: 6 face(s)</p> <p>Thermal Distributed</p> <p>Resistance:</p> <p>Value: 0.16(K.m²)/W</p> <p>Advanced: Node to surface</p>
Contact Set - BB Support to Baseplate		<p>Type: Thermal Resistance</p> <p>Entites: 6 face(s)</p> <p>Thermal Distributed</p> <p>Resistance:</p> <p>Value: 0.16(K.m²)/W</p> <p>Advanced: Node to surface</p>

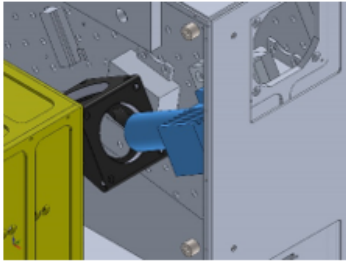
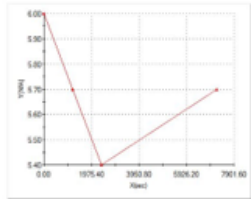
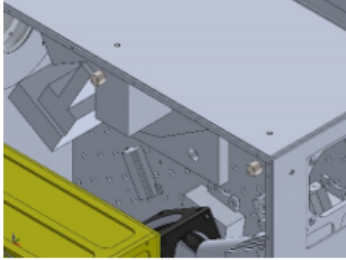
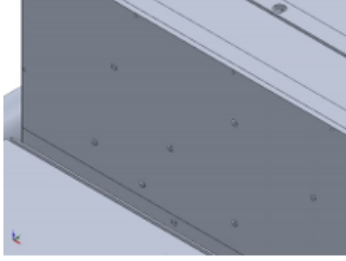
<p>Contact Set-16052</p>		<p>Type: Thermal Resistance Entites: 2 face(s) Thermal Resistance: Distributed Value: 0.2(K.m²)/W Advanced: Node to surface</p>
<p>Contact Set-16053</p>		<p>Type: Thermal Resistance Entites: 2 face(s) Thermal Resistance: Distributed Resistance: Distributed Value: 0.2(K.m²)/W Advanced: Node to surface</p>
<p>Contact Set-16055</p>		<p>Type: Thermal Resistance Entites: 2 face(s) Thermal Resistance: Distributed Resistance: Distributed Value: 0.2(K.m²)/W Advanced: Node to surface</p>
<p>Contact Set-16169</p>		<p>Type: Thermal Resistance Entites: 6 face(s) Thermal Resistance: Distributed Resistance: Distributed Value: 0.2(K.m²)/W Advanced: Node to surface</p>

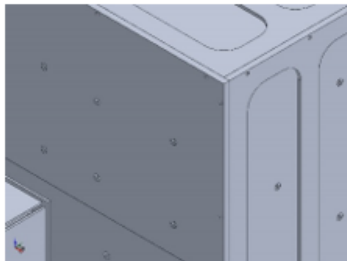
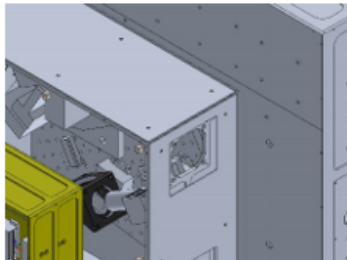
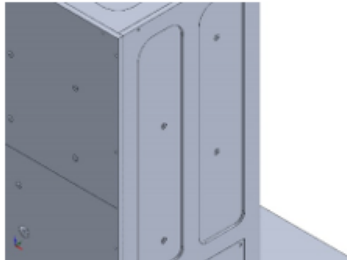
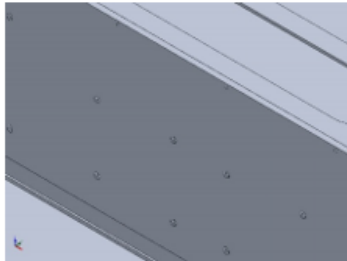
<p>Contact Set-16170</p>		<p>Type: Thermal Resistance Entites: 2 face(s) Thermal Resistance: Distributed Value: 0.5(K.m²)/W Advanced: Node to surface</p>
<p>Contact Set-17083</p>		<p>Type: Thermal Resistance Entites: 14 face(s) Thermal Resistance: Distributed Value: 0.16(K.m²)/W Advanced: Node to surface</p>
<p>Contact Set-17762</p>		<p>Type: Thermal Resistance Entites: 12 face(s) Thermal Resistance: Distributed Value: 0.16(K.m²)/W Advanced: Node to surface</p>
<p>Contact Set-18780</p>		<p>Type: Bonded contact pair Entites: 2 face(s)</p>

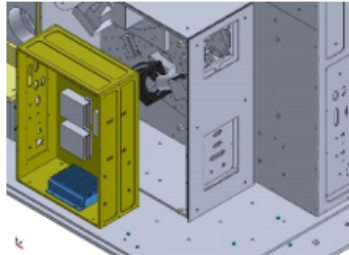
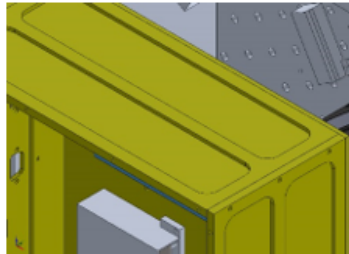
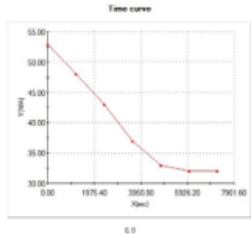
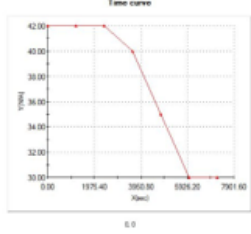
<p>Contact Set-19011</p>		<p>Type: Thermal Resistance Entites: 2 face(s) Thermal Resistance: Distributed Value: 0.12(K.m²)/W Advanced: Node to surface</p>
<p>Global Contact</p>		<p>Type: Bonded Components: 1 component(s) Options: Compatible mesh</p>

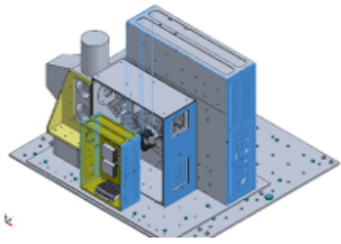
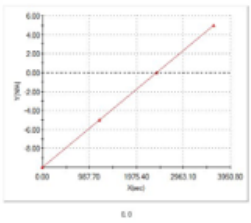
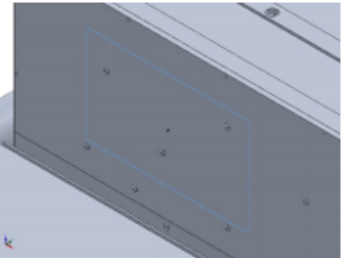
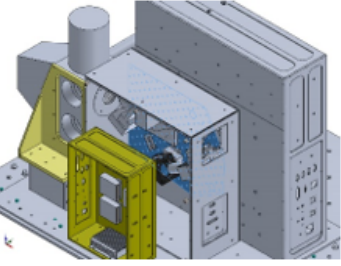
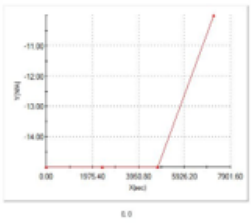
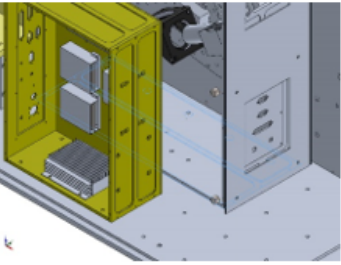
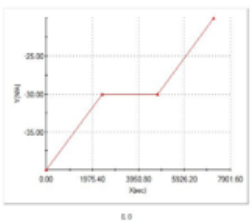
A.2 Ascent Phase: Part 2

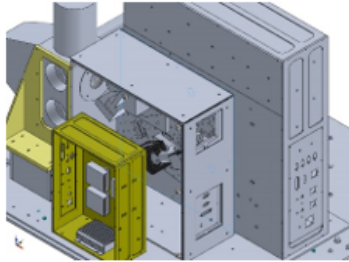
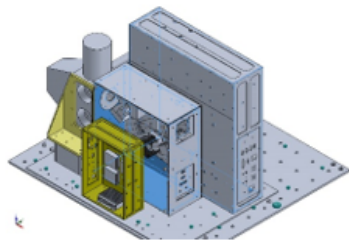
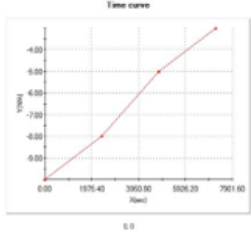
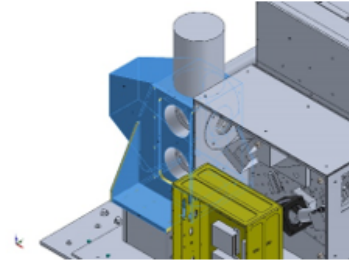
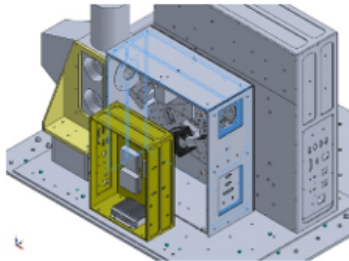
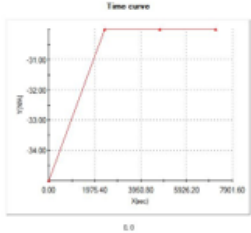
Load name	Load Image	Load Details	Function Curve
External_Atmosphere_Facing_Rad		Entities: 5 face(s) Radiation Type: Surface to ambient Ambient Temperature: 1 Celsius Emissivity: 0.77 View Factor: 0.9 Time variation: on	 <p>Time curve</p>
BB_Temp Controllers		Entities: 3 components Heat Power Value: 1.2 W Time variation: on	
Optics_Heater		Entities: 1 component Heat Power Value: 1 W Time variation: on	 <p>Time curve</p>
FTS		Entities: 1 component Heat Power Value: 1 W Time variation: on	

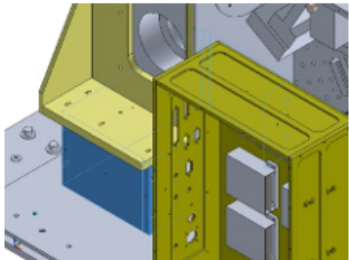
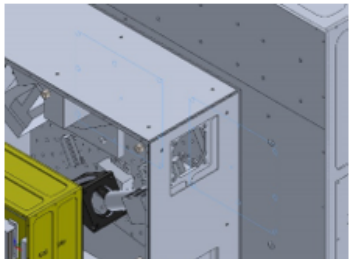
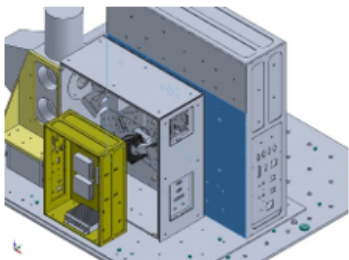
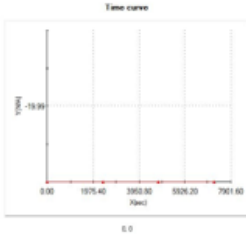
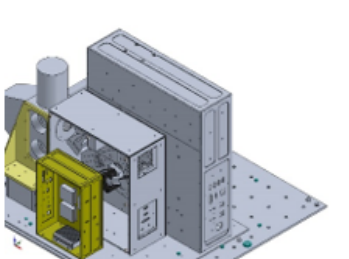
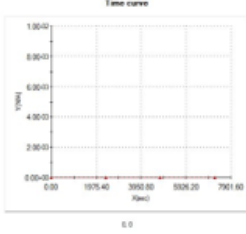
<p>MCT_Camera</p>		<p>Entities: 1 component Heat Power: 1 W Value: on Time variation:</p>	 <p>Time curve</p>
<p>Ethernet_Switch</p>		<p>Entities: 1 component Heat Power: 6 W Value:</p>	
<p>VIPAC</p>		<p>Entities: 1 component Heat Power: 24 W Value:</p>	
<p>FTS_Control Board</p>		<p>Entities: 1 component Heat Power: 5 W Value:</p>	

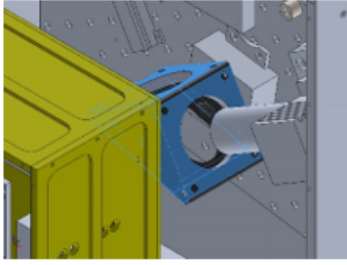
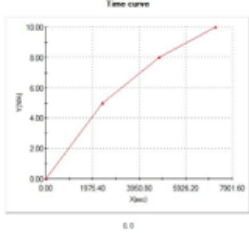
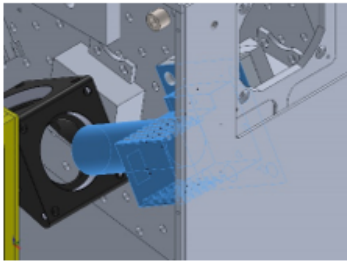
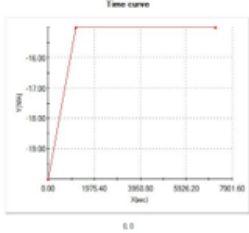
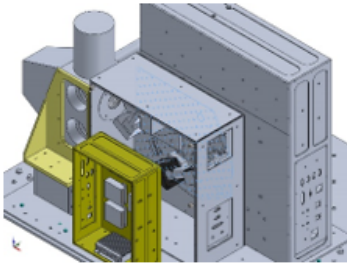
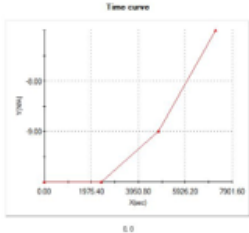
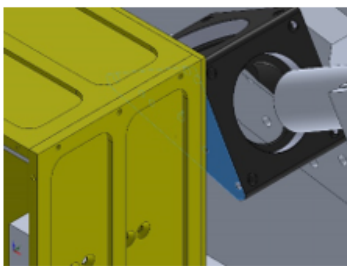
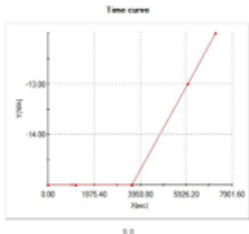
<p>CPU_Stack_ 1</p>		<p>Entities: 1 component Heat Power 1.25 W Value:</p>	
<p>DAQ_Boards</p>		<p>Entities: 2 components Heat Power 40 W Value:</p>	
<p>EBox_Temp _Controllers</p>		<p>Entities: 2 components Heat Power 1.2 W Value:</p>	
<p>CPU_Stack_ 2</p>		<p>Entities: 1 component Heat Power 13 W Value:</p>	

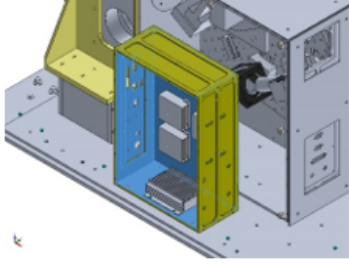
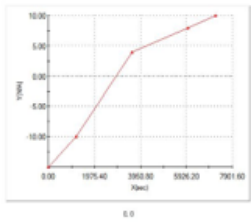
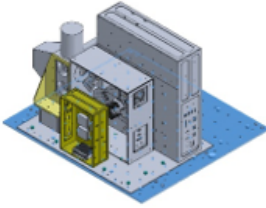
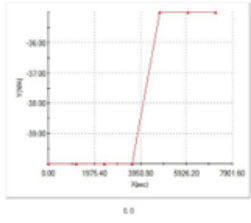
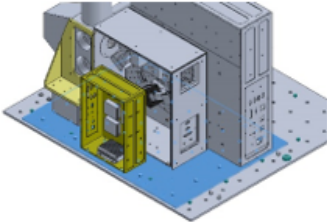
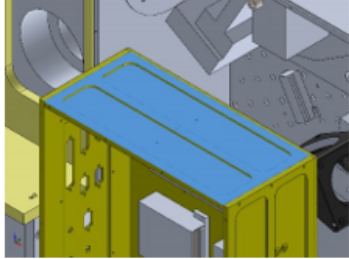
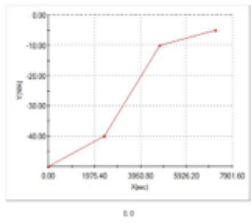
<p>DC-DC_Converter</p>		<p>Entities: 3 components Heat Power Value: 15.6 W</p>	
<p>Motor_Controller</p>		<p>Entities: 1 component Heat Power Value: 1.5 W</p>	
<p>EBox_Heater_1</p>		<p>Entities: 4 components Heat Power Value: 1 W Time variation: on</p>	 <p>Time curve</p>
<p>BB_EBox_Heater</p>		<p>Entities: 1 component Heat Power Value: 1 W Time variation: on</p>	 <p>Time curve</p>

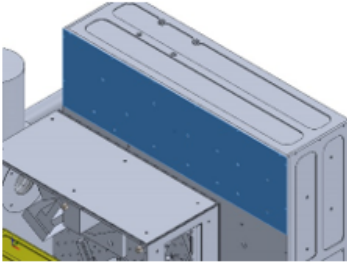
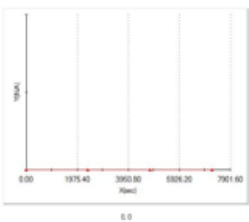
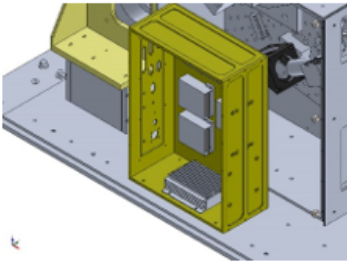
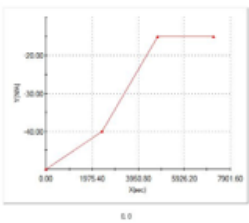
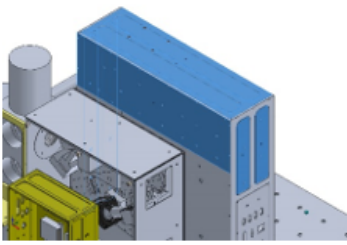
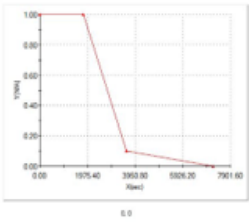
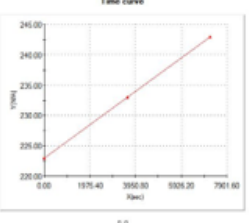
<p>External_Box_Rad</p>		<p>Entities: 28 face(s) Radiation Type: Surface to ambient Ambient Temperature: 1 Celsius Emissivity: 0.77 View Factor: 0.95 Time variation: on</p>	 <p>Time curve</p>
<p>BMXS_Rad</p>		<p>Entities: 2 face(s) Radiation Type: Surface to ambient Ambient Temperature: 10 Celsius Emissivity: 0.6 View Factor: 0.99</p>	
<p>Thor_Labs_Plate</p>		<p>Entities: 1 face(s) Radiation Type: Surface to ambient Ambient Temperature: 1 Celsius Emissivity: 0.77 View Factor: 0.4 Time variation: on</p>	 <p>Time curve</p>
<p>OB_Bottom_Plate_Rad</p>		<p>Entities: 3 face(s) Radiation Type: Surface to ambient Ambient Temperature: 1 Celsius Emissivity: 0.77 View Factor: 0.99 Time variation: on</p>	 <p>Time curve</p>

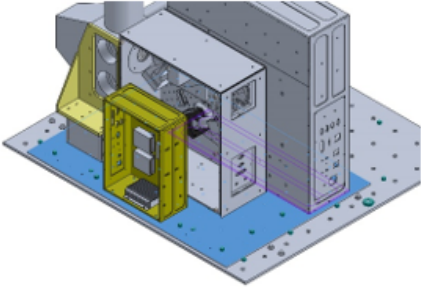
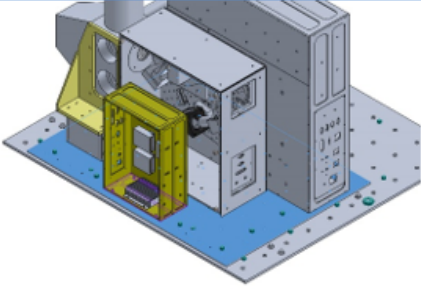
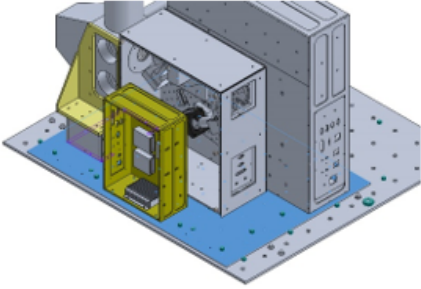
<p>OB_EBox_Facing_Plate_Rad</p>		<p>Entities: 1 face(s) Radiation Surface to ambient Type: ambient Ambient 5 Celsius Temperature: Emissivity: 0.77 View Factor: 0.99</p>	
<p>Internal_Box_Rad</p>		<p>Entities: 10 face(s) Radiation Surface to ambient Type: ambient Ambient 1 Celsius Temperature: Emissivity: 0.77 View Factor: 0.6 Time variation: on</p>	 <p>Time curve</p>
<p>BB_Rad</p>		<p>Entities: 24 face(s) Radiation Surface to ambient Type: ambient Ambient 15 Celsius Temperature: Emissivity: 0.05 View Factor: 0.9</p>	
<p>OB_Inner_Box_Rad</p>		<p>Entities: 20 face(s) Radiation Surface to ambient Type: ambient Ambient 1 Celsius Temperature: Emissivity: 0.77 View Factor: 0.95 Time variation: on</p>	 <p>Time curve</p>

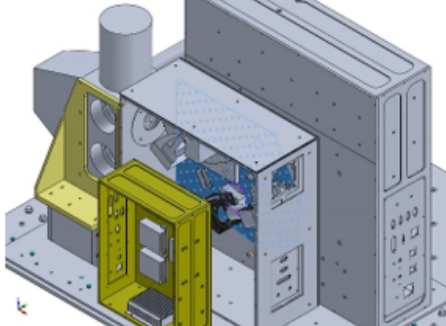
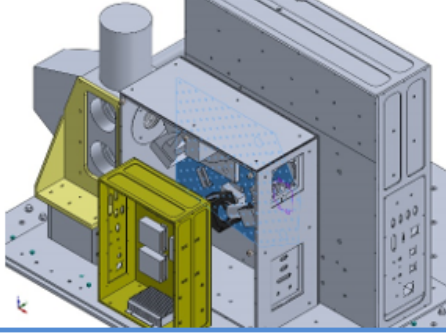
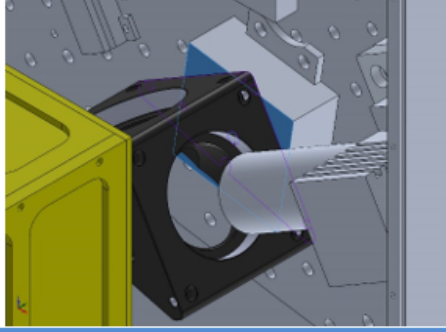
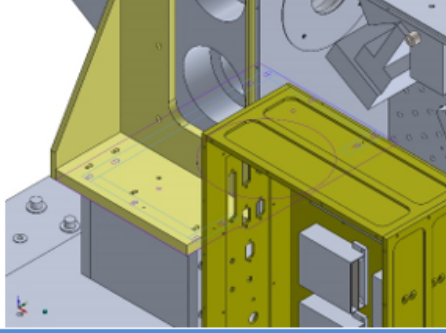
<p>BB_Support_Rad</p>		<p>Entities: 9 face(s) Radiation Surface to ambient Type: ambient Ambient 15 Celsius Temperature: Emissivity: 0.77 View Factor: 0.9</p>	
<p>DAQ_Boards_Rad</p>		<p>Entities: 2 face(s) Radiation Surface to ambient Type: ambient Ambient -5 Celsius Temperature: Emissivity: 0.6 View Factor: 0.95</p>	
<p>EBox_OB_Facing_Plate_Rad</p>		<p>Entities: 1 face(s) Radiation Surface to ambient Type: ambient Ambient 1 Celsius Temperature: Emissivity: 0.77 View Factor: 0.6 Time on variation:</p>	 <p>Time curve</p>
<p>Ebox_Cover_Plate</p>		<p>Entities: 1 face(s) Radiation Surface to ambient Type: ambient Ambient 1 Celsius Temperature: Emissivity: 0.77 View Factor: 0.95 Time on variation:</p>	 <p>Time curve</p>

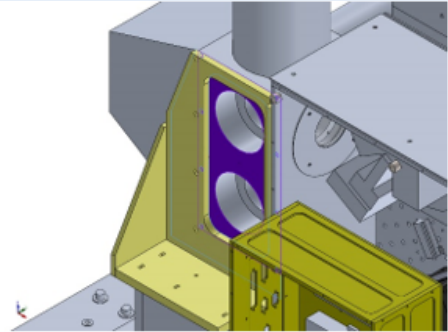
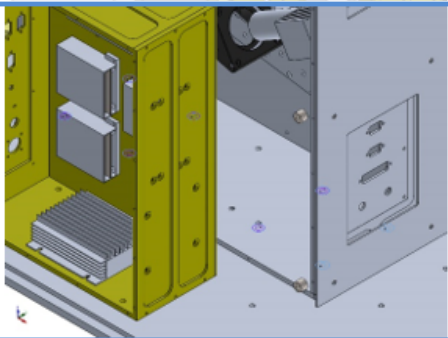
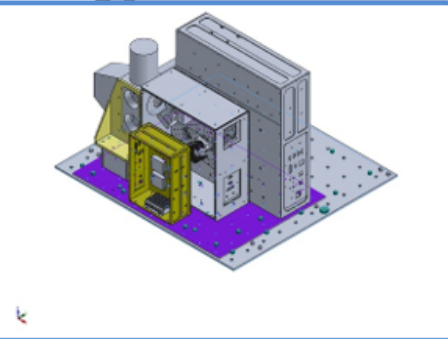
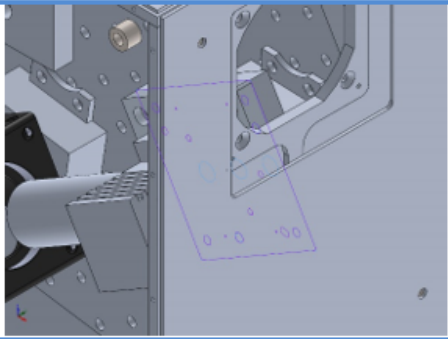
<p>Corner_Mirror</p>		<p>Entities: 7 face(s) Radiation Surface to ambient Type: ambient Ambient 1 Celsius Temperature: Emissivity: 0.77 View Factor: 0.8 Time on variation:</p>	 <p>Time curve</p>
<p>MCT_Detector_Rad</p>		<p>Entities: 33 face(s) Radiation Surface to ambient Type: ambient Ambient 1 Celsius Temperature: Emissivity: 0.95 View Factor: 0.95 Time on variation:</p>	 <p>Time curve</p>
<p>Thor_labs_rear_rad</p>		<p>Entities: 1 face(s) Radiation Surface to ambient Type: ambient Ambient 1 Celsius Temperature: Emissivity: 0.77 View Factor: 0.75 Time on variation:</p>	 <p>Time curve</p>
<p>Corner_mirror_top_rad</p>		<p>Entities: 1 face(s) Radiation Surface to ambient Type: ambient Ambient 1 Celsius Temperature: Emissivity: 0.77 View Factor: 0.95 Time on variation:</p>	 <p>Time curve</p>

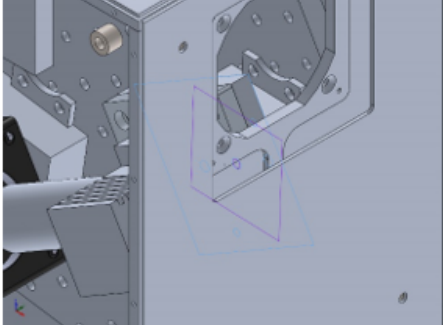
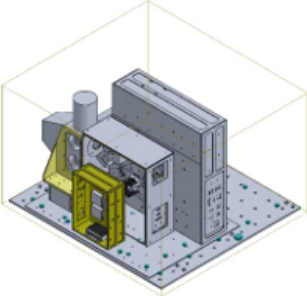
<p>bbebox_inner_rad</p>		<p>Entities: 6 face(s) Radiation Type: Surface to ambient Ambient: 1 Celsius Temperature: 0.77 Emissivity: 0.8 View Factor: on Time variation:</p>	 <p>Time curve</p>
<p>gondola_rad</p>		<p>Entities: 2 face(s) Radiation Type: Surface to ambient Ambient: 1 Celsius Temperature: 0.4 Emissivity: 0.85 View Factor: on Time variation:</p>	 <p>Time curve</p>
<p>instr_baseplate_top_rad</p>		<p>Entities: 2 face(s) Radiation Type: Surface to ambient Ambient: -35 Celsius Temperature: 0.77 Emissivity: 0.75 View Factor:</p>	
<p>bbebox_top_rad</p>		<p>Entities: 3 face(s) Radiation Type: Surface to ambient Ambient: 1 Celsius Temperature: 0.77 Emissivity: 0.85 View Factor: on Time variation:</p>	 <p>Time curve</p>

<p>Top_EBox_ OB_Facing_ Plate_Rad</p>		<p>Entities: 1 face(s) Radiation Surface to Type: ambient Ambient 1 Celsius Temperature: Emissivity: 0.77 View Factor: 0.99 Time on variation:</p>	 <p>Time curve</p>
<p>BBEbox_Cov er_Plate_Rad</p>		<p>Entities: 1 face(s) Radiation Surface to Type: ambient Ambient 1 Celsius Temperature: Emissivity: 0.77 View Factor: 0.8 Time on variation:</p>	 <p>Time curve</p>
<p>Convection-1</p>		<p>Entities: 8 face(s) Convection 1 Coefficient: W/(m².K) Time On variation: Temperature Off variation: Bulk 1 Kelvin Ambient Temperature: Time On variation:</p>	 <p>Time curve</p>
 <p>Time curve</p>			

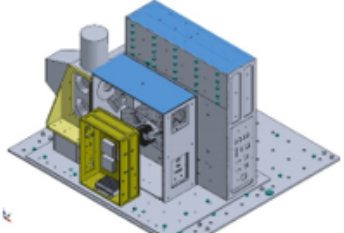
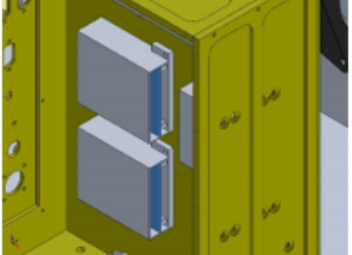
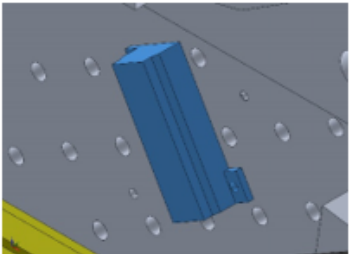
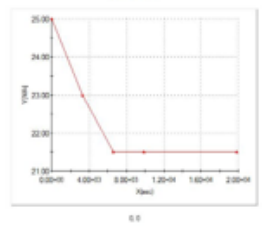
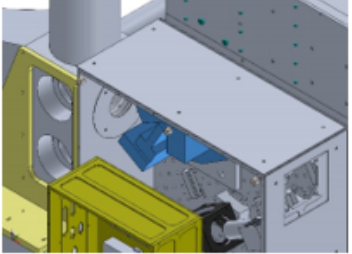
Contact	Contact Image	Contact Properties
<p>Contact Set - Ebox to Baseplate</p>		<p>Type: Thermal Resistance Entites: 6 face(s) Thermal Distributed Resistance: Value: 0.16(K.m²)/W Advanced: Node to surface</p>
<p>Contact Set - BBEbox to Baseplate</p>		<p>Type: Thermal Resistance Entites: 6 face(s) Thermal Distributed Resistance: Value: 0.16(K.m²)/W Advanced: Node to surface</p>
<p>Contact Set - BB Support to Baseplate</p>		<p>Type: Thermal Resistance Entites: 6 face(s) Thermal Distributed Resistance: Value: 0.16(K.m²)/W Advanced: Node to surface</p>

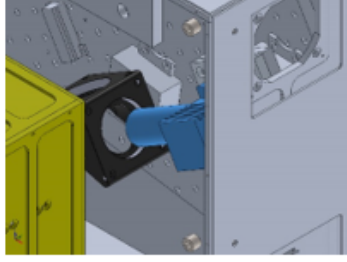
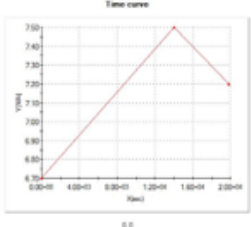
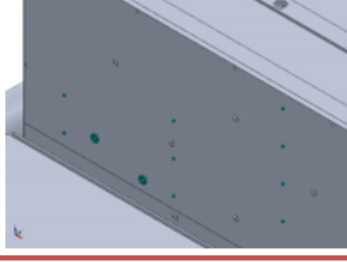
Contact Set-16052		<p>Type: Thermal Resistance</p> <p>Entites: 2 face(s)</p> <p>Thermal Resistance: Distributed</p> <p>Value: 0.2(K.m²)/W</p> <p>Advanced: Node to surface</p>
Contact Set-16053		<p>Type: Thermal Resistance</p> <p>Entites: 2 face(s)</p> <p>Thermal Resistance: Distributed</p> <p>Resistance:</p> <p>Value: 0.2(K.m²)/W</p> <p>Advanced: Node to surface</p>
Contact Set-16055		<p>Type: Thermal Resistance</p> <p>Entites: 2 face(s)</p> <p>Thermal Resistance: Distributed</p> <p>Resistance:</p> <p>Value: 0.2(K.m²)/W</p> <p>Advanced: Node to surface</p>
Contact Set-16169		<p>Type: Thermal Resistance</p> <p>Entites: 6 face(s)</p> <p>Thermal Resistance: Distributed</p> <p>Resistance:</p> <p>Value: 0.2(K.m²)/W</p> <p>Advanced: Node to surface</p>

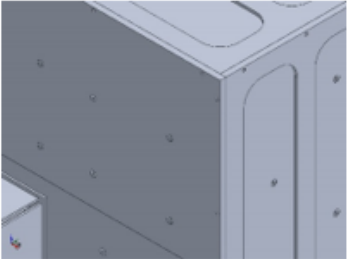
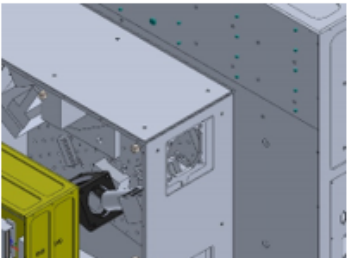
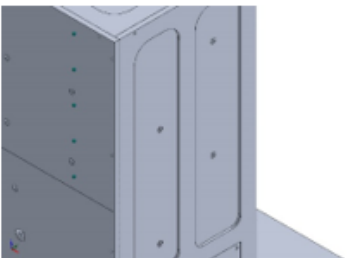
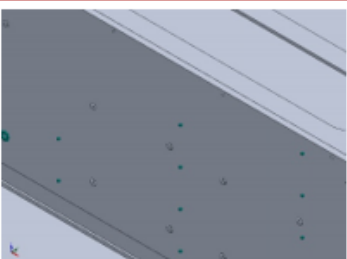
<p>Contact Set-16170</p>		<p>Type: Thermal Resistance Entites: 2 face(s) Thermal Resistance: Distributed Value: 0.5(K.m²)/W Advanced: Node to surface</p>
<p>Contact Set-17083</p>		<p>Type: Thermal Resistance Entites: 14 face(s) Thermal Resistance: Distributed Resistance: 0.16(K.m²)/W Advanced: Node to surface</p>
<p>Contact Set-17762</p>		<p>Type: Thermal Resistance Entites: 12 face(s) Thermal Resistance: Distributed Resistance: 0.16(K.m²)/W Advanced: Node to surface</p>
<p>Contact Set-18780</p>		<p>Type: Bonded contact pair Entites: 2 face(s)</p>

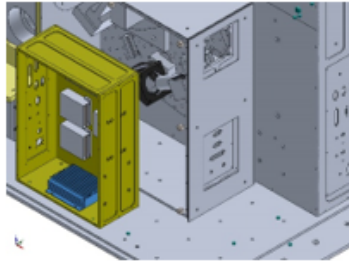
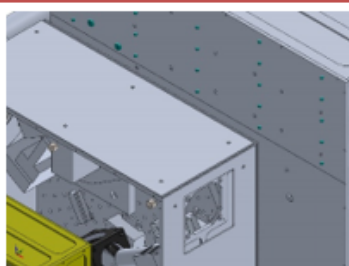
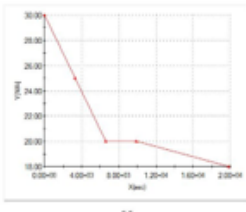
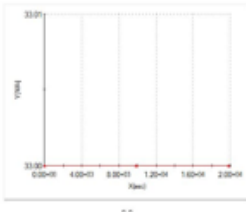
<p>Contact Set-19011</p>		<p>Type: Thermal Resistance Entites: 2 face(s) Thermal Resistance: Distributed Value: $0.12(\text{K}\cdot\text{m}^2)/\text{W}$ Advanced: Node to surface</p>
<p>Global Contact</p>		<p>Type: Bonded Components: 1 component(s) Options: Compatible mesh</p>

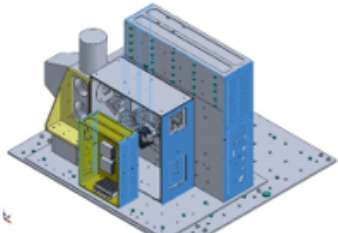
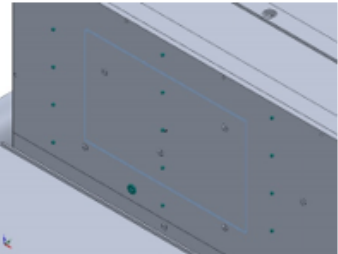
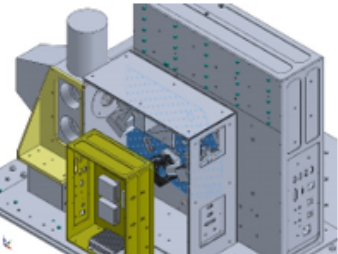
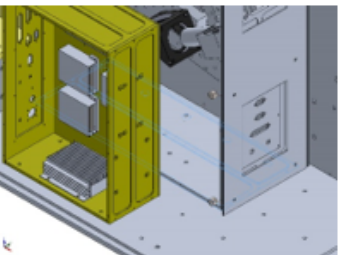
A.3 Float Phase

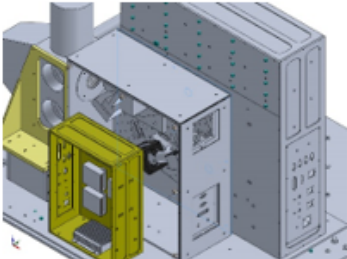
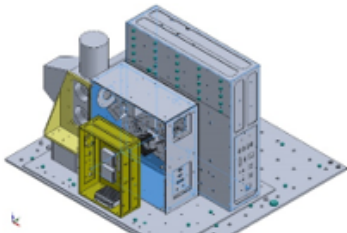
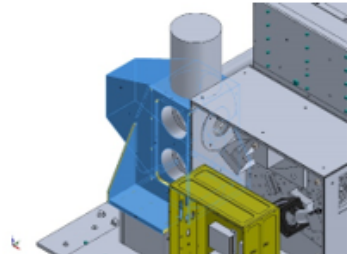
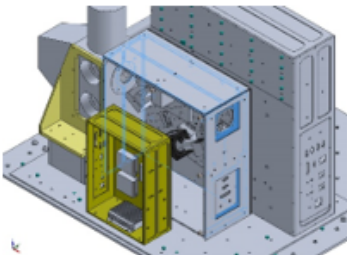
Load name	Load Image	Load Details	Function Curve
External_Atmosphere_Facing_Rad		<p>Entities: 5 face(s)</p> <p>Radiation Surface to ambient</p> <p>Type: ambient</p> <p>Ambient -30 Celsius</p> <p>Temperature:</p> <p>Emissivity: 0.77</p> <p>View Factor: 0.8</p>	
BB_Temp_Controller		<p>Entities: 3 components</p> <p>Heat Power 1.2 W</p> <p>Value:</p>	
Optics_Heater		<p>Entities: 1 component</p> <p>Heat Power 1 W</p> <p>Value: on</p> <p>Time variation:</p>	 <p>Time curve</p>
FTS		<p>Entities: 1 component</p> <p>Heat Power 1 W</p> <p>Value:</p>	

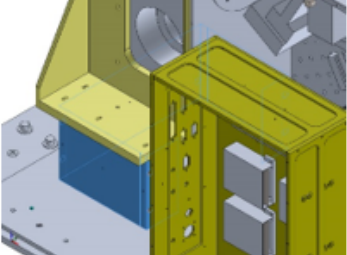
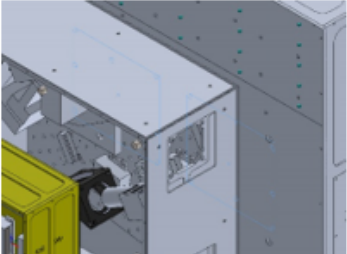
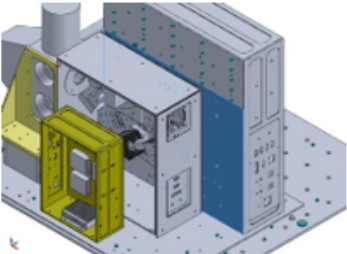
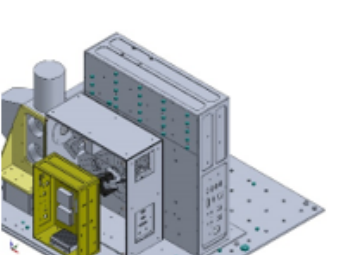
<p>MCT_Camera</p>		<p>Entities: 1 component Heat Power 1 W Value: Time on variation:</p>	 <p>Time curve</p>
<p>Ethernet_Switch</p>		<p>Entities: 1 component Heat Power 6 W Value:</p>	
<p>VIPAC</p>		<p>Entities: 1 component Heat Power 24 W Value:</p>	
<p>FTS_Control Board</p>		<p>Entities: 1 component Heat Power 5 W Value:</p>	

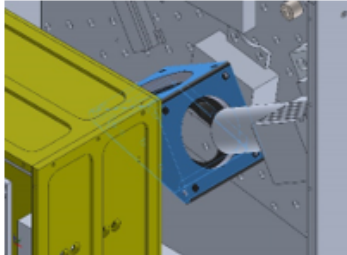
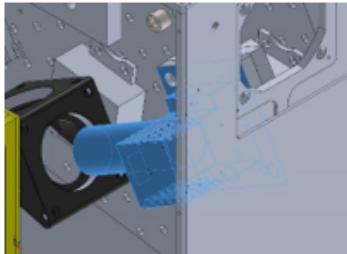
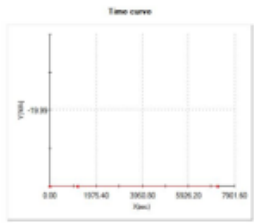
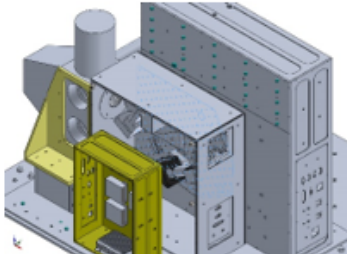
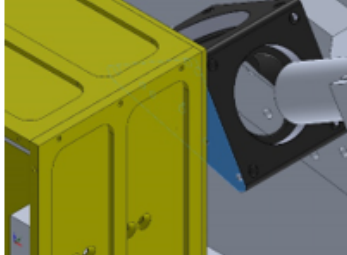
CPU_Stack_ 1		Entities: 1 component Heat Power 1.25 W Value:	
DAQ_Boards		Entities: 2 components Heat Power 40 W Value:	
EBox_Temp _Controllers		Entities: 2 components Heat Power 1.2 W Value:	
CPU_Stack_ 2		Entities: 1 component Heat Power 13 W Value:	

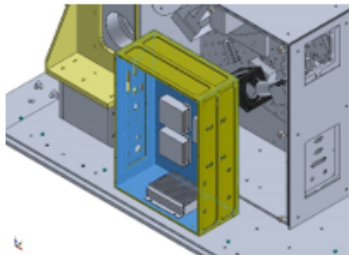
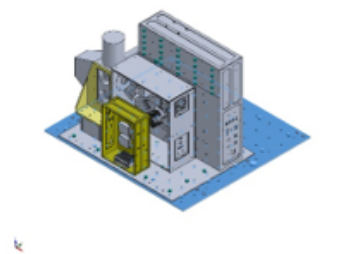
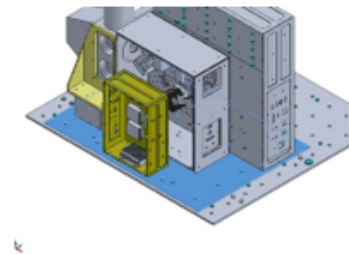
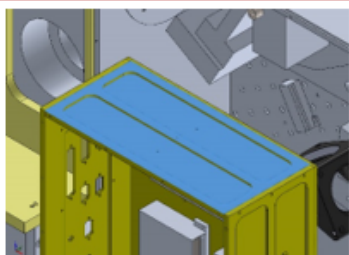
<p>DC- DC_Converte r</p>		<p>Entities: 3 components Heat Power 15.6 W Value:</p>	
<p>Motor_Contr oller</p>		<p>Entities: 1 component Heat Power 1.5 W Value:</p>	
<p>EBox_Heater _1</p>		<p>Entities: 4 components Heat Power 1 W Value: Time on variation:</p>	<p>Time curve</p>  <p>Time curve</p>
<p>BB_EBox_H eater</p>		<p>Entities: 1 component Heat Power 1 W Value: Time on variation:</p>	<p>Time curve</p>  <p>Time curve</p>

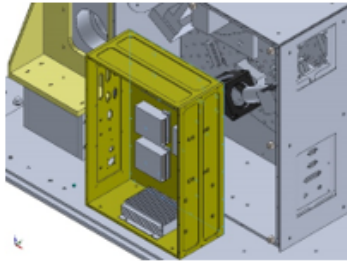
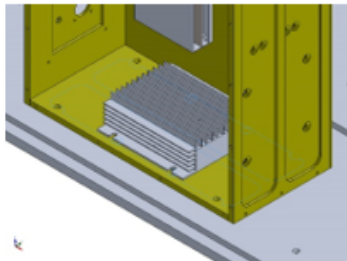
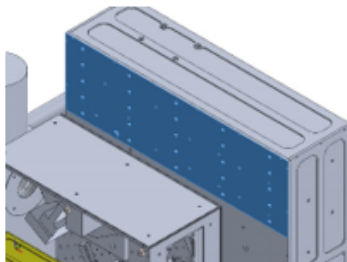
External_Box _Rad		Entities: 27 face(s) Radiation Surface to Type: ambient Ambient 0 Celsius Temperature: Emissivity: 0.77 View Factor: 0.95	
BMXS_Rad		Entities: 2 face(s) Radiation Surface to Type: ambient Ambient 10 Celsius Temperature: Emissivity: 0.6 View Factor: 0.99	
Thor_Labs_ Plate		Entities: 1 face(s) Radiation Surface to Type: ambient Ambient -5 Celsius Temperature: Emissivity: 0.77 View Factor: 0.4	
OB_Bottom_ Plate_Rad		Entities: 3 face(s) Radiation Surface to Type: ambient Ambient -20 Celsius Temperature: Emissivity: 0.77 View Factor: 0.99	

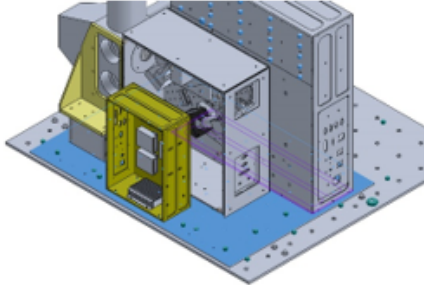
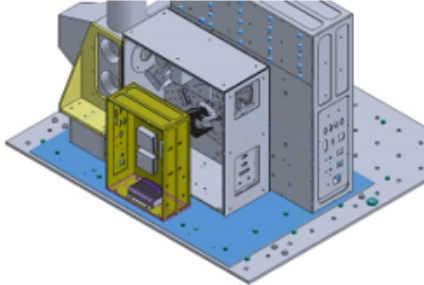
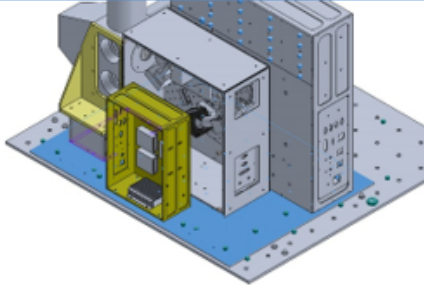
<p>OB_EBox_Facing_Plate_Rad</p>		<p>Entities: 1 face(s) Radiation Type: Surface to ambient Ambient Temperature: 5 Celsius Emissivity: 0.77 View Factor: 0.99</p>	
<p>Internal_Box_Rad</p>		<p>Entities: 10 face(s) Radiation Type: Surface to ambient Ambient Temperature: -5 Celsius Emissivity: 0.77 View Factor: 0.6</p>	
<p>BB_Rad</p>		<p>Entities: 24 face(s) Radiation Type: Surface to ambient Ambient Temperature: -10 Celsius Emissivity: 0.3 View Factor: 0.9</p>	
<p>OB_Inner_Box_Rad</p>		<p>Entities: 20 face(s) Radiation Type: Surface to ambient Ambient Temperature: -15 Celsius Emissivity: 0.77 View Factor: 0.95</p>	

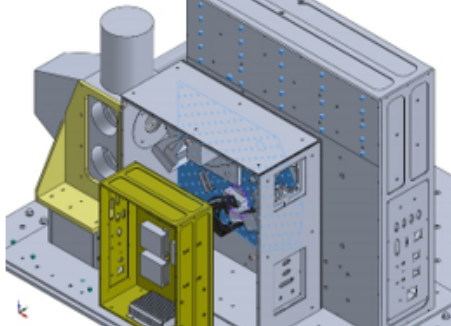
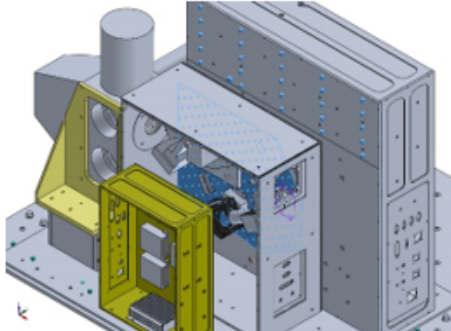
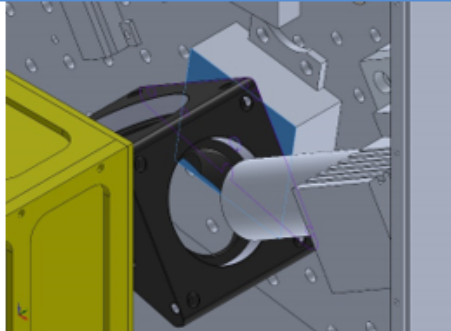
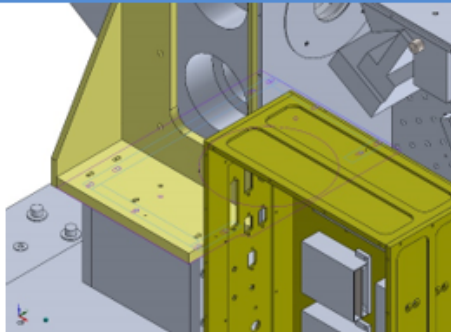
<p>BB_Support_ Rad</p>		<p>Entities: 9 face(s) Radiation Surface to Type: ambient Ambient 15 Celsius Temperature: Emissivity: 0.77 View Factor: 0.9</p>	
<p>DAQ_Boards _Rad</p>		<p>Entities: 2 face(s) Radiation Surface to Type: ambient Ambient -5 Celsius Temperature: Emissivity: 0.6 View Factor: 0.95</p>	
<p>EBox_OB_F acing_Plate_ Rad</p>		<p>Entities: 1 face(s) Radiation Surface to Type: ambient Ambient -25 Celsius Temperature: Emissivity: 0.77 View Factor: 0.7</p>	
<p>Ebox_Cover_ Plate</p>		<p>Entities: 1 face(s) Radiation Surface to Type: ambient Ambient 5 Celsius Temperature: Emissivity: 0.77 View Factor: 0.95</p>	

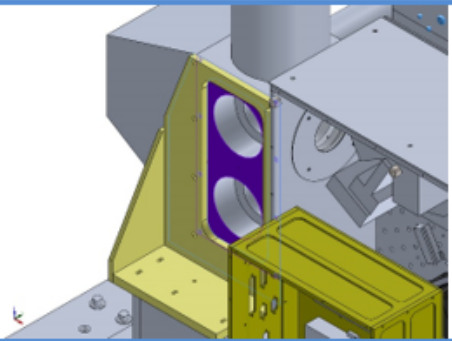
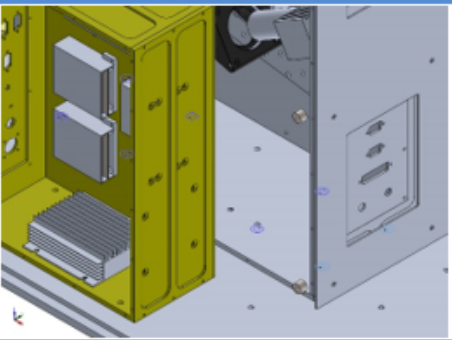
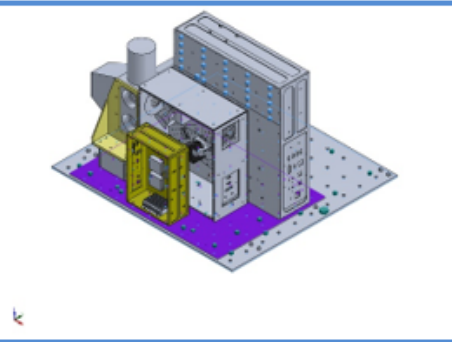
<p>Corner_Mirror</p>		<p>Entities: 7 face(s) Radiation Type: Surface to ambient Ambient Temperature: 10 Celsius Emissivity: 0.77 View Factor: 0.8</p>	
<p>MCT_Detector_Rad</p>		<p>Entities: 33 face(s) Radiation Type: Surface to ambient Ambient Temperature: 1 Celsius Emissivity: 0.95 View Factor: 0.95 Time on variation:</p>	 <p>Time curve</p>
<p>Thor_labs_rear_rad</p>		<p>Entities: 1 face(s) Radiation Type: Surface to ambient Ambient Temperature: -7 Celsius Emissivity: 0.77 View Factor: 0.75</p>	
<p>Corner_mirror_top_rad</p>		<p>Entities: 1 face(s) Radiation Type: Surface to ambient Ambient Temperature: -2.65 Celsius Emissivity: 0.77 View Factor: 0.95</p>	

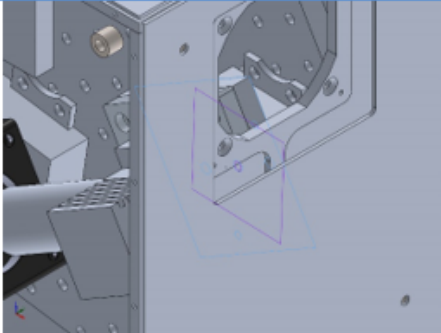
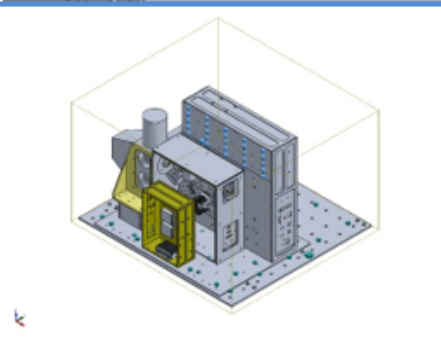
bbebox_inner_rad		Entities: 6 face(s) Radiation Type: Surface to ambient Ambient Temperature: 12 Celsius Emissivity: 0.77 View Factor: 0.8	
gondola_rad		Entities: 2 face(s) Radiation Type: Surface to ambient Ambient Temperature: -40 Celsius Emissivity: 0.4 View Factor: 0.85	
instr_baseplate_rad		Entities: 2 face(s) Radiation Type: Surface to ambient Ambient Temperature: -40 Celsius Emissivity: 0.77 View Factor: 0.75	
bbebox_top_rad		Entities: 3 face(s) Radiation Type: Surface to ambient Ambient Temperature: -10 Celsius Emissivity: 0.77 View Factor: 0.85	

<p>bbebox_rear_rad</p>		<p>Entities: 1 face(s) Radiation Surface to Type: ambient Ambient -5 Celsius Temperature: Emissivity: 0.77 View Factor: 0.9</p>	
<p>bbebox_bottom_rad</p>		<p>Entities: 2 face(s) Radiation Surface to Type: ambient Ambient -20 Celsius Temperature: Emissivity: 0.77 View Factor: 0.99</p>	
<p>Radiation-27</p>		<p>Entities: 1 face(s) Radiation Surface to Type: ambient Ambient -25 Celsius Temperature: Emissivity: 0.77 View Factor: 0.9</p>	

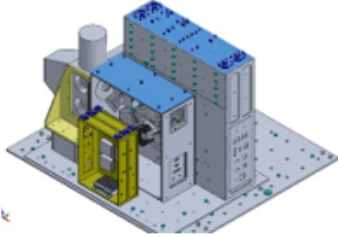
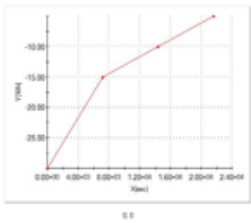
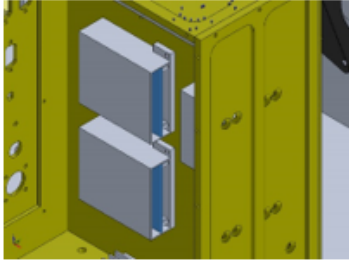
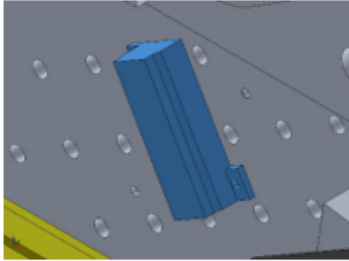
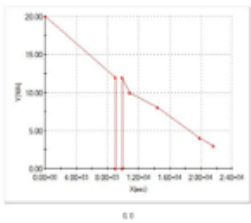
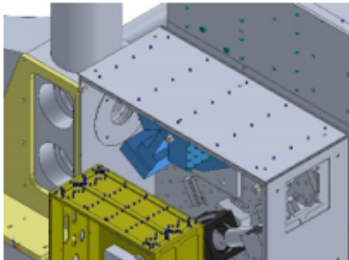
Contact	Contact Image	Contact Properties
Contact Set - Ebox to Baseplate		<p>Type: Thermal Resistance</p> <p>Entites: 6 face(s)</p> <p>Thermal Distributed</p> <p>Resistance:</p> <p>Value: 0.16(K.m²)/W</p> <p>Advanced: Node to surface</p>
Contact Set - BBEbox to Baseplate		<p>Type: Thermal Resistance</p> <p>Entites: 6 face(s)</p> <p>Thermal Distributed</p> <p>Resistance:</p> <p>Value: 0.16(K.m²)/W</p> <p>Advanced: Node to surface</p>
Contact Set - BB Support to Baseplate		<p>Type: Thermal Resistance</p> <p>Entites: 6 face(s)</p> <p>Thermal Distributed</p> <p>Resistance:</p> <p>Value: 0.16(K.m²)/W</p> <p>Advanced: Node to surface</p>

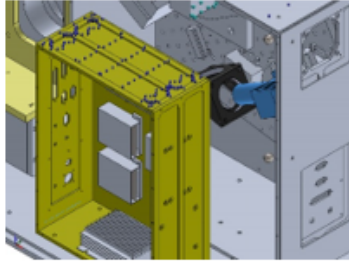
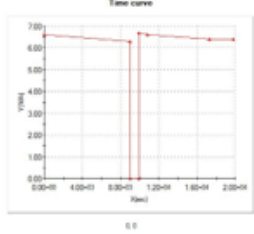
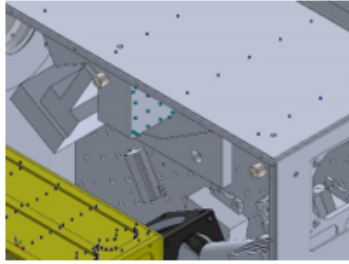
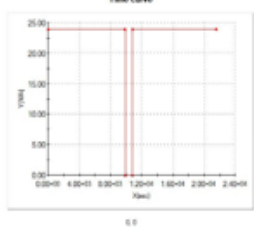
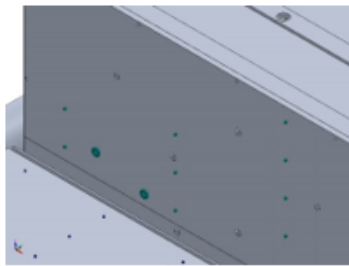
<p>Contact Set-16052</p>		<p>Type: Thermal Resistance Entites: 2 face(s) Thermal Distributed Resistance: Value: $0.2(K.m^2)/W$ Advanced: Node to surface</p>
<p>Contact Set-16053</p>		<p>Type: Thermal Resistance Entites: 2 face(s) Thermal Distributed Resistance: Value: $0.2(K.m^2)/W$ Advanced: Node to surface</p>
<p>Contact Set-16055</p>		<p>Type: Thermal Resistance Entites: 2 face(s) Thermal Distributed Resistance: Value: $0.2(K.m^2)/W$ Advanced: Node to surface</p>
<p>Contact Set-16169</p>		<p>Type: Thermal Resistance Entites: 6 face(s) Thermal Distributed Resistance: Value: $0.2(K.m^2)/W$ Advanced: Node to surface</p>

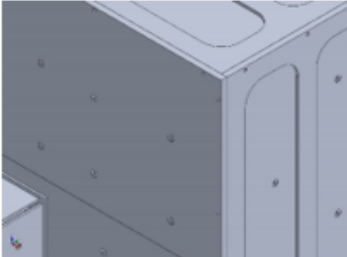
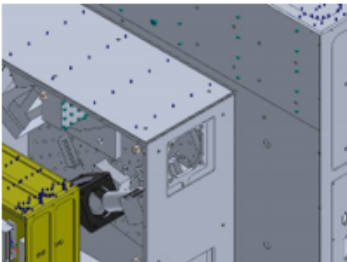
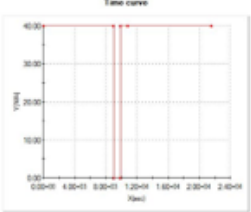
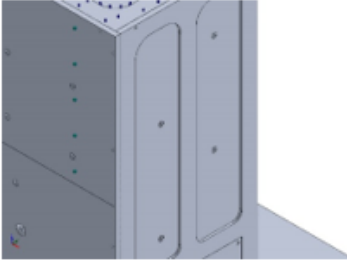
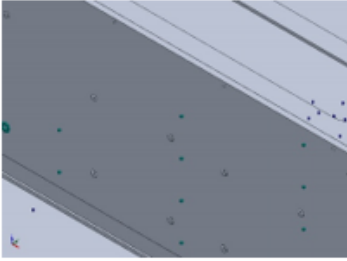
<p>Contact Set-16170</p>		<p>Type: Thermal Resistance Entites: 2 face(s) Thermal Resistance: Distributed Value: $0.5(K.m^2)/W$ Advanced: Node to surface</p>
<p>Contact Set-17083</p>		<p>Type: Thermal Resistance Entites: 14 face(s) Thermal Resistance: Distributed Resistance: Value: $0.16(K.m^2)/W$ Advanced: Node to surface</p>
<p>Contact Set-17762</p>		<p>Type: Thermal Resistance Entites: 12 face(s) Thermal Resistance: Distributed Resistance: Value: $0.16(K.m^2)/W$ Advanced: Node to surface</p>
<p>Contact Set-18780</p>		<p>Type: Bonded contact pair Entites: 2 face(s)</p>

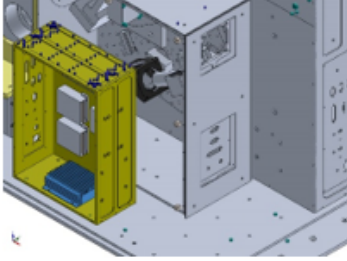
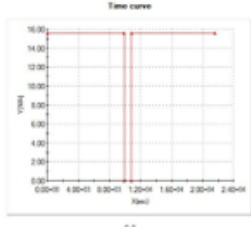
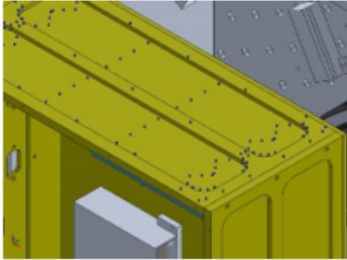
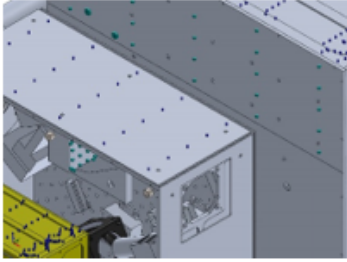
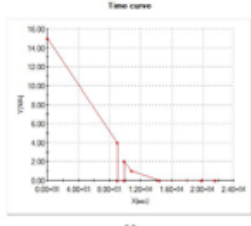
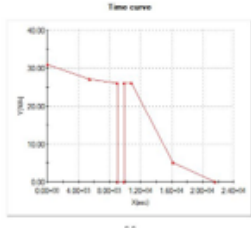
<p>Contact Set-19011</p>		<p>Type: Thermal Resistance</p> <p>Entites: 2 face(s)</p> <p>Thermal Resistance: Distributed</p> <p>Value: 0.12(K.m²)/W</p> <p>Advanced: Node to surface</p>
<p>Global Contact</p>		<p>Type: Bonded</p> <p>Components: 1 component(s)</p> <p>Options: Compatible mesh</p>

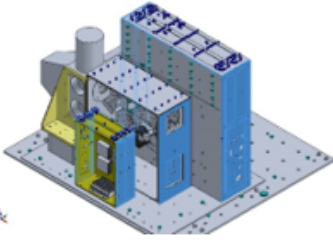
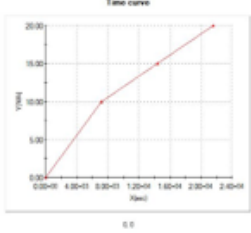
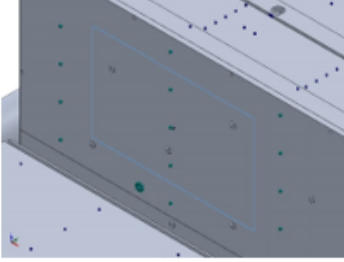
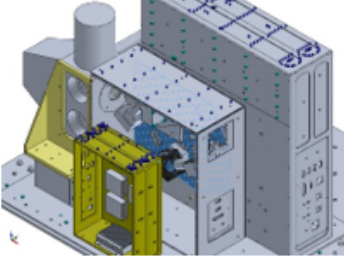
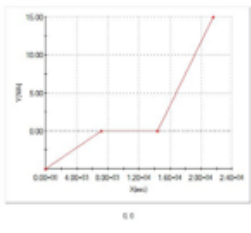
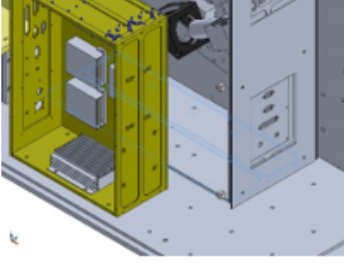
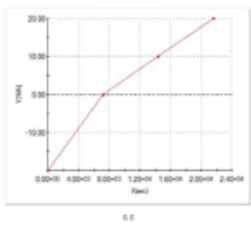
A.4 Sunrise Phase

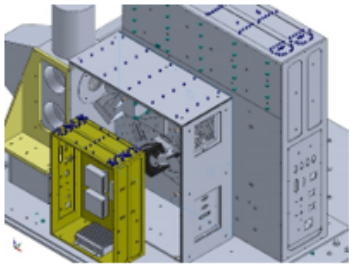
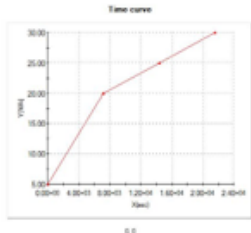
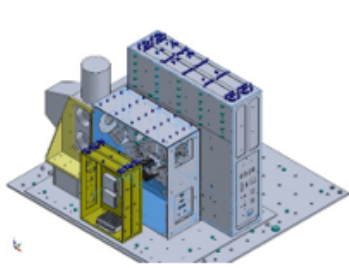
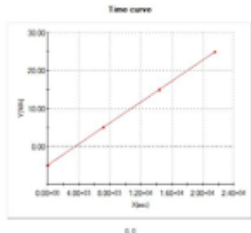
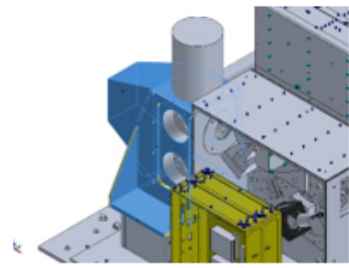
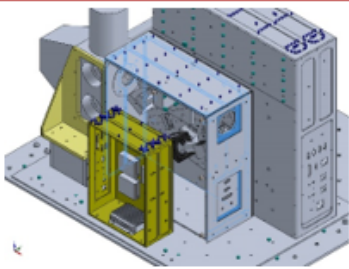
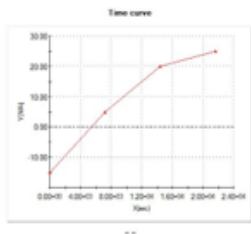
Load name	Load Image	Load Details	Function Curve
External_Atmosphere_Facing_Rad		<p>Entities: 5 face(s) Radiation Type: Surface to ambient Ambient Temperature: 1 Celsius Emissivity: 0.77 View Factor: 0.8 Time variation: on</p>	 <p>Time curve</p>
BB_Temp_Controller		<p>Entities: 3 components Heat Power Value: 1.2 W</p>	
Optics_Heater		<p>Entities: 1 component Heat Power Value: 1 W Time variation: on</p>	 <p>Time curve</p>
FTS		<p>Entities: 1 component Heat Power Value: 3 W</p>	

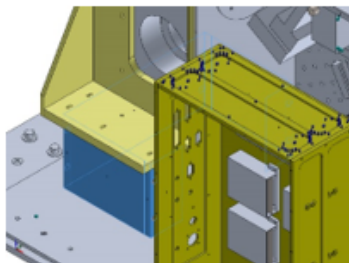
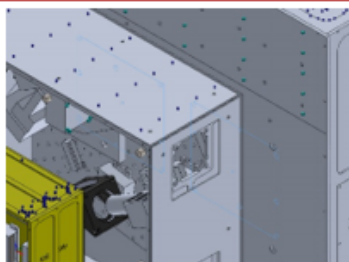
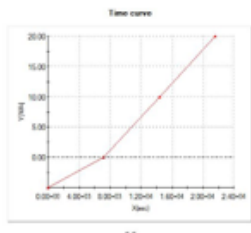
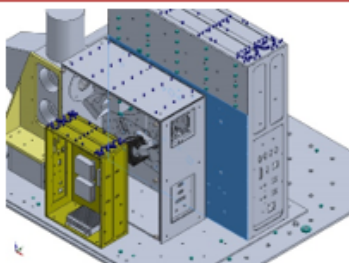
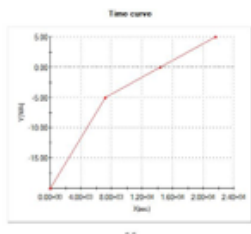
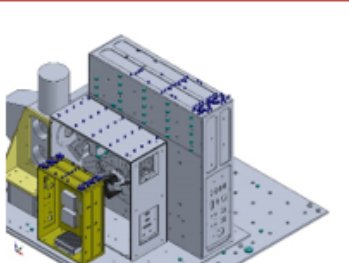
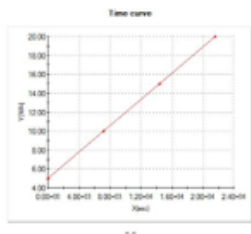
<p>MCT_Camera</p>		<p>Entities: 1 component Heat Power: 1 W Value: Time: on variation:</p>	 <p>Time curve</p>
<p>Ethernet_Switch</p>		<p>Entities: 1 component Heat Power: 6 W Value:</p>	
<p>VIPAC</p>		<p>Entities: 1 component Heat Power: 1 W Value: Time: on variation:</p>	 <p>Time curve</p>
<p>FTS_Control_Board</p>		<p>Entities: 1 component Heat Power: 5 W Value:</p>	

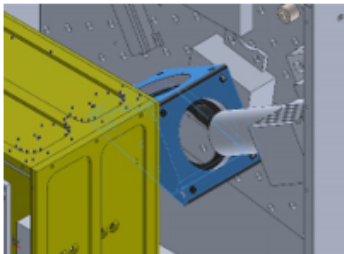
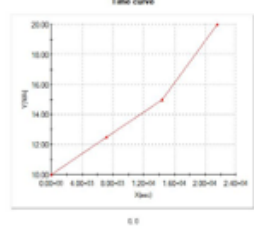
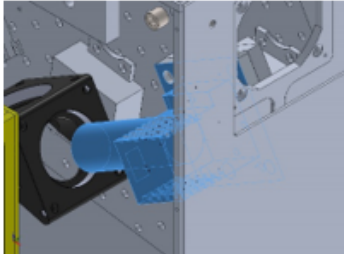
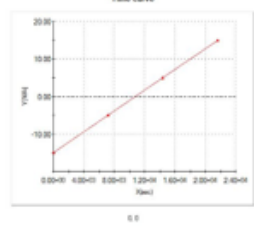
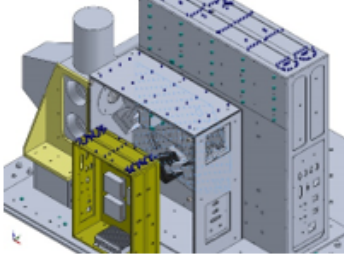
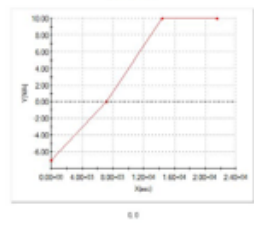
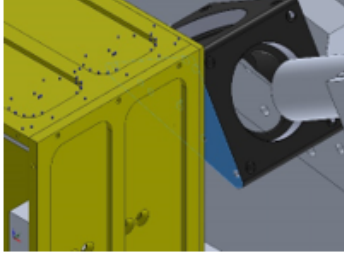
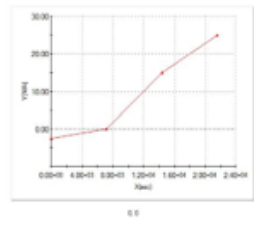
CPU_Stack_ 1		Entities: 1 component Heat Power Value: 1.25 W	
DAQ_Boards		Entities: 2 components Heat Power Value: 1 W Time variation: on	 <p style="text-align: center;">Time curve</p>
EBox_Temp _Controllers		Entities: 2 components Heat Power Value: 1.2 W	
CPU_Stack_ 2		Entities: 1 component Heat Power Value: 13 W	

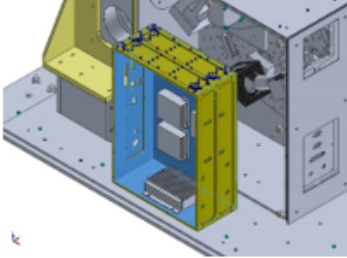
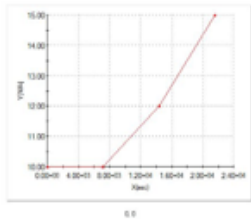
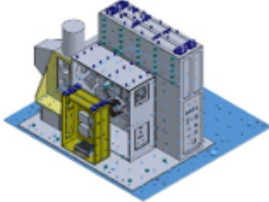
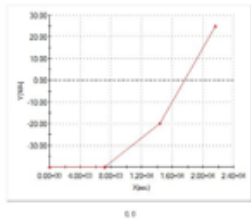
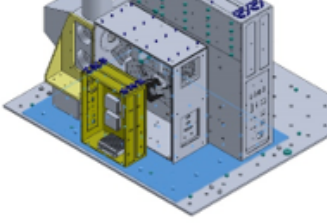
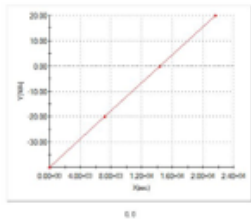
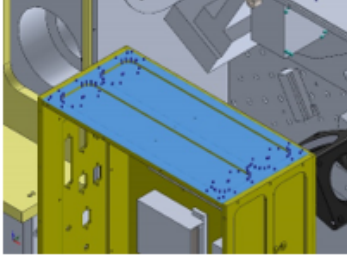
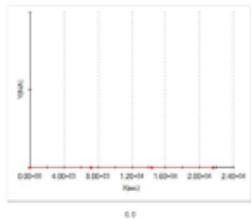
<p>DC-DC_Converter</p>		<p>Entities: 3 components Heat Power: 1 W Value: Time: on variation:</p>	 <p>Time curve</p>
<p>Motor_Controller</p>		<p>Entities: 1 component Heat Power: 1.5 W Value: Time: variation:</p>	
<p>EBox_Heater_1</p>		<p>Entities: 4 components Heat Power: 1 W Value: Time: on variation:</p>	 <p>Time curve</p>
<p>BB_EBox_Heater</p>		<p>Entities: 1 component Heat Power: 1 W Value: Time: on variation:</p>	 <p>Time curve</p>

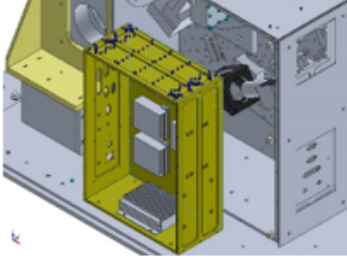
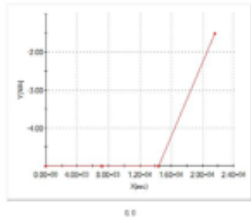
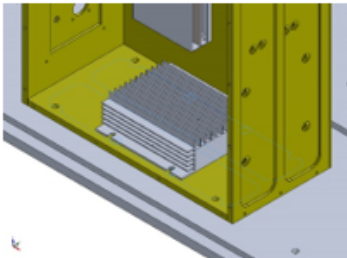
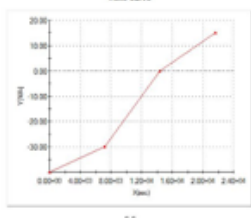
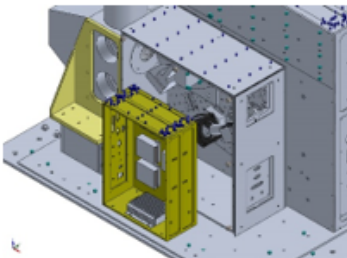
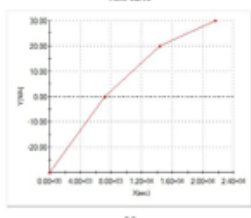
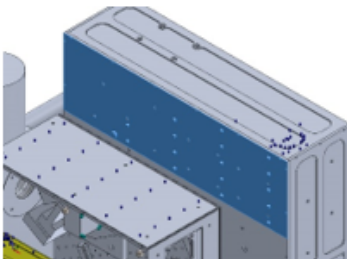
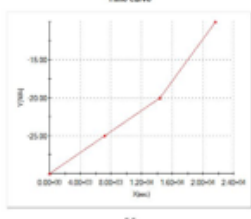
<p>External_Box _Rad</p>		<p>Entities: 26 face(s) Radiation Surface to Type: ambient Ambient 1 Celsius Temperature: Emissivity: 0.77 View Factor: 0.95 Time on variation:</p>	 <p>Time curve</p>
<p>BMXS_Rad</p>		<p>Entities: 2 face(s) Radiation Surface to Type: ambient Ambient 10 Celsius Temperature: Emissivity: 0.6 View Factor: 0.99</p>	
<p>Thor_Labs Plate</p>		<p>Entities: 1 face(s) Radiation Surface to Type: ambient Ambient 1 Celsius Temperature: Emissivity: 0.77 View Factor: 0.6 Time on variation:</p>	 <p>Time curve</p>
<p>OB_Bottom Plate_Rad</p>		<p>Entities: 3 face(s) Radiation Surface to Type: ambient Ambient 1 Celsius Temperature: Emissivity: 0.77 View Factor: 0.99 Time on variation:</p>	 <p>Time curve</p>

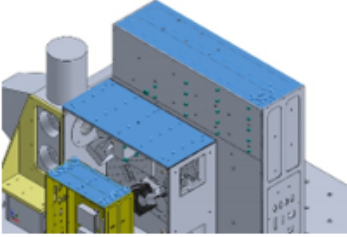
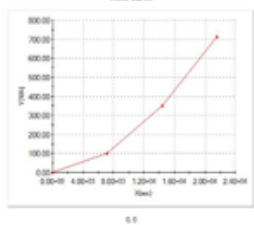
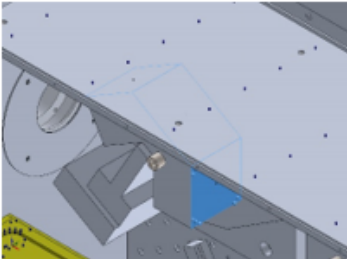
<p>OB_EBox_Facing_Plate_Rad</p>		<p>Entities: 1 face(s) Radiation Surface to Type: ambient Ambient 1 Celsius Temperature: Emissivity: 0.77 View Factor: 0.99 Time on variation:</p>	 <p>Time curve</p>
<p>Internal_Box_Rad</p>		<p>Entities: 10 face(s) Radiation Surface to Type: ambient Ambient 1 Celsius Temperature: Emissivity: 0.77 View Factor: 0.6 Time on variation:</p>	 <p>Time curve</p>
<p>BB_Rad</p>		<p>Entities: 24 face(s) Radiation Surface to Type: ambient Ambient 15 Celsius Temperature: Emissivity: 0.3 View Factor: 0.9</p>	
<p>OB_Inner_Box_Rad</p>		<p>Entities: 20 face(s) Radiation Surface to Type: ambient Ambient 1 Celsius Temperature: Emissivity: 0.77 View Factor: 0.95 Time on variation:</p>	 <p>Time curve</p>

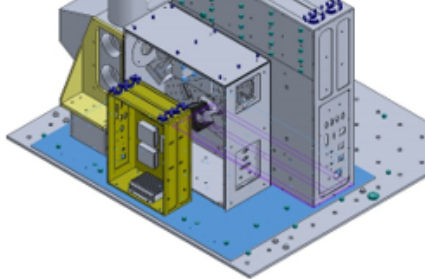
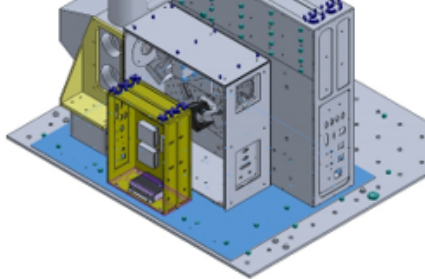
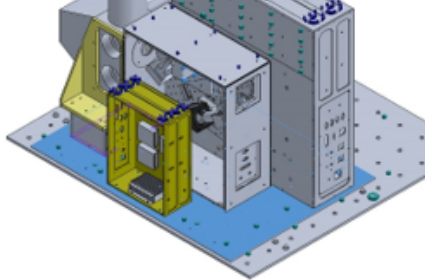
BB_Support_Rad		<p>Entities: 9 face(s) Radiation Surface to Type: ambient Ambient 15 Celsius Temperature: Emissivity: 0.77 View Factor: 0.9</p>	
DAQ_Boards_Rad		<p>Entities: 2 face(s) Radiation Surface to Type: ambient Ambient 1 Celsius Temperature: Emissivity: 0.6 View Factor: 0.95 Time on variation:</p>	 <p>Time curve</p>
EBox_OB_Facing_Plate_Rad		<p>Entities: 1 face(s) Radiation Surface to Type: ambient Ambient 1 Celsius Temperature: Emissivity: 0.77 View Factor: 0.95 Time on variation:</p>	 <p>Time curve</p>
Ebox_Cover_Plate		<p>Entities: 1 face(s) Radiation Surface to Type: ambient Ambient 1 Celsius Temperature: Emissivity: 0.77 View Factor: 0.95 Time on variation:</p>	 <p>Time curve</p>

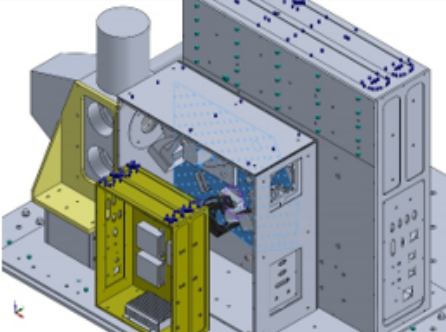
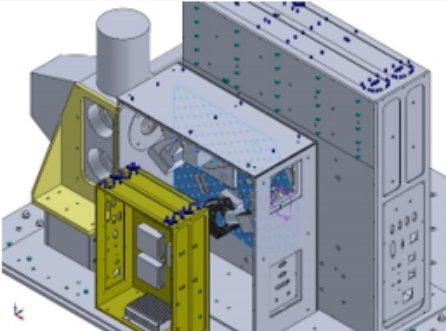
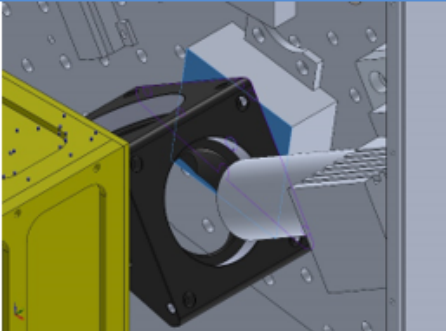
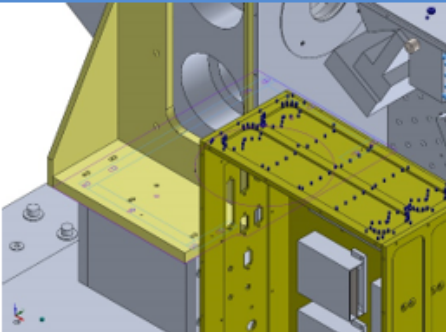
<p>Corner_Mirror</p>		<p>Entities: 7 face(s) Radiation Type: Surface to ambient Ambient Temperature: 1 Celsius Emissivity: 0.77 View Factor: 0.8 Time variation: on</p>	 <p>Time curve</p>
<p>MCT_Detector_Rad</p>		<p>Entities: 33 face(s) Radiation Type: Surface to ambient Ambient Temperature: 1 Celsius Emissivity: 0.95 View Factor: 0.95 Time variation: on</p>	 <p>Time curve</p>
<p>Thor_labs_radar_rad</p>		<p>Entities: 1 face(s) Radiation Type: Surface to ambient Ambient Temperature: 1 Celsius Emissivity: 0.77 View Factor: 0.75 Time variation: on</p>	 <p>Time curve</p>
<p>Corner_mirror_top_rad</p>		<p>Entities: 1 face(s) Radiation Type: Surface to ambient Ambient Temperature: 1 Celsius Emissivity: 0.77 View Factor: 0.95 Time variation: on</p>	 <p>Time curve</p>

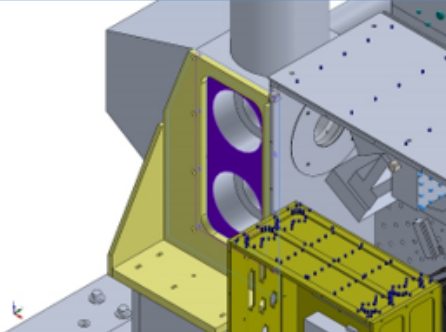
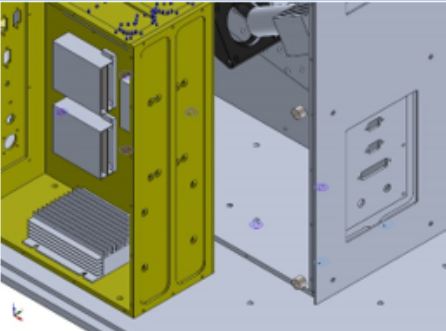
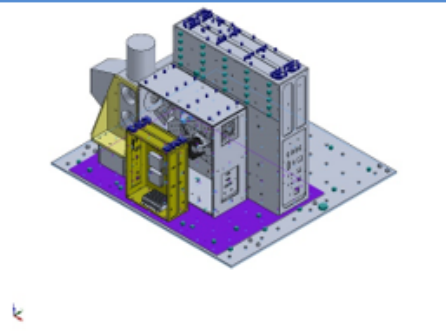
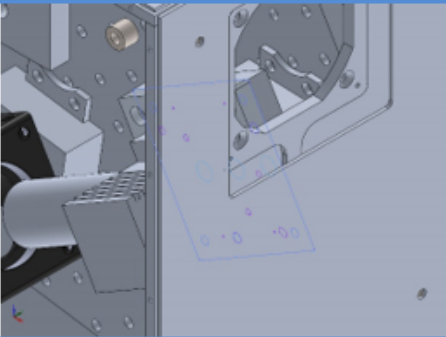
<p>bbebox_inner_rad</p>		<p>Entities: 6 face(s) Radiation Surface to Type: ambient Ambient 1 Celsius Temperature: Emissivity: 0.77 View Factor: 0.8 Time on variation:</p>	 <p>Time curve</p>
<p>gondola_rad</p>		<p>Entities: 2 face(s) Radiation Surface to Type: ambient Ambient 1 Celsius Temperature: Emissivity: 0.4 View Factor: 0.85 Time on variation:</p>	 <p>Time curve</p>
<p>instr_baseplate_rad</p>		<p>Entities: 2 face(s) Radiation Surface to Type: ambient Ambient 1 Celsius Temperature: Emissivity: 0.77 View Factor: 0.75 Time on variation:</p>	 <p>Time curve</p>
<p>bbebox_top_rad</p>		<p>Entities: 3 face(s) Radiation Surface to Type: ambient Ambient 1 Celsius Temperature: Emissivity: 0.77 View Factor: 0.85 Time on variation:</p>	 <p>Time curve</p>

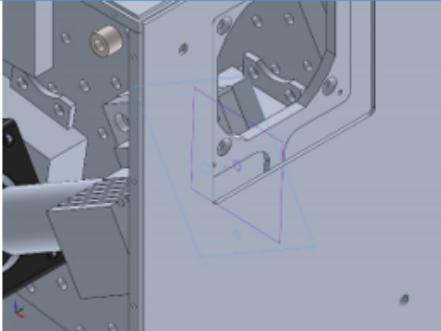
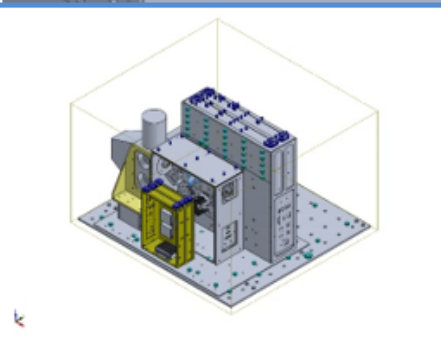
bbebox_rear_rad		<p> Entities: 1 face(s) Radiation Surface to Type: ambient Ambient 1 Celsius Temperature: Emissivity: 0.77 View Factor: 0.9 Time on variation: </p>	 <p>Time curve</p>
bbebox_bottom_rad		<p> Entities: 2 face(s) Radiation Surface to Type: ambient Ambient 1 Celsius Temperature: Emissivity: 0.77 View Factor: 0.99 Time on variation: </p>	 <p>Time curve</p>
optics_out_facing_plate_rad		<p> Entities: 1 face(s) Radiation Surface to Type: ambient Ambient 1 Celsius Temperature: Emissivity: 0.77 View Factor: 0.5 Time on variation: </p>	 <p>Time curve</p>
Radiation-28		<p> Entities: 1 face(s) Radiation Surface to Type: ambient Ambient 1 Celsius Temperature: Emissivity: 0.77 View Factor: 0.95 Time on variation: </p>	 <p>Time curve</p>

Heat Flux-1		Entities: 7 face(s) Heat Flux 1 W/m ² Value: Time on variation:	 <p style="text-align: center;">Time curve</p>
Radiation-30		Entities: 3 face(s) Radiation Surface to Type: ambient Ambient 30 Celsius Temperature: Emissivity: 0.3 View Factor: 0.9	

Contact	Contact Image	Contact Properties
Contact Set - Ebox to Baseplate		Type: Thermal Resistance Entites: 6 face(s) Thermal Distributed Resistance: Value: 0.16(K.m ²)/W Advanced: Node to surface
Contact Set - BBEbox to Baseplate		Type: Thermal Resistance Entites: 6 face(s) Thermal Distributed Resistance: Value: 0.16(K.m ²)/W Advanced: Node to surface
Contact Set - BB Support to Baseplate		Type: Thermal Resistance Entites: 6 face(s) Thermal Distributed Resistance: Value: 0.16(K.m ²)/W Advanced: Node to surface

<p>Contact Set-16052</p>		<p>Type: Thermal Resistance Entites: 2 face(s) Thermal Distributed Resistance: Value: $0.2(K.m^2)/W$ Advanced: Node to surface</p>
<p>Contact Set-16053</p>		<p>Type: Thermal Resistance Entites: 2 face(s) Thermal Distributed Resistance: Value: $0.2(K.m^2)/W$ Advanced: Node to surface</p>
<p>Contact Set-16055</p>		<p>Type: Thermal Resistance Entites: 2 face(s) Thermal Distributed Resistance: Value: $0.2(K.m^2)/W$ Advanced: Node to surface</p>
<p>Contact Set-16169</p>		<p>Type: Thermal Resistance Entites: 6 face(s) Thermal Distributed Resistance: Value: $0.2(K.m^2)/W$ Advanced: Node to surface</p>

<p>Contact Set-16170</p>		<p>Type: Thermal Resistance Entites: 2 face(s) Thermal Distributed Resistance: Value: $0.5(K.m^2)/W$ Advanced: Node to surface</p>
<p>Contact Set-17083</p>		<p>Type: Thermal Resistance Entites: 14 face(s) Thermal Distributed Resistance: Value: $0.16(K.m^2)/W$ Advanced: Node to surface</p>
<p>Contact Set-17762</p>		<p>Type: Thermal Resistance Entites: 12 face(s) Thermal Distributed Resistance: Value: $0.16(K.m^2)/W$ Advanced: Node to surface</p>
<p>Contact Set-18780</p>		<p>Type: Bonded contact pair Entites: 2 face(s)</p>

<p>Contact Set-19011</p>		<p>Type: Thermal Resistance Entites: 2 face(s) Thermal Distributed Resistance: Value: $0.12(\text{K}\cdot\text{m}^2)/\text{W}$ Advanced: Node to surface</p>
<p>Global Contact</p>		<p>Type: Bonded Components: 1 component(s) Options: Compatible mesh</p>